STUDY OF A CATALYTIC PLATE REACTOR DESIGNED WITH DISTRIBUTED COATINGS OF REFORMING AND COMBUSTION CATALYSTS FOR HYDROGEN PRODUCTION BY COMBUSTION ASSISTED METHANE STEAM REFORMING

ÉTUDE D'UN RÉACTEUR À PLAQUES CATALYTIQUES CONÇU AVEC DES REVÊTEMENTS RÉPARTIS DE CATALYSEURS DE REFORMAGE ET DE COMBUSTION POUR LA PRODUCTION D'HYDROGÈNE PAR REFORMAGE DE VAPEUR DE MÉTHANE ASSISTÉE PAR LA COMBUSTION

A Thesis Submitted to the Division of Graduate Studies
of the Royal Military College of Canada
by

Mayur Mundhwa

In Partial Fulfillment of the Requirements for the Degree of
Doctor of Philosophy

January, 2018

This dissertation is lovingly dedicated to my
parents Rajuben & Arjunbhai Mundhwa
for their unconditional love & support

Acknowledgments

It is my pleasure to acknowledge and extend my gratitude to my supervisor, my family, friends and colleagues who were instrumental for completion of my Ph.D. work.

My deepest appreciation belongs to my parents Rajuben and Arjunbhai Mundhwa and my wife Parul Mundhwa for their love, emotional support, patience and understanding throughout my study.

I would like to say special thanks to my supervisor Dr. Christopher P. Thurgood for giving me the opportunity to pursue Ph.D. study and for the financial support. I especially admire his patience, calmness and words of encouragement during some bumpy rides of PhD study. I would like to acknowledge my friends Dr. Rajesh Parmar and Mr. Barath Jayasankar. It was a great pleasure working with them and I appreciate their ideas and help in developing Comsol models and Matlab programing code. I would also like to acknowledge Dr. Aidu Qi, Mr. Bob Whitehead, Dr. Wojtek Halliop, and Mrs. Elzbieta Halliop for their help and suggestions in conducting an experimental study.

I would also like to say special thanks to Dr. Barbara Zeeb and Dr. Danny Pagé for their encouragement to think positive during some difficult phase of life.

I would like to express my gratitude to the Ph.D. committee members: Dr. Kim McAuley, Dr. Kiari Goni Boulama, Dr. Danny Pagé and the Ph.D. committee chair: Dr. Daniel Lagace-Roy.

These acknowledgements would not be completed without mentioning my friends and colleagues: Harsh Dhingra, Nakkiran Arulmozhi, Aida Khosravi, Negar Manafi, and Trevor Wartman.

Abstract

Syngas plays an important role in various catalytic processes such as Fisher-Tropsch synthesis, methanol synthesis and hydroformylation. Hydrogen from syngas is widely used in the production of ammonia, in petroleum industry and as a clean energy carrier in fuel cells. Increase in energy consumption due to population growth and the pressure of decarbonizing the earth's atmosphere demands the deployment of more clean energy technologies such as fuel cell. It is expected that fuel cell will play a key role in combating against global pollution while a transition from carbon economy to low-carbon economy takes place. Thus, the demand for hydrogen, the most important fuel for fuel cells and now emerging as a universal energy carrier, will also continue to rise. To produce hydrogen via reforming, methane is the desired fuel of choice due to its lowest carbon content and low cost. Due to the missing hydrogen infrastructure, on-board hydrogen production via methane steam reforming (MSR) in an efficient reformer is one of the most cost-effective solutions to increase the use of fuel cells.

MSR is highly endothermic process, thus, requires an efficient way of supplying heat. This can be achieved by spatial segregation of MSR and heat exchanging medium (*e.g.* exothermic methane combustion (MC)) in a catalytic plate reactor (CPR). In a CPR design, MSR and the exothermic MC are carried out in alternating parallel channels. However, the use of highly exothermic MC creates large thermal gradients and hot-spot due to the imbalance of heat liberating at faster rate in MC and absorbing at relatively slower rate in MSR. Such imbalance of heat causes problems of catalysts delamination, material failure, reduction in catalytic surface area and low conversions in a conventional CPR where reforming and combustion catalysts are coated continuously.

With the aim of making CPR design free from large thermal gradients and hotspot, this study proposes a novel concept of distributed coating design for both reforming and combustion catalysts. Detailed multiphysics 2-D steady-state numerical models of a CPR are developed to investigate the performance of distributed coatings of reforming and combustion catalysts compared to the conventional continuous coatings. It is found that the proposed distributed coating design not only improves the production of hydrogen but also reduces hotspot and thermal gradients significantly compared to the continuous coatings. As a result, it is concluded that the proposed distributed coatings of reforming and combustion catalysts can resolve the problems of catalysts delamination, material failure, reduction in catalytic surface area and low conversions. The thesis also determined that the distributed coatings improve the utilization of both reforming and combustion catalysts by saving the quantity of combustion-catalyst up to 74% and reforming-catalyst up to 28%. To make the MSR more energy efficient, this study also conducted an experimental investigation of MSR over nickel-spinel catalyst at low SC ratios in a packed bed reactor. To fit the experimental data, sensitive parameters of a surface microkinetic model of MSR over Ni catalyst are optimized. It is found that the microkinetic model predicts the experimental data quite well after optimizing only 12 out of 78 kinetic parameters.

Résumé

Le gaz de synthèse joue un rôle important dans divers processus catalytiques tels que la synthèse de Fischer-Tropsch, la synthèse du méthanol et l'hydroformylation. L'hydrogène issu du gaz de synthèse est largement utilisé dans la production d'ammoniac, dans l'industrie pétrolière et comme vecteur d'énergie propre dans les piles à combustible. L'augmentation de la consommation d'énergie due à la croissance démographique et à la pression de la décarbonisation de l'atmosphère terrestre exige le déploiement de technologies plus propres telles que les piles à combustible. On s'attend à ce que la pile à combustible joue un rôle clé dans la lutte contre la pollution mondiale alors qu'une transition de l'économie de carbone vers une économie sobre en carbone a lieu. Ainsi, la demande l'hydrogène, le carburant le plus important pour les piles à combustible et qui émerge aujourd'hui en tant que vecteur énergétique universel, continuera également d'augmenter. Pour produire de l'hydrogène en le reformant, le méthane est le combustible de choix en raison de sa teneur en carbone la plus faible et de son faible coût. En raison de l'infrastructure d'hydrogène manquante, la production d'hydrogène embarquée par reformage à la vapeur de méthane (MSR) dans un reformeur efficace est l'une des solutions les plus rentables pour augmenter l'utilisation des piles à combustible.

MSR est un processus hautement endothermique, donc, nécessite un moyen efficace de fournir de la chaleur. Ceci peut être réalisé par une ségrégation spatiale de MSR et de milieu d'échange de chaleur (par exemple, combustion de méthane exothermique (MC)) dans un réacteur à plaques catalytiques (CPR). Dans une conception de CPR, MSR et le MC exothermique sont effectués dans des canaux parallèles alternatifs. Cependant, l'utilisation de MC hautement exothermique crée de grands gradients thermiques et un point chaud en raison du déséquilibre de la chaleur libérée à un rythme plus rapide dans le MC et absorbant à un rythme relativement plus lent dans le MSR. Un tel déséquilibre de chaleur cause des problèmes de délaminage des catalyseurs, de rupture de matériau, de réduction de la surface catalytique et de faibles conversions dans un CPR classique où les catalyseurs de reformage et de combustion sont revêtus en continu.

Dans le but de rendre la conception de CPR exempte de grands gradients thermiques et de hotspot, cette étude propose un nouveau concept de conception de revêtement distribué pour les catalyseurs de reformage et de combustion. Des modèles numériques multi-physiques détaillés à l'état d'équilibre 2D d'un CPR sont développés pour étudier la performance de revêtements distribués de catalyseurs de reformage et de combustion par rapport aux revêtements continus conventionnels. On trouve que la conception de revêtement distribué proposée améliore non seulement la production d'hydrogène, mais réduit également les gradients thermiques et les points chauds de façon significative par rapport aux revêtements continus. En conséquence, il est conclu que les revêtements distribués proposés des catalyseurs de reformage et de combustion peuvent résoudre les problèmes de délaminage des catalyseurs, de défaillance des matériaux, de réduction de la surface catalytique et de faibles conversions. La thèse a également déterminé que les revêtements distribués améliorent l'utilisation des catalyseurs de reformage et de combustion en économisant jusqu'à 74% de catalyseur de combustion et 28% de catalyseur de reformage. Pour rendre le MSR plus économe en énergie, cette étude a également mené une étude expérimentale de MSR sur un catalyseur nickel-spinelle à des rapports SC bas dans un réacteur à lit fixe. Pour ajuster les données expérimentales, les paramètres sensibles d'un modèle microkinésique de surface du catalyseur MSR sur Ni sont optimises. On trouve que le modèle microkinétique prédit assez bien les données expérimentales après l'optimisation de seulement 12 des 78 paramètres cinétiques.

Co-Authorship Statement

The technical contents presented in Chapters 3, 4 and 5 have been published in the refereed journals as indicated in the respective chapters. Chapter 6 is submitted and is currently under review in a scientific journal. I prepared the manuscript drafts with all analysis, calculations, equations, figures and tables. Dr. Thurgood is the co-author of all four manuscripts and Dr. Rajesh D. Parmar is the co-author of the manuscript presented in Chapter 4 only. Dr. Thurgood has suggested revisions for this thesis and provided technical advice.

Table of Contents

List of Tables

List of Figures

List of Nomenclatures

Acronyms

ATR	AutoThermal Reforming
CCCR	Continuous Combustion-catalyst and Continuous Reforming-catalyst
CCSR	Continuous Combustion-catalyst and Segmented Reforming-catalyst
CFD	Computational Fluid Dynamics
CLCC	Continuous Layers of Combustion-catalyst
COP	Conference of Parties
CPR	Catalytic Plate Reactor
DCCR	Distributed Combustion-catalyst and Continuous Reforming-catalyst
DCDR	Distributed Combustion-catalyst and Distributed Reforming-catalyst
FEM	Finite Element Method
GHG	Greenhouse Gases
LHV	Lower Heating Value
MC	Methane Combustion
MSR	Methane Steam Reforming
PCM	Phase Change Material
POX	Partial Oxidation
SC	Steam to Carbon ratio
SCCR	Segmented Combustion-catalyst and Continuous Reforming-catalyst
SCSR	Segmented Combustion-catalyst and Segmented Reforming-catalyst
SLCC	Segmented Layers of Combustion-catalyst
SR	Steam Reforming
STP	Standard Temperature and Pressure
USA	United States of America
YSZ	Yttria Stabilized Zirconia

Greek symbols

β	temperature parameter
Γ	site density, $\mathrm{mol\cdot m^{-2}}$

δ	thickness, mm
ε	porosity
η	effectiveness factor
θ	surface coverage
κ	permeability, m^2
μ	viscosity, kg s^{-1} m^{-1}
ρ	density, kg m^{-3}
σ	site occupancy number
τ	tortuosity
v	diffusion volume

Notations

$\mathrm{H_2}$	hydrogen
$\mathrm{H_2O}$	steam or water
k_B	Boltzmann constant, 1.38064852 × 10^{-23} J/K
$\mathrm{N_2}$	nitrogen
N_A	Avogadro number, 6.0221409 × 10^{23} atoms/mol
$\mathrm{O_2}$	oxygen
R_g	ideal-gas constant
$\mathrm{Y_2O_3}$	yttrium(III) oxide
$\mathrm{ZrO_2}$	zirconium dioxide
A_s	specific surface area, $m^2 \cdot m^{-3}$
C_p	heat capacity, $J \cdot kg^{-1} \cdot K^{-1}$
2D	two-dimensional
Al	aluminium
$\mathrm{CH_4}$	methane
$\mathrm{CO_2}$	carbon dioxide
CO	carbon monoxide
Cr	chromium
D	dispersion
E	efficiency, %
Fe	iron
L	total length of active catalyst, mm or cm
m	mass flow rates ratio
Ni	nickel
O	oxygen atom
Pt	platinum

Rh	rhodium,
Ru	ruthenium
S	selectivity
X	conversion, %
Y	yield, %
A	pre-exponential factor
C	concentration, mol·m^{-3}
D	diffusion coefficient, m^{2}·s^{-1}
E	energy, J
M	molecular weight, g·mol^{-1}
N	molar flow rate, mol·h^{-1}
P	pressure, atm., or Pa
R	reaction rate, mol·m^{-3}
S	sticking coefficient
T	temperature, K
V	volume, cm^{3}
d	diameter, nm
k	rate constant
k	thermal conductivity, W·m^{-1}·K^{-1}
l	active length of each distributed section or inter-catalysts space distance, mm
m	mass, g
r	reaction, mol·m^{-2}·s^{-1}
s	overall reaction rate, mol·m^{-2}·s^{-1}
subscript	
MC	methane combustion
MSR	methane steam reforming
a	activation
$active$	active catalyst
$blank$	inter-catalyst space
c	combustion
i	chemical specie i
j	chemical specie j
$plate$	metal plate between reforming and combustion flow channels
r	reforming
Superscript	
F	Fickian
K	Knudsen

MS	Maxwell-Stefan
ads	adsorption
cat	catalyst
des	desorption

Chapter 1

Introduction

Worldwide population growth and industrialization have threatened the continuous production and supply of energy. Increase in energy consumption and the pressure of decarbonizing the earth's atmosphere demands the deployment of more clean energy production technologies such as fuel cells. It is expected that fuel cell will play a key role in combating against the global pollution while a transition from the carbon economy to low-carbon economy and eventually carbon-free economy takes place.

1.1. World's future energy demand and greenhouse gas emission

As per the World Energy Outlook 2015 report [1], published by the International Energy Agency (IEA), the world's primary energy demand will grow to 45% and electricity demand is projected to grow 81% by 2035. Hence, it is expected that the emission of the greenhouse gases will also increase if all nations continue to produce required energy using fossil fuels. United Nations' Climate Conference (COP21) held in Paris during 2015 had negotiated the Paris Agreement to achieve the target for global warming to peak at 2 °C above the temperature in the pre-industrial era and had sought to deliver a clear pathway with short and long-term milestones [2].

Fig. 1.1(A) illustrates the top 20 largest greenhouse gas (GHG) emitter countries in 2015, accounting for 79.25 % of the world's total emission [3]. In the list of top 20, China, the United States, India and Russia are the four largest GHG emitters, sharing 56% of the world's total. Even though developing countries like India is in the list of the top four, its emission per capita is very low (ranked 125). Amongst 20 largest emitters, Australia, Saudi Arabia, the USA and Canada have occupied the top four spots for the largest GHG emitters per capita, respectively. Fig. 1.1 (B) shows GHG emission per capita data from 1990 to 2015 for Australia, Saudi Arabia, the USA and Canada [3]. To mitigate the problems of GHG emission, Canada has recently announced an ambitious target to reduce its emission per capita to 20% below 2015 level by 2030 [4].

To achieve Canada's target of reducing its GHG emission, fuel cell technology can play an important role in producing clean electricity while keeping the GHG emission at minimum level. Due to the commitment made by many countries to move forward in the direction of low-carbon economy, it is expected that the demand of fuel cells along with other clean energy technologies will continue to increase all over the world. Thus, the demand for hydrogen (H_2), the most important fuel for fuel cells and now emerging as a universal energy carrier, will also continue to rise. In 2015, global H_2 production was amounted between 61 and 65 million metric tons and

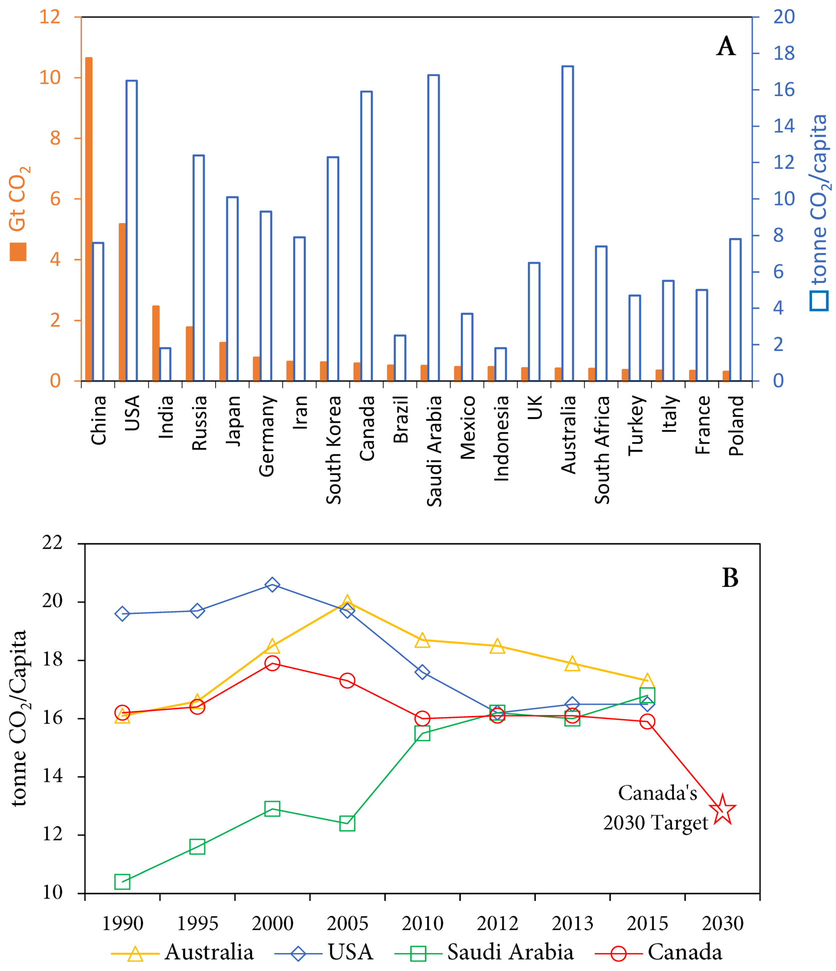

Fig. 1.1 (A) *Top 20 largest greenhouse gas emitter countries in 2015*, (B) *Greenhouse gas emission per capita (1990 to 2015) of Australia, Saudi Arabia, the USA and Canada*.

is expected to grow further [5]. Prediction suggested that H_2 usage for sectors other than petroleum and chemicals will grow to nearly 3.5 billion kg by 2030 [6].

1.2. Hydrogen production

Unlike electric batteries, a fuel-cell does not run down or require recharging; it produces continuous electricity as long as H_2 and oxidizer are supplied continuously to the cell. Though H_2 is considered as the most abundant fuel in the universe, pure H_2 exists in a very limited quantity on our planet. Therefore, various methods are developed to produce H_2 from its primary sources. Two methods most commonly in use are: (1) reforming and (2) electrolysis. Reforming involves H_2 separation from water and carbon compounds such as methane (CH_4), whereas electrolysis involves H_2 separation from oxygen (O_2) in water (H_2O). The production of H_2 via electrolysis is not a viable choice for the power backup option and off-grid locations, because it requires electricity to produce H_2. Hence, to increase the wide spread use of fuel cells, onsite production of H_2 via reforming of hydrocarbons could be the effective solution. To produce H_2 via reforming, CH_4 is the desired fuel of choice due to its lowest carbon content and recent discoveries of vast reserves of shale gas have further strengthen its choice for the next 30 to 40 years [7]. The selection of methane in this work to investigate the reforming operation can also be considered as a representative component for the reforming of higher hydrocarbons such as ethanol, gasoline, or diesel. Recently, Parmar [8] studied the gas-phase and surface kinetics of diesel reforming and reported that after the first millimetre of a reforming-catalyst, higher hydrocarbons fragment into smaller hydrocarbons and reforming of smaller hydrocarbons is responsible for hydrogen generation. Thus, CH_4 being the smaller component in the series of hydrocarbons, could be considered as a representative component for higher hydrocarbons and results of reforming operation obtained using CH_4 could be utilize for deducing the performance of a reformer for the reforming of higher hydrocarbons. To sustain the fuel cell technology for a long-term, biomass-derived biogas (mainly CH_4) or biofuels (*e.g.* bioethanol, biodiesel) are the promising pathway for the production of carbon-neutral hydrogen.

The production of H_2 from CH_4 is carried out by three major processes: (1) steam reforming (SR), (2) autothermal reforming (ATR) and (3) partial oxidation (POX). SR is a highly endothermic process, whereas POX is the exothermic and ATR is a combination of SR and POX. Among these three major processes, SR provides the maximum H_2 concentration and H_2 yield [9]. However, due to its highly endothermic nature, SR requires an efficient way of supplying heat to its endothermic reaction sites. Mostly, SR is carried out in a fixed-bed catalytic reactor with high residence time [10]. But the fixed-bed reactor design suffers from limitations such as heat-transfer and internal diffusion, which has led to the study of alternative and efficient reactor design such as catalytic plate reactor/reformer (CPR).

A CPR design provides an excellent heat and mass transfer characteristics compared to the conventional fixed-bed design [11]. In a CPR design (Fig 1.2), thin metal plates coated with appropriate catalysts are closely arranged in a parallel fashion, where the endothermic methane steam reforming (MSR) and the exothermic catalytic methane combustion (catalytic MC) are carried out in alternating channels [11]. Due to channel's dimensions in the micrometer to millimeter range, a CPR design can intensify both MSR and MC by increasing the rates of heat, mass and momentum transfer and by improving the surface area to volume ratio [12]. Consequently, conversion, yield and catalysts utilization can be improved, which reduces capital

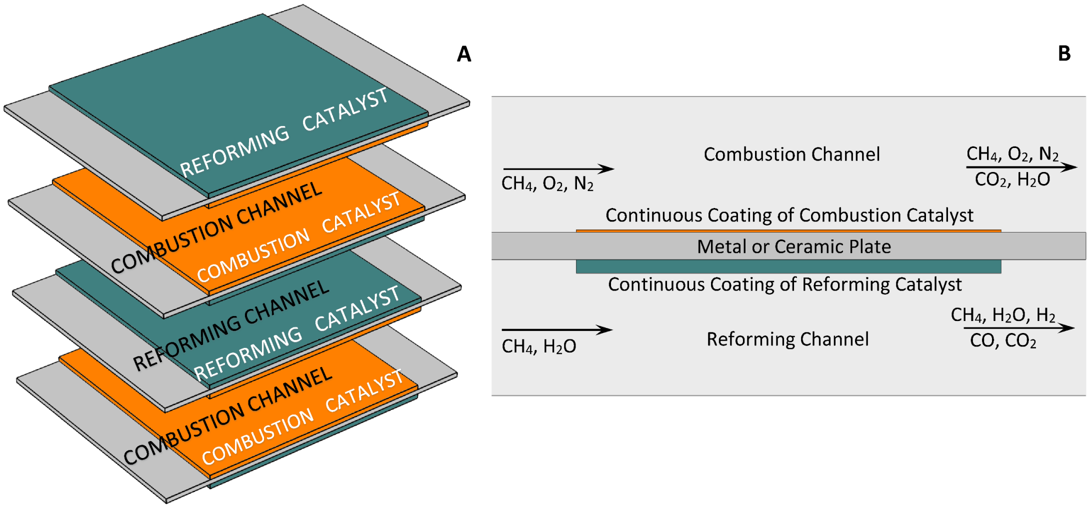

Fig. 1.2 (A) *3D view of a simplified catalytic plate reactor (CPR) design*, (B) *2D view of a simplified catalytic plate reactor (CPR) design*.

and operating cost of the MSR process. Thus, adopting a CPR design and supplying the heat by the exothermic MC can greatly enhance the efficiency, effectiveness and productivity of a CPR. Also, the use of catalytic combustion to supply heat offers advantages over the gas-phase combustion. Catalytic combustion takes place at a lower temperature than the gas-phase combustion, which reduces NO_x formation and the lower operating temperature allows more material choices in designing a CPR [11]. However, the use of highly exothermic MC creates steep thermal gradients and hot-spot in a CPR due to an imbalance of the heat liberating at a faster rate in MC and absorbing at a relatively slower rate in MSR [13]. Such thermal imbalance causes problems of material failure and catalyst delamination due to different thermal expansion coefficients of the coated catalyst and the metal plate. Large thermal-gradients also reduce the catalytic active surface area, and as a result conversion of reactants [14].

As show in Fig. 1.2, CPR design looks simple but physical and chemical phenomena happening on both sides of the plate is very complex and hence it is not easy to capture all phenomena experimentally. To co-ordinate all physical and chemical phenomena and resolve issues of hot-spot and thermal gradients, development of an accurate numerical model is necessary which can predict CPR performance under varying design and operating parameters.

Catalyst layers that are coated on both sides of the plate surfaces (Fig. 1.2) in fact consisting of porous structures. To increase the active surface area, active sites of catalyst are distributed inside the porous structures. In a CPR, reactants in the flow channels diffuse from the bulk gas phase to the porous catalyst layers and react at the active sites of the catalyst. After reaction, products diffuse back to the bulk flow from the catalyst layer through pores. The diffusion rates of the reactants and products toward and away from the active sites may lead to a reduced overall reaction rate. At low temperatures, chemical reactions are slow, and therefore their kinetics is the rate limiting step of the process. At higher temperatures, when the rate of diffusion is slow compared to the intrinsic rate of reaction, mass transport does affect the rate of reaction, and the process becomes diffusion limited. Therefore, it becomes important to include internal mass transfer limitations in CPR model to accurately predict its performance.

Traditionally, the production of H_2 via MSR is carried out over nickel (Ni) based catalysts with steam to carbon (SC) ratio of three or above to avoid carbon formation [15–19]. The SC ratio of three or above is very high compared to the reforming reaction stoichiometric ratio of one. High SC ratio dilutes the syngas content and is energetically unfavorable due to the requirements of more energy to produce excess steam in a boiler at the reformer upstream and to condense unreacted steam in a condenser at the reactor downstream. Noble metals such as rhodium (Rh) and ruthenium (Ru) based catalysts are more resistant to carbon formation than the traditional Ni based catalysts. However, due to excessive cost and limited availability of the noble metals, it is more profitable to use Ni based catalysts which can be more resistant to carbon accumulation and can exhibit long term stability at low SC ratios.

1.3. Thesis aims

The main aim of the present work is to study the novel distributed coating design for both combustion and reforming catalysts in a CPR using computational fluid dynamic (CFD) tool with the objective to reduce steep thermal gradients and thermal hot spots by balancing the liberation of heat in the exothermic MC and absorption of heat in the endothermic MSR. The mathematical models are based on two-dimensional flow with energy and species continuity equations. Chemical reactions at the surface are computed by implementing multi-step microkinetic model. The second aim of this thesis is to carry out experimental work of MSR over a promising Ni based catalyst at low SC ratios. As mentioned earlier the use of low SC ratio in MSR could reduce the intake of energy at reactor's upstream and downstream. With these aims, following sub-steps are carried out in this study.

1. Perform CFD study of different distributed (or segmented) coating configurations between reforming and combustion catalysts to identify their influence on the overall performance of a CPR and compare the designs with the conventional continuous coating design.
2. Investigate the influence of distributed combustion-catalyst on the performance of MSR by varying design and operating parameters.
3. Carry out experimental study to test Ni based catalyst at low SC ratios and validate a microkinetic model by optimizing the kinetic parameters of the most sensitive reaction steps.
4. Carry our detail numerical modeling study of various patterns of the distributed reforming and combustion catalysts in a CPR by implementing an optimized microkinetic model to determine the best performing distributed coating design at low SC ratio.

1.4. Thesis structure

The thesis is divided into seven chapters. Chapter 1 introduces the need of a clean technologies to generate required energy and outlines the issues associated with the catalytic plate reactor design to generate hydrogen from methane followed by the thesis's objectives and its structure. Chapter 2 introduces briefly various reforming processes to produce hydrogen from methane and provides a review of the existing literature on the surface kinetics of MSR over Ni catalyst, kinetics of catalytic MC over platinum catalyst and identifies the current research needs based on a literature review of catalytic plate reactor for MSR. Chapter 3 investigates the performance of a CPR designed with various coating configurations between reforming and combustion catalysts using numerical approach and discusses how various coating configurations affect the distribution of temperature and productivity in a CPR. Chapter 3 is published in the *Fuel Processing Technology* journal. Chapter 4 investigates the influence of distributed coating design of a combustion-catalyst on MSR under varying design and operating parameters. The results obtained with distributed combustion-catalyst are compared against the conventional continuous coating design. Chapter 4 is published in the *Journal of Power Sources*. Chapter 5 discusses experimental work of MSR over promising Ni-spinel catalyst at low SC ratios in a packed bed reactor under plug-flow condition. Chapter 5 also presents the optimization procedure of estimating kinetic parameters of the most sensitive reaction steps from a multi-step microkinetic model. Chapter 5 is published in the Fuel Processing Technology journal. Chapter 6 presents a numerical analysis of a CPR designed with different patterns of distributed coatings of reforming and combustion catalysts by implementing an optimized microkinetic model of MSR over Ni-spinel catalyst to obtain the best performing distributed coating design. Chapter 6 also presents the study of internal diffusion limitation by considering different thickness of reforming and combustion catalysts as well as investigates the performance of distributed and continuous catalysts layers coated on different plate-thicknesses. Chapter 7 presents an overall summary, conclusions and contributions of the thesis and concluded by recommending the future work.

1.5. References

[1] International Energy Agency (2015), World Energy Outlook Report. Retrieved from http://www.iea.org/publications/freepublications/publication/WEO2015.pdf

[2] Robbins A. How to understand the results of the climate change summit: Conference of Parties21 (COP21) Paris 2015. Journal of Public Health Policy. 2016 1-4.

[3] Olivier JG, Janssens-Maenhout G, Muntean M, Peters JA. Trends in global CO_2 emissions: 2015 report. The Hague, Netherlands: PPBL Netherlands Environmental Assessment Agency; Ispra: European Commission, Joint Research Centre. 2015.

[4] McDiarmid M. Canada sets carbon emissions reduction target of 30% by 2030. Retrieved from http://www.cbc.ca/news/politics/canada-sets-carbon-emissions-reduction-target-of-30-by-2030-1.3075759.

[5] Joseck F, Nguyen T, Klahr B, Talapatra A. Current U.S. hydrogen production. DOE Hydrogen and Fuel Cells Program Record. 2016 May 24.

[6] Navigant Research. Demand for hydrogen for fuel cells and other emerging markets will climb sharply through 2030. Retrieved from, http://www.navigantresearch.com/newsroom/demand-for-hydrogen-for-fuel-cellsand-other-emerging-markets-will-climb-sharply-through-2030.

[7] Gür TM. Comprehensive review of methane conversion in solid oxide fuel cells: Prospects for efficient electricity generation from natural gas. Progress in Energy and Combustion Science. 2016 May 31;54:1-64.

[8] Parmar RD. A combined gas-phase and surface reaction mechanistic model of diesel surrogate reforming for SOFC application. Ph.D. thesis, Queen's University, Kingston, Canada; 2013.

[9] Kolb G. Fuel processing: for fuel cells. Wiley-VCH Verlag GmbH & Co. KGaA; 2008.

[10] Rostrup-Nielsen JR, Christiansen LJ, Hansen JH. Activity of steam reforming catalysts: role and assessment. Applied Catalysis. 1988 Jan 1;43(2):287-303.

[11] Zanfir M, Gavriilidis A. Catalytic combustion assisted methane steam reforming in a catalytic plate reactor, Chemical Engineering Science 58 2003 Sep 30;58(17):3947-60.

[12] Lerou JJ, Tonkovich AL, Silva L, Perry S, McDaniel J. Microchannel reactor architecture enables greener processes. Chemical Engineering Science. 2010 Jan 1;65(1):380-5.

[13] Pattison RC, Baldea M. Robust autothermal microchannel reactors. Computers & Chemical Engineering. 2015 Oct 4;81:171-9.

[14] Bartholomew CH. Mechanisms of catalyst deactivation. Applied Catalysis A: General. 2001 Apr 30;212(1):17-60.

[15] Xu J, Froment GF. Methane steam reforming, methanation and water-gas shift: I. Intrinsic kinetics. AIChE Journal. 1989 Jan 1;35(1):88-96.

[16] Trimm DL. Catalysts for the control of coking during steam reforming. Catalysis Today. 1999 Feb 24;49(1):3-10.

[17] Hou K, Hughes R. The kinetics of methane steam reforming over a Ni/α-Al2O3 catalyst. Chemical Engineering Journal. 2001 Mar 15;82(1):311-28.

[18] Wei J, Iglesia E. Isotopic and kinetic assessment of the mechanism of reactions of CH4 with CO2 or H2O to form synthesis gas and carbon on nickel catalysts. Journal of Catalysis. 2004 Jun 10;224(2):370-83.

[19] Rostrup-Nielsen J. 40 years in catalysis. Catalysis Today. 2006 Jan 15;111(1-2):4-11.

Chapter 2

Literature

This chapter introduces briefly main chemical processes to produce hydrogen and provides a review of the existing literature on surface kinetics of methane steam reforming (MSR) over Ni catalysts, surface kinetics of methane combustion (MC) over platinum catalysts and identifies the current research needs based on a literature review on catalytic plate reactor (CPR) for MC assisted MSR.

2.1 Reforming of methane

Rostrup-Nielsen [1] reviewed briefly a historical footprint of syngas ($CO+H_2$) production and reported that the first patent application on the main principles of catalytic partial oxidation and MSR to syngas over nickel was filed in 1912 by Mittasch and Schneider [2] of Badische Anilin & Soda Fabrik (BASF) group. In 1930, Standard Oil in Baton Rouge installed the first tubular reformer for natural gas (95% methane) reforming. However, the commercial breakthrough in the reforming process was achieved in 1962 by the Imperial Chemical Industries (ICI). The process was carried out in a tubular reformer operating at 15 bar pressure and elevated temperature of 850 °C. After years of research and better understanding of the reforming process, recent years have shown improved and cheaper reforming plants with better control over carbon limits and flexibility in type of fuel use [1].

Based on the requirements of compositions distribution in a product stream, reforming of methane is carried out in a reformer by three different routes: Steam reforming (SR), catalytic partial oxidation (CPO) and autothermal reforming (ATR) [3].

2.1.1. Steam reforming (SR)

Steam reforming (SR) technology is the oldest and most feasible route to convert CH_4 into H_2. SR is the process of producing the mixture of H_2 and CO by combining steam (H_2O) and fuel (CH_4) and reacting in a reformer in the presence of active catalyst according to the reaction (2.1):

$$\mathrm{CH_4 + H_2O \leftrightarrow CO + 3H_2} \quad \Delta \mathrm{H}^{\circ}_{298} = +206\ \mathrm{kJ/mol} \tag{2.1}$$

The SR process is an endothermic in nature and hence requires a supply of heat to the reaction sites. In addition to the syngas (H_2 + CO), a reformate stream usually contains CO_2 and unconverted H_2O and CH_4. Additional H_2 is formed by the water-gas shift (WGS) reaction (2.2) and by the steam reforming of methane to CO_2 reaction (2.3):

$$\mathrm{CO + H_2O \leftrightarrow CO_2 + H_2} \quad \Delta \mathrm{H}^{\circ}_{298} = -41\ \mathrm{kJ/mol} \tag{2.2}$$

$$\mathrm{CH_4 + 2H_2O \leftrightarrow CO_2 + 4H_2} \quad \Delta \mathrm{H}^{\circ}_{298} = +165\ \mathrm{kJ/mol} \tag{2.3}$$

The WGS is an exothermic reaction and reaches equilibrium quickly at the elevated temperature. Due to its exothermic nature, elevated temperature in the reformer favours the reverse WGS reaction. For higher hydrocarbons reforming, a reformate stream may contain light hydrocarbons like methane, ethylene and propylene, which require further purification stages to make reformate stream rich in hydrogen [3].

2.1.2. Catalytic partial oxidation (CPOX)

Catalytic partial oxidation (CPO) is a process of converting methane under an oxygen deficient environment according to the reaction (2.4):

$$\mathrm{CH_4 + 0.5O_2 \leftrightarrow CO + 2H_2 \quad \Delta H^{\circ}_{298} = -36\ kJ/mol} \tag{2.4}$$

The CPO proceeds at fast rate compared to the SR. The main advantage of the CPO is that it requires only air with methane, which eliminates the water vaporization process as required for the SR. On the other hand, the production of carbon monoxide is greater compared to the SR. This puts an additional load onto the subsequent separation operations, but only where CO sensitive fuel cells are connected to the fuel reformer [3].

2.1.3. Autothermal reforming (ATR)

Autothermal reforming (ATR) uses O_2 and steam or CO_2 in a reaction with methane to form syngas. The ATR reaction takes place in a single chamber where methane is partially oxidized using air or pure O_2 (reaction (2.5):

$$\mathrm{2CH_4 + 0.5O_2 + H_2O \leftrightarrow 2CO + 5H_2 \quad \Delta H^{\circ}_{298} = +170\ kJ/mol} \tag{2.4}$$

The addition of air or oxygen in ATR limits coke formation on the catalyst surface. Theoretically the reaction becomes autothermal when the heat generated by the CPO reaction balances the heat consumption of the SR reaction. In realism, heat losses to the surroundings should be considered to calculate the optimum amount of oxygen in the feed. The main disadvantage of the ATR over SR is that its reformate stream contains N_2, which is not acceptable for certain types of fuel cells. An alternative path is to feed pure oxygen along with methane and steam, which obviously increases the cost of ATR [3].

Among three methods discussed above, the MSR produces more hydrogen rich syngas stream compared to the partial oxidation and autothermal reforming [3]. A production of hydrogen rich syngas via MSR process is mainly achieved heterogeneously in the presence of a nickel based solid catalyst at 700 °C and above.

2.2 Reforming catalyst

Reforming catalysts are based on transition metals like nickel, cobalt and noble metals [4]. Due to high operating temperature (>700 °C) of the reforming process, deactivation of the reforming catalysts is ubiquitous and inevitable over a period. There are three main reasons of reforming catalysts to deactivate: (1) sintering is caused by the mobility of active metals at high operating temperatures, (2) coking is caused by carbon formation through Boudouard reaction (CO disproportionation to C and CO_2) and by hydrocarbon cracking, and (3) sulphur poisoning caused by organic sulphur present in hydrocarbon fuels [5]. Catalysts based on noble metals like rhodium or ruthenium are more resistant to carbon formation but are more expensive. This motivates researchers to develop effective catalysts based on more cheaper and easily available non-noble metals like nickel. In 1915, Mittasch and Schneider [6] demonstrated the first use of nickel as a catalyst for the SR and the CPO of methane above 700 °C. The reforming catalysts must have sufficient resistance to carbon formation and stability to be active under severe operating conditions [4]. To develop catalysts with such characteristics, reforming catalysts can be modified by introducing supports or promoters.

It is now well established that supports play an equally significant role in coordination with the active metal component in the performance of reforming catalysts. Due to the chemical bonding between a support and an active metal, the reactivity of an active metal component can be affected significantly by the choice of supports [7]. Supports provide stability and high active surface area with its porous structure, which results in a longer stability and lifespan of a catalyst. Research work has identified that carbon formation on nickel-based catalysts is sensitive to the acidic and the basic nature of a support. For example, support such as zirconium dioxide (ZrO_2) with strong Lewis basicity has shown a strong interaction with active nickel which has eventually lead to the formation of small nickel crystallites and supress the carbon formation [8-12]. Support such as alumina (Al_2O_3) increases acidic nature of a catalyst [13]. An acidic support promotes cracking of methane and thus produce carbon [14]. Lahousse et al. [15] have reported that addition of support with basic nature to a catalyst plays a crucial role in catalyst performance by balancing Lewis acidity and hence formation of carbon.

The use of stable support such as ZrO_2 increases thermal stability and oxygen vacancies in nickel-based catalysts [16]. Along with its strong Lewis basicity, ZrO_2 is also characterized by high chemical resistance and its stable crystalline structure at wide range of operating temperature. It is found that the stability range of ZrO_2 support can be further enhanced by introducing ions of lower valence than 4^+, such as Y^{3+}, La^{3+}, Mg^{2+} and Ca^{2+} into the ZrO_2 lattice [17]. The replacement of Zr^{4+} cation with lower positive charge leads to a negative overall charge that is compensated by an increased number of oxygen vacancies. These modifications in the ZrO_2 support can activate the gaseous oxygen-producing O^{2-} or O^- species [18], such as adsorption of H_2O. Bellido and Assaf [19] have carried out a comparative study of methane dry reforming over 5% Ni catalyst supported on ZrO_2 and 5% Ni catalyst supported on ZrO_2 + Y_2O_3. They have reported that modification of ZrO_2 support with the addition of Y_2O_3 has increased the specific surface area and surface oxygen vacancies. Surface oxygen vacancies could provide the active sites required for obtaining more energetic oxygen radicals and thus reduce the rate of carbon formation [19]. The Ni-spinel catalyst supported by YSZ and alumina employed in this study has been developed by Fauteux-Lefebvre et al. [20] at the Université de Sherbrooke, Québec, Canada. Their Ni-spinel catalyst has shown promising potential to implement in diesel steam reforming [21], methane dry reforming [22] and naphthalene reforming [23]. The use of such catalyst in reformers provides flexibility in selecting wide range of fuels that are available at various locations to generate hydrogen and hence can further increase the usage of fuel cells.

2.3 Reforming reaction rates

To evaluate the performance of catalytic reformer design, quantitative and sufficiently accurate information about the catalytic MSR reaction rates is required based on the underlying physical and chemical phenomena. Kinetics of MSR is dependent on the types of catalysts used, primarily on the active metal and up to certain extent on the type of support [24]. Various approaches have been considered for the development of reaction mechanism/rate expression to describe an intrinsic kinetics of MSR. Early work on the development of reforming kinetics assumed adsorption of CH_4 as a rate determining step, which agreed with the assumption of the first-order dependence of methane concentration [25]. However, most reaction mechanisms proposed in early work have been found to be applicable only in a limited range of operating conditions.

In 1964, Bodrov et al. [45] proposed the mechanism (Eq. 2.5) of MSR kinetics by assuming methane adsorption to be the rate determining step:

$$r = \frac{k p_{\mathrm{CH_4}}}{1 + a\left(\frac{p_{H2O}}{p_{H2}}\right) + b p_{CO}} \tag{2.5}$$

However, it has been observed that under some conditions, hydrogen restricts the progress of the reforming reaction, which cannot be explained by the rate expression (2.5) [26]. Khomenko et al. [27] proposed the rate expression (2.6) based on Temkin's general kinetic identity:

$$r = k p_{\mathrm{CH_4}} p_{H2O} \frac{1 - (p_{CO} p_{H2}^{3} K_{eq} p_{\mathrm{CH_4}} p_{H2O})}{f(p_{H2O}, p_{H2}) + (1 + K_{H2O} p_{H2O}/p_{H2})} \tag{2.6}$$

where, k is the reaction rate constant, K_{eq} is the equilibrium constant for the overall reaction and $f(p_{H2O}, p_{H2})$ is a polynomial in p_{H2O} and p_{H2}. However, it has been determined that at high pressure, the rate constant in Eq. (2.8) is dependent on partial pressures [26].

During late 1980s, Xu and Froment [28] proposed complex LHHW rate expressions for the MSR kinetics over Ni/$MgAl_2O_4$ catalyst. They measured 280 experimental data points within the temperature range of 773-848 K, pressures between 3 and 15 bar and steam to carbon ratio between 3 and 5. They proposed a detailed reaction kinetics steps with three rate determining steps one each for three main reactions: (i) methane steam reforming to CO (Eq. 2.1), (ii) the water gas shift reaction (Eq. 2.2) and (iii) methane steam reforming to CO_2 (Eq. 2.3):

$$r_1 = \frac{k_1}{p_{H2}^{2.5}}\left(p_{\mathrm{CH_4}} p_{H2O} - \frac{p_{CO} p_{H2}^{3}}{K_{eq,1}}\right) / DEN^2 \tag{2.7}$$

$$r_2 = \frac{k_2}{p_{H2}}\left(p_{\mathrm{CO}} p_{H2O} - \frac{p_{CO2} p_{H2}}{K_{eq,2}}\right) / DEN^2 \tag{2.8}$$

$$r_3 = \frac{k_3}{p_{H2}^{3.5}}\left(p_{\mathrm{CH_4}} p_{H2O}^{2} - \frac{p_{CO2} p_{H2}^{4}}{K_{eq,3}}\right) / DEN^2 \tag{2.9}$$

where, $DEN = 1 + K_{CO} p_{CO} + K_{H2} p_{H2} + K_{CH4} p_{CH4} + K_{H2O} p_{H2O}/p_{H2}$, and $K_{eq,1}$, $K_{eq,2}$, $K_{eq,3}$ are the equilibrium constants for the reactions (2.1), (2.2) and (2.3) respectively, p_k are the partial pressures and K_k are the adsorption constants of chemical species k.

Similarly, Hou and Hughes [29] also reported three rate expressions for the MSR over a commercial Ni/α-Al_2O_3 catalyst and suggested surface reactions between adsorbed species were rate controlling. Wei and Iglesia [30] postulated a reaction sequence of steam and dry reforming of methane on Ni/MgO catalysts. They concluded based on isotopic measurements that reforming reaction rates were solely depend on the concentration of methane and unaffected by the partial pressures of co-reactants. Differences in kinetics rate expressions suggest that the MSR is a complex process to describe in a single step and no simple analytical rate expression can be valid over a wide range of operating conditions.

Aparicio [26] observed that Xu and Froment's rate expressions involve a negative heat of adsorption for steam and thus their kinetics model is unable to predict the decrease in rate observed experimentally when steam is replaced by CO_2. So, instead of adopting LHHW approach, Aparicio [26] applied surface microkinetic principles to understand the MSR. Aparicio used Xu and Froment's [28] experimental data to adjust the parameters of surface microkinetic model. He concluded that the slowest steps in his model are methane adsorption and dehydrogenation, the formation of a C-O bond and the formation of a O=C-O bond. Under some conditions, one of these steps can be the process limiting step, but in most cases combination of slowest steps determines the overall rate of the reforming process. Chen et al. [31, 32] extended Aparicio's microkinetic model by including carbon formation and deactivation steps. Their model predicted the results very well for both dry and MSR over Ni/MgO-Al_2O_3 and Ni/CaO-Al_2O_3 catalysts at a pressure range of 0.1 to 2 MPa and a temperature range of 500 °C to 650 °C.

Wang et al. [33, 34] investigated CO_2 reforming of CH_4 on Ni (111) using density functional theory calculations. They concluded that CH_4 dissociation into CH_3 and H is the rate-determining step and HCO as key intermediate surface species. On the other hand, Blaylock et al. [35] investigated the MSR on Ni (111) using density functional theory in combination with a statistical thermodynamic. The authors proposed a detailed kinetic model containing adsorbed HCO and CHOH species as the most important intermediates. Maier et al. [36] developed a detailed multi-step microkinetic model which is applicable to steam reforming and partial oxidation of methane. Their modeling results indicated that the availability of surface oxygen plays a key role in determining the rate of reforming process. In this work, microkinetic model developed by Maier et al. [36] is adopted for the simulation of a CPR. Delgado et al. [37] extended Maier et al. model for dry reforming and total oxidation of methane.

2.4 Combustion of methane

Catalytic methane combustion has so far found limited applications. However, the need for small scale power generation devices has rendered catalytic methane combustion an attractive choice. Since the steam reforming reactions of methane (Eq. 2.1, Eq. 2.3) are endothermic, continuous supply of heat to the reforming reaction sites can be achieved via highly exothermic combustion of methane (Eq. 2.10) either homogeneously or heterogeneously.

$$\mathrm{CH_4} + 2\mathrm{O_2} \leftrightarrow \mathrm{CO_2} + 2\mathrm{H_2O} \quad \Delta \mathrm{H}_{298}^{\circ} = -890\ \mathrm{kJ/mol} \tag{2.10}$$

Homogeneous combustion limits the choice of materials for reactor fabrication due to the high temperatures associated with it. Also, at high temperatures, chances of NO_x formation increase significantly. On the other hand, due to lower operating temperature than homogeneous combustion, catalytic combustion can increase the operating window and choice of materials for reactor. Also, if catalytic combustion can be carried out under fuel-lean conditions, chances of NO_x and CO formation can be eliminated completely [38]. The most common catalysts used in methane combustion are mainly based on noble metals like platinum, palladium and rhodium.

2.5 Combustion reaction rates

Numerous studies related to the kinetics of catalytic methane combustion have been reported in literature [38-53]. Literature search on the reaction kinetics suggest that most rate expressions for the catalytic methane combustion have been modeled either by the power-law type equation (Eq. 2.11) or by the Langmuir-Hinshelwood (LH) type equation (Eq. 2.12):

$$r = k C_{CH4}^{\alpha_{CH4}} C_{O2}^{\alpha_{O2}} = A e^{-E_a/(R_{gas}T)} C_{CH4}^{\alpha_{CH4}} C_{O2}^{\alpha_{O2}} \tag{2.11}$$

$$r = \frac{k K_{\mathrm{CH_4}} p_{\mathrm{CH_4}} \sqrt{K_{\mathrm{O_2}} p_{\mathrm{O_2}}}}{\left(1 + K_{\mathrm{CH_4}} p_{\mathrm{CH_4}} + \sqrt{K_{\mathrm{O_2}} p_{\mathrm{O_2}}}\right)^2} \tag{2.12}$$

where, r is the reaction rate (mol/g_{cat}/s), k is the reaction rate constant, p_{k} is the partial pressure of the k^{th} component, K_{CH_4} and K_{O_2} are the equilibrium constants, C_{k} is the concentration of chemical species k (mol/m^3), A is the pre-exponential factor, E_a is the activation energy (J/mol), R_{gas} is the ideal gas constant (J/mol/K), and T is the temperature (K). The development of kinetic models based on the LH isotherm are valid only under limited operating condition due to the underlying assumptions for rate determining steps. Combustion kinetic models based on microkinetic approach can provide more insights of the reaction pathways [54]. Few studies [54–59] in the literature have been reported so far on surface microkinetics of methane combustion over different catalysts.

2.6 Catalytic plate reactor (CPR)

The concept of process intensification has long been around in the chemical engineering industry. It relies on the development of novel technologies that are inherently safer, can substantially reduce the equipment-size/production-capacity ratio, and improve energy efficiencies [60]. Catalytic Plate Reactors (CPRs) are an example of a heat-exchanger reactor used for process intensification. Compared to conventional chemical reactors, CPRs have the potential to provide higher product throughputs, greater heat transfer rates and lower manufacturing costs. A CPR design is composed of a number of thin metal plates coated with suitable catalyst and organized in a stacked configuration.

Process intensification in CPRs can be achieved via two methods. In one method, a hot flue gas exchanges heat with an endothermic reaction taking place in an alternate channel [61]. In the second method, studied in this thesis, exothermic and endothermic reactions take place in alternative channels [62]. The use of exothermic reaction creates steep thermal gradients and hot-spots in CPRs due to different rates of heat liberation on the combustion-side and heat absorption on the reforming-side. Such thermal imbalance between two sides of a plate causes problems of material failure and catalyst delamination due to different thermal expansion coefficients of coated catalysts and metal plate. Large thermal-gradients also reduce the catalytic active surface area, and as a result conversion rate of reactants [63]. Very few studies have attempted to address the issues of steep thermal gradients, hot and cold spots by changing the design of a CPR at various levels.

In a recent study, Pattison et al. [64,65] proposed a complex design for a microchannel CPR designed with 60 cm plate-length, where a layer of phase change material (PCM) placed between the two plates of the reforming and combustion sides. The PCM layer acted as an energy storage buffer, which absorbs an excess thermal energy that transfers from the combustion-side plate to the reforming-side plate. Along with the concept of PCM layer, they also proposed a temperature control strategy to address the issue of persistent disturbances. Pattison et al. [66] also proposed a distributed coating design for a combustion-catalyst. They investigated numerically, a method for emulating distributed feed configuration in a CPR via two to four distributed coating layers of a combustion-catalyst, consisting of alternating active and catalytically inactive sections. Their study showed that increasing the number of distributed sections allowed for more precise tuning of a plate temperature. However, in their study, they considered only two to four relatively longer (centimeter range) distributed sections of a combustion-catalyst. Similarly, Jeon et al. [67] conducted an optimization study to determine an optimum length of the distributed sections of a combustion-catalyst, an optimum number of combustion-catalyst sections, and an optimum length for an inter-catalyst space to reduce the thermal hot-spots in a microchannel CPR consisting of relatively shorter plate-length of 5 cm. They considered the distributed combustion-catalyst only for the initial fifty percent of the plate-length and did not address the issue of the longitudinal thermal gradients for the remaining plate-length. They reported that optimization of inter-catalyst space length is more effective in minimizing the thermal hot-spots. However, they restricted their study to 1 mm length for the inter-catalyst space on the combustion-side of a microchannel CPR. Ramaswamy et al. [68, 69] analyzed dynamic and steady-state behavior of a heat exchanger reactor with counter-flow and co-flow modes for the coupling of exothermic MC and endothermic MSR reactions using the pseudo-homogeneous plug-flow model. They reported thermal hot-spots in both reactor designs and higher temperature peak in the case of counter-flow mode. They suggested that catalyst activity profiling can reduce steep thermal gradients and hot-spots with co-flow arrangement. Similar study was carried out by Zanfir et al. [70] to investigate the influence of flow arrangement between the MC and MSR and catalyst distribution. They showed reduction in severe hot-spots condition by selecting appropriate overlapping locations for the reforming-catalyst and combustion-catalyst and suggested that more number of distributed sections of the combustion-catalyst can improve the longitudinal temperature distribution. Kolios et al. [71] proposed a distributed feed design for the counter current flow operation between the reforming and combustion sides. For their proposed design, reactants on the combustion-side are entered at multiple points located along the reactor to ease steep temperature gradients in the flow direction. Kolios et al. [72] also investigated the influence of periodic switching of the exothermic and endothermic reactions to eliminate the cold and hot-spots in a CPR. The concept of distributed feed requires access of all flow channels at multiple points along the length, which makes the design of a chemical reactor more complex and difficult to build. Complex CPR design also makes the loading and unloading operation of the plates difficult. Recently, Settar et al. [73] carried out a comparative numerical study between the distributed and conventional continuous coatings of a reforming-catalyst for the endothermic MSR by steady state two-dimensional model of a single reforming-channel by considering channel wall as a heat providing source and showed performance enhancement factor up to two for CH_4 conversion with the distributed reforming-catalyst. They kept the amount of a reforming-catalyst in the distributed coating same as continuous coating by considering the same total length of active reforming-catalyst. To achieve this, they distributed coating sections of a reforming-catalyst over an extended plate-length compared to the continuous coating design.

In contrast to above reviewed few literatures of the novel ideas and concepts to solve the aforementioned issues of CPRs, many research articles are available in the literature on a CPR designed with conventional continuous coatings.

Zanfir and Gavriilidis [74] have performed a parametric investigation of reforming-catalyst thickness and flow-channel height of a CPR for operating conditions like conventional industrial methane reformer. They have developed a simplified 2D model of a CPR by implementing Xu and Froment's [28] kinetic model for MSR and power law rate model for CMC. Zanfir and Gavriilidis [74] have observed that by increasing reforming-channel height at constant inlet velocity, methane conversion in MSR ($X_{CH4,\ MSR}$) decreases. They have concluded that MSR coupled with CMC is feasible in a CPR if flow-rates, catalyst thickness and channel heights are properly designed. Zanfir and Gavriilidis [75] have also conducted numerical study of co-flow and counter-flow modes between MSR and CMC. They have determined higher X_{CH4} on the reforming-side with counter-flow than co-flow design. They have also observed thermal hot-spots in counter-flow mode and have suggested to optimize combustion-catalyst distribution to reduce thermal hot-spots. In a separate study, Zanfir and Gavriilidis [62] have carried out a sensitivity analysis of several design and operating parameters including reaction kinetic parameters. They have demonstrated that different catalysts can show similar thermal behavior and performance but exhibit different sensitivity behavior. The major finding of their study is that the strongest influence on reactor sensitivity comes from the reaction activation energies. Stefanidis and Vlachos [76] have studied MSR on a rhodium catalyst coupled with propane combustion over a platinum catalyst in a CPR and have reported that increasing catalyst loading and decreasing possible internal mass transfer limitations results in considerable process time reduction. Also, by lowering steam to carbon (SC) ratio yielded higher power output at relatively low reactor temperatures. In a different study, Stefanidis et al. [77] have reported that the use of low thermal conductivity plate materials increases fuel conversion and power output in the incomplete conversion regime. However, the use of very low thermal conductivity materials has shown high thermal-gradients in the CPR and thus recommended to use intermediate thermal conductivity materials, such as stainless steel as a trade-off between thermal-gradients and conversion. Zhai et al. [78] have developed 2D computational fluid dynamic (CFD) model of a CPR using surface microkinetics for MSR on rhodium and LHHW type kinetic model for CMC on platinum. They have investigated the influence of wall thermal conductivity, ratio of combustion to reforming feed, channel size and space time. They have reported that the performance of the metallic wall is superior against ceramic wall and recommended to use the wall material with intermediate thermal conductivity to avoid hot-spot formation. Arzamendi et al. [79] have developed a 3D CFD-model of a microchannel reactor integrating MSR and CMC. They have implemented the simplified rate expressions [80] for MSR on Ni catalyst and have simulated the effect of various parameters: catalyst loading, flow direction between the two channels, and gas hourly space velocity (GHSV). Their results have shown the possibility of 96% of methane conversion with 2–4 mg/cm^2 of catalyst at 930–1000 °C in the range of 10,000–30,000 h^{-1} GHSV. In a separate work, Arzamendi et al. [81] have developed 3D CFD-models of a plate reactor with square microchannel and microslits design to investigate the effects of characteristic dimension with different aspect ratios. Their results have shown that methane conversion decreases with increase in characteristic dimension; however, the microchannel design has provided methane conversion slightly higher than that of the microslits design. Cao et al. [82] have carried out CFD study of MSR in an integrated microchannel reactor by applying elementary reaction kinetics and compared the performance of Rh and Ni catalysts under inner-heating and outer heating modes. They have demonstrated that well prepared Ni catalyst with high loading can exhibit excellent performance comparable to the rhodium catalyst.

2.7 Summary

Literature review on catalytic plate reactor for MC assisted MSR revealed that limited studies have addressed the issue of thermal hot-spots, longitudinal thermal gradients, catalyst delamination, and material failure in a CPR due to thermal imbalance between the reforming and combustion sides. This review has also found that many studies have considered simplified rate expressions without experimental validation. Also, no study exists about distributed coatings of combustion and reforming catalysts over the entire plate-length and addressing abovementioned problems associated with CPRs. No literature study exists about the influence of various operating and design parameters on the performance of a CPR designed with various coating configurations of reforming and combustion catalysts. Also, no literature study was found on internal diffusion limitation with respect to coating thickness and with detailed reaction kinetics. The studies carried out in this thesis are intended to address the abovementioned issues by developing detailed two-dimensional steady-state numerical models of a CPR designed with various coating configurations of reforming and combustion catalysts. Also, to make MSR process more energy efficient, a potential Ni-spinel catalyst applicable for multi-fuel is tested at low steam to carbon ratios under plug-flow condition.

2.8 References

[1] Rostrup-Nielsen JR. An industrial perspective on the impact of Haldor Topsøe on research and development in synthesis gas production. Journal of Catalysis. 2015 Aug 31;328:5-10.

[2] A. Mittasch, C. Schneider, DRP 296866, BASF, 1912.

[3] Kolb G. Fuel Processing: For Fuel Cells. Weinheim, Germany: Wiley-VCH Verlag GmbH # Co. KGaA; 2008 May 5.

[4] Rostrup-Nielsen JR, Christiansen LJ, Hansen JH. Activity of steam reforming catalysts: role and assessment. Applied Catalysis. 1988 Jan 1;43(2):287-303.

[5] Fauteux-Lefebvre C, Abatzoglou N, Blanchard J, Gitzhofer F. Steam reforming of liquid hydrocarbons over a nickel–alumina spinel catalyst. Journal of Power Sources. 2010 May 15;195(10):3275-83.

[6] Mittasch A, Schneider C. Process of producing hydrogen. U.S. Patent 1128804, October 20, 1913.

[7] Van Beurden P. On the catalytic aspects of steam-methane reforming. Energy Research Centre of the Netherlands (ECN), Technical Report I-04-003. 2004 Dec.

[8] Hegarty ME, O'Connor AM, Ross JR. Syngas production from natural gas using ZrO_2-supported metals. Catalysis Today. 1998 Jul 9;42(3):225-32.

[9] Dong WS, Roh HS, Jun KW, Park SE, Oh YS. Methane reforming over Ni/Ce-ZrO_2 catalysts: effect of nickel content. Applied Catalysis A: General. 2002 Mar 28;226(1):63-72.

[10] Choudhary VR, Banerjee S, Rajput AM. Hydrogen from step-wise steam reforming of methane over Ni/ZrO_2: factors affecting catalytic methane decomposition and gasification by steam of carbon formed on the catalyst. Applied Catalysis A: General. 2002 Aug 8;234(1):259-70.

[11] Takeguchi T, Furukawa SN, Inoue M, Eguchi K. Autothermal reforming of methane over Ni catalysts supported over CaO–CeO_2–ZrO_2 solid solution. Applied Catalysis A: General. 2003 Feb 10;240(1):223-33.

[12] Takahashi R, Sato S, Sodesawa T, Yoshida M, Tomiyama S. Addition of zirconia in Ni/SiO_2 catalyst for improvement of steam resistance. Applied Catalysis A: General. 2004 Oct 8;273(1):211-5.

[13] Pines H, Haag WO. Alumina: catalyst and support. I. alumina, its intrinsic acidity and catalytic activity. Journal of the American Chemical Society. 1960 May;82(10):2471-83.

[14] Van Beurden P. On the catalytic aspects of steam-methane reforming. Energy Research Centre of the Netherlands (ECN), Technical Report I-04-003. 2004 Dec.

[15] Lahousse C, Aboulayt A, Maugé F, Bachelier J, Lavalley JC. Acidic and basic properties of zirconia—alumina and zirconia—titania mixed oxides. Journal of molecular catalysis. 1993 Oct 25;84(3):283-97.

[16] Maia TA, Assaf JM, Assaf EM. Performance of cobalt catalysts supported on $Ce_xZr_{1-x}O_2$ ($0< x<1$) solid solutions in oxidative ethanol reforming. Reaction Kinetics, Mechanisms and Catalysis. 2013 Jun 1;109(1):181-97.

[17] Teterycz H, Klimkiewicz R, Łaniecki M. The role of Lewis acidic centers in stabilized zirconium dioxide. Applied Catalysis A: General. 2003 Aug 28;249(2):313-26.

[18] Bellido JD, Assaf EM. Nickel catalysts supported on ZrO_2, Y_2O_3-stabilized ZrO_2 and CaO-stabilized ZrO_2 for the steam reforming of ethanol: effect of the support and nickel load. Journal of Power Sources. 2008 Feb 15;177(1):24-32.

[19] Bellido JD, Assaf EM. Effect of the Y_2O_3–ZrO_2 support composition on nickel catalyst evaluated in dry reforming of methane. Applied Catalysis A: General. 2009 Jan 15;352(1):179-87.

[20] Fauteux-Lefebvre C, Abatzoglou N, Blanchard J, Gitzhofer F. Steam reforming of liquid hydrocarbons over a nickel–alumina spinel catalyst. Journal of Power Sources. 2010 May 15;195(10):3275-83.

[21] Fauteux-Lefebvre C, Abatzoglou N, Braidy N, Achouri IE. Diesel steam reforming with a nickel–alumina spinel catalyst for solid oxide fuel cell application. Journal of Power Sources. 2011 Sep 15;196(18):7673-80.

[22] Blanchard J, Nsungui AJ, Abatzoglou N, Gitzhofer F. Dry Reforming of Methane with a Ni/Al_2O_3-YSZ Catalyst: The Role of the Catalyst Preparation Protocol. The Canadian Journal of Chemical Engineering. 2007 Dec 1;85(6):889-99.

[23] Bangala DN, Abatzoglou N, Chornet E. Steam reforming of naphthalene on Ni–Cr/Al_2O_3 catalysts doped with MgO, TiO_2, and La_2O_3. AIChE Journal. 1998 Apr 1;44(4):927-36.

[24] Rostrup-Nielsen J. Reaction kinetics and scale-up of catalytic processes. Journal of Molecular Catalysis A: Chemical. 2000 Dec 4;163(1):157-62.

[25] Van Hook JP. Methane-steam reforming. Catalysis Reviews—Science and Engineering. 1980 Jan 1;21(1):1-51.

[26] Aparicio LM. Transient isotopic studies and microkinetic modeling of methane reforming over nickel catalysts. Journal of Catalysis. 1997 Jan 15;165(2):262-74.

[27] Khomenko AA, Apel'baum LO, Shub FS. Kinetics of the methane–steam reactions and the reverse reaction of carbon monoxide hydrogenation on the nickel surface. Kinet. Katal. 1971;12(2):423.

[28] Xu J, Froment GF. Methane steam reforming, methanation and water-gas shift: I. Intrinsic kinetics. AIChE journal. 1989 Jan 1;35(1):88-96.

[29] Hou K, Hughes R. The kinetics of methane steam reforming over a Ni/α-Al_2O catalyst. Chemical Engineering Journal. 2001 Mar 15;82(1):311-28.

[30] Wei J, Iglesia E. Isotopic and kinetic assessment of the mechanism of reactions of CH_4 with CO_2 or H_2O to form synthesis gas and carbon on nickel catalysts. Journal of Catalysis. 2004 Jun 10;224(2):370-83.

[31] Chen D, Lødeng R, Omdahl K, Anundsks A, Olsvik O, Holmen A. A model for reforming on Ni catalyst with carbon formation and deactivation. Studies in Surface Science and Catalysis. 2001;139:93-100.

[32] Chen D, Lødeng R, Anundskås A, Olsvik O, Holmen A. Deactivation during carbon dioxide reforming of methane over Ni catalyst: microkinetic analysis. Chemical Engineering Science. 2001 Feb 28;56(4):1371-9.

[33] Wang SG, Cao DB, Li YW, Wang J, Jiao H. CO_2 reforming of CH_4 on Ni (111): a density functional theory calculation. The Journal of Physical Chemistry B. 2006 May 25;110(20):9976-83.

[34] Wang SG, Liao XY, Hu J, Cao DB, Li YW, Wang J, Jiao H. Kinetic aspect of CO_2 reforming of CH_4 on Ni (111): a density functional theory calculation. Surface science. 2007 Mar 1;601(5):1271-84.

[35] Blaylock DW, Ogura T, Green WH, Beran GJ. Computational investigation of thermochemistry and kinetics of steam methane reforming on Ni (111) under realistic conditions. The Journal of Physical Chemistry C. 2009 Feb 27;113(12):4898-908.

[36] Maier L, Schädel B, Delgado KH, Tischer S, Deutschmann O. Steam reforming of methane over nickel: development of a multi-step surface reaction mechanism. Topics in catalysis. 2011 Sep 1;54(13-15):845.

[37] Delgado KH, Maier L, Tischer S, Zellner A, Stotz H, Deutschmann O. Surface reaction kinetics of steam-and CO_2-reforming as well as oxidation of methane over nickel-based catalysts. Catalysts. 2015 May 29;5(2):871-904.

[38] Deshmukh SR, Vlachos DG. A reduced mechanism for methane and one-step rate expressions for fuel-lean catalytic combustion of small alkanes on noble metals. Combustion and Flame. 2007 Jun 30;149(4):366-83.

[39] Anderson RB, Stein KC, Feenan JJ, Hofer LJ. Catalytic oxidation of methane. Industrial & Engineering Chemistry. 1961 Oct;53(10):809-12.

[40] Firth JG, Holland HB. Catalytic oxidation of methane over noble metals. Transactions of the Faraday Society. 1969;65:1121-7.

[41] Trimm DL, Lam CW. The combustion of methane on platinum—alumina fibre catalysts—I: kinetics and mechanism. Chemical Engineering Science. 1980 Jan 1;35(6):1405-13.

[42] Yao YF. Oxidation of alkanes over noble metal catalysts. Industrial & Engineering Chemistry Product Research and Development. 1980 Sep;19(3):293-8.

[43] Niwa M, Awano K, Murakami Y. Activity of supported platinum catalysts for methane oxidation. Applied catalysis. 1983 Sep 15;7(3):317-25.

[44] Cullis CF, Willatt BM. Oxidation of methane over supported precious metal catalysts. Journal of Catalysis. 1983 Oct 1;83(2):267-85.

[45] Otto K. Methane oxidation over Pt on gamma-alumina: kinetics and structure sensitivity. Langmuir. 1989 Nov;5(6):1364-9.

[46] Song X, Williams WR, Schmidt LD, Aris R. Bifurcation behavior in homogeneous-heterogeneous combustion: II. Computations for stagnation-point flow. Combustion and Flame. 1991 Apr 1;84(3-4):292-311.

[47] Ma L, Trimm DL, Jiang C. The design and testing of an autothermal reactor for the conversion of light hydrocarbons to hydrogen I. The kinetics of the catalytic oxidation of light hydrocarbons. Applied Catalysis A: General. 1996 May 9;138(2):275-83.

[48] Kolaczkowski ST, Serbetcioglu S. Development of combustion catalysts for monolith reactors: a consideration of transport limitations. Applied Catalysis A: General. 1996 May 9;138(2):199-214.

[49] Aryafar M, Zaera F. Kinetic study of the catalytic oxidation of alkanes over nickel, palladium, and platinum foils. Catalysis Letters. 1997 Oct 1;48(3-4):173-83.

[50] Kuper WJ, Blaauw M, Van Der Berg F, Graaf GH. Catalytic combustion concept for gas turbines. Catalysis Today. 1999 Jan 1;47(1):377-89.

[51] Garetto TF, Apesteguıa CR. Oxidative catalytic removal of hydrocarbons over Pt/Al_2O_3 catalysts. Catalysis Today. 2000 Nov 10;62(2):189-99.

[52] Aubé F, Sapoundjiev H. Mathematical model and numerical simulations of catalytic flow reversal reactors for industrial applications. Computers & Chemical Engineering. 2000 Dec 1;24(12):2623-32.

[53] Fullerton DJ, Westwood AV, Brydson R, Twigg MV, Jones JM. Deactivation and regeneration of Pt/γ-alumina and Pt/ceria–alumina catalysts for methane combustion in the presence of H_2S. Catalysis today. 2003 Jul 1;81(4):659-71.

[54] Deutschmann O, Behrendt F, Warnatz J. Modelling and simulation of heterogeneous oxidation of methane on a platinum foil. Catalysis Today. 1994 Dec 2;21(2-3):461-70.

[55] Hickman DA, Schmidt LD. Steps in CH_4 oxidation on Pt and Rh surfaces: High-temperature reactor simulations. AIChE Journal. 1993 Jul 1;39(7):1164-77.

[56] Dooling DJ, Rekoske JE, Broadbelt LJ. Microkinetic models of catalytic reactions on nonuniform surfaces: Application to model and real systems. Langmuir. 1999 Aug 31;15(18):5846-56.

[57] Deutschmann O, Maier LI, Riedel U, Stroemman AH, Dibble RW. Hydrogen assisted catalytic combustion of methane on platinum. Catalysis today. 2000 Jun 10;59(1):141-50.

[58] Schwiedernoch R, Tischer S, Deutschmann O, Warnatz J. Experimental and numerical investigation of the ignition of methane combustion in a platinum-coated honeycomb monolith. Proceedings of the combustion institute. 2002 Jan 1;29(1):1005-11.

[59] Mhadeshwar AB, Vlachos DG. Hierarchical multiscale mechanism development for methane partial oxidation and reforming and for thermal decomposition of oxygenates on Rh. The Journal of Physical Chemistry B. 2005 Sep 8;109(35):16819-35.

[60] Anxionnaz Z, Cabassud M, Gourdon C, Tochon P. Heat exchanger/reactors (HEX reactors): concepts, technologies: state-of-the-art. Chemical Engineering and Processing: Process Intensification. 2008 Nov 30;47(12):2029-50.

[61] Mundhwa M, Thurgood CP, Dhingra H, Parmar RD, Peppley BA. A comparative computational study of diesel steam reforming in a catalytic plate heat-exchange reactor. AIChE Journal. 2017 Mar 1;63(3):1102-13.

[62] Zanfir M, Gavriilidis A. An investigation of catalytic plate reactors by means of parametric sensitivity analysis. Chemical engineering science. 2002 May 31;57(9):1653-9.

[63] Bartholomew CH. Mechanisms of catalyst deactivation. Applied Catalysis A: General. 2001 Apr 30;212(1):17-60.

[64] Pattison RC, Baldea M. A thermal-flywheel approach to distributed temperature control in microchannel reactors. AIChE journal. 2013 Jun 1;59(6):2051-61.

[65] Baldea M, Pattison RC, inventors; Board of regents, system, assignee. Catalytic plate reactors. United States patent application US 20,150,217,259. 2015 Aug 6.

[66] Pattison RC, Estep FE, Baldea M. Pseudodistributed feed configurations for catalytic plate microchannel reactors. Industrial & Engineering Chemistry Research. 2013 Aug 9;53(13):5028-37.

[67] Jeon SW, Yoon WJ, Baek C, Kim Y. Minimization of hot spot in a microchannel reactor for steam reforming of methane with the stripe combustion catalyst layer. international journal of hydrogen energy. 2013 Oct 25;38(32):13982-90.

[68] Ramaswamy RC, Ramachandran PA, Duduković MP. Recuperative coupling of exothermic and endothermic reactions. Chemical engineering science. 2006 Jan 31;61(2):459-72.

[69] Ramaswamy RC, Ramachandran PA, Duduković MP. Coupling exothermic and endothermic reactions in adiabatic reactors. Chemical engineering science. 2008 Mar 31;63(6):1654-67.

[70] Zanfir M, Baldea M, Daoutidis P. Optimizing the catalyst distribution for countercurrent methane steam reforming in plate reactors. AIChE Journal. 2011 Sep 1;57(9):2518-28.

[71] Kolios G, Frauhammer J, Eigenberger G. Efficient reactor concepts for coupling of endothermic and exothermic reactions. Chemical Engineering Science. 2002 May 31;57(9):1505-10.

[72] Kolios G, Glöckler B, Gritsch A, Morillo A, Eigenberger G. Heat-Integrated Reactor Concepts for Hydrogen Production by Methane Steam Reforming. Fuel Cells. 2005 Feb 1;5(1):52-65.

[73] Settar A, Nebbali R, Madani B, Abboudi S. Numerical study on the effects of the macropatterned active surfaces on the wall-coated steam methane reformer performances. International Journal of Hydrogen Energy. 2017 Jan 12;42(2):1490-8.

[74] Zanfir M, Gavriilidis A. Catalytic combustion assisted methane steam reforming in a catalytic plate reactor. Chemical Engineering Science. 2003 Sep 30;58(17):3947-60.

[75] Zanfir M, Gavriilidis A. Influence of flow arrangement in catalytic plate reactors for methane steam reforming. Chemical Engineering Research and Design. 2004 Feb 1;82(2):252-8.

[76] Stefanidis GD, Vlachos DG. Millisecond methane steam reforming via process and catalyst intensification. Chemical engineering & technology. 2008 Aug 1;31(8):1201-9.

[77] Stefanidis GD, Vlachos DG, Kaisare NS, Maestri M. Methane steam reforming at microscales: Operation strategies for variable power output at millisecond contact times. AIChE Journal. 2009 Jan 1;55(1):180-91.

[78] Zhai X, Ding S, Cheng Y, Jin Y, Cheng Y. CFD simulation with detailed chemistry of steam reforming of methane for hydrogen production in an integrated micro-reactor. International Journal of Hydrogen Energy. 2010 Jun 30;35(11):5383-92.

[79] Arzamendi G, Diéguez PM, Montes M, Odriozola JA, Sousa-Aguiar EF, Gandía LM. Methane steam reforming in a microchannel reactor for GTL intensification: A computational fluid dynamics simulation study. Chemical Engineering Journal. 2009 Nov 15;154(1):168-73.

[80] Rostrup-Nielsen JR. Sulfur-passivated nickel catalysts for carbon-free steam reforming of methane. Journal of Catalysis. 1984 Jan 1;85(1):31-43.

[81] Arzamendi G, Uriz I, Navajas A, Diéguez PM, Gandía LM, Montes M, Centeno MA, Odriozola JA. A CFD study on the effect of the characteristic dimension of catalytic wall microreactors. AIChE Journal. 2012 Sep 1;58(9):2785-97.

[82] Cao C, Zhang N, Chen X, Cheng Y. A comparative study of Rh and Ni coated microchannel reactor for steam methane reforming using CFD with detailed chemistry. Chemical Engineering Science. 2015 Dec 1;137:276-86.

Chapter 3

Numerical study of methane steam reforming and methane combustion over the segmented and continuously coated layers of catalysts in a plate reactor

Published in Fuel Processing Technology, 158 (2017) 57-72

Abstract

Four separate 2D steady state numerical models are developed for a catalytic plate reactor (CPR), designed with the four different configurations between segmented and continuously coated layers of combustion and reforming catalysts for hydrogen production by combustion assisted methane steam reforming (MSR). MSR is simulated on one side of a plate by implementing experimentally validated surface microkinetic model for nickel/alumina catalyst. Required heat to an endothermic MSR is provided by simulating catalytic methane combustion (CMC) on an opposed-side of the plate by implementing reduced surface microkinetic model for platinum/alumina catalyst. Four different combinations of coating configurations between reforming and combustion catalysts are studied in terms of reaction heat flux and reactor plate temperature distributions as well as in terms of methane and hydrogen mole fraction distributions. These combinations are: (1) continuous combustion-catalyst and continuous reforming-catalyst (conventional CPR design), (2) continuous combustion-catalyst and segmented reforming-catalyst, (3) segmented combustion-catalyst and continuous reforming-catalyst, and (4) segmented combustion-catalyst and segmented reforming-catalyst. For the same reforming-side gas hourly space velocity, the study has shown that the CPR designed with the segmented catalysts requires 66% less combustion- catalyst to achieve similar methane conversion and hydrogen yield in MSR compared to the conventional CPR design. The study has also shown that maximum reactor plate temperature, thermal hot spots and axial thermal-gradients are reduced significantly in the CPR designed with the segmented catalysts than the CPR designed with the conventional continuous catalysts configuration.

3.1. Introduction

Fuel cells are expected to have extensive applications as an alternative clean power source from stationary use to distributed use. Due to an increase in global energy demand and as a result increase in environmental pollution, it is also expected that the demand of alternative clean power sources such as fuel cells will continue to rise. Consequently, the demand for hydrogen, the most important fuel for fuel cells and now emerging as universal energy carrier with energy security, will also continue to rise [1–3]. Though hydrogen is considered as the most abundant fuel in the universe, pure hydrogen exists in very limited quantity on our planet. Therefore, to fulfill the demand of hydrogen, various methods are developed to produce hydrogen from its primary sources. Two methods are most commonly in use to produce hydrogen: reformation and electrolysis. Reformation involves hydrogen separation from the water and carbon compounds such as methane, whereas electrolysis separates hydrogen from oxygen in water [3]. Fuel cells combined with electrolysis is not a viable solution for electricity generation, because electrolysis requires electricity to produce hydrogen. Hence, to increase the wide spread use of fuel cells, onsite production of hydrogen via methane reformation is the most cost-effective solution, especially after the recent discoveries of vast reserves of shale gas [4]. In reformation, steam reforming (SR) of hydrocarbons provides the maximum hydrogen concentration compared to other processes such as catalytic partial oxidation (CPOX) and autothermal reforming (ATR) [5]. However, SR is highly endothermic process and requires an effective way of supplying heat in a reactor. Mostly, SR is carried out in a fixed-bed catalytic reactor with high residence time [6]. But the fixed-bed design suffers from limitations such as heat-transfer and internal diffusion, which has led to the study of alternate reactor design such as catalytic plate reactor (CPR). A CPR design provides excellent heat and mass transfer characteristics compared to the conventional fixed-bed design. It allows to carry out highly endothermic reactions like methane steam reforming (MSR) and exothermic reactions like catalytic methane combustion (CMC) side by side in the separate flow channels [7]. The close proximate of exothermic heat source with endothermic reaction sites, reduces significantly the overall heat transfer resistance [8]. Also, the use of catalytic combustion to supply heat offers advantages over gas-phase combustion. Catalytic combustion takes place at a lower temperature than the gas-phase combustion, which reduces NOx formation and the lower operating temperature allows more material choices for designing a CPR [9]. However, the use of catalytic combustion in a CPR creates localized thermal-gradients (hot-spot) especially near the inlets due to the imbalance between generated and absorbed heat in combustion and reforming reaction zones respectively [10]. Such localized thermal imbalance causes problems of material failure and catalyst delamination due to different thermal expansion coefficients of the coated catalyst and the metal plate. Large thermal-gradient also reduces the catalytic active surface area, and as a result conversion rate of reactants [11]. To overcome these issues, recently Pattison et al. [12] and Jeon et al. [13] have proposed a segmented layers of combustion-catalyst (SLCC) for CMC coupled with MSR in a microchannel CPR. Pattison et al. [12] have explored numerically, a method for emulating distributed feed configuration in a microchannel CPR via SLCC macromorphology, consisting of alternating active and catalytically inactive sections. They have employed LHHW(Langmuir-Hinshelwood-Hougen-Watson) type Xu and Froment's [14] global kinetic model for MSR on nickel catalyst and power law type global rate expressions for both gas-phase methane combustion and CMC on platinum catalyst. Similarly, Jeon et al. [13] have proposed a stripe configuration for combustion-catalyst to minimize the formation of hot-spots in a microchannel CPR. They have considered nearly 50% combustion-side plate section coated with SLCC and the remaining 50% with the continuous layer of combustion-catalyst. They have also employed LHHW type Xu and Froment's global kinetic model for MSR on nickel catalyst and power law type global rate expression for CMC on palladium catalyst. Both studies have shown disappearance of hot-spots without any loss of methane conversion in MSR. Recently Settar et al. [15] have proposed a segmented reforming-catalyst layers' pattern for MSR with non-reactive metal foam to improve the mixing and hence methane conversion for a micro combined heat and power (CHP) system. With the segmented reforming-catalyst layers' pattern, they have predicted faster methane conversion compared to the conventional continuously coated reforming-catalyst. Use of non-reactive metal foam has improved mixing of reactants and hence better heat-transfer is achieved and resulted into increased hydrogen production. Settar et al. [16] have also carried out a computational comparative study between the segmented and conventional continuous reforming catalyst layers. Their numerical analysis has shown performance enhancement factor up to two in terms of methane conversion with the segmented reforming-catalyst layers for MSR. However, no experimental evidence has been reported to support their finding. Mundhwa et al. [17] have investigated the internal diffusion limitation of continuously coated reforming-catalyst by evaluating the effectiveness factors for the steam reforming of diesel surrogate as a function of the CPR length. The study has found that independent of the type of catalysts, the initial 20% of the CPR length has shown high diffusion limitations. Therefore, the use of graded or segmented reforming-catalyst can be an advantageous in optimizing the amount of reforming-catalyst for its maximum utilization.

Many numerical studies of MSR coupled with CMC in a CPR have been carried out for various applications. However, except Pattison et al. [12], Jeon et al. [13] and Settar et al. [15–16], all literature reviewed in this study, have investigated MSR coupled with catalytic combustion of hydrocarbons over conventional continuously coated layers of reforming and combustion catalysts.

Zanfir and Gavriilidis [18] have carried out a sensitivity analysis of several design and operating parameters including reaction kinetic parameters. They have demonstrated that different catalysts can show similar thermal behavior and performance but exhibit different sensitivity behavior. Major finding of their study is the strongest influence on the reactor sensitivity comes from the reaction activation energies. Zanfir and Gavriilidis [9] have also performed parametric investigation of reforming-catalyst thickness and flow-channels height of a CPR for operating conditions like conventional industrial methane reformer. They have developed a simplified 2D model of a CPR by implementing Xu and Froment's global kinetic model for MSR and power law rate expression for CMC. Zanfir and Gavriilidis have observed that by increasing reforming-channel height at constant inlet velocity, methane conversion decreases. They have concluded that MSR is feasible, if flowrates, catalyst thickness and channel heights are properly designed. In a separate study, Zanfir and Gavriilidis [19] have conducted numerical study of co-flow and counter-flow modes between MSR and CMC. They have determined higher methane conversion on the reforming-side with counter-flow than co-flow design. However, they have observed the thermal hot-spots in counter-flow configuration and suggested to optimize catalyst distribution on the combustion-side to reduce them.

Arzamendi et al. [20] have developed a 3D computational fluid dynamic (CFD) model of a microchannel reactor integrating MSR and CMC. They have implemented simplified rate expressions [21] for MSR and CMC. They have investigated the influence of catalyst loading, flow-modes between the two channels, and gas hourly space velocities (GHSVs). Their results have shown the possibility of 96% of methane conversion with 2–4 mg/cm2 of catalyst loading at 930–1000 °C in the range of 10,000–30,000 h−1 reforming-side GHSVref. In a separate work, Arzamendi et al. [22] have developed 3D CFD models of a plate reactor with square microchannel and microslits designs to investigate the effects of characteristic dimension with different aspect ratios. Their results have shown that methane conversion decreases with increase in characteristic dimension, however microchannel design has provided methane conversion slightly higher than that of the microslits design. Stefanidis and Vlachos [23] have studied MSR on a rhodium catalyst coupled with propane combustion over a platinum catalyst in a CPR and have reported that increasing catalyst loading and decreasing possible internal mass transfer limitations results in considerable process time reduction. Also, by lowering steam to carbon (SC) ratio yielded higher power output at relatively low reactor temperatures. In another study, Stefanidis et al. [24] have reported that the use of low thermal conductivity plate materials increases fuel conversion and power output in the incomplete conversion regime. However, the use of very low thermal conductivity materials has shown high thermal-gradients in a CPR and thus recommended to use intermediate thermal conductivity materials, such as stainless steel to trade-off between thermal-gradients and conversion. Zhai et al. [25] have developed 2D computational fluid dynamic (CFD) model of a CPR using surface microkinetic for MSR on rhodium and LHHW type global kinetic model for CMC on platinum. They have investigated the influence of wall thermal conductivity, ratio of combustion to reforming feed, channel size and space time. They have reported that the performance of the metallic wall is superior against ceramic wall and recommended to use the wall material with intermediate thermal conductivity to avoid the thermal hotspots formation.

This work presents the four separate 2D steady state numerical models of a CPR to study the influence of segmented layers of reforming and combustion catalysts on composition and temperature distributions in a CPR compared to the continuous catalysts layers. In the first model, abbreviated as CCCR, reacting flows of CMC and MSR are simulated over conventional continuously coated layers of combustion and reforming catalysts respectively. In the second

Table 3.1. *Geometric parameters of the four CPR-models*

	CCCR	CCSR	SCCR	SCSR
Plate				
length, mm	70.0	70.0	70.0	70.0
width, mm	50.0	50.0	50.0	50.0
thickness, mm	0.2	0.2	0.2	0.2
Reforming & Combustion Channels				
length, mm	70.0	70.0	70.0	70.0
width, mm	50.0	50.0	50.0	50.0
height, mm	2.0	2.0	2.0	2.0
half-height, mm	1.0	1.0	1.0	1.0
Reforming-Catalyst				
length of active catalyst segment, mm	50.0	2.0	50.0	2.0
width of active catalyst segment, mm	50.0	50.0	50.0	50.0
thickness of active catalyst segment, mm	0.1	0.1	0.1	0.1
number of active catalyst segments	1.0	17.0	1.0	17.0
total volume of the coated catalyst, mm^3	250.0	170.0	250.0	170.0
length of inactive catalyst segment, mm	NA	1.0	NA	1.0
width of inactive catalyst segment, mm	NA	50.0	NA	50.0
number of inactive catalyst segments	NA	16.0	NA	16.0
total length of active catalyst, mm	50.0	34.0	50.0	34.0
total length of inactive segment, mm	NA	16.0	NA	16.0
catalyst bulk density, kg/m^3	2366.7	2366.7	2366.7	2366.7
catalyst amount coated on one plate, g	0.592	0.402	0.592	0.402
Combustion-Catalyst				
length of active catalyst segment, mm	50.0	50.0	1.0	1.0
width of active catalyst segment, mm	50.0	50.0	50.0	50.0
thickness of active catalyst segment, mm	0.02	0.02	0.02	0.02
number of active catalyst segments	1.0	1.0	17.0	17.0
total volume of the coated catalyst, mm^3	50.0	50.0	17.0	17.0
length of inactive catalyst segment, mm	NA	NA	2.0	2.0
width of inactive catalyst segment, mm	NA	NA	50.0	50.0
number of inactive catalyst segments	NA	NA	16.0	16.0
total length of active catalyst, mm	50.0	50.0	17.0	17.0
total length of inactive segment, mm	NA	NA	32.0	32.0
catalyst bulk density, kg/m^3	2366.7	2366.7	2366.7	2366.7
catalyst amount coated on one plate, g	0.118	0.118	0.040	0.040

model, abbreviated as CCSR, CMC is simulated over continuously coated layer of the combustion- catalyst but MSR is simulated over segmented layer of the reforming-catalyst. In the third model, abbreviated as SCCR, CMC is simulated over the segmented combustion-catalyst, whereas MSR is simulated over the continuous reforming-catalyst. In the fourth model, abbreviated as SCSR, both CMC and MSR are simulated over the segmented layers of combustion and reforming catalysts respectively. For this study, methane flow-rate of 9.94 mol/h at the inlet of the reforming-side is determined based on the required inlet hydrogen flow-rate of 29.80 mol/h in a 1 kW fuel-cell, consisting of 158 cells with 0.7 cell voltage and 90% hydrogen utilization on the anode-side and based on the stoichiometric ratio of 3:1 for hydrogen and methane in MSR. The inlet flow selection of methane based on the required hydrogen flow-rate in a 1 kW fuel-cell may facilitate the future engineering and scaling calculations to integrate the CPR with the fuel-cell stack. To avoid any carbon formation on the reforming-catalyst, steam to carbon ratio (SC) of 3.0 is considered for MSR. Based on the total inlet flowrate and geometric information of CPR listed in Table 3.1, the calculated reforming-side inlet $GHSV_{ref}$ at normalized condition (298.15 K and 1 atm) is equal to 97,234 h^{-1}. GHSV is defined as the ratio of total volume flow of feed to catalyst volume. Same $GHSV_{ref}$ of 97,234 h^{-1} at the inlet of the reforming-channel and same total mass flow-rates ratio ($m_{comb/ref}$) of 2.0 between the combustion-side and the reforming-side at the inlet of the combustion-channel are considered for the comparative study of the four different CPR configurations.

3.2. Reaction kinetics

To simulate MSR, a surface microkinetic model developed by Maier et al. [26] for Ni/Al_2O_3 catalyst is implemented on the reforming-side of the CPR after validating it against the experimental data obtained from the literature [27]. To simulate CMC, a reduced surface microkinetic model, developed and validated by Deshmukh and Vlachos [28] for Pt/Al_2O_3 catalyst, is employed on the combustion-side of the CPR.

Reaction kinetics can be investigated by multi-step microkinetic approach or by global kinetic approach. In a global kinetic approach, reaction kinetic parameters are determined based on experiments carried out at specific operating conditions and hence their applicability is also valid within those conditions with prior knowledge of rate determining step (RDS) [29]. Hence, the applicability of global reaction kinetic parameters is also valid within those conditions. In reality, each reaction proceeds via many elementary reactions, *e.g.* as illustrated in Fig. 3.1, MSR

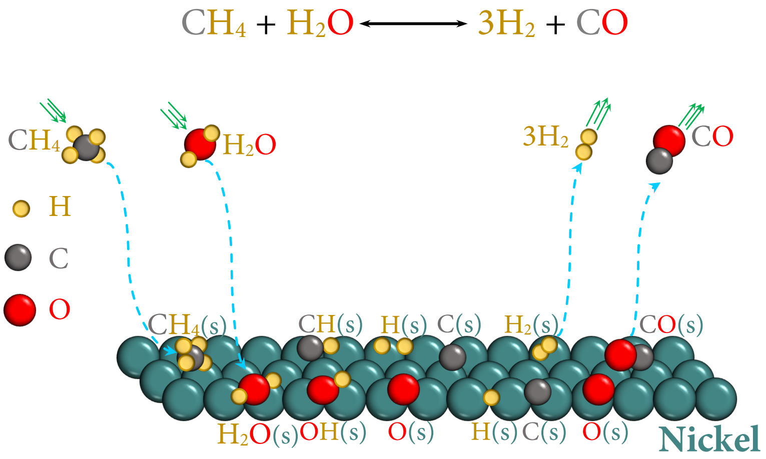

Fig. 3.1. *Illustration of elementary multi-steps of catalytic MSR reaction.*

Table 3.2. *Microkinetic model of MSR over Ni/Al_2O_3 catalyst developed by Maier et al. [26].*

No.	Elementary Reactions	A [cm, mol, s]	β	E_a
r_1	$H_2 + NI(s) + NI(s) \rightarrow H(s) + H(s)$	$0.010 \times 10^{-00\dagger}$	0	0.0
r_2	$O_2 + NI(s) + NI(s) \rightarrow O(s) + O(s)$	$0.010 \times 10^{-00\dagger}$	0	0.0
r_3	$CH_4 + NI(s) \rightarrow CH_4(s)$	$8.000 \times 10^{-03\dagger}$	0	0.0
r_4	$H_2O + NI(s) \rightarrow H_2O(s)$	$0.100 \times 10^{-00\dagger}$	0	0.0
r_5	$CO_2 + NI(s) \rightarrow CO_2(s)$	$1.000 \times 10^{-05\dagger}$	0	0.0
r_6	$CO + NI(s) \rightarrow CO(s)$	$5.000 \times 10^{-01\dagger}$	0	0.0
r_7	$H(s) + H(s) \rightarrow NI(s) + NI(s) + H_2$	$2.545 \times 10^{+19}$	0	81.21
r_8	$O(s) + O(s) \rightarrow NI(s) + NI(s) + O_2$	$4.283 \times 10^{+23}$	0	474.95
r_9	$CH_4(s) \rightarrow CH_4 + NI(s)$	$8.705 \times 10^{+15}$	0	37.55
r_{10}	$H_2O(s) \rightarrow H_2O + NI(s)$	$3.732 \times 10^{+12}$	0	60.79
r_{11}	$CO_2(s) \rightarrow CO_2 + NI(s)$	$6.447 \times 10^{+07}$	0	25.98
r_{12}	$CO(s) \rightarrow CO + NI(s)$	$3.563 \times 10^{+11}$	0	$111.27 - 50\vartheta_{CO(s)}$
r_{13}	$H(s) + O(s) \rightarrow OH(s) + NI(s)$	$5.000 \times 10^{+22}$	0	97.9
r_{14}	$OH(s) + NI(s) \rightarrow H(s) + O(s)$	$1.781 \times 10^{+21}$	0	36.09
r_{15}	$H(s) + OH(s) \rightarrow H_2O(s) + NI(s)$	$3.000 \times 10^{+20}$	0	42.7
r_{16}	$H_2O(s) + NI(s) \rightarrow H(s) + OH(s)$	$2.271 \times 10^{+21}$	0	91.76
r_{17}	$OH(s) + OH(s) \rightarrow H_2O(s) + O(s)$	$3.000 \times 10^{+21}$	0	100.0
r_{18}	$H_2O(s) + O(s) \rightarrow OH(s) + OH(s)$	$6.373 \times 10^{+23}$	0	210.86
r_{19}	$C(s) + O(s) \rightarrow CO(s) + NI(s)$	$5.200 \times 10^{+23}$	0	148.1
r_{20}	$CO(s) + NI(s) \rightarrow C(s) + O(s)$	$1.354 \times 10^{+22}$	-3	$116.12 - 50\vartheta_{CO(s)}$
r_{21}	$CO(s) + O(s) \rightarrow CO_2(s) + NI(s)$	$2.000 \times 10^{+19}$	0	$123.6 - 50\vartheta_{CO(s)}$
r_{22}	$CO_2(s) + NI(s) \rightarrow CO(s) + O(s)$	$4.653 \times 10^{+23}$	-1	89.32
r_{23}	$HCO(s) + NI(s) \rightarrow CO(s) + H(s)$	$3.700 \times 10^{+21}$	0	$50\vartheta_{CO(s)}$
r_{24}	$CO(s) + H(s) \rightarrow HCO(s) + NI(s)$	$4.019 \times 10^{+20}$	-1	132.23
r_{25}	$HCO(s) + NI(s) \rightarrow CH(s) + O(s)$	$3.700 \times 10^{+24}$	0	95.8
r_{26}	$CH(s) + O(s) \rightarrow HCO(s) + NI(s)$	$4.604 \times 10^{+20}$	0	109.97
r_{27}	$CH_4(s) + NI(s) \rightarrow CH_3(s) + H(s)$	$3.700 \times 10^{+21}$	0	57.7
r_{28}	$CH_3(s) + H(s) \rightarrow CH_4(s) + NI(s)$	$6.034 \times 10^{+21}$	0	61.58
r_{29}	$CH_3(s) + NI(s) \rightarrow CH_2(s) + H(s)$	$3.700 \times 10^{+24}$	0	100.0
r_{30}	$CH_2(s) + H(s) \rightarrow CH_3(s) + NI(s)$	$1.293 \times 10^{+23}$	0	55.33
r_{31}	$CH_2(s) + NI(s) \rightarrow CH(s) + H(s)$	$3.700 \times 10^{+24}$	0	97.1
r_{32}	$CH(s) + H(s) \rightarrow CH_2(s) + NI(s)$	$4.089 \times 10^{+24}$	0	79.18
r_{33}	$CH\ (s) + NI(s) \rightarrow C(s) + H(s)$	$3.700 \times 10^{+21}$	0	18.8
r_{34}	$C(s) + H(s) \rightarrow CH(s) + NI(s)$	$4.562 \times 10^{+22}$	0	161.11
r_{35}	$CH_4(s) + O(s) \rightarrow CH_3(s) + OH(s)$	$1.700 \times 10^{+24}$	0	88.3
r_{36}	$CH_3(s) + OH(s) \rightarrow CH_4(s) + O(s)$	$9.876 \times 10^{+22}$	0	30.37
r_{37}	$CH_3(s) + O(s) \rightarrow CH_2(s) + OH(s)$	$3.700 \times 10^{+24}$	0	130.1
r_{38}	$CH_2(s) + OH(s) \rightarrow CH_3(s) + O(s)$	$4.607 \times 10^{+21}$	0	23.62
r_{39}	$CH_2(s) + O(s) \rightarrow CH(s) + OH(s)$	$3.700 \times 10^{+24}$	0	126.8
r_{40}	$CH(s) + OH(s) \rightarrow CH_2(s) + O(s)$	$1.457 \times 10^{+23}$	0	47.07
r_{41}	$CH(s) + O(s) \rightarrow C(s) + OH(s)$	$3.700 \times 10^{+21}$	0	48.10
r_{42}	$C(s) + OH(s) \rightarrow CH(s) + O(s)$	$1.625 \times 10^{+21}$	0	128.61
				†sticking coefficient

reaction is composed of: (1) adsorption of methane and water molecules at the catalyst surface from the gas-phase, (2) reactions among adsorbed species at the catalyst surface, (3) the resulting surface species may participate further into intermediate surface reactions and (4) desorption of final products hydrogen and carbon monoxide from the catalyst surface to the gas-phase. Therefore, every reaction, simple or complex, can be studied in terms of elementary reactions. As shown in Fig. 3.1, MSR involves many intermediate reaction steps, where multiple reactions can be in equilibrium at the same time and hence, it is possible that several paths to the desired product formation can exist [30]. Existence of several possible paths to the product formation makes it difficult to decide a single rate determining step (RDS), even for catalysts prepared using the same active component. To develop a reaction kinetic model using the global kinetic approach, a knowledge of RDS is prerequisite and hence, different global reaction kinetic models or kinetic parameters are required to predict the performance of the MSR over catalysts that are prepared using the same active component. Whereas, the multi-step microkinetic approach does not require priori knowledge of the RDS and hence, it may be implemented to predict the performance of the MSR over different catalysts that are prepared using the same active component. Therefore, in this study to evaluate the performance of the CPRs designed with the four different configurations of catalysts, a detailed multi-step microkinetic model for MSR developed by Maier et al. [26] and reduced microkinetic model for CMC developed by Deshmukh and Vlachos [28] are implemented. The microkinetic model of Maier et al. [26] is consists of six gas phase species (N_g), thirteen surface-species (N_s) including nickel and 42 elementary reactions listed in Table 3.2. CMC also proceeds via many elementary reactions rather than a single global reaction as shown in Fig. 3.1 for MSR. Deshmukh and Vlachos [28] have developed the reduced microkinetic model for CMC based on the thermodynamically consistent and experimentally validated reaction mechanism proposed by Mhadeshwar and Vlachos [31]. To reduce their model, Deshmukh and Vlachos [28] have employed the computer-aided reduction methodology [32] to identify the key steps and reaction intermediates. They have validated their one step rate expression extensively with the relevant experimental data of methane combustion on different platinum-based catalysts under a wide range of operating conditions.

To implement the multi-step microkinetic with CFD model, the microkinetic modeling employs mean-field approximation approach, which neglects the effect of lateral interactions of the adsorbates and non-uniformity of the catalyst surface [33]. In the mean-field approximation, every adsorbates and adsorbent are defined as surface species. The coverage of surface species is then defined as:

$$\theta_{\mathrm{i}} = \frac{\text{Number of adsorption sites occupied by species } i}{\text{Total number of adsorption sites available}} \tag{3.1}$$

In this approximation, it is assumed that adsorbates are randomly distributed over the catalyst surface and the coverage of surface species depends on macroscopic position in the reactor and time, but they are averaged over microscopic local fluctuations, therefore, the surface is assumed to be uniform [33]. Under the mean-field approximation, rate expressions for the gas-phase species and the surface species are defined as:

$$s_i = \sum_{r=1}^{R} \mathrm{v}_{ir} k_r \prod_{j=1}^{N_g+N_s} c_j^{\mathrm{v}'_{jr}} \tag{3.2}$$

where, s_i is the overall rate expression for gas-phase or surface species i, r is the considered reaction and R is the total number of catalytic reactions, c_j is the concentration of j species, which is given in mol/m^2 for the adsorbed species and mol/m^3 for gaseous species [34]. The concentration c_j of an adsorbed species equals the surface coverage (θ_{j}) multiplied by the surface site density (Γ). $k_{f,r}$ is the reaction rate coefficient, v_{ir} is the difference of the right side (v''_{ir}) and left side (v'_{ir}) stoichiometric coefficients of species i in reaction r [34]. $\mathrm{N_g}$ and $\mathrm{N_s}$ represent the total number of gas-phase and surface species respectively. Because of the binding states of the adsorption of all species vary with the surface coverages, the reaction rate coefficients are determined using the modified Arrhenius expression [33]:

$$k_r = A_r T^{\beta_r} \exp\left(-\frac{E_{a_r}}{R_g T}\right) \theta_i^{\mu_{ir}} \exp\left[\frac{\varepsilon_{ir}\theta_i}{R_g T}\right] \tag{3.3}$$

where, E_{a_r} is the activation energy of the reaction r and θ_i is the fraction of the surface coverage of species i. μ_{ir} and ε_{ir} describe the dependence of the rate constants on the surface coverage of species i. For adsorption reactions, sticking coefficients are commonly used, which can be converted to conventional rate constants [26] as:

$$k_r^{ads} = \frac{S_i^0}{\Gamma_{Ni}^{\tau}} \sqrt{\frac{R_g T}{2\pi M_i}} \tag{3.4}$$

where, τ is the number of occupied adsorption sites of species i, S_i^0 is the initial (uncovered surface) sticking coefficient, Γ_{Ni} is the site density for nickel. The value of Γ_{Ni} is 2.6×10^{-5} mol/m^2, which is calculated by assuming a site area of 6.4×10^{-2} nm^2 as observed for nickel [26]. Surface coverage of the i^{th} species is calculated from the relationship between its concentration and site occupancy number, and surface site density. Thus, the time variation of the surface coverage of the i^{th} species is given as [33]:

$$\frac{\partial \theta_i}{\partial t} = \frac{s_i \sigma_i}{\Gamma_{Ni}}, \qquad \text{where} \sum_{i=1}^{N_s} \theta_i = 1 \tag{3.5}$$

To compute the species consumption and production rates for CMC, as mentioned earlier, reaction rate expression developed by Deshmukh and Vlachos [28] is implemented on the combustion-side. A rate expression for CMC on platinum is defined as:

$$s_{CH_4} = \frac{k_{CH_4}^{ads} c_{CH_4}}{\left(1 + \sqrt{\frac{k_{O_2}^{ads} c_{O_2}}{k_{O_2}^{des}}}\right)^2}, \tag{3.6}$$

where, k^{ads} and k^{des} are the reaction rate constant for adsorption and desorption respectively. They are computed using the modified Arrhenius equation form for adsorption and desorption respectively as:

$$k^{ads} = \frac{S_i^0}{\Gamma_{Pt}^{\tau}} \sqrt{\frac{R_g T}{2\pi M_i}} T^{\beta^{ads}} \exp\left(-\frac{E_a}{R_g T}\right) \tag{3.7}$$

$$k^{des} = A T^{\beta^{des}} \exp\left(-\frac{E_a}{R_g T}\right) \tag{3.8}$$

where, τ is the number of occupied adsorption sites of species i, S_i^0 is the initial (uncovered surface) sticking coefficient, Γ_{Pt} is the site density, which is equal to 2.48×10^{-5} mol/m^2 [28]. It should be noted that Deshmukh and Vlachos [28] have reported two sets of parameters. Out of the two sets, one set of parameters is provided to facilitate its use with the CHEMKIN. To facilitate its use with the CHEMKIN, they have refitted the parameters with temperature independent activation energies and converted the units of parameters (into mol, cm, and s). In this study, kinetic parameters reported by Deshmukh and Vlachos for the CHEMKIN are implemented and are listed in Table 3.3.

Table 3.3. *Kinetic parameters for catalytic methane combustion on platinum catalyst [28].*

S^0_{fuel}	$S^0_{O_2}$	β^{ads}_{fuel}	$\beta^{ads}_{O_2}$	$\beta^{des}_{O_2}$	$A^{des}_{O_2}$ [1/s]	$E^{ads}_{a\,fuel}$ [kcal/mol]	$E^{des}_{a\,O_2}$ [kcal/mol]
709.55	6.86×10^{-4}	-1.529	0.766	1.039	9.04×10^{18}	9.6	$49.5\text{-}32.0{\cdot}\theta_O$

To compute the rate of methane combustion using Eq. (3.6), one needs to know the coverage of oxygen because the activation energy of desorption is coverage-dependent (($49.5\text{-}32.0{\cdot}\theta_O$) kcal/mol). The oxygen coverage (θ_O) is computed using the following nonlinear relationship [28]:

$$\theta_O = \frac{\sqrt{k^{ads}_{O_2} c_{O_2} / k^{des}_{O_2}}}{1 + \sqrt{k^{ads}_{O_2} c_{O_2} / k^{des}_{O_2}}} \qquad (3.9)$$

3.3. Computational framework

Fig. 3.2 shows a schematic of the two-dimensional view of the four different catalysts configurations that are modeled in this work. Table 3.1 lists the geometric parameters of all four catalyst configurations. The study assumes that the CPR consists of 40 stacked fecralloy plates each having 7 cm length, 5 cm width and 0.2 mm thickness and coated with the Ni/Al_2O_3 catalyst on the reforming-side and with the Pt/Al_2O_3 catalyst on the combustion-side. The stacked arrangement of 40 plates, configures 20 reforming-channels and 20 combustion channels. For this study, the distance between the two-consecutive parallel stacked plates is assumed to be 2 mm. The stacked design of the CPR with alternate channels for reforming and combustion allows

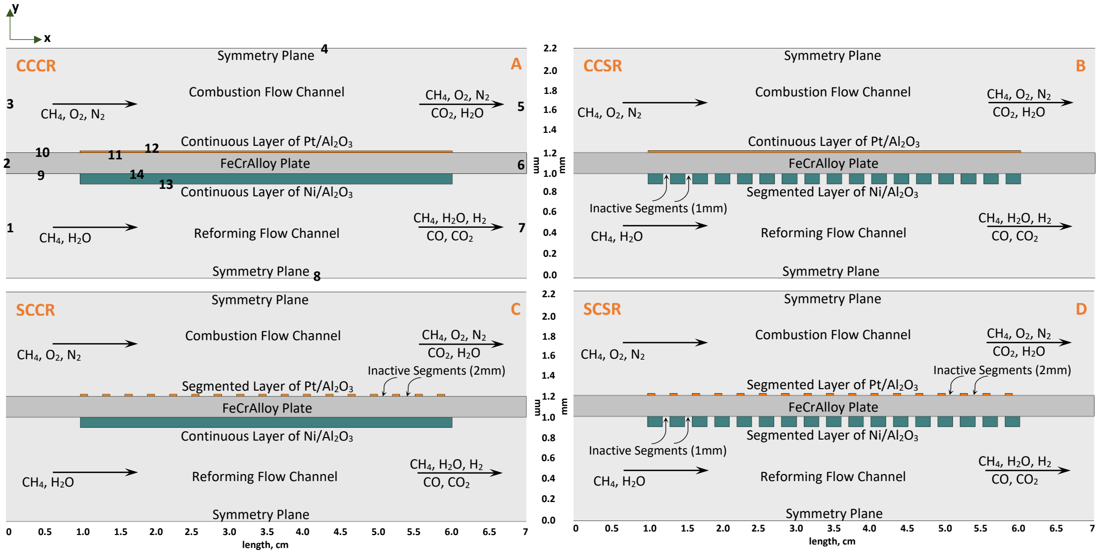

Fig. 3.2. *Two-dimensional view of simulated domains of a catalytic plate reactor designed with the four different catalyst configurations, (A) continuous combustion-catalyst and continuous reforming-catalyst (CCCR), (B) continuous combustion-catalyst and segmented reforming-catalyst (CCSR), (C) segmented combustion-catalyst and continuous reforming-catalyst (SCCR), (D) segmented combustion-catalyst and segmented reforming-catalyst (SCSR).*

to implement symmetry boundary conditions at the centre planes in both reforming and combustion channels. So, simulation of only one plate consists of appropriate coated catalysts and half channel height for fluid flow on its both sides is sufficient to do analysis of the results for the entire CPR consists of N number of plates and N/2 number of reforming as well as N/2 number of combustion channels. As illustrated in Fig. 3.2, symmetry boundary conditions are applied in both reforming and combustion flow channels at the 1 mm half channel height.

Fig. 3.2A shows the CCCR configuration consists of the fecralloy plate coated continuously with the Pt/Al_2O_3 catalyst of 5 cm × 5 cm × 20 µm size on the combustion-side and the Ni/Al_2O_3 catalyst of 5 cm × 5 cm × 100 µm size on the reforming-side. As shown in Fig. 3.2A, active catalysts on both reforming and combustion sides are deposited between x=1 cm and x=6 cm. On both sides of the fecralloy plate, catalytically inactive areas (bare plate surface) from x=0 to x=1 cm and from x=6 cm to x=7 cm with the size of 1 cm × 5 cm are considered to capture the influence of the inlets and outlets effect as well as to account for the hydrogen back-diffusion. The catalytically inactive section from x= 0 to x=1 cm, can also allow to capture the effect of convective and conductive heat transport from the combustion-catalyst to the incoming reactants and to the plate respectively. The CCSR configuration as illustrated in Fig. 3.2B, consists of the plate coated with the continuous layer of the Pt/Al_2O_3 catalyst of 5 cm × 5 cm × 20 µm size on the combustion-side and with 17 segmented layers of Ni/Al_2O_3 catalyst, each with the size of 2 mm × 5 cm × 100 µm on the reforming-side. To configure segmented reforming-catalyst, 32% of the Ni/Al_2O_3 catalyst is removed by considering catalytically inactive segment (bare plate surface) of 1 mm × 5 cm between the two consecutive catalytically active segments. Fig. 3.2C illustrates the SCCR configuration, which is consist of 17 segmented layers of the Pt/Al_2O_3 catalyst, each with the size of 1 mm × 5 cm × 20 µm on the combustion-side and the continuous layer of the Ni/Al_2O_3 catalyst of 5 cm × 5 cm × 100 µm size on the reforming-side. To configure segmented combustion-catalyst, 16 inactive segments (bare plate surfaces) each with the 2 mm × 5 cm size between the two consecutive catalytically active segments are considered. In total 66% of the combustion-catalyst is removed in the SCCR configuration compared to the CCCR configuration. Fig. 3.2D shows the SCSR configuration consists of 17 segmented layers of the combustion-catalyst and 17 segmented layers of the reforming-catalyst on the combustion-side and reforming-side respectively. The dimensions of the each active and catalytically inactive segment on the combustion-side and on the reforming-side are same as the segmented sections reported earlier for the SCCR and the CCSR configurations respectively.

Five different domains are identified to simulate the CPR as shown in Fig. 3.2: (1) combustion-channel, (2) combustion-catalyst, (3) fecralloy plate, (4) reforming-catalyst, and (5) reforming-channel. For the segmented configurations, only domains (2) and (4) are replaced accordingly, for example, continuous combustion-catalyst (domain (2)) in CCCR configuration is replacing with the segmented combustion-catalyst in the case of SCCR configuration as illustrated in Fig. 3.2B. Numerals at edges of the CPR geometry in Fig. 3.2A represents the domains boundaries. Numbers 1, 3 and 7, 5 represent inlet and outlet boundaries for the reforming and combustion channels, 4 and 8 illustrate symmetry boundaries, 12 represents the interface between the combustion-catalyst and combustion-channel and 13 represents the interface between the reforming-catalyst and reforming-channel, 9 and 10 shows the interfaces between the plate and the flow-channels, 2 and 6 represent insulated boundaries between the plate and the surrounding, and numbers 11 and 14 illustrate interfaces between the catalysts and the fecralloy plate. Similar boundaries are identified for the same interfaces depicted for the remaining three catalyst configurations.

To model the fluid-flow, compressible Navier-Stokes equations are implemented in both reforming and combustion flow channels; whereas to model the flow in porous catalysts due to pressure gradients, the Darcy-Brinkman model is employed. The convection-diffusion equations are implemented to solve the mass-fraction gradients of chemical species in both flow-channels. Most of the published literature solved the diffusive-fluxes by applying simplified diffusion approaches. These simplified approaches are strictly valid for diffusion of dilute species in a multicomponent mixture and for binary mixtures [35]. In this study, the diffusive fluxes are computed by employing the multi-component Maxwell-Stefan diffusion model. To account for the molecules collision with the catalysts walls, Knudsen diffusion is implemented with the convection-diffusion equations by calculating the effective diffusion coefficients for each chemical species. In order to avoid the violation of species conservation, the Bosanquet diffusion expression is applied to compute the effective diffusion coefficients [36]. Temperature profiles in both flow-channels are obtained by resolving convection-conduction equation, whereas temperature distributions in porous catalyst are obtained by solving pseudo-homogeneous heat-transfer model. Temperature distribution in solid fecralloy plate is obtained by employing the steady state conduction heat transfer equation.

The fecralloy plate in the present study act as a heat-transfer media between the reforming and combustion channels is considered an excellent substrate for coating of various catalysts as it has high structural stability and a melting point of approximately 1773 K [37]. Catacel™, an industrial heat exchanger manufacturer uses fecralloy foils/plates to design their CPRs. Their CPR patent [38] states that the use of metal plate/ foil for a heat exchanger with a thickness of 0.001–0.1 in. reduces expense using less material overall. The plate thickness of 0.2 mm that is used for the plate in this study lies within this range. In this study, the Fecralloy™ variant consists of 73.2% iron, 22% chromium and 4.8% aluminium with thermal conductivity of 16 W/m/K [39] is considered.

Individual thermal conductivities, heat capacities and viscosities of chemical components are calculated as a function of the temperature. Pure component temperature dependent parameters for heat capacities, viscosities, and thermal conductivities are obtained from Todd and Young [40]. The gas mixture heat capacity is evaluated using the weighted average heat capacity of the chemical species. The gas mixture viscosity is calculated using the method developed by Wilke [41]. The thermal conductivity of gas mixture is calculated using the Mason and Saxena method [41]. The effective thermal conductivities (k_{eff}) of the catalyst layers are calculated using a volume weighted average as:

$$k_{eff} = \varepsilon k_{mix} + (1 - \varepsilon) k_{cat} \tag{3.10}$$

where, k_{cat} is the solid phase catalyst thermal conductivity. The solid catalyst thermal conductivity (k_{cat}) is approximated based on alumina and is calculated by Eq. (3.11), where temperature T is in degree Celsius [42]:

$$k_{cat} = 5.85 + 15360 \frac{exp(-0.002T)}{516 + T} \tag{3.11}$$

Both the multi-component Maxwell-Stefan diffusion [43] and the Knudsen diffusion models [44] are employed with the convection-diffusion equations to evaluate species diffusion fluxes inside the porous structure of the catalysts, whereas only the multicomponent Maxwell- Stefan diffusion model with the convection-diffusion equations is considered for the flow-channels. The Fuller equation [41] is used to obtain the binary diffusion coefficients (D_{ij}) for each species involved. To ensure species mass conservation, averaged Bosanquet diffusion expression [36] is employed to evaluate the effective diffusion coefficients ($D_{ij,eff}$) involving the Knudsen diffusion (D_i^K) and the binary diffusion coefficients (D_{ij}).

$$D_{ij,eff} = D_{ji,eff} = \frac{\varepsilon}{\tau}\frac{1}{2}\left(\frac{1}{1/D_i^K + 1/D_{ij}} + \frac{1}{1/D_j^K + 1/D_{ji}}\right) \tag{3.12}$$

where, D_i^K and D_j^K are the Knudsen diffusion coefficients of chemical species i and j respectively; D_{ij} and D_{ji} are the binary diffusion coefficients of chemical species i and j. Mean particle size of 1 μm and porosity value of 0.4 are assumed in both reforming and combustion-catalyst. The values of tortuosity (τ) are calculated using the Bruggeman correlation [45]. Mean pore size is determined using Kozeny's equation for porosity, mean particle size and mean pore size [46]. Permeability value is estimated using Kozeny-Carman relationship (Eq. 3.13), where d_p is the average particle diameter. Specific surface area (A_{sr}) of 2.65×10^6 m^2/m^3 for the 8.28% (wt.) Ni/Al_2O_3 catalyst is obtained by validating the microkinetic model of Maier et al. [26] against the experimental data of Karakaya et al. [27], presented in the next section. For the Pt/Al_2O_3 catalyst, a specific surface area of 2.58×10^5 m^2/m^3 is calculated based on 2.2 wt. % Pt/Al_2O_3 with 2.48×10^{-5} mol/m^2 site density and 12% dispersion [47].

$$\kappa = \frac{\varepsilon^3 d_p^2}{72\tau(1-\varepsilon)^2} \tag{3.13}$$

To solve the coupled set of partial differential equations, commercially available simulation software package COMSOLTM 4.0 is used. COMSOL™ simulates the set of heat, mass and reacting flow equations using finite-element method (FEM). The CPR models are based on a distributed mapped mesh. More mesh elements are employed at the catalyst inlets where larger variations in reaction rates and thermal-gradients are occurred. All solutions are resolved using a finer mesh, and a mesh-independent solution is obtained for all runs with convergence criteria of 1.0×10^{-05} absolute error. In the model solutions, it is ensured that the conservation of mass in both the reforming and combustion channels are satisfied. All model equations and boundary conditions are listed in Appendix A. Few assumptions are made to develop the numerical models in this study, which are: (1) Ideal gas law (elevated temperature and low-pressure conditions), (2) fully-developed laminar flow in both half-channels, (3) catalyst layers are isotropic and all reactions take place in the catalyst layers, (4) catalyst particles are spherical in shape, and (5) body forces are neglected.

3.4. Model Validation

The microkinetic model developed by Maier et al. [26] over 3.0 wt.% Ni/Al_2O_3 catalyst was validated against the experimental data of Karakaya et al. [27] of MSR in a CPR. Karakaya et al. carried out experimental study of MSR over continuously wall coated Ni (8.28 wt.%) catalyst supported on Al_2O_3. They have reported methane conversion at five different inlet space-times (τ_s) between 12.86 and 77.14 ms, at four different temperatures between 873 and 1073 K and at four different steam to carbon ratios between 1.5 and 3. Model validation was carried out with the 2D computational approach using reactor geometric parameters exactly reported by Karakaya et al. for their experimental CPR. To validate the model, an active nickel surface area was adjusted to 2.65×10^6 m^2/m^3 with no changes in any other kinetic parameters reported by Maier et al. An adjustment in active surface area value was necessary due to difference in nickel content used by Maier et al. (3 wt.% Ni) and Karakaya et al. (8.28 wt.% Ni) in their catalysts. Table 3.4 list the parameters used in 2D model of experimental microchannel CPR of Karakaya

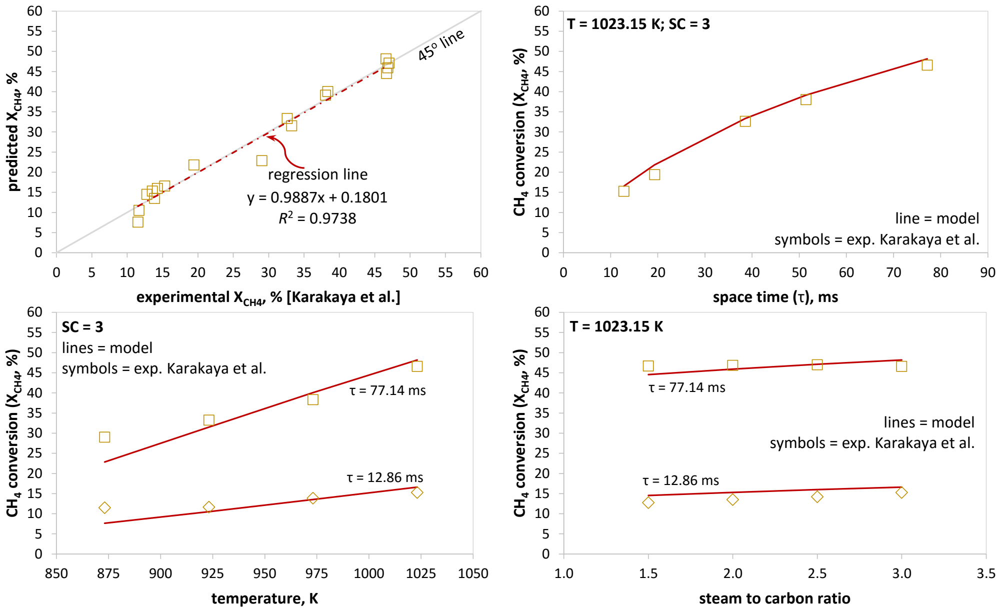

Fig. 3.3. *Validation of multi-step microkinetic model of Maier et al. [26] for MSR on Ni/*Al_2O_3 *catalyst against the experimental data of Karakaya et al. [27] for microchannel CPR*

et al. Fig. 3.3 has shown an excellent agreement between the predicted and the experimental methane conversion in MSR for varying inlet space-times, temperatures, and steam to carbon ratios with the R-squared value of 0.9738.

Table 3.4. *Parameters for 2D model of experimental microchannel reactor used by Karakaya et al. [27] for model validation.*

Channel height	0.75 mm – catalyst thickness
Channel width	3.0 mm
Catalyst length	20.0 mm
Catalyst thickness	100.0 µm
Amount of catalyst	14.2 mg
Catalyst loading on single plate	23.667 mg/cm^2
Nickel content	8.28 %
Catalyst density	2366.7 kg/m^3
Porosity (ε)	0.4
Tortuosity	$1/\varepsilon^{1/2}$
Surface area	2.65 $\times 10^6$ m^2/m^3

3.5. Results and discussion

The 2D steady-state computational models developed in this study are utilized to investigate the influence of four different configurations between segmented and continuous layers of reforming and combustion catalysts on MSR to produce hydrogen. All four catalyst configurations are compared in terms of temperature, heat distribution and effective thermal conductivity as well as in terms of methane and hydrogen mole-fraction distribution and in terms of H_2/CO ratio and CO selectivity (S_{CO}) at the reforming-channel outlet. It should be noted that in the case of segmented reforming-catalyst (CCSR, SCSR) configurations, the amount of reforming-catalyst is reduced by 32% and hence to keep the reforming-side inlet $GHSV_{ref}$ and combustion to reforming mass flow-rates ratio constant, total inlet flow-rates in both reforming and combustion sides are reduced by 32% compared to the CCCR and SCCR configurations. Required inlet parameters are listed in Table 3.5 for the all four catalyst configurations. It should also be noted that the size of the segmented layers for both reforming and combustion catalysts and distance of interspacing (inactive sections) among active catalytic segments are not optimized in this study. Thus, optimizations of interspacing distance and segmented catalyst size may further improve the CPR performance.

Table 3.5. *Inlet conditions and catalyst parameters for the four configurations between combustion and reforming catalysts.*

	CCCR		CCSR		SCCR		SCSR	
Inlet Conditions	**Reforming**	**Combustion**	**Reforming**	**Combustion**	**Reforming**	**Combustion**	**Reforming**	**Combustion**
CH_4 molar flow in 20 channels, mol/h	9.936	3.892	6.7565	2.6466	9.936	3.892	6.7565	2.6466
CH_4 molar flow in one channel, N_{CH4}, mol/h	0.4968	0.1946	0.3378	0.1323	0.4968	0.1946	0.3378	0.1323
Steam to Carbon ratio (SC)	3	n/a	3	n/a	3	n/a	3	n/a
Oxygen to Carbon ratio (O_2/C)	n/a	2.5	n/a	2.5	n/a	2.5	n/a	2.5
H_2O molar flow in one channel, N_{H2O}, mol/h	SC × N_{CH4}	n/a	SC × N_{CH4}	n/a	SC × N_{CH4}	n/a	SC × N_{CH4}	n/a
O_2 molar flow in one channel, N_{O2}, mol/h	n/a	$(O_2/C) \times N_{CH4}$	n/a	$(O_2/C) \times N_{CH4}$	n/a	$(O_2/C) \times N_{CH4}$	n/a	$(O_2/C) \times N_{CH4}$
N_2 molar flow in one channel, N_{N2}, mol/h	n/a	$(79/21) \times N_{O2}$	n/a	$(79/21) \times N_{O2}$	n/a	$(79/21) \times N_{O2}$	n/a	$(79/21) \times N_{O2}$
GHSV at 298.15K, 1 atm., h^{-1}	97,234	6.1438×10^5	97,234	4.1778×10^5	97,234	1.8070×10^6	97,234	1.2288×10^6
Mass flow rates ratio (m_{comb}/m_{ref})	2		2		2		2	
Temperature, K	800		800		800		800	
Pressure, atm.	1		1		1		1	
Catalyst Layers								
Total volume of the coated catalyst, mm^3	250	50	170.0	50.0	250.0	17.0	170.0	17.0
Catalyst amount coated on one plate, g	0.592	0.118	0.402	0.118	0.592	0.040	0.402	0.040
Specific surface area, m^2/m^3	2.65×10^6	2.58×10^5	2.65×10^6	2.58×10^5	2.65×10^6	2.58×10^5	2.65×10^6	2.58×10^5
Site density, mol/m^2	2.6×10^{-5} [15]	2.48×10^{-5} [17]	2.6×10^{-5} [15]	2.48×10^{-5} [17]	2.6×10^{-5} [15]	2.48×10^{-5} [17]	2.6×10^{-5} [15]	2.48×10^{-5} [17]

Performance of the CPR designed with the four different catalyst configurations is evaluated by methane conversion (X_{CH4}), hydrogen yield (Y_{H2}) and CO selectivity (S_{CO}). The methane conversion in both reforming and combustion sides is defined as the ratio between converted methane at a position along the channel and the inlet molar rate of methane:

$$X_{CH4} = 100 \times \left[\frac{N_{CH_{4,in}} - N_{CH_4}}{N_{CH_{4,in}}}\right] \tag{3.14}$$

where, $N_{CH_{4,in}}$ is the inlet molar flow-rate of methane and N_{CH_4} is the molar flow-rate of methane at a position along the channel-length. Hydrogen yield (Y_{H2}) characterizes the performance of the reactor with respect to the hydrogen production. It is defined as the ratio of the molar rate of produced hydrogen (N_{H_2}) to the theoretical maximum amount of hydrogen that can be produced in MSR and water gas shift (WGS) reaction:

$$Y_{H2} = 100 \times \left[\frac{1}{4}\frac{N_{H_2}}{N_{CH_{4,in}}}\right] \tag{3.15}$$

CO selectivity (S_{CO}) is defined as the ratio of the produced carbon monoxide (N_{CO}) to the molar rate of methane consumption:

$$S_{CO} = 100 \times \left[\frac{N_{CO}}{N_{CH_{4,in}} - N_{CH_4}}\right] \tag{3.16}$$

3.5.1. Heat distribution and temperature

Fig. 3.4A shows the absorption and production of heat in the reforming-catalyst and combustion-catalyst respectively, in terms of average values of absolute heat-flux as a function of the plate-length for the CPR designed with the continuous catalysts layers (CCCR). Due to the high reaction rate of CMC, combustion-side heat-flux value quickly decreases from 84 kWm^{-2} at x = 1 cm to 0.19 kWm^{-2} within 50% (x = 3.5 cm) of the total plate-length (7.0 cm). This also

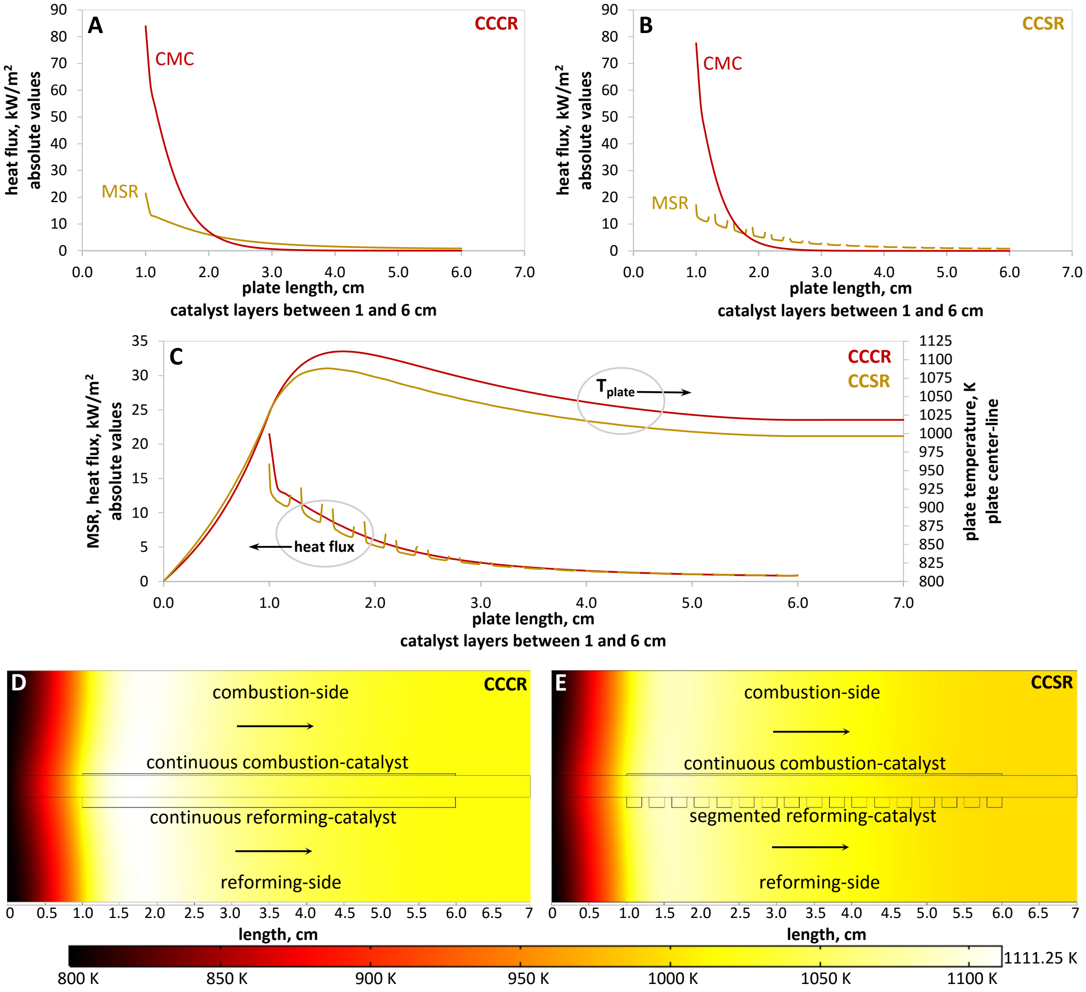

Fig. 3.4. *Average absolute values of heat-flux generated in combustion-catalyst and consumed in reforming-catalyst as a function of the plate-length for (A) CCCR, and for (B) CCSR. (C) Comparison of average absolute values of heat-flux consumed in reforming-catalyst and comparison of plate temperature observed at the center of the plate as a function of the plate length between CCCR and CCSR configurations. (D) Temperature distribution in a CPR designed with CCCR, and with (E) CCSR.*

signifies that 100% of methane on the combustion-side is consumed within 50% of the plate-length and hence its effect is also observed on the reforming-side in terms of decrease in absorption of heat in reforming-catalyst from 21.5 kWm^{-2} at x=1 cm to 2.0 kWm^{-2} within 50% of the plate-length. Similarly, Fig. 3.4B shows the average heat-flux values for the CPR configured with the continuous combustion-catalyst and segmented reforming-catalyst layers (CCSR). The production of heat in combustion-catalyst with the CCSR configuration, decreases from 77.6 kW m^{-2} at x = 1 cm to 0.03 kW m^{-2} within 50% of the plate-length, whereas absorption of heat in reforming-side is decreased from17.1 kWm^{-2} at x=1 cm to 1.85kWm^{-2} within 50% of the plate length. Fig. 3.4B has also shown heat-flux peaks at the leading and ending edges of MSR catalyst. This behaviour is endowed to the supply of heat from CMC to MSR through the catalytically inert sections among catalytic active segments, resulting to raise reforming-side stream temperature when it passes over the inert sections and as a result increases sharply the absorption of heat in MSR at the leading and ending edges of each reforming-catalyst segment.

To understand how effective heat is distributed in the CPR, it is important to study the temperature profiles of the fecralloy plate, which separates the combustion-side reacting flow from the reforming-side and act as a conductive media for the transfer of heat from the combustion- side to the reforming-side. Fig. 3.4C shows the axial temperature profiles at the centerline (y = 1.1 mm) of the fecralloy plate and reforming-side average absolute heat-flux values between the CCCR and CCSR configurations. Maximum plate temperatures of 1111.14 K at x=1.7 cm and 1088.26 K at x=1.55 cm is obtained for the CPR designed with the CCCR and CCSR respectively at the same reforming-side inlet GHSVref of 97,234 h^{-1}. Overall the plate temperature in the case of CCSR is lower than the CCCR. This is due to the slightly higher methane conversion at the beginning of the reforming-catalyst in the case of CCSR compared to the CCCR. From Fig. 3.4C, it is also observed that the differences between the maximum plate temperature and the plate temperature at the inlets (x = 0) are about 311.14 K and 288.26 K for the CCCR and CCSR respectively. And the differences between the maximum plate temperature and at the outlets (x=7 cm) are about 92.68 K and 91.63 K for the CCCR and CCSR respectively. Such significant differences in plate temperatures indicate the formation of large thermal-gradients and possible hot-spots near the reactor inlets. Bright areas (hotspots) between x = 1 and 3 cm are clearly visible in Fig. 3.4D and E due to the imbalance between the production of heat at faster rate by CMC and the absorption of heat at relatively slower rate by MSR. Formation of hot-spots and large thermal-gradients causes problem of catalysts delamination due to different thermal expansion coefficients of the plate and the coated catalysts.

Similarly, Fig. 3.5A and B illustrates the average absolute heat-flux values in the reforming-catalyst and combustion-catalyst as a function of the plate-length for the CPR designed with the SCCR and SCSR respectively. Since the reforming and combustion are catalytic reactions, the heat-flux values are zero in segmented catalyst configurations, where the plate surface is inert or catalyst free. In both Fig. 3.5A and B, heat-flux peaks are observed at the leading and ending edges of the active segmented reforming and combustion catalysts. This behaviour is due to the continuous supply of heat to the reforming-side from the combustion-side through the interspacing among active catalytic segments, resulting to raise reforming-side reactants temperature and consequently increase the endothermic heat at the leading and ending edges of the segmented reforming catalyst. The reverse is true in the case of segmented combustion catalyst. The transfer of heat from the combustion-side to the reforming-side through the interspacing slightly lowers the combustion- side reactants temperature between the two active segments of combustion-catalyst layers, resulting to move exothermic combustion reaction in the forward direction when combustion-side fluid stream comes in contact with the edges of the catalytically active segments and consequently increases the production of exothermic heat at the leading and ending edges of the segmented combustion- catalyst.

Unlike CCCR and CCSR configurations, heat-flux values in the case of SCCR and SCSR are not falling to near zero within very short distance of the plate-length from the reactor inlets. As shown in Fig. 3.5A, combustion-side heat-flux in the case of SCCR is decreased from 66.69 kW m^{-2} at x = 1 cm to 12.18 kW m^{-2} at x = 3.5 cm (50% of the plate-length). Whereas, absorption of heat in terms of heat-flux in reforming-side is decreased from 14.07 kWm^{-2} at x = 1 cm to 3.12 kWm^{-2} at x=3.5 cm. Similarly, Fig. 3.5B shows the combustion- side heat-flux in the case of SCSR is decreased from69 kWm^{-2} at x = 1 cm to 4.6 kWm^{-2} at x = 3.5 cm, whereas reforming side heat flux decreases from 12.94 kWm^{-2} at x = 1 cm to 2.6 kWm^{-2} at x = 3.5 cm. If the heat-flux values in combustion and reforming catalysts among all four configurations (CCCR, CCSR, SCCR and SCSR) at 50% plate-length (x = 3.5 cm) are compared, one can see that the SCCR configuration has shown high heat-flux values on both sides of the plate followed by the SCSR, CCCR and CCSR. This signifies that both MSR and CMC processes are intensified further downstream of the CPR in the case of SCCR and SCSR compared to the CCCR and CCSR.

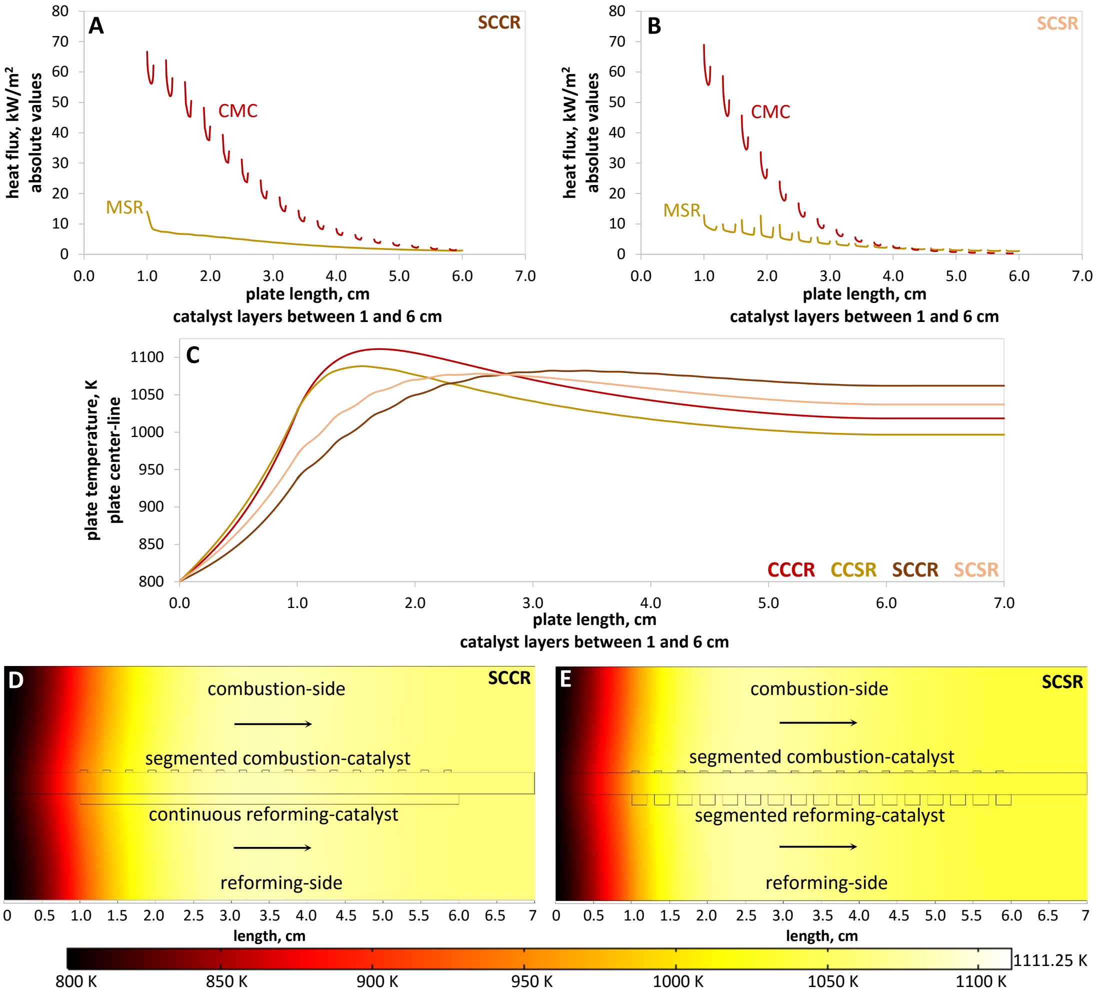

Fig. 3.5. *Average absolute values of heat-flux generated in combustion catalyst and consumed in reforming-catalyst as a function of the plate-length for (A) SCCR, and for (B) SCSR. (C) Comparison of plate temperature observed at the center of the plate as a function of the plate length for CCCR, CCSR, SCCR and SCSR configurations. (D) Temperature distribution in a CPR designed with SCCR, and with (E) SCSR.*

Fig. 3.5C compares the axial temperature profiles at the centerline (y=1.1mm) of the plate for the CCCR, CCSR, SCCR and SCSR configurations. Maximum plate temperatures of 1111.14 K at x = 1.7 cm, 1088.26 K at x = 1.55 cm, 1082.24 K at x = 3.17 cm and 1078.11 K at x = 2.54 cm are predicted for the CCCR, CCSR, SCCR and SCSR respectively for the same reforming-side GHSV$_{ref}$ = 97.234 h^{-1} and for the same combustion-side to reforming-side inlet mass flow-rates ratio of 2.0. It is clearly observed from Fig. 3.5C that maximum temperatures and axial thermal gradients are minimize in the case of SCCR and SCSR as compared with the CCCR and CCSR

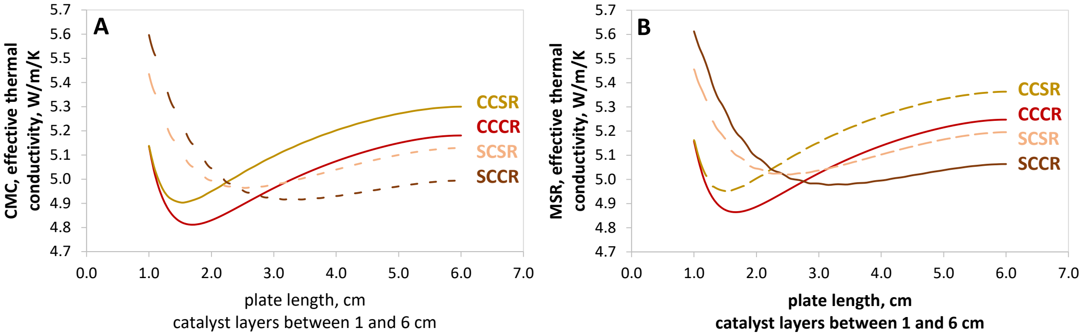

Fig. 3.6. *(A) combustion-side and (B) reforming-side effective thermal conductivity for CCCR, CCSR, SCCR, and SCSR configurations.*

configurations. Wave like plate temperature profiles between x = 1 cm and x = 3 cm in the case of SCCR and SCSR are obtained due to the active and catalytically inactive segments of the combustion-side catalyst increases and decreases production of heat. By comparing temperature profiles of continuous combustion-catalyst (CCCR and CCSR) and segmented combustion-catalyst (SCCR and SCSR), proves that segmented combustion-catalyst has played significant role in minimizing the maximum plate temperature and reducing the axial thermal gradients by distributing the exothermic heat in a more uniform fashion as compared to the continuous combustion- catalyst design. Fig. 3.5D and E have further strengthened the viewpoint of the significant role being played by the segmented combustion-catalyst by illustrating the disappearance of the bright areas (hot-spots) which otherwise are clearly visible in the Fig. 3.4D and E in the case of CCCR and CCSR configured CPR respectively. It should be noted that the temperature scale in Fig. 3.5D and E is kept identical to that shown in Fig. 3.4D and E for a comparative study. From the temperature distribution study, maximum plate temperature and axial thermal-gradients are minimized in the CPR designed with the SCCR and SCSR configurations compared to the CPR designed with the CCCR and CCSR configurations.

3.5.2. Effective thermal conductivity

Fig. 3.6A and B illustrate the effective thermal conductivity (Eq. (3.10)) profiles for the combustion and reforming-side catalysts respectively as a function of the plate-length, for the four configurations. It should be noted that the broken lines for the CCSR, SCCR and SCSR in Fig. 3.6 are due to the presence and absence of the segmented catalyst sections, as effective thermal conductivity (k_{eff}) values are applicable only to catalyst covered plate segments. Fig. 3.6A and B clearly illustrate that both combustion-side and reforming-side k_{eff} values for the SCSR and SCCR configurations are improved noticeably for the first 44% and 36% of the catalyst-length, compared to the conventional CCCR configuration. Whereas, k_{eff} values for the CCSR improved noticeably for the entire catalyst length compared to the CCCR design. The improved k_{eff} values for the segmented reforming-catalyst and segmented combustion-catalyst configurations compared to the conventional CCCR indicate that segmented catalyst design can play the important role in intensifying the MSR and CMC in a CPR. Also, this study indicates the requirement of further study of segmented catalysts by varying thermal conductivity of plate to intensify the plate reactor performance.

3.5.3. Methane and hydrogen mole-fractions

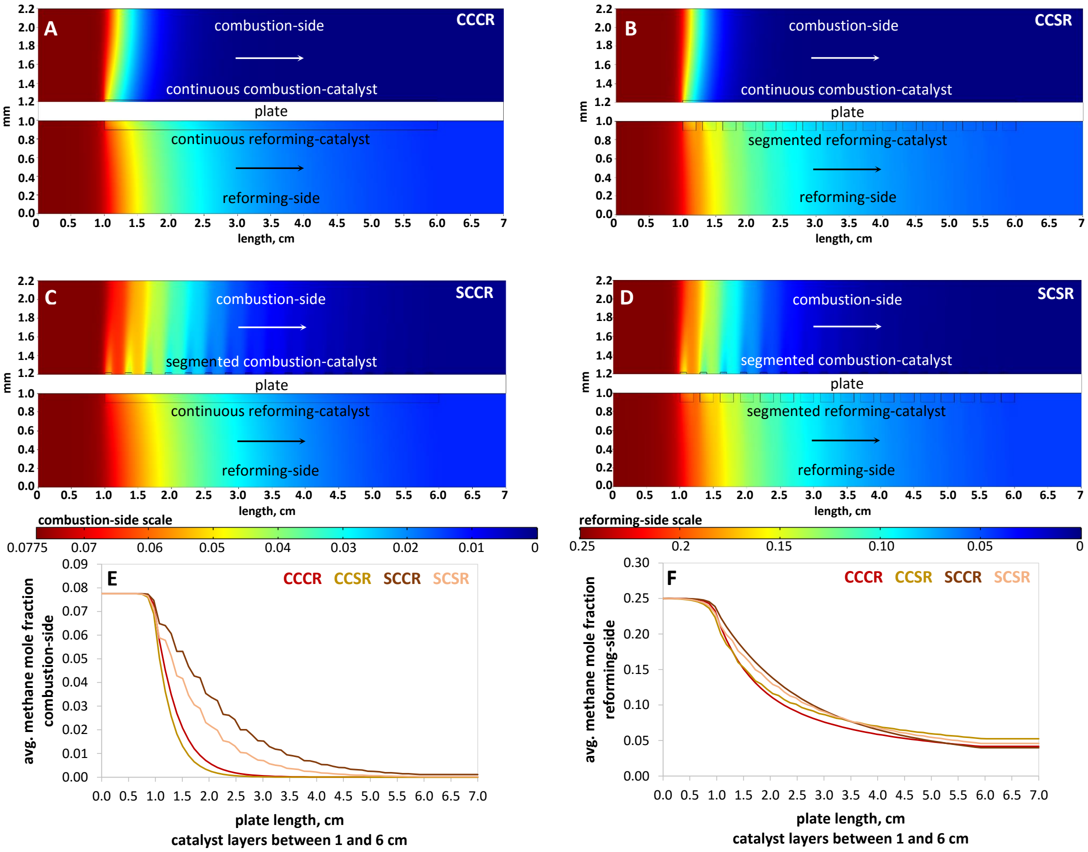

Fig. 3.7. *Methane mole-fraction distribution in combustion and reforming channels for (A) CCCR, (B) CCSR, (C) SCCR, and (D) SCSR. (E) Average mole-fraction of methane in combustion-channel and (F) in reforming-channel as a function of the plate-length for CCCR, CCSR, SCCR and SCSR configurations.*

To study the distribution of methane conversion in both reforming and combustion channels, the methane mole-fraction distribution in the CPR designed with the four different catalysts configurations is illustrated in Fig. 3.7. The distribution of the methane agrees with the behaviour of temperature distribution shown in Fig. 3.4 and in Fig. 3.5. It is displayed clearly in Fig. 3.7, that combustion-side methane consumption rate is slow in the case of CPR designed with the SCCR and SCSR (Fig. 3.7C and D) compared to the CPR designed with the CCCR and CCSR (Fig. 3.7A and B) configurations. Hence, more uniform temperature distribution (Fig. 3.5D and E) is achieved at the reactor downstream in the CPR designed with the SCCR and SCSR. The influence of the methane consumption in CMC is clearly visible on the methane consumption in MSR. Relatively uniform temperature distribution obtained using the segmented combustion-catalyst (SCCR, SCSR), resulted into high reforming-side methane conversion of 77.91% and 76.14% with the SCCR and SCSR respectively for the same reforming-side $GHSV_{ref}$. If one compares the performance between the CCSR and SCSR, the influence of the segmented combustion-catalyst on MSR is significant compared to the continuous combustion-catalyst. Due to relatively slow methane consumption in the combustion-side (Fig. 3.7E) and hence the achievement of relatively more uniform temperature distribution (Fig. 3.5E) has resulted high methane consumption in MSR in the case of SCSR than CCSR (Fig. 3.7F). Based on the methane

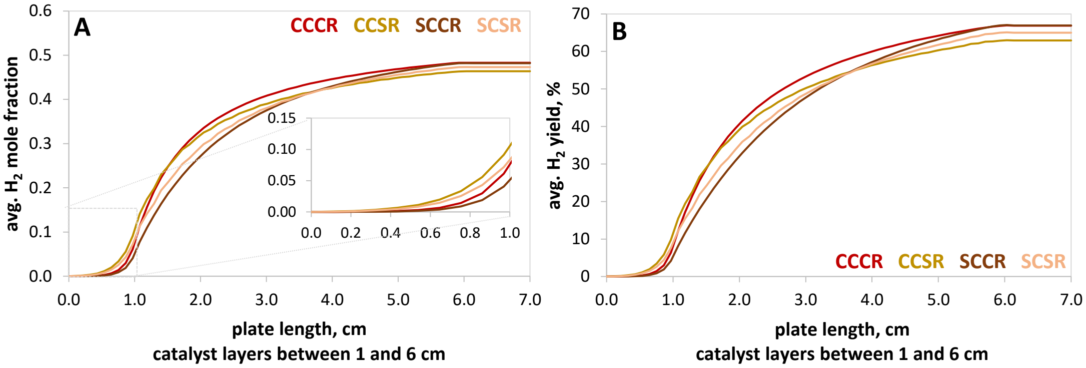

Fig. 3.8. *(A) Average hydrogen mole-fraction and (B) Average hydrogen yield in reforming-channel as a function of the plate-length for the CCCR, CCSR, SCCR and SCSR configurations.*

flow-rates at the reforming-side inlets and outlets (Eq. (3.13)), 76.14% of methane conversion in MSR is achieved by implementing the SCSR configuration compared to 72.11% with the CCSR. The difference of more than 4% of methane conversion in MSR signifies that segmented combustion-catalyst compared to the continuous combustion-catalyst is more effective configuration for intensifying both MSR and CMC. Fig. 3.7F also illustrates that mole fractions of methane at the outlet of the reforming-side in the case of CCCR is slightly lower than SCSR (76.91% methane-conversion with CCCR and 76.14%with SCSR). However, high maximum plate temperature and larger axial-thermal gradients (Fig. 3.4C, D) in the CPR designed with the CCCR configuration makes the CPR designed with the SCSR configuration, a desirable choice. Almost 100% methane conversion in CMC is achieved in all four catalyst configurations as can be concluded from Fig. 3.7E in terms of methane mole-fraction reaches to near zero value at the exit of the combustion-channel.

Fig. 3.8A and B illustrate the hydrogen mole-fraction (yH2) and hydrogen yield (YH2) as a function of the plate-length respectively, for the four configurations. Almost same hydrogen production and yields (around y_{H2} = 0.4825, Y_{H2} = 66.9%) is achieved with the CCCR and SCCR configurations followed by the SCSR (y_{H2} = 0.4730, Y_{H2} = 65.01%) and CCSR (y_{H2} = 0.4637, Y_{H2} = 62.91%). Fig. 3.8A has also clearly depicted the hydrogen back-diffusion from the leading edge of the reforming-catalyst (x = 1 cm) to the reforming-channel inlet (x = 0) due to high diffusivity of hydrogen. One can observe that hydrogen back-diffusion is reducing when segmented combustion-catalyst is employed (SCCR, SCSR) due to low upstream temperature than in the CPR designed with the CCCR and CCSR configurations (Fig. 3.5C). With the SCCR configuration, hydrogen back-diffusion is reduced on average by 35% compared to the CCCR and with the SCSR, it is reduced by 23% than the CCSR between x = 0 and x = 1 cm. Low back-diffusion of hydrogen allows more reactants (CH_4 and H_2O) to get adsorbed on the catalytic surface relatively easy, and hence increases the utilization of the reforming-catalyst than the situation where more hydrogen is diffusing in reverse direction and competing with the reactants in adsorption step at the active sites of the reforming-catalyst.

3.5.4. H_2/CO ratio and CO-selectivity

Fig. 3.9 illustrates the average H_2/CO ratios and CO selectivity (S_{CO}) at the reforming-channel outlet for the four-catalyst configurations. Fig. 3.9 clearly shows that CCSR configuration has predicted highest H_2/CO ratio (7.3) followed by CCCR (6.66), SCSR (6.48) and SCCR (6.12). Hence, S_{CO} has displayed the reverse trend, SCCR being the highest in predicting S_{CO} (56.18%) followed by SCSR (53.46%), CCCR (52.24%) and CCSR (48.14%). The CCSR configuration has predicted lower methane conversion (Fig. 3.7F) at the reforming- channel outlet and hence high H_2/CO ratio compared to the other three configurations. This can be attributed to the lower consumption of water at low methane conversion and thus the presence of excess water favors the water-gas shift reaction. As a result, as methane conversion increases in other three configurations, both the excess water and H_2/CO ratio decrease, and CO selectivity increases as shown in Fig. 3.9.

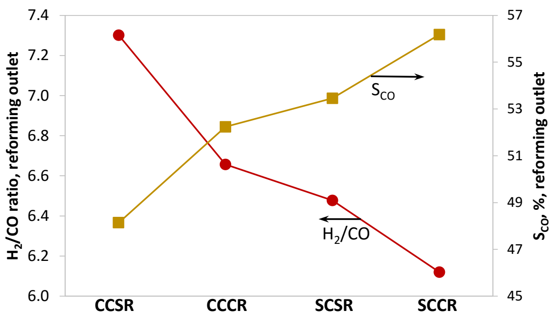

Fig. 3.9. *Average H_2/CO ratio and CO selectivity at the reforming-channel outlet for CCSR, CCCR, SCSR and SCCR configurations.*

3.5.5. Methane reaction rates

Fig. 3.10A and B illustrate an average methane reaction rate in combustion-catalyst and an average methane reaction rate in reforming-catalyst as a function of the plate-length respectively. The methane reaction rates in CMC and in MSR take zero values, where catalytically inert sections are present on the plate surface, for example from x=0 to x=1 cm and from x=6 cm to x=7 cm and between the catalytically active sections in the case of segmented reforming-catalyst (CCSR and SCSR) and segmented combustion-catalyst configurations (SCCR and SCSR) between x=1 cm and x=6 cm. The methane reaction rates follow the behaviour of heat-flux values illustrated in Figs. 3.4A, B and 3.5A, B. They take non-zero values at the active segments of catalysts where reactants react with each other and form the products. In the case of continuous catalyst configurations whether it is reforming or combustion catalyst, show peaks only at the leading edge of the catalyst, whereas in the case of segmented catalyst configurations, peaks appear at the both leading and ending edges of each catalytically active segment. The peaks are high at the leading edges and low at the ending edges in both segmented reforming-catalyst and segmented combustion-catalyst. As explained earlier this behaviour is endowed to the continuous supply of thermal energy from the combustion-side to the reforming-side through the interspacing among active catalytic segments, resulting to raise back methane reaction rates at the leading and ending edges of each segment. As methane is getting consume on the combustion-side at faster rate than on the reforming-side, the methane

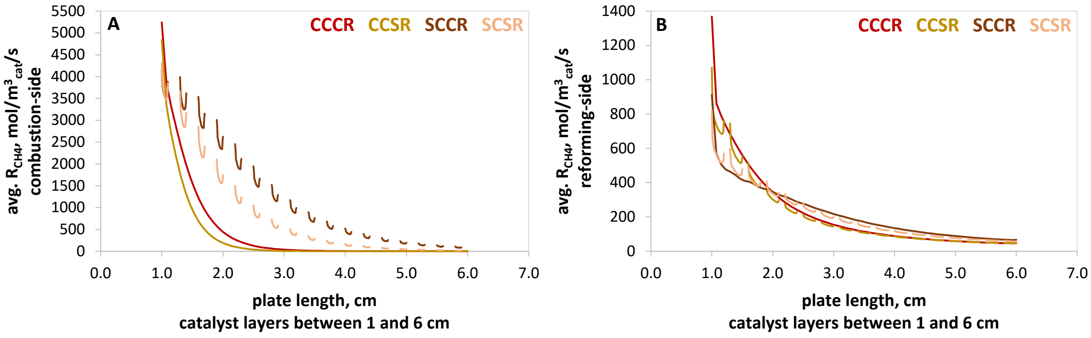

Fig. 3.10. *Average methane reaction rate in (A) combustion-catalyst and (B) in reforming-catalyst as a function of the plate-length for CCCR, CCSR, SCCR and SCSR configurations.*

reaction rate peaks in segmented catalyst configurations are disappearing slowly with respect to the positive x-direction. In all four cases, minimum values of methane reaction rate in CMC and in MSR are found at the end of last catalyst segment at x = 6 cm. From this study, it is concluded that the use of segmented catalysts has extended both reforming and combustion reaction processes, resulting to achieve similar methane conversion and hydrogen yield as with the continuous catalyst configurations but using very low combustion-catalyst loadings and with lower maximum operating temperature as well as with minimized axial-thermal gradients.

3.6. Conclusions

In this study, four separate computational models with four different combinations of segmented and continuous configurations (CCCR, CCSR, SCCR and SCSR) between the combustion-catalyst and reforming-catalyst are developed and are utilized to simulate the methane steam reforming (MSR) and catalytic methane combustion (CMC) in a catalytic plate reactor (CPR). The study has successfully integrated continuum scale transport, heat and mass transfer with the reduced microkinetic model of CMC and with the experimentally validated multi-step surface microkinetic model of MSR. The performance of the CPR designed with the four different configurations of reforming and combustion catalysts is investigated in terms of plate temperature, reaction heat and effective thermal conductivity distributions and in terms of methane and hydrogen mole fractions, and methane reaction rates distributions as well as in terms of H_2/CO ratio and CO selectivity.

The study has shown that similar methane conversion and hydrogen yield in MSR can be obtained for the same $GHSV_{ref}$ by saving 66% combustion-catalyst, when a CPR is configured with the segmented combustion-catalyst (SCCR, SCSR) instead of conventional catalyst design (CCCR). The improvement with the SCCR and SCSR configurations is due to the continuous supply of heat to the reforming-side from the combustion-side through the interspacing among active catalytic segments, contributing significantly to avoid cold zones and to maintain a balanced thermal distribution in the reforming-catalyst. Significant reduction and the complete disappearance of the thermal hot spots at the initial length of the catalysts are observed with the SCSR and SCCR configurations respectively, compared to the conventional CCCR design. The study has also shown that the maximum temperature predicted in the conventional CPR designed with the CCCR is reduced by 28.9 °C and 33 °C, when the SCCR and SCSR configurations are applied respectively, with no loss in methane conversion and hydrogen yield in MSR. A significant reduction in axial thermal gradients at the reactor downstream with the SCSR and SCCR configurations is due to the achievement of uniform heat distribution compared to the CCCR and CCSR. The study has found that both reforming-side and combustion-side effective thermal conductivities are improved noticeably for the first 44% and 36% of the catalyst length in a CPR designed with the SCSR and SCCR configurations respectively, compared to the CCCR configuration. The study has also determined that the influence of the segmented combustion-catalyst on the segmented reforming-catalyst is significant compared to its counterpart continuous combustion-catalyst.

3.7. References

[1] Chiuta S, Everson RC, Neomagus HW, Le Grange LA, Bessarabov DG. A modelling evaluation of an ammonia-fuelled microchannel reformer for hydrogen generation. international journal of hydrogen energy. 2014 Jul 24;39(22):11390-402.

[2] Cao C, Zhang N, Chen X, Cheng Y. A comparative study of Rh and Ni coated microchannel reactor for steam methane reforming using CFD with detailed chemistry. Chemical Engineering Science. 2015 Dec 1;137:276-86.

[3] Bromaghim G, Gibeault K, Serfass J, Serfass P, Wagner E. Hydrogen and fuel cells: the US market report. In National Hydrogen Association 2010 Mar (Vol. 22).

[4] Gür TM. Comprehensive review of methane conversion in solid oxide fuel cells: Prospects for efficient electricity generation from natural gas. Progress in Energy and Combustion Science. 2016 May 31;54:1-64.

[5] Kolb G. Fuel processing: for fuel cells. Wiley-VCH Verlag GmbH & Co. KGaA; 2008.

[6] Rostrup-Nielsen JR, Christiansen LJ, Hansen JH. Activity of steam reforming catalysts: role and assessment. Applied Catalysis. 1988 Jan 1;43(2):287-303.

[7] Hunter JB, McGuire G, inventors; Matthey Bishop, Inc., assignee. Method and apparatus for catalytic heat exchange. United States patent US 4,214,867. 1980 Jul 29.

[8] Kolb G, Hessel V. Micro-structured reactors for gas phase reactions. Chemical Engineering Journal. 2004 Mar 15;98(1):1-38.

[9] Zanfir M, Gavriilidis A. Modelling of a catalytic plate reactor for dehydrogenation–combustion coupling. Chemical Engineering Science. 2001 Apr 30;56(8):2671-83.

[10] Wang F, Zhou J, Wang G. Transport characteristic study of methane steam reforming coupling methane catalytic combustion for hydrogen production. international journal of hydrogen energy. 2012 Sep 30;37(17):13013-21.

[11] Bartholomew CH. Mechanisms of catalyst deactivation. Applied Catalysis A: General. 2001 Apr 30;212(1):17-60.

[12] Pattison RC, Estep FE, Baldea M. Pseudodistributed feed configurations for catalytic plate microchannel reactors. Industrial & Engineering Chemistry Research. 2013 Aug 9;53(13):5028-37.

[13] Jeon SW, Yoon WJ, Baek C, Kim Y. Minimization of hot spot in a microchannel reactor for steam reforming of methane with the stripe combustion catalyst layer. international journal of hydrogen energy. 2013 Oct 25;38(32):13982-90.

[14] Xu J, Froment GF. Methane steam reforming, methanation and water-gas shift: I. Intrinsic kinetics. AIChE Journal. 1989 Jan 1;35(1):88-96.

[15] Settar A, Nebbali R, Madani B, Abboudi S. Numerical investigation on the wall-coated steam methane reformer improvement: Effects of catalyst layer patterns and metal foam insertion. International Journal of Hydrogen Energy. 2015 Aug 3;40(29):8966-79.

[16] Settar A, Nebbali R, Madani B, Abboudi S. Numerical study on the effects of the macropatterned active surfaces on the wall-coated steam methane reformer performances. International Journal of Hydrogen Energy. 2017 Jan 12;42(2):1490-8.

[17] Mundhwa M, Thurgood CP, Dhingra H, Parmar RD, Peppley BA. A comparative computational study of diesel steam reforming in a catalytic plate heat-exchange reactor. AIChE Journal. 2017 Mar 1;63(3):1102-13.

[18] Zanfir M, Gavriilidis A. An investigation of catalytic plate reactors by means of parametric sensitivity analysis. Chemical engineering science. 2002 May 31;57(9):1653-9.

[19] Zanfir M, Gavriilidis A. Influence of flow arrangement in catalytic plate reactors for methane steam reforming. Chemical Engineering Research and Design. 2004 Feb 29;82(2):252-8.

[20] Arzamendi G, Diéguez PM, Montes M, Odriozola JA, Sousa-Aguiar EF, Gandía LM. Methane steam reforming in a microchannel reactor for GTL intensification: A computational fluid dynamics simulation study. Chemical Engineering Journal. 2009 Nov 15;154(1):168-73.

[21] J.R. Rostrup-Nielsen, Catalytic steam reforming, in: J.R. Anderson, M. Boudart (Eds.), Catalysis-Science and Technology, vol.5, Springer-Verlag, Berlin, 1984, p.51.

[22] Arzamendi G, Uriz I, Navajas A, Diéguez PM, Gandía LM, Montes M, Centeno MA, Odriozola JA. A CFD study on the effect of the characteristic dimension of catalytic wall microreactors. AIChE Journal. 2012 Sep 1;58(9):2785-97.

[23] Stefanidis GD, Vlachos DG. Millisecond methane steam reforming via process and catalyst intensification. Chemical engineering & technology. 2008 Aug 1;31(8):1201-9.

[24] Stefanidis GD, Vlachos DG, Kaisare NS, Maestri M. Methane steam reforming at microscales: Operation strategies for variable power output at millisecond contact times. AIChE journal. 2009 Jan 1;55(1):180-91.

[25] Zhai X, Ding S, Cheng Y, Jin Y, Cheng Y. CFD simulation with detailed chemistry of steam reforming of methane for hydrogen production in an integrated micro-reactor. international journal of hydrogen energy. 2010 Jun 30;35(11):5383-92.

[26] Maier L, Schädel B, Delgado KH, Tischer S, Deutschmann O. Steam reforming of methane over nickel: development of a multi-step surface reaction mechanism. Topics in Catalysis. 2011 Sep 1;54(13-15):845-58.

[27] Karakaya M, Keskin S, Avci AK. Parametric study of methane steam reforming to syngas in a catalytic microchannel reactor. Applied Catalysis A: General. 2012 Jan 16;411:114-22.

[28] Deshmukh SR, Vlachos DG. A reduced mechanism for methane and one-step rate expressions for fuel-lean catalytic combustion of small alkanes on noble metals. Combustion and Flame. 2007 Jun 30;149(4):366-83.

[29] L. Kunz, L. Maier, S. Tischer, O. Deutschmann, Modeling the Rate of Heterogeneous Reactions, in: Modeling and Simulation of Heterogeneous Catalytic Reactions, Wiley-VCH Verlag GmbH & Co. KGaA, 2012:113-148.

[30] Dixit M, Baruah R, Parikh D, Sharma S, Bhargav A. Autothermal reforming of methane on rhodium catalysts: Microkinetic analysis for model reduction. Computers & Chemical Engineering. 2016 Jun 9;89:149-57.

[31] Mhadeshwar AB, Vlachos DG. Hierarchical multiscale mechanism development for methane partial oxidation and reforming and for thermal decomposition of oxygenates on Rh. The Journal of Physical Chemistry B. 2005 Sep 8;109(35):16819-35.

[32] Deshmukh SR, Mhadeshwar AB, Vlachos DG. Microreactor modeling for hydrogen production from ammonia decomposition on ruthenium. Industrial & Engineering Chemistry Research. 2004 Jun 9;43(12):2986-99.

[33] Karadeniz H. Numerical Modeling of Stagnation Flows Over Porous Catalytic Surfaces. KIT Scientific Publishing; 2016 Apr 8.

[34] Deutschmann O, Schmidt LD. Modeling the partial oxidation of methane in a short-contact-time reactor. AIChE Journal. 1998 Nov 1;44(11):2465-77.

[35] Krishna R, Wesselingh JA. The Maxwell-Stefan approach to mass transfer. Chemical Engineering Science. 1997 Mar 31;52(6):861-911.

[36] Bessler WG, Gewies S, Vogler M. A new framework for physically based modeling of solid oxide fuel cells. Electrochimica Acta. 2007 Dec 31;53(4):1782-800.

[37] Venkataraman K, Wanat EC, Schmidt LD. Steam reforming of methane and water-gas shift in catalytic wall reactors. AIChE Journal. 2003 May 1;49(5):1277-84.

[38] Whittenberger WA, inventor; Catacel Corp., assignee. Heat exchanger. United States patent US D560,276. 2008 Jan 22.

[39] Matweb, Resistalloy International Fecralloy^{TM} 135 Electrical Resistance Steel, Available at http://www.resistalloytrading.co.uk/pages/fecralloyproperties (Accessed December 2015).

[40] Todd B, Young JB. Thermodynamic and transport properties of gases for use in solid oxide fuel cell modelling. Journal of power Sources. 2002 Jul 20;110(1):186-200.

[41] Poling BE, Prausnitz JM, John Paul OC, Reid RC. The properties of gases and liquids. New York: McGraw-Hill; 2001.

[42] MUNRO M. Evaluated Material Properties for a Sintered alpha-Alumina. Journal of the American Ceramic Society. 1997 Aug 1;80(8):1919-28.

[43] Bird RB, Stewart WE, Lightfoot EN. Transport Phenomena. New York, USA: John Wiley & Sons, revised second ed. 2007.

[44] Welty JR, Wicks CE, Rorrer G, Wilson RE. Fundamentals of momentum, heat, and mass transfer. John Wiley & Sons; 2009 Oct 1.

[45] Tjaden B, Cooper SJ, Brett DJ, Kramer D, Shearing PR. On the origin and application of the Bruggeman correlation for analysing transport phenomena in electrochemical systems. Current Opinion in Chemical Engineering. 2016 May 31;12:44-51.

[46] Skorokhod VV, Get'man OI, Zuev AE, Rakitin SP. Correlation between the particle size, pore size, and porous structure of sintered tungsten. Soviet powder metallurgy and metal ceramics. 1988 Dec 1;27(12):941-7.

[47] Ronane MJ. An investigation of gauze supported platinum alumina and cobalt supported oxide oxidation catalysts (Master dissertation, Dublin City University).

Chapter 4

A comparative parametric study of a catalytic plate methane reformer coated with segmented and continuous layers of combustion catalyst for hydrogen production

Published in the Journal of Power Sources, 344 (2017) 85-102

Abstract

A parametric comparison study is carried out between segmented and conventional continuous layer configurations of the coated combustion-catalyst to investigate their influence on the performance of methane steam reforming (MSR) for hydrogen production in a catalytic plate reactor (CPR). MSR is simulated on one side of a thin plate over a continuous layer of nickel-alumina catalyst by implementing an experimentally validated surface microkinetic model. Required thermal energy for the MSR reaction is supplied by simulating catalytic methane combustion (CMC) on the opposite side of the plate over segmented and continuous layer of a platinum-alumina catalyst by implementing power law rate model. The simulation results of both coating configurations of the combustion-catalyst are compared using the following parameters: (1) co-flow and counter-flow modes between CMC and MSR, (2) gas hourly space velocity and (3) reforming-catalyst thickness. The study explains why CPR designed with the segmented combustion-catalyst and co-flow mode shows superior performance not only in terms of high hydrogen production but also in terms of minimizing the maximum reactor plate temperature and thermal hot-spots. The study shows that the segmented coating requires 7% to 8% less combustion-side feed flow and 70% less combustion-catalyst to produce the required flow of hydrogen (29.80 mol/h) on the reforming-side to feed a 1 kW fuel-cell compared to the conventional continuous coating of the combustion-catalyst.

4.1. Introduction

The production of electricity using small scale internal combustion engine (1–10 kW) has low efficiency of about 15% to 25% [1]. Reducing the environmental impact by minimizing the emission of greenhouse gases from such low efficiency systems is of concern in many parts of the world, where electricity generators running on natural-gas/diesel/kerosene are used as power backup for small businesses and residences, especially in all developing countries [2]. Apart from greenhouse gases, conventional generators also emit NO_x and particulates that have significant impact on health [3]. By comparison, fuel-cell based electricity generators produce no particulates and no NO_x due to the absence of high-temperature gas-phase combustion. Unlike electric batteries, a fuel-cell does not run down or require recharging; it produces continuous electricity if hydrogen and an oxidizer are supplied continuously to the cell. At present, there is no hydrogen infrastructure to employ wide spread use of fuel-cell generators. An alternative solution is to develop an efficient and compact fuel reformer to produce hydrogen, which can take advantage of the natural-gas (95% methane) supply infrastructure in many countries. Compact reformers can be integrated easily with fuel cell generators which are deployed for stationary and portable use.

A fuel reformer can be built in a variety of configurations depending on the desired system efficiency, dynamic response and ease of manufacture. Three possible reformer designs to produce hydrogen from methane are: (1) Steam Reforming (SR), (2) Autothermal Reforming (ATR) and (3) Partial Oxidation (POX). SR is a highly endothermic reaction, whereas POX is exothermic. ATR is a combination of SR and POX and can offer the advantage of thermoneutral operation. SR provides the maximum hydrogen concentration as compared to ATR and POX [4], however, due to its highly endothermic nature, SR requires an effective way of supplying heat to the reaction sites. One efficient solution is to supply the heat indirectly by means of a catalytic combustion of methane.

Indirect supply of heat from catalytic combustion of methane can be achieved effectively in a catalytic plate reactor (CPR). A CPR design consists of number of thin metal plates, each having both sides coated with appropriate catalysts for the endothermic and exothermic reactions and are arranged in a stacked configuration [5]. The close association of the exothermic and endothermic reaction zones reduces significantly the overall heat transfer resistance [6]. The use of catalytic combustion to supply heat offers advantages over gas-phase combustion. Catalytic combustion takes place at a lower temperature than gas-phase combustion which reduces NO_x formation, and the lower operating temperature allows more material choices in designing the plate reactors [7]. However, the use of catalytic combustion in a CPR creates localized thermal-gradients or hot-spots especially near the inlets due to the imbalance between the rate of heat generation in combustion and the rate of heat absorption in reforming [8]. Such localized thermal imbalance causes problems of material failure and catalyst delamination due to different thermal expansion coefficients of the coated catalyst and the metal plate. Large thermal-gradients also reduce catalytic active surface area as well as catalyst support area, and thus reactants conversion rates [9]. To overcome these issues, recently Pattison et al. [10] and Jeon et al. [11] have proposed a segmented layer of combustion-catalyst (SLCC) configuration for catalytic methane combustion (CMC) coupled with methane steam reforming (MSR) in a microchannel CPR. Pattison et al. [10] have explored numerically, a method for emulating distributed feed configuration in the microchannel CPR via SLCC macromorphology, consisting of alternating active and catalytically inactive sections. They have employed LHHW (Langmuir-Hinshelwood-Hougen-Watson) type Xu and Froment's [12] kinetic model for MSR and power law rate models for gas-phase and catalytic methane combustion. Similarly, Jeon et al. [11] have proposed a stripe configuration of combustion-catalyst to minimize the formation of hot-spots in a microchannel CPR. They have considered nearly half the combustion-side plate section coated with SLCC and the remaining half coated with a continuous layer of combustion-catalyst (CLCC) configuration. They have also employed Xu and Froment's [12] kinetic model for MSR and power law rate model for CMC. Both studies have shown disappearance of hot-spots without any loss of methane conversion (X_{CH4}) in reforming. More recently, in one of our studies [13], we have proposed a segmented combustion-catalyst and segmented reforming catalyst configurations over the entire length of the plate by employing one-step reduced microkinetic model for CMC and multistep microkinetic model for MSR. The study has illustrated that apart from reducing hot-spots, segmented catalyst configuration has improved effective thermal conductivity of both reforming and combustion catalysts and decreased the back diffusion of hydrogen in the reforming-channel for the SLCC configuration compared to the CLCC configuration.

Many numerical studies of CMC coupled with MSR in a CPR have been carried out for various applications. However, except Pattison et al. [10], Jeon et al. [11] and Mundhwa and Thurgood [13], none of the literature reviewed in this study have investigated MSR coupled with CMC over SLCC. None of the studies in our knowledge have investigated the influence of reactor parameters on MSR coupled with CMC over SLCC in a CPR and its comparative study with the CPR coated with CLCC.

Zanfir and Gavriilidis [14] have performed a parametric investigation of reforming-catalyst thickness and flow-channel height of a CPR for operating conditions like conventional industrial methane reformer. They have developed a simplified 2D model of a CPR by implementing Xu and Froment's [12] kinetic model for MSR and power law rate model for CMC. Zanfir and Gavriilidis [14] have observed that by increasing reforming-channel height at constant inlet velocity, X_{CH4} decreases. They have concluded that MSR coupled with CMC is feasible in a CPR if flow-rates, catalyst thickness and channel heights are properly designed. Zanfir and Gavriilidis [15] have also conducted numerical study of co-flow and counter-flow modes between MSR and CMC. They have determined higher X_{CH4} on the reforming-side with counter-flow than co-flow design. They have also observed thermal hot-spots in counter-flow mode and have suggested to optimize combustion-catalyst distribution to reduce thermal hot-spots. In a separate study, Zanfir and Gavriilidis [16] have carried out a sensitivity analysis of several design and operating parameters including reaction kinetic parameters. They have demonstrated that different catalysts can show similar thermal behavior and performance but exhibit different sensitivity behavior. The major finding of their study is that the strongest influence on reactor sensitivity comes from the reaction activation energies. Stefanidis and Vlachos [17] have studied MSR on a rhodium catalyst coupled with propane combustion over a platinum catalyst in a CPR and have reported that increasing catalyst loading and decreasing possible internal mass transfer limitations results in considerable process time reduction. Also, by lowering steam to carbon (SC) ratio yielded higher power output at relatively low reactor temperatures. In a different study, Stefanidis et al. [18] have reported that the use of low thermal conductivity plate materials increases fuel conversion and power output in the incomplete conversion regime. However, the use of very low thermal conductivity materials has shown high thermal-gradients in the CPR and thus recommended to use intermediate thermal conductivity materials, such as stainless steel as a trade-off between thermal-gradients and conversion. Zhai et al. [19] have developed 2D computational fluid dynamic (CFD) model of a CPR using surface microkinetics for MSR on rhodium and LHHW type kinetic model for CMC on platinum. They have investigated the influence of wall thermal conductivity, ratio of combustion to reforming feed, channel size and space time. They have reported that the performance of the metallic wall is superior against ceramic wall and recommended to use the wall material with intermediate thermal conductivity to avoid hot-spot formation. Arzamendi et al. [20] have developed a 3D CFD-model of a microchannel reactor integrating MSR and CMC. They have implemented the simplified rate expressions [21] for MSR on Ni catalyst and have simulated the effect of various parameters: catalyst loading, flow direction between the two channels, and gas hourly space velocity (GHSV). Their results have shown the possibility of 96% of methane conversion with 2–4 mg/cm^2 of catalyst at 930–1000 ºC in the range of 10,000–30,000 h^{-1} GHSV. In a separate work, Arzamendi et al. [22] have developed 3D CFD-models of a plate reactor with square microchannel and microslits design to investigate the effects of characteristic dimension with different aspect ratios. Their results have shown that methane conversion decreases with increase in characteristic dimension; however, the microchannel design has provided methane conversion slightly higher than that of the microslits design. Cao et al. [23] have carried out CFD study of MSR in an integrated microchannel reactor by applying elementary reaction kinetics and compared the performance of Rh and Ni catalysts under inner-heating and outer heating modes. They have demonstrated that well prepared Ni catalyst with high loading can exhibit excellent performance comparable to the rhodium catalyst.

In this study, two separate two-dimensional steady state computational models of a CPR are developed for a parametric comparison study with different combustion-catalyst coating configurations. One model simulates MSR on one side of a thin fecralloy plate over a continuous layer of nickel/alumina (Ni/Al_2O_3) catalyst and CMC on the opposite side of the plate over segmented layers of platinum/alumina (Pt/Al_2O_3) catalyst. From now on, this model is called as SLCC-model (Segmented Layer of Combustion- Catalyst). Whereas, the second model simulates MSR and CMC over continuous layer of Ni/Al_2O_3 catalyst and Pt/Al_2O_3 catalyst respectively. From now on, this model is called as CLCC-model (Continuous Layer of Combustion-Catalyst). Inlet methane flowrate of 9.94 mol/h for MSR in both models is calculated based on the requirement of hydrogen feed rate of 29.80 mol/h in a 1 kW fuel-cell consisting of 158 individual cells with 0.7 cell voltage and 90% hydrogen utilization on the anode-side and based on a 3:1 stoichiometric ratio of hydrogen and methane in MSR reaction. The inlet flow selection based on the required hydrogen feed rate in a 1 kW fuel-cell may facilitate future engineering and scaling calculations to integrate the CPR with the fuel-cell. To simulate MSR, a surface microkinetic model developed by Maier et al. [24] for Ni/ Al_2O_3 catalyst is employed after validating it against experimental data obtained from the literature [25]. To simulate CMC, a power law model for CMC over Pt/Al_2O_3 catalyst is employed [14]. Unlike few previous studies in the literature, computational models developed in this study consider the practical inlet conditions that does not result in gas-phase methane combustion reactions at the reactor entrance by keeping the combustion-side inlet feed temperature (800 K) below the auto-ignition temperature (850 K) of methane. Catalytically inactive plate sections are considered before and after the nickel and platinum catalyst layers to capture the influence of the reactor inlets and outlets on the temperature and concentration profiles. Another aspect of considering inactive plate sections at the inlets, is to allow fluid flow to develop fully laminar flow [26]. Compressible Navier-Stokes equations are applied to model the flow in both reforming and combustion flow-channels, whereas the Darcy-Brinkman model is employed to model the flow inside porous catalysts due to the pressure gradients. The convection-diffusion equations are employed to solve species concentration gradients in both flow-channels. Most of the published literature solved the diffusive fluxes by applying simplified binary diffusion approach. These simplified approaches are strictly valid for diffusion of dilute species in a multicomponent mixture and for binary mixtures [27]. In this study, the diffusive fluxes are evaluated by employing the multi-component Maxwell-Stefan diffusion model. To account for molecules colliding with the catalyst walls, Knudsen diffusion is considered by calculating effective diffusivity for each chemical species. Effective diffusivities are calculated by applying an average Bosanquet formulation [28]. To avoid the violation of species conservation, excess component's (H_2O for MSR and N_2 for CMC) mass-fraction profiles are solved using mass constraint approach, which states that the sum of all mass fractions must be equal to 1. Mean particle size of 1 mm and porosity value of 0.4 are assumed for both reforming and combustion catalysts with the bulk density of 2366.7 kg/m^3 [25]. The values of tortuosity are calculated using Bruggeman correlation [29]. Mean pore size is determined using Kozeny's equation which relates the pore size with porosity and mean particle size [30]. Permeability (κ) values are estimated using the Kozeny-Carman equation [28] (Eq. 3.13). Temperature profiles in both flow-channels are obtained by solving the convection-conduction equation, whereas temperature distributions in the porous catalysts are obtained by solving the convection-conduction equation for porous media. The porous media heat-transfer equation assumes thermal equilibrium between porous matrix and fluid. Temperature distribution in solid plate between the two channels are obtained by employing the steady state conduction heat transfer equation.

4.2. Computational framework

Fig. 4.1(A) illustrates a 3D schematic of a simplified stacked plate reactor. Study assumes that reactor consists of 40 plates (excluding top and bottom plates), each coated with Ni/Al_2O_3 catalyst on the reforming-side along with segmented layers of Pt/Al_2O_3 catalyst on the combustion-side in SLCC-model and continuous layer (not shown) in CLCC-model. The stacked arrangement of 40 plates configures 19 reforming-channels and 20 combustion-channels with 2 mm size for fluid flow between the two parallel plates. The top and bottom plates are not coated with the catalysts; thus, as shown in Fig. 4.1(A), channel height for reforming flow in the top and the bottom-most channels is assumed to be 1 mm, which by combining makes the 20th reforming-channel with combined 2 mm channel-height for the reforming flow. So, the stacked plate reactor built with N number of plates coated both sides with the appropriate catalysts configures N/2 number of reforming and N/2 number of combustion flow-channels.

Fig. 4.1(B) and (C) illustrate schematic of two-dimensional views of fecralloy plate coated with appropriate catalysts for MSR and CMC for the CLCC and SLCC configurations respectively. The stacked configuration with alternate channels for reforming and combustion allows to implement symmetry boundary conditions at the centre planes in both flow-channels with 1 mm half channel height. To simulate the CPR, five different domains are identified in Fig. 4.1(B) and (C): (1) combustion-channel, (2) combustion-catalyst, (3) fecralloy plate, (4) reforming-catalyst, and (5) reforming-channel. For the SLCC-model, continuous layer of the coated

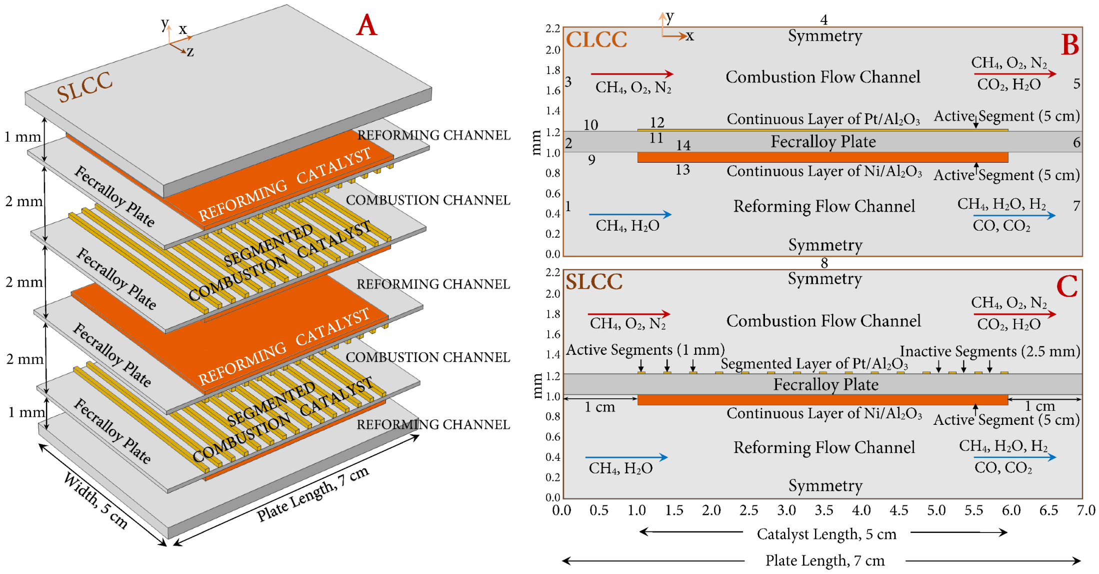

Fig. 4.1. *(A) 3D schematic of a simplified stacked plate reactor designed with the segmented layers of combustion-catalyst (SLCC) and continuous layers of reforming-catalyst, (B) 2D schematic of simulated domains of a CPR designed with CLCC and (C) with SLCC.*

combustion- catalyst domain in Fig. 4.1(B) is replaced with the segmented layers of the combustion-catalyst as shown in Fig. 4.1(C). Numbers in Fig. 4.1(B) represents the domain boundaries. Numbers 1, 3 and 7, 5 represent inlet and outlet boundaries for the reforming and combustion channels, 4 and 8 illustrate symmetry boundaries, 13 represents the interface between reforming-catalyst and reforming-channel and 12 represents the interface between combustion-catalyst and combustion-channel, 9 and 10 shows the interface between the plate and the flow-channels, 2 and 6 represents insulated boundaries between the plate and the surroundings, and numbers 11 and 14 illustrate the interface between the catalysts and the plate. Similar boundaries are identified for the same interfaces depicted in Fig. 4.1(C) for the segmented configuration.

Table 4.1 lists the geometric parameters of the simulated 2D domains shown in Fig. 4.1(B) and (C). To accommodate hydrogen back diffusion and to account for the influence of inlets and outlets, catalytically inactive sections (1 cm each) are considered by considering active catalyst layers from x = 1 cm to x = 6 cm on a 7 cm long plate. The reforming-catalyst layer is coated continuously with the size of 5 cm × 5 cm × 100 mm. Each segmented layer of combustion-catalyst in SLCC-model is coated with the size of 1 mm × 5 cm × 20 mm. In total 15 such layers of the catalyst are considered with 2.5 mm distance between each of them. For the parametric comparison study between SLCC and CLCC, the size of continuous layer of the combustion-catalyst is 5 cm × 5 cm × 20 mm in CLCC-model. When the continuous layer of combustion-catalyst is employed, simulation results showed that within the first 30% (i.e. 15 mm) of combustion-catalyst length, almost 100% methane gets combusted to CO_2 and H_2O. Based on this finding, in total fifteen segmented sections, each with 1 mm × 5 cm × 20 mm size are coated along the 5 cm length with 2.5 mm gap between each of them, which is in total equivalent to 30% of continuous combustion-catalyst in CLCC. In other words, 70% of combustion-catalyst is removed from the CLCC-model to form the fifteen segmented layers of combustion-catalyst for the SLCC model.

Table 4.1. *Geometric parameters of the CPR and thermal/physical properties of fecralloy plate*

	Reforming-side	**Combustion-side**
Channel half height (y-direction)	1.0 mm	1.0 mm
Channel width (z-direction)	50.0 mm	50.0 mm
Channel Length (x-direction)	70.0 mm	70.0 mm
Number of channels	20	20
Number of catalyst segments on each plate	1	15 for SLCC 1 for CLCC
Length of each catalyst segment	50.0 mm	1mm for SLCC model 50 mm for CLCC model
Distance between catalyst segments	n/a	2.5mm
Catalyst thickness	100 µm	20 µm
FeCrAlloy plate dimension	Thickness = 0.2 mm, Length = 70.0 mm Width = 50.0 mm	
FeCrAlloy plate thermal/physical properties	Fe = 73.2 %, Cr = 22 %, Al = 4.8 % Thermal conductivity = 16.0 W/m/K Density = 7250 kg/m^3	

Catacel™, an industrial heat exchanger manufacturer uses fecralloy foils/plates to design their CPRs. Their CPR patent [31] states that the use of metal plate/foil for a heat exchanger with a thickness of 0.001–0.1 inches reduces expense using less material overall. The plate thickness of 0.2mmin this study lies within this range. The plate properties for the Fecralloy™ variant (Fe 73.2/Cr 22/Al 4.8) listed in Table 4.1 are obtained from the material property database [32].

Individual thermal conductivities, heat capacities and viscosities are calculated as a function of the temperature. Pure component temperature dependent parameters for heat capacities, viscosities, and thermal conductivities are obtained from Todd and Young [33]. The gas mixture heat capacity is evaluated using the weighted average heat capacity of the chemical species. The gas mixture viscosity is calculated using the method developed by Wilke [34]. The thermal conductivity of low pressure gas mixture is calculated using the Mason and Saxena method [34]. The effective thermal conductivities (k_{eff}) of the catalyst layers are calculated using a volume weighted average as:

$$k_{eff} = \varepsilon k_{mix} + (1-\varepsilon) k_{cat} \tag{4.1}$$

where, k_{mix} is the gas mixture thermal conductivity obtained, k_{cat} is the solid phase catalyst thermal conductivity. The solid catalyst thermal conductivity (k_{cat}) is approximated based on alumina and is calculated by Eq. (4.2), where temperature T is in degree Celsius [35].

$$k_{cat} = 5.85 + 15360 \frac{exp(-0.002T)}{516+T} \tag{4.2}$$

Both the multi-component Maxwell-Stefan diffusion [36] and the Knudsen diffusion models [37] are employed with the convection-diffusion equations to evaluate species diffusion fluxes inside the porous structure of the catalysts, whereas only the multicomponent Maxwell-Stefan diffusion model with the convection-diffusion equations is considered for the flow-channels. To avoid the violation of species mass conservation in the convection-diffusion equations, species mass transport equations can be solved by employing species density [38]. However, it is possible to solve the species mass transport equation using species mass-fraction without violating the mass conservation by implementing the mass constraint approach defined in Eq. (4.3) (i.e. the sum of all mass fractions must be equal to 1). In this study, the mass transport equations for H_2O in MSR and for N_2 in CMC are evaluated using the mass constraint approach, whereas all other species mass transport equations are resolved independently.

$$\omega_j = 1 - \left(\sum_{\substack{i=1 \\ i \neq j}}^{N_g - 1} \omega_i \right) \tag{4.3}$$

The Fuller equation [34] is employed to calculate the binary diffusion coefficients (D_{ij}) for each chemical species involved. To incorporate Knudsen (D_j^K) and binary (D_{ij}) diffusion coefficients with the species mass-transport equations for porous catalyst layers, an averaged Bosanquet equation [28] is employed to calculate the effective diffusion coefficient (D_{ij}^{eff}).

$$D_{ij,eff} = D_{ji,eff} = \frac{\varepsilon}{\tau}\frac{1}{2}\left(\frac{1}{1/D_i^K + 1/D_{ij}} + \frac{1}{1/D_j^K + 1/D_{ji}} \right) \tag{4.4}$$

To solve the coupled set of partial differential equations, commercially available simulation software package COMSOL™4.0 is used. COMSOL™ simulates the coupled set of heat, mass and reactive flow equations using the finite-element method (FEM). The CPR models are based on a distributed mapped mesh. More mesh elements are employed at the catalyst inlets where larger variations in reaction rates and thermal-gradients occur. All solutions are resolved using a finer mesh, and a mesh-independent solution is obtained for all runs with convergence criteria of 1 × 10^{-05} absolute error. In the model solutions, it is ensured that the conservation of mass in both reforming and combustion channels are satisfied. Governing equations and boundary conditions are listed in Appendix A. A few assumptions are made to formulate the computational models: (1) Compressible ideal gas flow (high temperature and low pressure conditions), (2) fully developed laminar flow in both half-channels, (3) a single plate for 2D model development (consisting of multiple stacked plates), due to the symmetry conditions at the centre-plane of flow channels, (4) catalyst layers are isotropic and all reactions take place in the catalyst layers, (5) catalyst particles are spherical in shape, (6) body and external forces including gravitational force are neglected, (7) radiation heat-transfer is neglected.

4.3. Reaction kinetics

Chemical reactions are investigated as elementary or as global reactions. Kinetic parameters for global reactions are determined based on experiments carried out at specific operating conditions and hence their applicability is also valid within those measured conditions with prior knowledge of rate determining reaction step [39]. In reality, each reaction proceeds via number of elementary steps. As illustrated in Fig. 4.2, MSR reaction is composed of elementary steps: (1) adsorption of CH_4 and H_2O at the catalyst surface from gas-phase, (2) surface reactions of the adsorbed species; resulting surface species may participate further into intermediate surface reactions and (3) desorption of final products (H_2 and CO). Therefore, every reaction, simple or complex, can be studied by elementary steps. To investigate the reformer performance, a fundamental knowledge of the underlying surface catalytic phenomenon in MSR is required over a wide range of operating condition, which is provided by a detailed microkinetic model of MSR over Ni/Al_2O_3 catalyst developed by Maier et al. [24]. The microkinetic model of Maier et al. consists of six gas-phase species (N_g) thirteen surface-species (N_s) including vacant sites (nickel) and 42 elementary reactions listed in Table 3.2. Microkinetic modeling employs mean-field approximation approach, which neglects the effect of lateral interactions of the adsorbates and non-uniformity of the catalyst surface [40]. In the mean field approximation, all adsorbates and adsorbent are defined as surface species. The coverage of surface species is then defined as:

$$\theta_{\mathrm{i}} = \frac{\text{site occupancy number} \times \text{cocentration of adsorbed species } i}{\text{site density}} \tag{4.5}$$

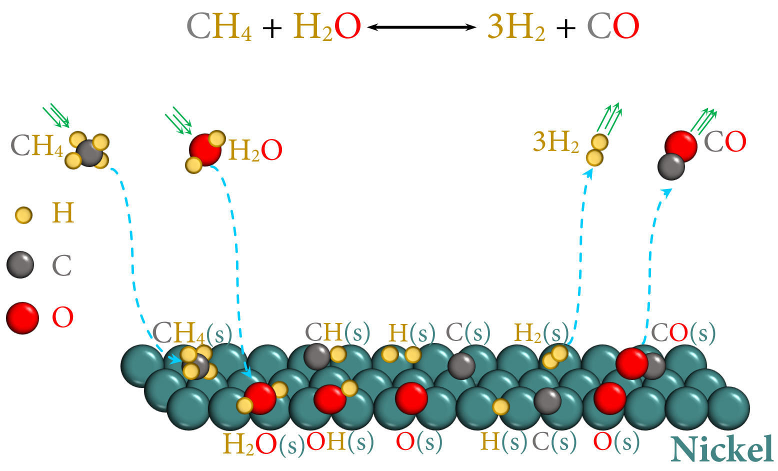

Fig. 4.2. *Illustration of the elementary multi-step MSR reaction over nickel catalyst.*

In this approximation, it is assumed that adsorbates are randomly distributed over the catalyst surface and the coverage of surface species depends on macroscopic position in the reactor and time, but they are averaged over microscopic local fluctuations. Therefore, the surface is assumed to be uniform [40]. Under the mean-field approximation, rate expressions for the gas-phase species and the surface species are defined as:

$$s_i = \sum_{r=1}^{R} \mathrm{v}_{ir} k_r \prod_{j=1}^{N_g+N_s} c_j^{\mathrm{v}'_{jr}} \tag{4.6}$$

where, s_i is the overall rate expression for gas-phase or surface species *i*, *r* is the considered reaction and R is the total number of reactions, c_j is the concentration of *j* species, which is given in mol/m^2 for the adsorbed species and mol/m^3 for gaseous species [41]. The concentration c_j of an adsorbed species equals the surface coverage (θ_{j}) multiplied by the surface site density (Γ). k_r is the reaction rate coefficient, v_{ir} is the difference of the right side (v''_{ir}) and left side (v'_{ir}) stoichiometric coefficients of species *i* in reaction *r* [41]. N_{g} and N_{s} represent the total number of gas-phase and surface species respectively. Because of the binding states associated with the adsorption of all species vary with the surface coverages, the reaction rate coefficients are determined using the modified Arrhenius expression [40]:

$$k_r = A_r T^{\beta_r} exp\left(-\frac{E_{a_r}}{\mathrm{R}_g T}\right) \theta_i^{\mu_{ir}} exp\left[\frac{\varepsilon_{ir}\theta_i}{\mathrm{R}_g T}\right] \tag{4.7}$$

where, E_{a_r} is the activation energy of the reaction *r* and θ_{i} is the fraction of the surface coverage of species *i*. μ_{ir} and ε_{ir} describe the dependence of the rate constants on the surface coverage of species *i*. For adsorption reactions, sticking coefficients are commonly used, which can be converted into conventional rate constants [24]:

$$k_r^{ads} = \frac{S_i^0}{\Gamma^\tau} \sqrt{\frac{\mathrm{R}_g T}{2\pi M_i}} \tag{4.8}$$

where, τ is the number of occupied adsorption sites of species *i*, S_i^0 is the initial (uncovered surface) sticking coefficient, Γ is the site density of nickel. The value of Γ is 2.6×10^{-5} mol/m^2, which was calculated by assuming a site area of 6.4×10^{-2} nm^2 observed for nickel [24]. Surface coverage of the *i*th species is calculated from its concentration, site occupancy number and surface site density according to Eq. (4.5). Thus, at steady state the time variation of the surface coverage of the *i*th species is zero [40]:

$$\frac{\partial\theta_i}{\partial t} = \frac{s_i\sigma_i}{\Gamma} = 0, \qquad \text{where} \sum_{i=1}^{N_s} \theta_i = 1 \tag{4.9}$$

Due to computationally intensive microkinetic approach adopted for MSR, rate-expressions for combustion-side chemical species are considered based on the global CMC model; so that available computational power can handle all computational runs carried out in this study. Thus, CMC rate, as observed with supported noble metal catalysts such as Pt, is assumed to be the first-order with respect to methane and zero-order with respect to oxygen. The activation energy and pre-exponential factor for CMC are obtained from the literature as: 90 kJ/mol and 4.0×10^8 s^{-1} [14].

4.4. Model validation

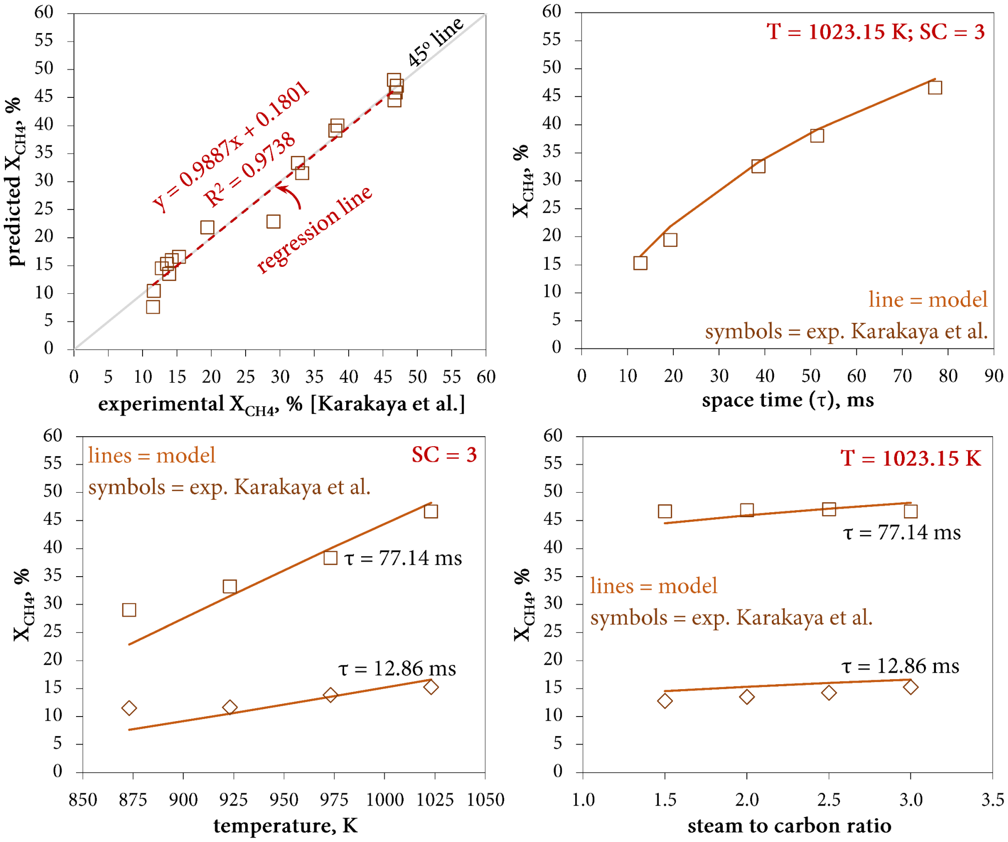

Fig. 4.3. *Validation of the multi-step microkinetic model of Maier et al. [24] against the experimental data of Karakaya et al. [25] for MSR over nickel-alumina catalyst in a microchannel CPR.*

The microkinetic model developed by Maier et al. [24] over 3 wt% Ni/Al_2O_3 catalyst was validated against the experimental data of Karakaya et al. [25] of MSR in a CPR. Karakaya et al. carried out experimental study of MSR over wall coated Ni/Al_2O_3 catalyst (Ni = 8.28 wt%). Required The explanation about model validation is already provided in section 3.4 of chapter 3. Table 3.4 presented the parameters used in 2D model of experimental microchannel CPR of Karakaya et al. Fig. 4.3 has shown an excellent agreement between the predicted and the experimental methane conversion in MSR for varying inlet space-times, temperatures, and steam to carbon ratios with the R-squared value of 0.9738.

4.5. Results and discussion

The computational models developed in this study are utilized to investigate the influence of SLCC and CLCC on MSR to produce hydrogen. Both models are compared with each other using the following parameters: (1) co-flow and counter-flow modes between reforming and combustion sides, (2) gas hourly space velocity (GHSV) in combustion and reforming channels, and (3) reforming-side catalyst thickness. The inlet molar flow of methane is determined based on the requirement of hydrogen to feed a 1kW fuel-cell, which requires hydrogen flow-rate of 29.80 mol/h. Therefore, reforming-side inlet molar flow-rate of methane is kept constant while varying other parameters.

Performance of the CPR can be measured by reactant conversion, product yield, product selectivity and thermal efficiency. Important performance parameters for MSR are X_{CH4}, Y_{H2}, and carbon-monoxide selectivity (S_{CO}). X_{CH4} in both reforming and combustion sides is defined as the ratio between converted methane at a position along the channel and the inlet molar rate of methane:

$$\mathrm{X_{CH4}} = 100 \times \left[\frac{N_{\mathrm{CH_{4,in}}} - N_{\mathrm{CH_4}}}{N_{\mathrm{CH_{4,in}}}}\right] \tag{4.10}$$

where, $N_{\mathrm{CH_{4,in}}}$ is the inlet molar flow-rate of methane and $N_{\mathrm{CH_4}}$ is the molar flow-rate of methane at a position along the channel length. Y_{H2} characterizes the performance of the reactor with respect to the hydrogen production. It is the ratio of the produced hydrogen to the theoretical maximum amount of hydrogen that can be produced in steam reforming and water-gas-shift reactions:

$$\mathrm{Y_{H2}} = 100 \times \left[\frac{1}{4}\frac{N_{\mathrm{H_2}}}{N_{\mathrm{CH_{4,in}}}}\right] \tag{4.11}$$

where, $N_{\mathrm{H_2}}$ is the molar flow-rate of hydrogen and $N_{\mathrm{CH_{4,in}}}$ is the inlet molar flow-rate of methane. S_{CO} is defined as the ratio of the produced CO to the produced molar rate of CO and CO_2:

$$\mathrm{S_{CO}} = 100 \times \left[\frac{N_{\mathrm{CO}}}{N_{\mathrm{CO}} + N_{\mathrm{CO_2}}}\right] \tag{4.12}$$

where, N_{CO} and $N_{\mathrm{CO_2}}$ are the molar flow-rate of carbon-monoxide and carbon-dioxide respectively, at a position along reforming-channel length. Another important parameter to evaluate the performance of the plate reformer is its overall efficiency ($E_{overall}$), which is the ratio of the Lower Heating Value (LHV) of hydrogen and carbon-monoxide produced to the LHV of methane consumed [4]. For a CPR, where MSR is coupled with CMC, LHV of methane consumed on the combustion-side is also accounted for in calculating the $E_{overall}$:

$$\mathrm{E_{overall}} = 100 \times \left[\frac{\mathrm{LHV_{H_2}} N_{\mathrm{H_2}} + \mathrm{LHV_{CO}} N_{\mathrm{CO}}}{\mathrm{LHV_{CH_4}}\left(N_{\mathrm{CH_{4,in}}} - N_{\mathrm{CH_4}}\right)_{\mathrm{reforming}} + \mathrm{LHV_{CH_4}}\left(N_{\mathrm{CH_{4,in}}} - N_{\mathrm{CH_4}}\right)_{\mathrm{combustion}}}\right] \tag{4.13}$$

The LHV of any fuel $\mathrm{C_xH}_y\mathrm{O}_z$ is calculated by the following formula [4]:

$$\mathrm{LHV}_{\mathrm{C_xH}_y\mathrm{O}_z}(\mathrm{kJ \cdot mol^{-1}}) = \left(\frac{y}{2} + 2x - z\right) 198.8 + 25.4 \tag{4.14}$$

4.5.1. Reference case

A reference case study is conducted to investigate initial performance of the CPR with the inlet conditions listed in Table 4.2. Both co-flow and counter-flow modes between reforming and combustion flow-channels are investigated by considering identical inlet conditions. The first section discusses the co-flow mode between SLCC and CLCC models, followed by the counter-flow mode. In co-flow mode, both sides fluid streams are flowing from left to right. The zero axial (x=0) coordinate, therefore, represents the inlets for both sides. Whereas, in counter-flow mode x=0 represents reforming-side inlet and combustion-side outlet. Based on the inlet conditions listed in Table 4.2, inlet GHSVs in reforming-channel ($GHSV_{ref}$) and in combustion-channel ($GHSV_{comb}$), are equal to 97,234 h^{-1} and 1.343×10^6 h^{-1} respectively, for the SLCC-model.

Table 4.2. *Inlet conditions and model parameters for the reference case*

	Reforming-side	**Combustion-side**	
		SLCC	**CLCC**
Inlet conditions			
Total CH4 molar flow for 20 channels	9.94 mol/h	2.55 mol/h	2.55 mol/h
CH_4 molar flow in one channel, $N_{\mathrm{CH_4,in}}$	0.50 mol/h	0.13 mol/h	0.13 mol/h
Steam to carbon ratio, SC	3.0	n/a	n/a
Oxygen to carbon ratio, O_2/C	n/a	2.50	2.50
H_2O molar flow in one channel, $N_{\mathrm{H_2O}_{in}}$	SC × $N_{\mathrm{CH_4,in,ref}}$	n/a	n/a
O_2 molar flow in one channel, $N_{\mathrm{O_2,in}}$	n/a	(O_2/C) × $N_{\mathrm{CH_4,in,comb}}$	(O_2/C) × $N_{\mathrm{CH_4,in,comb}}$
N_2 molar flow in one channel, $N_{\mathrm{N_2,in}}$	n/a	(0.79/0.21) × $N_{\mathrm{O_2,in}}$	(0.79/0.21) × $N_{\mathrm{O_2,in}}$
Temperature, T_{in}	800.0 K	800.0 K	800.0 K
Pressure, *p*	1.0 atm.	1.0 atm.	1.0 atm.
Catalyst Layers			
Catalyst thickness	100 µm	20 µm	20 µm
Mean particle diameter, d_p	1.0 µm	1.0 µm	1.0 µm
Mean pore size, d_{pore}	0.45 µm	0.45 µm	0.45 µm
Porosity, ε	0.4	0.4	0.4
Tortuosity, τ	$1/\varepsilon^{1/2}$	$1/\varepsilon^{1/2}$	$1/\varepsilon^{1/2}$
Density, $\rho_{\mathrm{cat.}}$	2366.7 kg/m^3	2366.7 kg/m^3	2366.7 kg/m^3
Combustion Parameters			
Activation energy, E_a	Table 3.2	90.0 kJ/mol	90.0 kJ/mol
Pre-exponential factor, A	Table 3.2	4.0×10^8 s^{-1}	4.0×10^8 s^{-1}

Both sides GHSVs are estimated at the normalized condition of 298.15K and 1 atm. and are defined as the ratio of the volume flow of feed ($\dot{V}_{feed}$) to the catalyst volume (V_{cat}) [4]:

$$GHSV\ [\mathrm{h}^{-1}] = \frac{\dot{V}_{feed}}{V_{cat}} \tag{4.15}$$

Due to longer overall length of combustion-catalyst, $GHSV_{comb}$ in the CLCC-model decreases to $4.029 \times 10^5 h^{-1}$ for the same volume flow of methane-air.

4.5.1.1. Co-flow

The most critical issue in a CPR is to examine how effective heat distribution is achieved throughout the reactor. Fig. 4.4(A) shows a comparison of heat-flux produced (kW/m^2) due to combustion reaction as a function of catalyst-length between CLCC and SLCC models. The heat flux shown in Fig. 4.4 (A) is in fact calculated based on volumetric heat-flux generated due to the combustion reaction rates. Fig. 4.4(A) depicts that heat flux rapidly falls near zero values within the first 30% of the catalyst-length in CLCC-model. This is due to the very high combustion reaction rate; 99.6% of methane is consumed within 30% of the catalyst-length (Fig. 4.4(B)). Whereas, in SLCC-model, heat-flux doesn't fall near zero values until the tail of combustion-catalyst (x = 6 cm). This is because active and catalytically inactive sections in SLCC-model have reduced the combustion rate and hence as shown in Fig. 4.4(B), only 76.2% methane is consumed within the first 30% of the catalyst-length. Fig. 4.4(B) also illustrates average plate temperature profiles for both models and clearly shows hot-spot in CLCC-model with maximum plate temperature of 1034 K at x = 1.4 cm and outlet plate temperature of 935 K at x = 7 cm. In comparison, a maximum plate temperature of 1006 K at x = 3 cm and the outlet plate temperature of 977 K are obtained for the SLCC-model. It is observed from Fig. 4.4(E) that axial

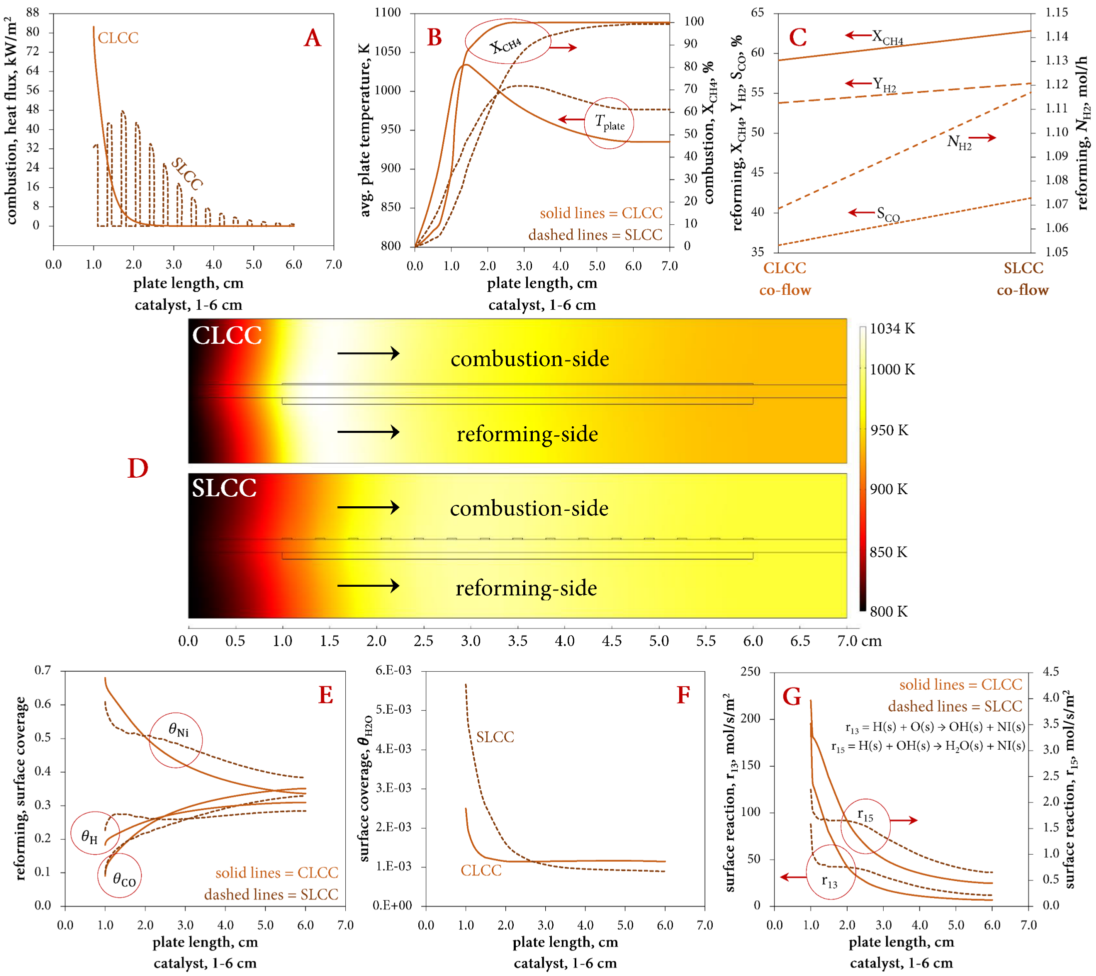

Fig. 4.4. *Co-flow (A) Comparison of combustion-side reaction heat flux at combustion-catalyst surface as a function of plate length between SLCC and CLCC. (B) Comparison of average plate temperature and combustion-side* X_{CH4} *as a function of plate length between SLCC and CLCC. (C) Comparison of reforming-side* X_{CH4}*,* Y_{H2}*,* S_{CO} *and* N_{H2} *at the reforming-channel outlet between SLCC and CLCC. (D) Temperature distribution in the CPR designed with CLCC and SLCC. (E) Comparison of reforming-side* θ_{CO}*,* θ_H *and* θ_{Ni} *as a function of plate length between SLCC and CLCC. (F) Comparison of* θ_{H2O} *in reforming-catalyst between SLCC and CLCC. (G) Comparison of the surface reaction rates* r_{13} *and* r_{15} *(Table 3.2) in reforming-catalyst between SLCC and CLCC.*

thermal-gradients are reduced significantly in SLCC-model due to the lower difference between the maximum plate temperature and outlet plate temperature as compared to CLCC-model. Low thermal-gradients obtained in SLCC-model can minimize thermal stresses and hence can slow down the thermal degradation rate of the plate material compared to CLCC-model.

Influence of SLCC and CLCC on the performance of MSR is compared in Fig. 4.4(C). Figure shows reforming-side X_{CH4}, Y_{H2}, S_{CO} and N_{H2} at the reforming-channel outlet (x = 7 cm). It should be noted that N_{H2} plotted is for the single reforming-channel and should be multiplied by the total number of reforming-channels for the total hydrogen production. In CLCC-model, 59.12% X_{CH4}, 53.80% Y_{H2}, 35.99% S_{CO}, and 21.37 mol/h N_{H2} are obtained for 97,234 h^{-1} $GHSV_{ref}$. Whereas, with SLCC-model for same inlet conditions, 62.83% X_{CH4}, 56.25% Y_{H2}, 41.89% S_{CO}, and 22.34 mol/h N_{H2} are obtained. This shows that by using segmented combustion-catalyst, N_{H2} is increased by 4.55%. The increase of 5.90% in S_{CO}, is because downstream temperature of the CPR in SLCC-model is higher than in CLCC-model as shown in Fig. 4.4(B). At high temperatures, reverse water-gas-shift favors CO production due to the Le Chatelier's principle and due to the equilibrium shift in the Boudouard reaction ($2CO \Leftrightarrow C + CO_2$) [24]. On the combustion-side, 100% and 99.3% in X_{CH4} are obtained with CLCC and SLCC models respectively. The overall thermal efficiency ($E_{overall}$) of 81.12% and 82.75% are predicted for the CLCC and SLCC models respectively.

Influence of SLCC and CLCC on the concentration of Most Abundant Reactive Intermediate (MARI) species at reforming-catalyst surface is compared in Fig. 4.4(E) as a function of reforming-catalyst length. For the conditions listed in Table 4.2, surface carbon-monoxide (CO(s)) and surface hydrogen (H(s)) are found to be the MARI species. Reactive intermediate with high surface coverage has a higher probability to interact with other intermediates and involve in surface reactions. It is observed that the first 30% of reforming-catalyst length in CLCC-model, is covered with more H(s) than CO(s) and remaining 70% is covered with more CO(s) than H(s). Whereas in SLCC-model, 40% of catalyst-length is covered with more H(s) and remaining 60% is covered with more CO(s). 10% increase in H(s) covered catalyst-length in SLCC-model is due to relatively low temperature at the initial section of reforming-catalyst in SLCC-model. This has decreased the desorption rate of surface water ($H_2O(s)$) and as a result more $H_2O(s)$ remain adsorbed (see Fig. 4.4(F)) at the surface and with time it dissociated to H(s) and O(s) via reactions r_{16} and r_{14} (Table 3.2). However, due to relatively low temperature than in CLCC, reaction rates of H(s) to OH(s) (reaction r_{13}) and back to $H_2O(s)$ (reaction r_{15}) are slower in SLCC-model as depicted in Fig. 4.4(G). The slow reaction rate (r_{13}) also explains why H(s) coverage in SLCC-model is 20% more than CLCC-model for the first 25% of reforming-catalyst length. Fig. 4.4(E) further illustrates that due to high-temperature at the reactor downstream, more vacant (nickel) sites are available for the adsorption in SLCC-model. At high-temperatures, desorption rate of adsorbed species is high, hence more vacant sites are available for surface reactions. Same can be concluded for lower surface coverage of H(s) and CO(s) at the downstream in SLCC-model. Hence, this explains at the fundamental level, why high X_{CH4}, S_{CO}, Y_{H2}, and N_{H2} are obtained in reforming-side with respect to SLCC-model than CLCC-model.

4.5.1.2. Counter-flow

In this section, the influence of counter-flow mode on heat-transfer effects arising in the CPR from the endothermic reforming and exothermic combustion reactions is studied using the identical set of parameters used for the co-flow mode. Like the co-flow mode, Fig. 4.5(A) shows a comparison of reaction heat-flux produced at combustion-catalyst surface as a function of the catalyst-length, between CLCC and SLCC models. Fig. 4.5(A) clearly depicts that heat flux rapidly falls near zero values within the first 22% of the catalyst-length in CLCC-model, whereas in SLCC-model, it falls near zero values within 85% of catalyst length. Note that, in counter-flow mode, combustion-side stream is flowing from x = 7 cm to x = 0. By comparing Figs. 4(A) and 5(A), it is observed that in both CLCC and SLCC models, heat-flux values at the start of combustion-catalyst section are larger in counter-flow mode than in co-flow. Thus, maximum plate temperatures (Fig. 4.5(B)) obtained in both CLCC and SLCC models are also higher in the case of counter-flow mode than co-flow. Unlike co-flow mode, it is interesting to see from Fig. 4.5(B) and (C) that both models have shown hot-spot regions in the CPR near the combustion-side inlet. Also, axial thermal gradients are very high compared to the co-flow mode in both CLCC and SLCC models,

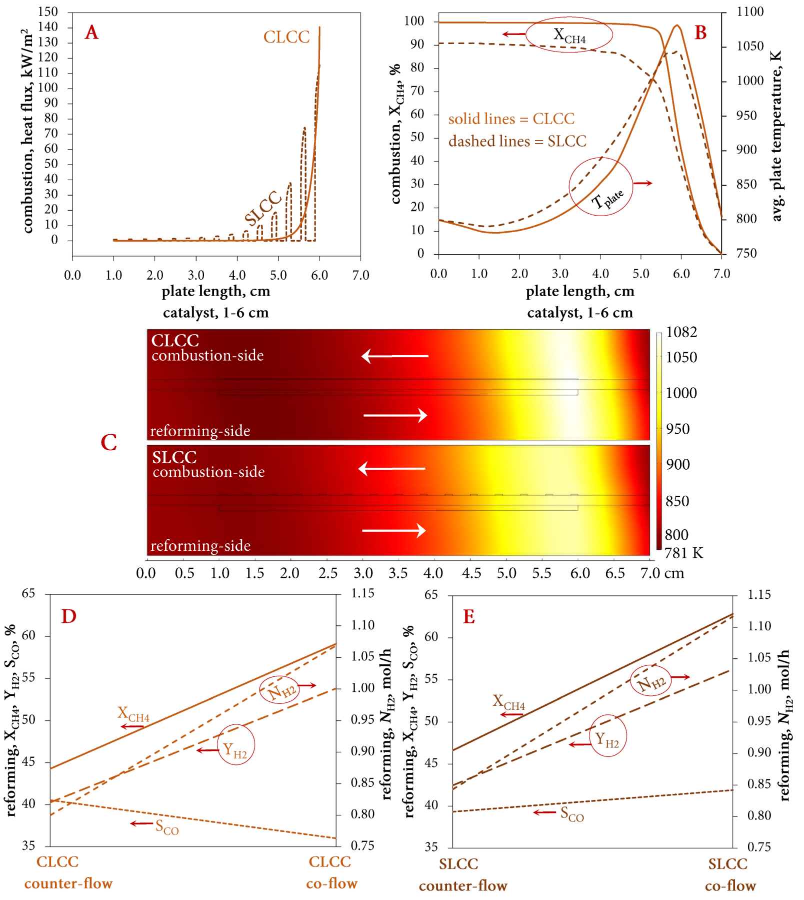

Fig. 4.5. *(A) Comparison of combustion-side reaction heat flux at combustion-catalyst surface as a function of plate length between SLCC and CLCC for counter-flow mode. (B) Comparison of average plate temperature and combustion-side methane conversion profiles as a function of plate length between SLCC and CLCC for counter-flow mode. (C) Temperature distribution in the CPR for counter-flow mode. (D) Comparison of reforming-side X_{CH4}, Y_{H2}, S_{CO} and N_{H2} at the reforming-channel outlet between counter-flow and co-flow modes for CLCC and (E) SLCC.*

as average reactor plate temperature decreases to 781 K at x = 1.4 cm from 1082 K at x = 5.5 cm in CLCC-model and 790.6 K at x = 1.2 cm from 1044 at x = 5.5 cm in SLCC-model. Due to lower downstream temperature (towards zero axial direction), only 90% combustion-side X_{CH4} is obtained in SLCC-model. Low conversion rate could be avoided by increasing flow-rate of methane-air in combustion-side, however, by doing that temperature can increase significantly near the inlets. Thus, heat distribution in counter-flow mode with SLCC requires detail investigation, which is outside the scope of this study now. Fig. 4.5(D) and (E) illustrate a comparative study of X_{CH4}, Y_{H2}, S_{CO} and N_{H2} obtained at reforming-channel outlet between co-flow and counter-flow modes for CLCC and SLCC models respectively. From this comparison study, it is concluded that the CPR designed with co-flow mode and SLCC or CLCC configuration has shown better performance compared to counter-flow mode. Hence only the co-flow mode has been considered for the remainder of this study.

4.5.2. Gas hourly space velocity

To evaluate the productivity performance of a CPR, GHSV is the most important parameter to study. In this study, the effect of $GHSV_{comb}$ and $GHSV_{ref}$ for the hydrogen production is examined for CLCC and SLCC models. Two different $GHSV_{ref}$ are considered against six different $GHSV_{comb}$. The $GHSV_{comb}$ is varied by changing volumetric flow-rate of methane-air mixture while keeping the $GHSV_{ref}$ constant. To keep the reforming-side inlet molar flow-rate of methane constant to obtain the desired hydrogen feed rate for a 1 kW fuel-cell, the $GHSV_{ref}$ is varied by changing the reforming-catalyst thickness. Two varied sizes of reforming-catalyst thickness are considered: 100 mm (reference case) and 200 mm; correspondingly the $GHSV_{ref}$ values are equal to 97,234 $h^{-1}$and 48,617 h^{-1} respectively. Thus, in total 24 simulation runs were conducted; 12 for CLCC-model and 12 for SLCC-model. The results obtained between the two-sides GHSVs are presented as a function of the mass flow-rates ratio ($m_{comb/ref} = m_{comb}/m_{ref}$) of the combustion and reforming feed rates. Except combustion-side volume feed rate and reforming-side catalyst thickness, all other parameters are kept identical to the reference case study.

Fig. 4.6(A) and (B) illustrate reforming-side X_{CH4} and $E_{overall}$ at reforming-channel outlet as a function of the $m_{comb/ref}$ obtained in SLCC and CLCC models for 97,234 h^{-1} (100 mm reforming-catalyst thickness) and 48,617 h^{-1} $GHSV_{ref}$ (200 mm reforming-catalyst thickness) respectively. The mass flow-rate ratio is varied between 1.32 and 5.01 by varying inlet flow-rate of methane-

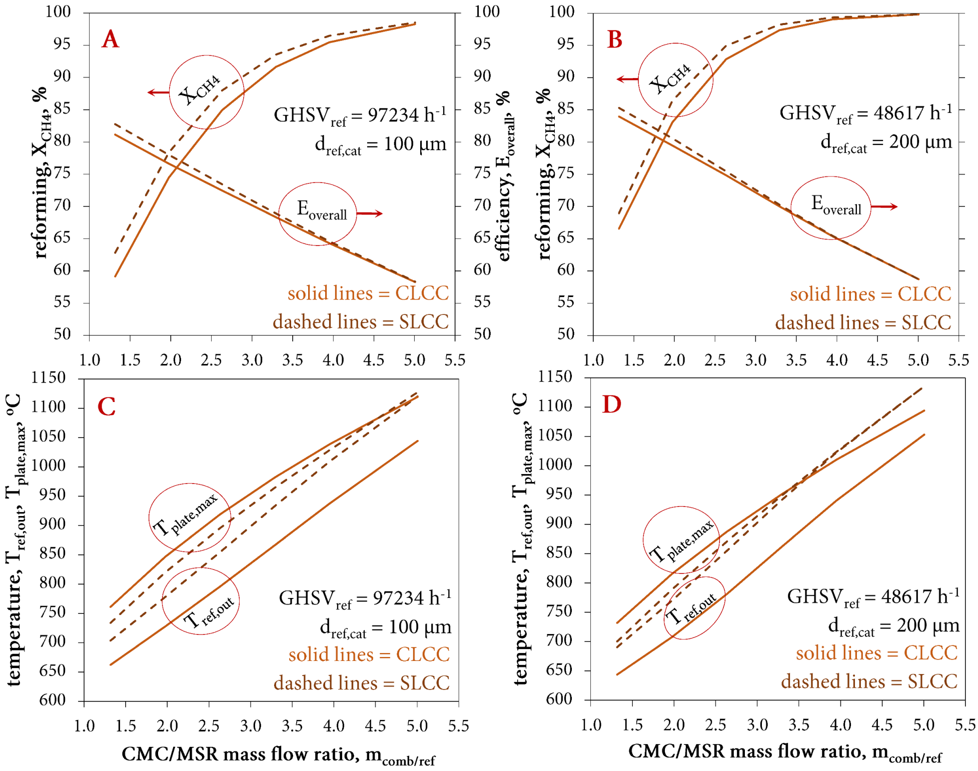

Fig. 4.6. *(A) Comparison of $E_{overall}$ and reforming-side X_{CH4} as a function of mass flow-rates ratio ($m_{comb/ref}$) between SLCC and CLCC for $GHSV_{ref}$ = 97,234 h^{-1} and (B) $GHSV_{ref}$ = 48,617 h^{-1}. (C) Comparison of average maximum plate temperature and average temperature at the reforming-channel outlet as a function of mass flow-rates ratio ($m_{comb/ref}$) between SLCC and CLCC for $GHSV_{ref}$ = 97,234 h^{-1} and (D) $GHSV_{ref}$ = 48,617 h^{-1}.*

air mixture in combustion-channel. Fig. 4.6(A) illustrates that X_{CH4} increases to 98% from around 60% when $m_{comb/ref}$ is increased to 5.01 from 1.32, however, $E_{overall}$ reduces from around 80% to 58% due to increase in combustion-side methane consumption. Similarly, it is observed from Fig. 4.6(B) that X_{CH4} reaches to almost 100% from around 67% when $m_{comb/ref}$ is increased to 5.01 from 1.32 and $E_{overall}$ reduces from around 85% to 58%. For both 97,234 h^{-1} and 48,617 h^{-1} $GHSV_{ref}$, near 100% X_{CH4} is obtained with 58% $E_{overall}$ in both SLCC and CLCC models. Fig. 4.6(A) and (B) also illustrate that under incomplete conversion regime (<98%), SLCC-model has predicted high X_{CH4} and high $E_{overall}$ as compared to CLCC-model.

Fig. 4.6(C) and (D) present the maximum plate temperature and reforming-side outlet temperature as a function of the $m_{comb/ref}$ in SLCC and CLCC models for 97,234 h^{-1} and 48,617 h^{-1} $GHSV_{ref}$ respectively. It is observed that maximum plate temperature obtained in CLCC-model is high for all studied $m_{comb/ref}$ compared to SLCC-model, except at $m_{comb/ref}$ = 5.01 for $GHSV_{ref}$ = 97,234 h^{-1} and above $m_{comb/ref}$ = 3.95 for $GHSV_{ref}$ = 48,617 h^{-1}, where maximum plate temperatures in CLCC-model are predicted slightly lower than SLCC-model. However, the difference between the maximum plate temperature and the reforming-side outlet stream temperature is always large in CLCC-model for both $GHSV_{ref}$. The significant difference between the two temperatures indicate high axial thermal-gradients in the CPR designed with CLCC than the CPR designed with SLCC. The low axial thermal gradient for the reactor plate makes

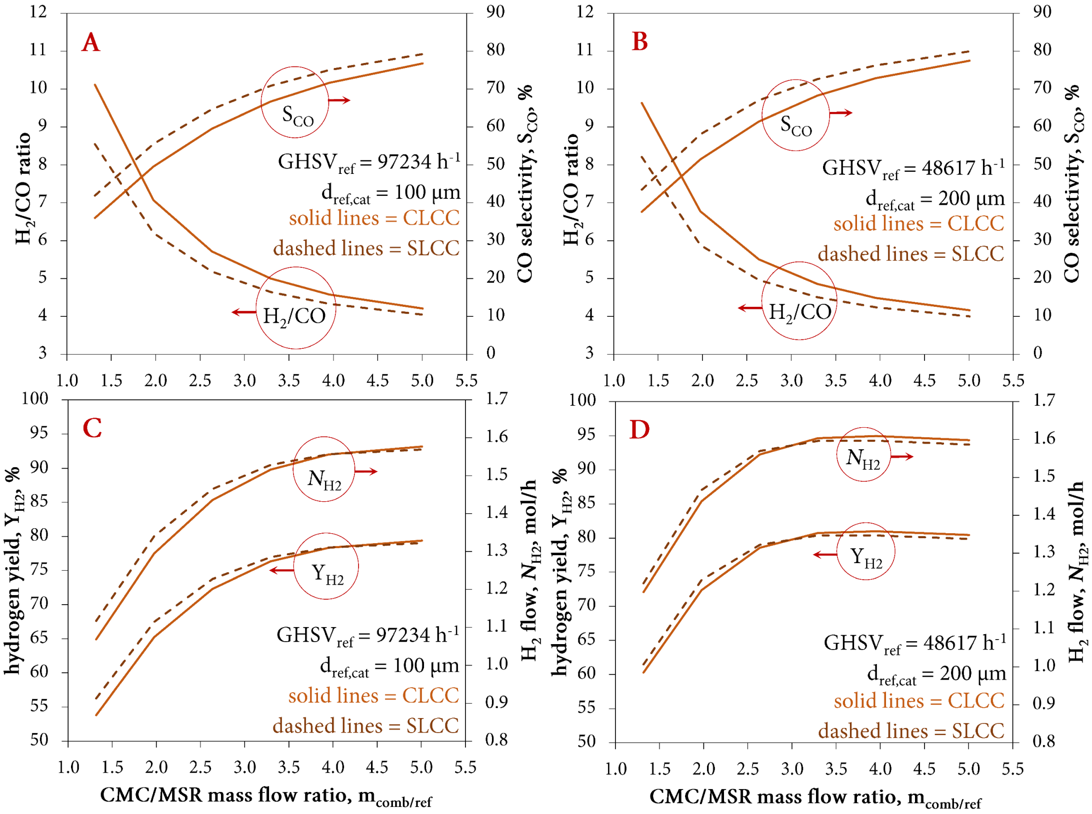

Fig. 4.7. *(A) Comparison of H_2/CO ratio and S_{CO} as a function of mass flow-rates ratio ($m_{comb/ref}$) between SLCC and CLCC for $GHSV_{ref}$ = 97,234 h^{-1} and (B) $GHSV_{ref}$ = 48,617 h^{-1}. (C) Comparison of Y_{H2} and N_{H2} as a function of mass flow-rates ratio ($m_{comb/ref}$) between SLCC and CLCC for $GHSV_{ref}$ = 97,234 $h^{-1}$and (D) $GHSV_{ref}$ = 48,617 h^{-1}.*

segmented layer of combustion-catalyst a desirable configuration from the stand-point of different thermal expansion coefficients for the coated catalyst and the reactor plate.

Fig. 4.7(A) and (B) present carbon-monoxide selectivity (S_{CO}) and hydrogen to carbon-monoxide (H_2/CO) ratio as a function of the mcomb/ref in SLCC and CLCC models for 97,234 h^{-1} and 48,617 h^{-1} $GHSV_{ref}$ respectively. It is observed that S_{CO} increases with increase in $m_{comb/ref}$. It is because temperature of the CPR goes up with increase in combustion-side feed flow-rate and hence at higher temperatures reverse water-gas-shift reaction favors CO production. Thus, H_2/CO ratio is bound to decrease as CO production increases. At the highest studied $m_{comb/ref}$ ratio of 5.01, 79.21% and 76.77% S_{CO} are obtained in SLCC and CLCC models respectively for 97,234 h^{-1} $GHSV_{ref}$; whereas 79.93% and 77.46% S_{CO} are obtained in SLCC and CLCC models for 48,617 h^{-1} $GHSV_{ref}$. H_2/CO ratios of 4.05 and 4.21 are predicted in SLCC and CLCC models respectively for 97,234 h^{-1} $GHSV_{ref}$; whereas 4.0 and 4.16 are predicted for 48,617 h^{-1} $GHSV_{ref}$. From Fig. 4.7(A) and (B), it is also observed that the differences in S_{CO} values and differences in H_2/CO values between CLCC and SLCC models decrease with increase in combustion-side feed flow-rate. This is because system approaches equilibrium at higher temperatures, as concentration distribution of all chemical species, regardless of the chemical reactor design follow the principle of thermodynamic equilibrium. Hence, at 100% X_{CH4} at high temperatures, all species concentration approaches to equilibrium values.

Fig. 4.7(C) and (D) illustrate N_{H2} and Y_{H2} as a function of the $mc_{omb/ref}$ for 97,234 h^{-1} and 48,617 h^{-1} $GHSV_{ref}$ respectively. For 97,234 h^{-1}, Y_{H2} of 79% and N_{H2} of 1.58 mol/h per channel are predicted in both CLCC and SLCC models for the highest studied $m_{comb/ref}$ = 5.01; whereas for 48,617 h^{-1}, Y_{H2} of 80% and N_{H2} of around 1.59 mol/h per channel are predicted. For 97,234 h^{-1} $GHSV_{ref}$, the required hydrogen flow-rate of 29.80 mol/h for 1 kW fuel-cell is obtained at 91.87% X_{CH4} with 2.88 $m_{comb/ref}$ ratio in SLCC-model, whereas in CLCC-model, required N_{H2} of 29.80 mol/h is obtained at 95.93% X_{CH4} with 3.06 $m_{comb/ref}$ ratio. This indicate that to achieve the required N_{H2} for a 1 kW fuel-cell, CLCC-model requires nearly 8% more combustion-side feed flow-rate than in SLCC-model.

4.5.3. Reforming catalyst thickness

The influence of the reforming-side catalyst thickness on the performance CPR is investigated for the constant feed composition and constant inlet flow-rates in CLCC and SLCC models. Three distinct size of the reforming-catalyst thickness (50 mm, 100 mm and 200 mm) are considered. Changes in reforming-catalyst thickness can influence considerably both the thermal behavior of a CPR and X_{CH4} in reforming-channel. Note that, due to the fixed distance between plates, the cross-sectional area of reforming-channel varies with the thickness of reforming-catalyst coated between 1 cm and 6 cm, i.e. greater the thickness of reforming-catalyst, lower the cross-sectional area in reforming flow channel. This contributes to lowering the residence time due to slight increase in volume flow but at the same time decreases external mass transfer resistance.

X_{CH4}, $E_{overall}$, Y_{H2} and N_{H2} are plotted in Fig. 4.8(A) and (B) as a function of reforming-catalyst thickness for CLCC and SLCC models. It is evident that all four performance indicator parameters (X_{CH4}, $E_{overall}$, Y_{H2} and N_{H2}) are increased with increase in reforming-catalyst thickness and again the performance of SLCC model is better than CLCC-model. Increase in X_{CH4} with reforming-catalyst thickness is expected as for kinetically controlled process, thicker layer of catalyst results in more active catalyst area exposed to the reactant which ultimately results in high conversion

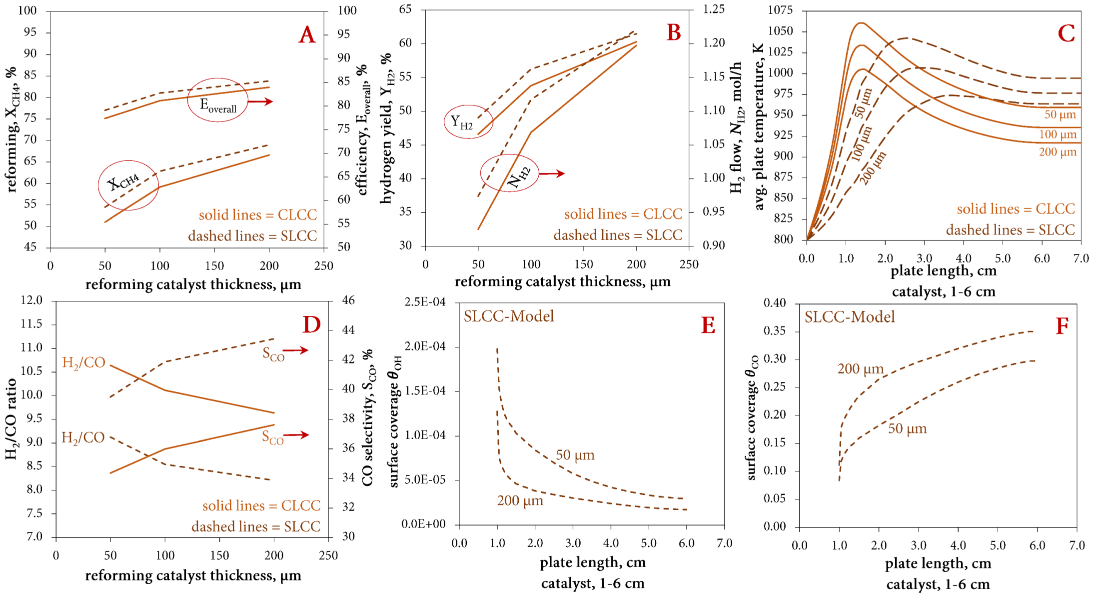

Fig. 4.8. *Comparison of (A) $E_{overall}$ and reforming-side X_{CH4}, (B) Y_{H2} and N_{H2}, as a function of reforming-catalyst thickness between SLCC and CLCC. (C) Comparison of average plate temperature as a function of the plate length between SLCC and CLCC for reforming-catalyst thickness of 50 mm, 100 mm and 200 mm. (D) Comparison of H_2/CO ratio and S_{CO} as a function of reforming-catalyst thickness between SLCC and CLCC. (E) Comparison of surface coverages of OH and (F) CO as a function of catalyst length between 50 mm and 200 mm for SLCC.*

and product yield. Maximum and minimum X_{CH4} of 66.57% and 50.97% in CLCC-model and 68.57% and 54.42% in SLCC-model are obtained for 200 mm and 50 mm thickness respectively. Maximum and minimum Y_{H2} of 60.30% and 46.59% in CLCC-model and 61.49% and 49.04% in SLCC-model are obtained for 200 mm and 50 mm thickness respectively. X_{CH4} is increased by the factor of 1.31 in CLCC-model and 1.27 in SLCC-model when reforming-catalyst thickness is increased by four times. This indicates that the influence of increase in reforming-catalyst thickness in SLCC-model is slightly lower compared to CLCC-model. Although reforming is kinetically controlled, increase in catalyst thickness by some factor does not result in increase in conversion by the same factor. This is due to the inefficient heat transfer through the catalyst layers of greater thickness that ultimately results in lower reforming temperature. Another aspect to account for is increase of internal mass-transfer resistance with increase in reforming-catalyst thickness. The study of internal mass-transfer resistance in coated catalyst requires thorough investigation and hence at this point it is beyond the scope of this study. Fig. 4.8(A) and (B) also illustrate $E_{overall}$ and N_{H2} respectively. It can be observed that efficiency is increased by 8.52% in CLCC-model and 7.87% in SLCC-model and N_{H2} by 29% in CLCC-model and 25% in SLCC-model when reforming-catalyst thickness increases from 50 mm to 200 mm.

Fig. 4.8(C) illustrates the influence of reforming-catalyst thickness on the temperature distribution in the reactor plate. Thinner the catalyst layer, higher the temperature in the CPR. It is due to the low methane conversion and lower rate of heat of absorption by reforming process due to the low overall active area available for reforming reactions to proceed. SLCC configuration has shown lower axial thermal-gradients in the reactor plate compared to CLCC for all three-studied reforming-catalyst thickness. Fig. 4.8(D) shows S_{CO} and H_2/CO ratio as a function of the reforming-catalyst thickness for CLCC and SLCC models. It is evident that S_{CO} is increased with increase in reforming-catalyst thickness and hence H_2/CO ratio shows reverse trend. The minimum and maximum S_{CO} of 34.37% and 37.61% in CLCC-model and 39.51% and 43.44% in SLCC-model are obtained for 50 mm and 200 mm reforming-catalyst thickness respectively. Whereas, maximum and minimum H_2/CO ratio of 10.64 and 9.63 in CLCC-model and 9.12 and 8.21 in SLCC-model are obtained for 50 mm and 200 mm thickness respectively.

Fig. 4.8(C) and (D) show that overall temperature of the reactor plate decreases with increase in reforming-catalyst thickness, but S_{CO} increases with increase in reforming-catalyst thickness or increases with decrease in overall reactor plate temperature. Stutz et al. [42] have explained the effect of catalyst thickness on S_{CO} and why S_{CO} is low for thin reforming-catalyst layer. According to Stutz et al., for the thin catalyst layer, splitting of the C–H bond is slow in methane molecule. Thus, oxygen atoms in OH do not form CO and CO_2, because for the CO and CO_2 to form, the carbon atom in methane molecule must split all four bonds with the H atom. On the other hand, because of the higher splitting rate of the carbon from the hydrogen in methane molecule for the thicker catalyst layer, it is more likely that the O atoms in surface OH split from H atoms and react with carbon atoms to form CO and CO_2. Thus, the surface H atoms from methane molecules and the surface OH can react to form the surface hydrogen molecules (H_2) that eventually desorb to the gas-phase. Fig. 4.8(E) and (F) shows the surface coverage of OH and CO for 50 mm and 200 mm reforming-catalyst thickness in SLCC-model. For the thicker catalyst layer, lower surface coverage of OH and higher surface coverage of CO is obtained. This indicates more oxygen atoms from OH are separated and reacted with carbons to form more CO for the thicker catalyst layer. This could be the reason for increase in S_{CO} with increase in reforming-catalyst thickness as shown in Fig. 4.8(D).

4.6. Conclusions

In this work, two computational models, one with segmented configuration (SLCC-model) and the second with continuous configuration (CLCC-model) of the coated combustion-catalyst (platinum-alumina) are developed to investigate their influence on MSR over a continuous coating of nickel-alumina catalyst for hydrogen production in a catalytic plate reactor (CPR). The study has successfully integrated continuum scale transport, heat and mass transfer with the experimentally validated multi-step surface microkinetic model of MSR. SLCC and CLCC models are compared with each other to understand the influence of flow direction, gas hourly space velocity (GHSV) and reforming-catalyst thickness on the performance of CPR. The CPR designed with SLCC and co-flow mode has shown superior performance not only in terms of high methane conversion and high hydrogen production but also in terms of minimizing the maximum reactor plate temperature, axial thermal-gradients and thermal hot-spots. The improvement with SLCC configuration is due to the continuous supply of heat to the reforming-side from the combustion-side through the interspacing among active combustion-catalyst segments, contributing significantly to avoid cold and hot zones by maintaining a balanced thermal distribution at the reactor downstream. The study has also shown that the CPR designed with SLCC configuration required 7 to 8% less combustion feed flow and 70% less combustion-catalyst to produce required hydrogen flow (29.80 mol/h) to feed a 1 kW fuel cell compared to the CPR designed with CLCC. Reforming-catalyst thickness study has shown that increasing reforming-catalyst thickness by some factor does not increase the reforming-side methane conversion by the same factor. This is due to low heat-transfer through the catalyst layers of greater thickness and possibly due to increase in internal mass-transfer resistance with increase in reforming-catalyst thickness. The flow direction study has shown that the CPR designed with

CLCC or SLCC and with counter-flow mode completes the combustion reaction in the first 20% to 30% of the combustion-catalyst length. This generates undesirable high-temperatures that drive the endothermic MSR reactions to absorb the heat released by combustion. Such undesirable high-temperature degrades the catalyst and the plate and thus makes co-flow mode a desirable choice if suitable material is not available to withstand the high-temperature in counter-flow mode.

4.7. References

[1] Beith R, editor. Small and micro combined heat and power (CHP) systems: Advanced design, performance, materials and applications. Elsevier; 2011 Apr 30.

[2] Mundhwa M, Thurgood CP, Dhingra H, Parmar RD, Peppley BA. A comparative computational study of diesel steam reforming in a catalytic plate heat-exchange reactor. AIChE Journal. 2016 Aug 1.

[3] Canadian Medical Association, Room NB. National Illness Costs of Air Pollution, Summary Report. 2008.

[4] Kolb G. Fuel processing: for fuel cells. Wiley-VCH Verlag GmbH & Co. KGaA; 2008.

[5] Hunter JB, McGuire G, inventors; Matthey Bishop, Inc., assignee. Method and apparatus for catalytic heat exchange. United States patent US 4,214,867. 1980 Jul 29.

[6] Kolb G, Hessel V. Micro-structured reactors for gas phase reactions. Chemical Engineering Journal. 2004 Mar 15;98(1):1-38.

[7] Zanfir M, Gavriilidis A. Modelling of a catalytic plate reactor for dehydrogenation–combustion coupling. Chemical Engineering Science. 2001 Apr 30;56(8):2671-83.

[8] Wang F, Zhou J, Wang G. Transport characteristic study of methane steam reforming coupling methane catalytic combustion for hydrogen production. international journal of hydrogen energy. 2012 Sep 30;37(17):13013-21.

[9] Bartholomew CH. Mechanisms of catalyst deactivation. Applied Catalysis A: General. 2001 Apr 30;212(1):17-60.

[10] Pattison RC, Estep FE, Baldea M. Pseudodistributed feed configurations for catalytic plate microchannel reactors. Industrial & Engineering Chemistry Research. 2013 Aug 9;53(13):5028-37.

[11] Jeon SW, Yoon WJ, Baek C, Kim Y. Minimization of hot spot in a microchannel reactor for steam reforming of methane with the stripe combustion catalyst layer. international journal of hydrogen energy. 2013 Oct 25;38(32):13982-90.

[12] Xu J, Froment GF. Methane steam reforming, methanation and water-gas shift: I. Intrinsic kinetics. AIChE Journal. 1989 Jan 1;35(1):88-96.

[13] Mundhwa M, Thurgood CP. Numerical study of methane steam reforming and methane combustion over the segmented and continuously coated layers of catalysts in a plate reactor. Fuel Processing Technology. 2017;158:57-72.

[14] Zanfir M, Gavriilidis A. Catalytic combustion assisted methane steam reforming in a catalytic plate reactor. Chemical Engineering Science. 2003 Sep 30;58(17):3947-60.

[15] Zanfir M, Gavriilidis A. Influence of flow arrangement in catalytic plate reactors for methane steam reforming. Chemical Engineering Research and Design. 2004 Feb 29;82(2):252-8.

[16] Zanfir M, Gavriilidis A. An investigation of catalytic plate reactors by means of parametric sensitivity analysis. Chemical engineering science. 2002 May 31;57(9):1653-9.

[17] Stefanidis GD, Vlachos DG. Millisecond methane steam reforming via process and catalyst intensification. Chemical engineering & technology. 2008 Aug 1;31(8):1201-9.

[18] Stefanidis GD, Vlachos DG, Kaisare NS, Maestri M. Methane steam reforming at microscales: Operation strategies for variable power output at millisecond contact times. AIChE journal. 2009 Jan 1;55(1):180-91.

[19] Zhai X, Ding S, Cheng Y, Jin Y, Cheng Y. CFD simulation with detailed chemistry of steam reforming of methane for hydrogen production in an integrated micro-reactor. international journal of hydrogen energy. 2010 Jun 30;35(11):5383-92.

[20] Arzamendi G, Diéguez PM, Montes M, Odriozola JA, Sousa-Aguiar EF, Gandía LM. Methane steam reforming in a microchannel reactor for GTL intensification: A computational fluid dynamics simulation study. Chemical Engineering Journal. 2009 Nov 15;154(1):168-73.

[21] J.R. Rostrup-Nielsen, Catalytic steam reforming, in: J.R. Anderson, M. Boudart (Eds.), Catalysis-Science and Technology, vol.5, Springer-Verlag, Berlin, 1984, p.51.

[22] Arzamendi G, Uriz I, Navajas A, Diéguez PM, Gandía LM, Montes M, Centeno MA, Odriozola JA. A CFD study on the effect of the characteristic dimension of catalytic wall microreactors. AIChE Journal. 2012 Sep 1;58(9):2785-97.

[23] Cao C, Zhang N, Chen X, Cheng Y. A comparative study of Rh and Ni coated microchannel reactor for steam methane reforming using CFD with detailed chemistry. Chemical Engineering Science. 2015 Dec 1;137:276-86.

[24] Maier L, Schädel B, Delgado KH, Tischer S, Deutschmann O. Steam reforming of methane over nickel: development of a multi-step surface reaction mechanism. Topics in Catalysis. 2011 Sep 1;54(13-15):845-58.

[25] Karakaya M, Keskin S, Avci AK. Parametric study of methane steam reforming to syngas in a catalytic microchannel reactor. Applied Catalysis A: General. 2012 Jan 16;411:114-22.

[26] Bosco M. Kinetic studies of the autothermal gasoline reforming for hydrogen production for fuel cell applications (Doctoral dissertation, Diss., Eidgenössische Technische Hochschule ETH Zürich, Nr. 16865, 2006).

[27] Krishna R, Wesselingh JA. The Maxwell-Stefan approach to mass transfer. Chemical Engineering Science. 1997 Mar 31;52(6):861-911.

[28] Bessler WG, Gewies S, Vogler M. A new framework for physically based modeling of solid oxide fuel cells. Electrochimica Acta. 2007 Dec 31;53(4):1782-800.

[29] Tjaden B, Cooper SJ, Brett DJ, Kramer D, Shearing PR. On the origin and application of the Bruggeman correlation for analysing transport phenomena in electrochemical systems. Current Opinion in Chemical Engineering. 2016 May 31;12:44-51.

[30] Skorokhod VV, Get'man OI, Zuev AE, Rakitin SP. Correlation between the particle size, pore size, and porous structure of sintered tungsten. Soviet powder metallurgy and metal ceramics. 1988 Dec 1;27(12):941-7.

[31] Whittenberger WA, inventor; Catacel Corp., assignee. Heat exchanger. United States patent US D560,276. 2008 Jan 22.

[32] Matweb, Resistalloy International Fecralloy^{TM} 135 Electrical Resistance Steel, Available at http://www.resistalloytrading.co.uk/pages/fecralloyproperties (Accessed May 2013).

[33] Todd B, Young JB. Thermodynamic and transport properties of gases for use in solid oxide fuel cell modelling. Journal of power Sources. 2002 Jul 20;110(1):186-200.

[34] Poling BE, Prausnitz JM, John Paul OC, Reid RC. The properties of gases and liquids. New York: McGraw-Hill; 2001.

[35] Munro M. Evaluated Material Properties for a sintered alpha-alumina. Journal of the American Ceramic Society. 1997 Aug 1;80(8):1919-28.

[36] Bird RB, Stewart WE, Lightfoot EN. Transport Phenomena. New York, USA: John Wiley & Sons, revised second ed. 2007.

[37] Welty JR, Wicks CE, Rorrer G, Wilson RE. Fundamentals of momentum, heat, and mass transfer. John Wiley & Sons; 2009 Oct 1.

[38] Lakhete P, Janardhanan VM. Modeling process intensified catalytic plate reactor for synthesis gas production. Chemical Engineering Science. 2014 May 3;110:13-9.

[39] L. Kunz, L. Maier, S. Tischer, O. Deutschmann, Modeling the Rate of Heterogeneous Reactions, in: Modeling and Simulation of Heterogeneous Catalytic Reactions, Wiley-VCH Verlag GmbH & Co. KGaA, 2012:113-148.

[40] Karadeniz H. Numerical Modeling of Stagnation Flows Over Porous Catalytic Surfaces. KIT Scientific Publishing; 2016 Apr 8.

[41] Deutschmann O, Schmidt LD. Modeling the partial oxidation of methane in a short-contact-time reactor. AIChE Journal. 1998 Nov 1;44(11):2465-77.

[42] Stutz MJ, Hotz N, Poulikakos D. Optimization of methane reforming in a microreactor—effects of catalyst loading and geometry. Chemical Engineering Science. 2006 Jun 30;61(12):4027-40.

Chapter 5

Methane steam reforming at low steam to carbon ratios over alumina and yttria-stabilized-zirconia supported nickel-spinel catalyst: Experimental study and optimization of microkinetic model

Published in Fuel Processing Technology, 168 (2017) 27-39

Abstract

An experimental work to acquire reaction kinetic data of methane steam reforming (MSR) to produce syngas was carried out over alumina and yttria-stabilized-zirconia (YSZ) supported nickel-spinel catalyst (Ni-spinel). With the aim of making MSR more energy efficient, the catalyst was tested at 1.25 and 1.50 steam to carbon (SC) ratios, slightly higher than the stoichiometric ratio of 1.0 but far less than normally considered 3.0. The experiments were conducted at isothermal plug-flow conditions and at near atmospheric pressure in a laboratory scale quartz reactor for five different space times (STP) between 55 ms and 277 ms at three different temperatures of 973 K, 1073 K, and 1123 K. Reaction kinetic data of MSR over Ni-spinel catalyst are presented in terms of methane conversion and products yield or selectivity. To simulate measured kinetic data in a 1D plug-flow reactor model, a surface microkinetic model of MSR over nickel-based catalyst was adopted from the literature and validated by optimizing the kinetic parameters of the most influential elementary reaction steps. A stepwise approach based on a partial equilibrium analysis and a local sensitivity analysis was implemented to scrutinize the most influential elementary reaction steps. With the adjustment of only 12 parameters out of 78, the optimized microkinetic model predicted the exit flow rates of chemical species accurately for the entire operating space. Adsorption of H_2O, desorption of H_2(s), and reaction pairs of surface dehydrogenation of CH_4(s) and CH_2(s) or formation of CH(s) were found to be the most influential reaction steps for the studied operating conditions. Surface coverages of H(s), CO(s) and H_2O(s) were increased in the case of optimized microkinetic model of the Ni-spinel catalyst compared to the original microkinetic model. Increased surface coverage of H_2O(s) in the case of optimized microkinetic model supports the experimental finding in the literature that the introduction of yttria to zirconia increases the activity of the oxygen pumping component.

5.1. Introduction

Syngas (H_2+ CO) plays a significant role in various catalytic processes such as Fisher-Tropsch synthesis, methanol synthesis, and hydroformylation. Hydrogen from syngas is widely used in the production of ammonia, hydrogenation processes in petroleum industry and as a clean energy carrier in fuel cells. In 2015, the global hydrogen production was amounted between 61 and 65 million metric tons and is expected to grow further [1]. Prediction suggested that hydrogen usage for sectors other than the petroleum and chemicals will grow to nearly 3.5 billion kg by 2030 [2]. Increased demand of energy due to population growth and the pressure of decarbonizing the earth's atmosphere demands the deployment of more clean energy sources such as fuel cell. It is expected that fuel cell will play a key role in combating against global pollution while transition from carbon economy to low-carbon economy takes place. Thus, the demand of fuel cells will continue to increase along with other clean energy sources. Consequently, the demand for hydrogen, the most important fuel for fuel cells and now emerging as a universal energy carrier with energy security, will also continue to rise. Though hydrogen is considered as the most abundant fuel in the universe, pure hydrogen exists in a very limited amount on our planet. Therefore, to fulfill the demand, various methods are developed to produce hydrogen from its primary sources. Two methods are commonly in use to produce hydrogen: (1) reformation and (2) electrolysis. Reformation involves hydrogen separation from water and carbon compounds such as methane; whereas, electrolysis separates hydrogen from oxygen in water [3]. Production of hydrogen by electrolysis is not a viable choice because it requires electricity to produce hydrogen.

To produce hydrogen via reformation, methane is the desired fuel of choice for the most fuel cells due to its lowest carbon content [4]. Also, recent discoveries of vast reserves of shale gas have strengthen the choice of methane as the desired fuel. Generally, the production of hydrogen rich syngas from methane is carried out by three major processes: (1) steam reforming (SR), (2) autothermal reforming (ATR) and (3) partial oxidation (POX). Among these three major processes, SR provides maximum hydrogen yield. Traditionally, the production of hydrogen is carried out over nickel (Ni) based catalysts via MSR with steam to carbon (SC) ratio of three or above to avoid carbon formation [5–10]. The SC ratio of three or above is very high compared to the reforming reaction stoichiometric ratio of one. High SC ratio dilutes the syngas content and is energetically unfavorable due to the requirements of more energy to produce excess steam in a boiler at the reactor upstream and to condense unreacted steam in a condenser at the reactor downstream. Noble metals such as rhodium and ruthenium-based catalysts are more resistant than the traditional nickel-based catalysts to carbon formation. However, due to excessive cost and limited availability of noble metals, it is more profitable to develop nickel-based catalysts which can be more resistant to carbon accumulation and can exhibit long term stability at low SC ratios [11].

It is well established fact that supports play an equally significant role in coordination with the active metal component in the performance of catalysts. Due to the chemical bonding between a support and an active metal, the reactivity of an active metal component can be affected significantly by the choice of supports [12]. Support in catalysts provides stability and high active surface area with its porous structure, which results in a longer stability and lifespan of catalysts. Research work has identified that carbon formation on nickel-based catalysts is sensitive to the acidic and the basic nature of the support. For example, support such as zirconium dioxide (ZrO_2) with strong Lewis basicity has shown a strong interaction with an active nickel which has eventually led to the formation of small nickel crystallites and suppress the carbon formation [13–17]. Support such as alumina increases acidic nature of catalysts [18]. The acidic support promotes cracking of methane and thus produce carbon [12]. Lahousse et al. [19] have reported that addition of support with basic nature to a catalyst plays a crucial role in catalyst performance by balancing Lewis acidity and hence the formation of carbon.

The use of stable support such as ZrO_2 increases thermal stability and oxygen vacancies in nickel-based catalysts [20]. Along with its strong Lewis basicity, ZrO_2 is also characterized by high chemical resistance and its stable crystalline structure at wide range of operating temperature. It is found that the stability range of ZrO_2 support can be further enhanced by introducing ions of lower valence than 4^+, such as Y^{3+}, La^{3+}, Mg^{2+} and Ca^{2+} into the ZrO_2 lattice [21]. The replacement of Zr^{4+} cation with lower positive charge leads to a negative overall charge that is compensated by an increased number of oxygen vacancies. These modifications in the ZrO_2 support can activate the gaseous oxygen (O^{2-} or O^-) pumping species [22], for example, an adsorption of H_2O (steam in MSR). Bellido and Assaf [23] have carried out a comparative study of methane dry reforming over 5% Ni catalyst supported on ZrO_2 and 5% Ni catalyst supported on ZrO_2+Y_2O_3. They have reported that modification of ZrO_2 support with the addition of Y_2O_3 has increased the specific surface area and surface oxygen vacancies. Surface oxygen vacancies could provide the active sites required for obtaining more energetic oxygen radicals and thus reduce the rate of carbon formation [23]. The Ni-spinel catalyst supported by YSZ and alumina employed in this study has been developed by Fauteux- Lefebvre et al. [24] at the Université de Sherbrooke, Québec, Canada. The Ni-spinel catalyst has shown promising potential to implement for diesel steam reforming [25], methane dry reforming [26] and naphthalene reforming [27]. The use of such catalyst in reformers provides flexibility in selecting wide range of fuels that are available at various locations to generate hydrogen and hence can further increase the usage of fuel cells.

To evaluate the performance of catalytic reactor designs, quantitative and sufficiently accurate information about the catalytic reaction rates are required based on the underlying physical and chemical phenomena. With increasing computer power, it is now possible to use first principle approach of multi-step microkinetic model to understand the catalytic reactions in terms of elementary steps and their relationships with each other [28]. Chemical reaction rates can also be evaluated by applying a global kinetic approach [5,7]. In the global kinetic approach, kinetic parameters are determined based on experiments carried out at specific operating conditions and with prior knowledge of a rate determining step (RDS) [29]. Hence, the applicability of the kinetic parameters obtained via global kinetic approach is valid within those conditions only. In reality, all chemical reactions proceed via many elementary reaction steps, e.g. MSR involves: (1) adsorption of methane (CH_4) and steam (H_2O) at the catalyst surface from the gas-phase, (2) surface reactions of the adsorbed species; resulting surface species may participate further into intermediate surface reactions and (3) desorption of final products hydrogen (H_2) and carbon monoxide (CO) from the catalyst surface to the gas-phase. Therefore, all chemical reactions can be studied by elementary reaction steps. MSR involves many intermediate reaction steps, where multiple reactions can be in equilibrium at the same time and hence it is possible that several paths to the desired product formation can exist [30]. Existence of several possible paths to the product formation makes it difficult to decide a single rate determining step (RDS) even for catalysts prepared using the same active metal component. For the development of reaction rate expressions using global kinetic approach, a knowledge of RDS is prerequisite. Hence, different global rate expressions are required to predict the performance of MSR over catalysts that are prepared using the same active metal component. Whereas, microkinetic approach does not require priori knowledge of the RDS and hence it may be implemented to predict the performance of MSR carried out over different catalysts that are prepared using the same active metal component after optimizing the kinetic parameters of the most sensitive reaction steps.

The objectives of this work were to obtain effective kinetic data of methane steam reforming (MSR) for low SC ratios at different temperatures over the Ni-spinel catalyst and to optimize the kinetic parameters of a microkinetic model. To simplify the kinetic model development stage and optimization procedure, a surface microkinetic model of MSR over a nickel-alumina (Ni/Al_2O_3) catalyst, developed by Maier et al. [31] was adopted. The surface microkinetic model of Maier et al. [31] was validated against the experimental data of MSR over Ni-spinel catalyst by optimizing the kinetic parameters of the most influential elementary reaction steps that were scrutinized based on a partial equilibrium analysis (PEA) and a local sensitivity analysis (LSA).

5.2. Experimental

5.2.1. Ni-spinel catalyst

The Ni-spinel catalyst for which the reaction kinetic data collected in this work was developed and supplied by Fauteux-Lefebvre et al. [24,25] from the Université de Sherbrooke, Québec, Canada. Fauteux- Lefebvre et al. [25] prepared the catalyst by the wet impregnation method. Al_2O_3 (50%) and YSZ (50%) (Y_2O_3(7%) + ZrO_2) support was prepared by mixing the two powders mechanically. Mean powder size of Al_2O_3 was 40 µm and YSZ powder size distribution had an upper limit of 20 µm. The Al_2O_3 and YSZ powder was impregnated with a hexahydrate nickel nitrate ($Ni(NO_3)_2{\cdot}6H_2O$) aqueous solution (for 5% weight nickel (Ni) load in the final formulation) [24]. The mixture was stirred for 90 min at room temperature followed by heating for 60 min at 368.15 K to vaporize the water. The resulting impregnated powder was dried overnight at 378 K. The impregnated powder was crushed comminuted and calcined at 1173.15 K for 6 h to form the Ni-spinel ($NiAl_2O_4$). The final objective of this work in future is to apply a thin coating of the Ni-spinel catalyst on the surface of a fecralloy plate to study the performance of a catalytic plate reactor (CPR) with different coating configurations. It was determined that the addition of more alumina can enhance the adhesion property of this catalyst on the surface of the plate. Hence, the Ni-spinel catalyst was further calcined at 773.15 K for 120 min after mechanical mixing with 40% additional alumina. Thus, the final compositions of the Ni-spinel catalyst on average were 3.6% nickel, 62.5% alumina, and 33.9% YSZ (7% Y_2O_3).

The present study only focuses on the experimental work of collecting effective kinetic data for optimizing the microkinetic parameters of the most sensitive elementary reaction steps. More detailed information as well as characteristics of the Ni-spinel catalyst are presented elsewhere [24–27,32].

5.2.2. Quartz reactor and catalyst bed

Measurements of the effective kinetic data for MSR over Ni-spinel catalyst were carried out in a fixed-bed down-flow quartz reactor (10.92 mm ID and 610 mm length). The powdered Ni-spinel catalyst was first pelletized using a hydraulic press and a pellet die by applying a constant pressure of 4000 psi for 600 s. These pellets were then crushed and sieved using 40/45 mesh screens (425 µm)/(355 µm). A 0.0752 g sample of the Ni-spinel catalyst with mean particle size of 390 µm, diluted with 0.752 g quartz particles of the same size, was loaded at the center of the quartz reactor. To obtain uniform radial dispersion and to avoid any local cavities, both catalyst and quartz particles were loaded carefully into the reactor using a snowstorm like filling funnel. The radial dispersion action in a funnel can reduce the particles aggregation at the center of the bed and as a result contribute to the uniformity of the bed structure [33]. The measured bulk density of the active bed (catalyst + quartz) was 1021 $kg{\cdot}m^{-3}$, whereas bulk density of the Ni-spinel catalyst was 1222.5 $kg{\cdot}m^{-3}$. To satisfy the plug-flow conditions, two inert beds consisting of the same size (40/45 mesh) quartz particles were placed before and after the active catalyst bed with 32.5 mm and 20.5 mm heights respectively. The entire bed (inert beds+ active catalyst bed) with the total height (or length) of 61.7 mm was supported by the quartz wool plug at the downstream end. To verify whether the prepared bed satisfied the plug-flow conditions or not, Froment & Bischoff [34] and Rase & Holmes [35] reported that axial mixing and concentration gradients in radial directions can be avoided if an internal diameter (D) of a reactor and a length (L) of a catalyst bed are ten times and fifty times the particle diameter (d_p) respectively. Also, the pressure drop across the bed should be less than 5% of inlet pressure to satisfy the plug-flow criteria [36]. In this study, the ratios of D/d_p= 28 and L/d_p ≈158 indicated that axial mixing and concentration gradients in radial directions were negligible. Also, the pressure drops estimated using the Ergun equation [37], across the bed were less than 5% for all studied inlet flow rates. Hence, the chosen design of the bed had satisfied all required conditions of the plug-flow reactor.

5.2.3. Reaction test procedure

A schematic diagram of the MSR experimental set-up used in this work is presented in Fig. 5.1. As illustrated in the figure, water was injected into the vaporizer at the desired flow rate using a precision pump manufactured by the Parker Autoclave Engineer Research. Temperature of the vaporizer was set at 473.15 K to convert liquid water into steam. Methane (99.9%) and nitrogen (99.9%) were supplied from their respective gas-cylinders at the controlled flow rates via mass-flow controllers (Brooks 5850E) and passed through the vaporizer where they were mixed with the water vapor at 473.15 K. Feed compositions for SC ratio of 1.50 were 10% CH_4, 15% H_2O and 75% N_2 and for SC ratio of 1.25 were 12% CH_4, 15% H_2O and 73% N_2. The vaporizer was connected to the quartz reactor inlet (top) via the heated transfer line maintained at 573.15

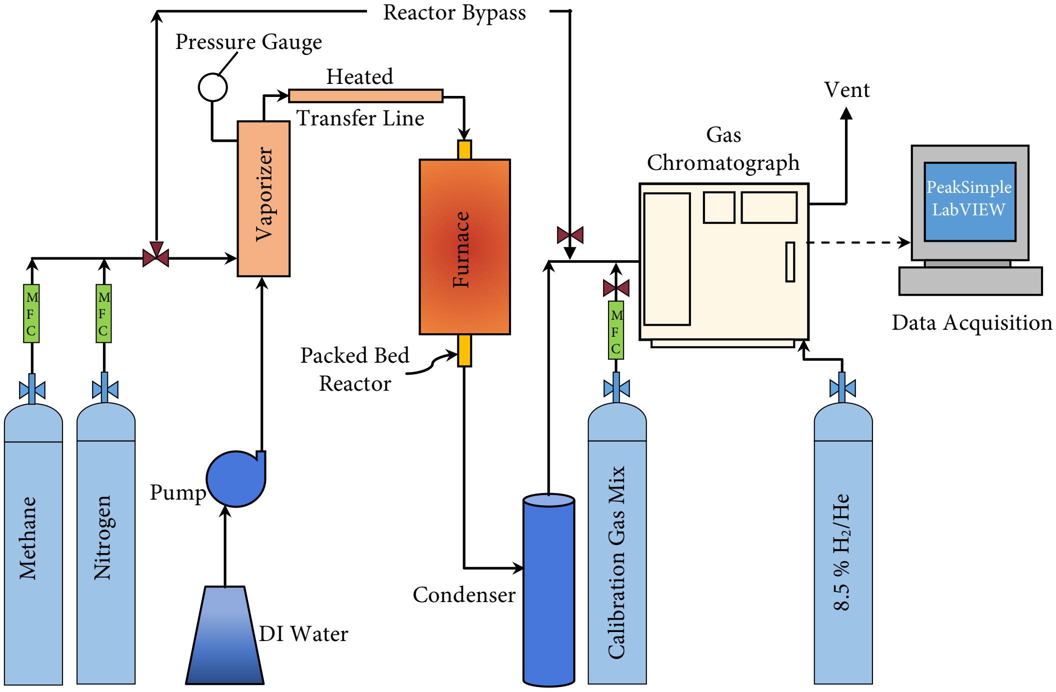

Fig. 5.1. *A schematic diagram of MSR experimental set-up.*

K to keep the water in the vapor state. Both mass-flow controllers for CH_4 and N_2 gases were calibrated using the soap bubble meter. The average error associated with the CH4 mass-flow controller was 1.98% and with the N_2 mass-flow controller was 0.73%. A pressure transducer (Omega PX302-050GV) with 0.25% accuracy was installed between the vaporizer and the quartz reactor to record any changes in pressure. The average absolute inlet pressure was 17.50 (± 0.05) psi. Operational settings for the mass-flow controllers and temperature settings for the vaporizer and the transfer line were controlled by an in-house program implemented in LabVIEW system design software (National Instruments™) installed on a PC with the windows-7 operating system. The LabVIEW system software was also utilized to store and record all flow rates, pressure and temperature data at a specified time interval. The temperature control of the reaction was ensured via an electrical furnace supplied with three different heating zones, each operated by a universal reactor controller (Parker Autoclave Engineer Research). The temperature of the catalyst bed was measured with a K-type thermocouple (with ± 2.2 °C uncertainty) placed at the center of the active catalyst bed. The gaseous products were analyzed by an online gas chromatograph (GC) (Shimadzu 17A) installed with a Supelco Carboxen 1000 column. Unreacted water at the reactor downstream was trapped in a condenser placed inside a refrigerated bath (Neslab RTE-17) maintained at 273.15 K before the reformate gas was sent to the GC. The GC was calibrated using the known composition of a standard mixture of gases: H_2 (30% by mole), CO (20%), CO_2 (20%), CH_4 (5%), N_2 (20%), C_2H_4 (2%), C_2H_6 (2%), and C_3H_8 (1%) and by pure CH_4, H_2 and N_2. The composition analysis of the gas-mixture was done by the PeakSimple software installed on the PC. Uncertainties associated with respect to H_2, CH_4, CO_2, N_2 and CO compositions were 1.38%, 1.16%, 0.90%, 0.88%, and 0.84% respectively.

After preparing the catalyst bed mentioned in the previous section, catalyst was reduced at 1073.15 K using 8.5% H_2/Ar gas-mixture at inlet flow rate of 25 ml/min for 30 min. For the nickel spinel formation, temperature of 1073.15 K or above is required for the complete reduction [38,39]. After reducing the Ni-spinel catalyst at 1073.15 K, the reactor temperature was adjusted to the desired reaction temperature and only upon reaching the set point temperature, the gas-mixture of steam, nitrogen and methane was introduced into the reactor. For each steam-to-carbon ratio (1.25 and 1.50) and for each temperature (973.15 K, 1073.15 K and 1123.15 K), the flow rate was increased incrementally, and compositions data were collected. Flow rate of the exit reformate stream was constantly monitored by a digital flow meter to ensure steady state condition for each run. The total reformate flow rate was determined based on the flow rate of inert gas N_2 and its output composition. The output composition for each chemical species was estimated based on the average of three GC readings. All experimental runs were performed within 120 h without noticing visible carbon formation. Error associated with the reproducibility of exit composition was estimated based on the standard deviations and mean values for each chemical species. For dry gas mixture consisting of CH_4, CO, H_2 and CO_2 chemical species, the reproducibility accuracy on average was within 3.37%, 2.49%, 1.74% and 4.36% respectively. The carbon balance on average was within± 3%; determined by difference between the conversion of methane calculated by considering inlet and outlet CH_4 flow rates (Eq. (1)) and the conversion of methane calculated by considering outlet flow rates of CO and CO_2 (Eq. (2)). Periodically a baseline run (at SC= 1.5, T= 1073.15 K, GHSV = 39,256.5 h^{-1}) was carried out to confirm any change in catalyst activity. To estimate the propagation of errors, a simpler approach of added in quadrature [40] was adopted. Experimental data are listed in Appendix C. The CH_4 conversion (X_{CH4}), H_2 yield (Y_{H2}) and CO selectivity (S_{CO}) were calculated by applying the following equations:

CH_4 conversion (X_{CH4}):

$$\mathrm{X}_{CH_4} = 100 \times \left[\frac{N_{CH_{4,in}} - N_{CH_{4,out}}}{N_{CH_{4,in}}}\right] \tag{5.1}$$

$$\mathrm{X}_{CH_4} = 100 \times \left[\frac{N_{CO_{out}} + N_{CO_{2,out}}}{N_{CH_{4,in}}}\right] \tag{5.2}$$

H_2 yield (Y_{H2}):

$$\mathrm{Y}_{H_2} = 100 \times \left[\frac{1}{4}\frac{N_{H_{2,out}}}{N_{CH_{4,in}}}\right] \tag{5.3}$$

CO selectivity (S_{CO}):

$$\mathrm{S}_{CO} = 100 \times \left[\frac{N_{CO,out}}{N_{CO_{out}} + N_{CO_{2,out}}}\right] \tag{5.4}$$

5.3. Results and discussion

In this study, reaction kinetic data of MSR over Ni-spinel catalyst were collected experimentally at three different temperatures (973.15 K, 1073.15 K, and 1123.15 K) and two SC ratios (1.25 and 1.50) for five different inlet gas hourly space velocities (GHSVs) between 13,000 h^{-1} to 65,000 h^{-1} or space times between 277 ms and 55 ms. GHSV was calculated at the standard condition of 273.15 K and 1 atm. It is defined as the ratio of the volume flow of feed to the catalyst volume. The first two sections discuss the experimental data in terms of X_{CH4}, S_{CO}, Y_{H2}, and H_2/CO ratio as a function of the reaction temperature and space time. The third section discuss the optimization procedure of microkinetic parameters and stepwise approach of selecting the most influential reaction steps based on a PEA and a LSA. The third section further discusses the evolution of surface species in the optimized microkinetic model in comparison to the original microkinetic model. The fourth section shows the comparison between the predicted data obtained by the optimized microkinetic model and the experimental data. The fifth or concluding section discusses the thermodynamic consistency of the optimized microkinetic model compared to the original microkinetic model at equilibrium condition.

5.3.1. Reaction temperature

Fig. 5.2 illustrates the effect of temperature on X_{CH4} (Fig. 5.2(A), (B)), S_{CO} (Fig. 5.2(C), (D)) and H_2/CO ratio (Fig. 5.2(E), (F)) at three different GHSVs (13,649.7 h^{-1}, 39,256.5 h^{-1}, and 64,833 h^{-1}) for SC ratios of 1.50 and 1.25. Fig. 5.2 also illustrates equilibrium X_{CH4}, S_{CO} and H_2/CO ratio for both 1.50 and 1.25 SC ratios. It is shown by comparing equilibrium X_{CH4} and experimental X_{CH4} in Fig. 5.2(A) and (B) that all experimentally measured data for both SC ratios were below equilibrium X_{CH4}, so that any noticeable catalyst deactivation can be readily identified. As mentioned previously, all experimental runs were conducted without noticing visible carbon formation. Fig. 5.2(A) and (B) show that experimental X_{CH4} reached 94.4% and 95.6% at the lowest studied GHSVs of 13,649 h^{-1} for SC ratio of 1.50 and 13,266 h^{-1} for SC ratio of 1.25 respectively, for the highest studied temperature (1123.15 K). Due to the endothermic nature of MSR, lower X_{CH4} of 20.8% and 17.1% were observed at the lowest studied temperature (973.15 K) for the highest studied GHSVs of 64,833 h^{-1} for SC = 1.50 and 58,370.9 h^{-1} for SC= 1.25 respectively. Due to increased X_{CH4} with increase in temperature, S_{CO} (Fig. 5.2(C) and (D)) was also increased for both SC ratios, because at elevated temperatures reverse water-gas shift favors CO production due to the Le Chatelier's principle [31]. Thus, highest S_{CO} of 88.3% and 92.8% were obtained for SC ratios of 1.50 and 1.25 respectively, at the highest studied

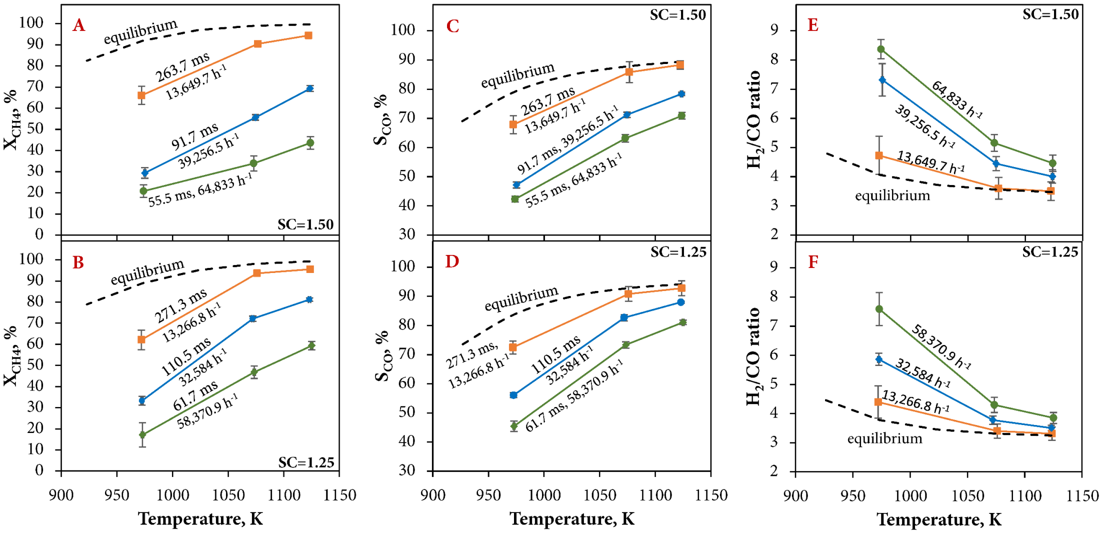

Fig. 5.2. *Experimentally measured methane conversion (X_{CH4}), CO selectivity (S_{CO}) and H_2/CO ratio as a function of temperature for SC ratios of 1.50 and 1.25 at different gas hourly space velocities (GHSVs, h^{-1}).*

temperature (1123.15 K) for the lowest studied GHSVs. And the lowest S_{CO} of 42.3% and 45.4% were obtained for SC ratios of 1.50 and 1.25 respectively, at the lowest studied temperature (973.15 K) for the highest studied GHSVs. Due to an increase in S_{CO} with increase in temperature, it was expected that H_2/CO ratio as illustrated in Fig. 5.2(E) and (F) decreased with increase in temperature. High H_2/CO ratio of 8.37 for SC = 1.50 and 7.59 for SC= 1.25 were measured for the highest studied GHSV at 973.15 K, whereas low H_2/CO ratios of 3.5 for SC = 1.50 and 3.31 for SC =1.25 were measured for the lowest studied GHSV at 1123.15 K. H_2/CO ratio increased when SC ratio was increased from 1.25 to 1.50 for the equivalent GHSV. Increase in steam content increased the production of hydrogen and hence resulted into higher H_2/CO ratio at 1.50 compared to 1.25 SC ratio.

5.3.2. Space time

Fig. 5.3(A) and (B) illustrates the effect of space time on X_{CH4} at three different temperatures (973.15 K, 1073.15 K and 1123.15 K) for SC ratios of 1.50 and 1.25 respectively. As expected X_{CH4} decreased with decrease in space time for all studied temperatures and for both SC ratios. This was attributed to the short contact times at low space times that limit the extent to which the reforming reaction occurs on the catalyst surface. The lower X_{CH4} was more apparent for low space time at low temperature (973.15 K). Due to decreased X_{CH4} with decrease in space time and with decrease in temperature, Y_{H2} also decreased with decrease in space time and temperature as illustrated in Fig. 5.3(C) and (D). Maximum Y_{H2} of 67% and 68% was obtained for SC ratios of 1.50 and 1.25 respectively at the highest studied temperature (1123.15 K) for the highest studied space time (263 ms). Fig. 5.3(E) and (F) illustrates H_2/CO ratio as a function of space time at the three studied temperatures for SC ratios of 1.50 and 1.25 respectively. Figures show that high H_2/CO ratios were measured at the lowest studied space time for both SC ratios at the lowest studied temperature of 973.15 K, whereas low H_2/CO ratios were recorded at elevated temperature for high space times. Maximum H_2/CO ratio of 8.37 was measured at 973.15 K for SC = 1.5 and 7.59 for SC= 1.25 as illustrated in Fig. 5.3(E) and (F) respectively.

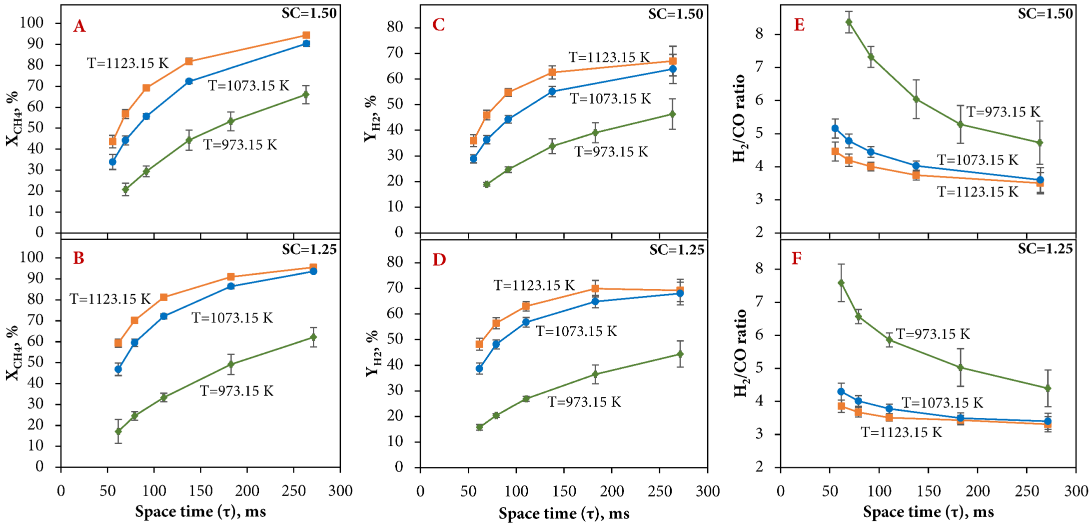

Fig. 5.3. *Experimentally measured X_{CH4}, hydrogen yield (Y_{H2}) and H_2/CO ratio as a function of space time for SC ratios of 1.50 and 1.25 at different temperatures.*

5.3.3. Optimization of the microkinetic parameters

The surface microkinetic model developed by Maier et al. [31] for MSR over a Ni/Al_2O_3 catalyst was adopted to simulate the experimentally measured kinetic data of MSR over Ni-spinel catalyst under plug-flow isothermal conditions at 17.5 psi. The model was validated against the experimental data by optimizing the kinetic parameters of the most influential or sensitive reaction steps. Table 3.2 illustrates the reaction steps of the microkinetic model with the corresponding kinetic parameters reported by Maier et al. [31]. The model consists of 42 elementary reactions among 7 gas-phase species and 13 surface species including vacant sites of adsorbent nickel. Sticking coefficients were applied for the adsorption of H_2, O_2, CH_4, H_2O, CO_2, and CO in reactions r_1 to r_6 respectively. The microkinetic model is comprised of partial and total oxidation reactions, water-gas shift reactions, carbon formation reactions, and methanation reactions [31].

Microkinetic modeling employs mean-field approximation approach, which neglects the effect of lateral interactions of the adsorbates and non-uniformity of the catalyst surface [41]. In the mean-field approximation, every adsorbates and adsorbent are defined as surface species. The coverage (θ) of surface species i is then defined as:

$$\theta_i = \frac{\text{site occupancy number} \times \text{concentration of adsorbed species } i}{\text{site density}} \tag{5.5}$$

It is assumed that adsorbates are randomly distributed over the catalyst surface and the coverage of surface species depends on macroscopic position in the reactor and time, but they are averaged over microscopic local fluctuations. Therefore, the surface is assumed to be uniform [41]. Under the mean-field approximation, rate expressions for the gas-phase species and the surface species are defined as:

$$s_i = \sum_{r=1}^{\mathrm{R}} \mathrm{v}_{i\mathrm{r}} k_\mathrm{r} \prod_{j=1}^{N_g+N_s} c_j^{\mathrm{v}'_{j\mathrm{r}}} \tag{5.6}$$

where, s_i is the overall or net reaction rate for gas-phase or surface species i, r is the considered reaction and R is the total number of reactions, c_j is the concentration of j species, which is given in mol/m^2 for the adsorbed species and mol/m^3 for gaseous species [42]. The concentration c_j of an adsorbed species equals the surface coverage (θ_j) multiplied by the surface site density (Γ), k_r is the reaction rate constant, v_{ir} is the difference of the right side (v_{ir}'') and left side (v_{ir}') stoichiometric coefficients of species i in reaction r [42]. N_g and N_s represent the total number of gas-phase and surface species respectively. Because of the binding states of the adsorption of all species vary with surface coverages, the reaction rate coefficients are determined using the modified Arrhenius expression [41]:

$$k_\mathrm{r} = A_\mathrm{r} T^{\beta_\mathrm{r}} exp\left(-\frac{E_{a_\mathrm{r}}}{\mathrm{R}_g T}\right) \theta_i^{\mu_{i\mathrm{r}}} exp\left[\frac{\varepsilon_{i\mathrm{r}}\theta_i}{\mathrm{R}_g T}\right] \tag{5.7}$$

where, E_{a_r} is the activation energy of the reaction r and θ_i is the fraction of the surface coverage of species i. $\mu_{i\mathrm{r}}$ and $\varepsilon_{i\mathrm{r}}$ describe the dependence of the rate constants on the surface coverage of species i. For adsorption reactions, sticking coefficients were used, which can be converted to conventional rate constants [31] as:

$$k_{f,r}^{ads} = \frac{S_i^0}{\Gamma^\tau}\sqrt{\frac{\mathrm{R}_g T}{2\pi M_i}} \tag{5.8}$$

where, τ is the number of occupied adsorption sites of species i, S_i^0 is the initial (uncovered surface) sticking coefficient, Γ is the site density. The value of Γ is 2.6× 10^{-5} mol/m^2, which was calculated by assuming a site area of 6.4 × 10^{-2} nm^2 as observed for nickel [31]. Surface coverage of the i^{th} species is calculated from the relationship between its concentration and site occupancy number, and surface site density [41]. Thus, the time variation of the surface coverage of the i^{th} species is given as:

$$\frac{\partial\theta_i}{\partial t} = \frac{c_i\sigma_i}{\Gamma}, \qquad \text{where} \sum_{i=1}^{N_s}\theta_i = 1 \tag{5.9}$$

where, σ_i represents the number of surface sites that are occupied by species i. It should be noted that the values of the kinetic parameters reported by Maier et al. [31] in their microkinetic model are obtained from various sources. Examples of these sources are surface spectroscopy study, isotope-trace study, temperature programmed desorption study, density functional theory calculations, previously published literature and by fitting experimental data. Hence, the assumptions made by Maier et al. [31] in deriving their microkinetic model of MSR over Ni-alumina catalyst are equally applicable in the present study.

To optimize the effective kinetic parameters that can represent experimental data of MSR over Ni-spinel catalyst accurately, it was important to first identify the most influential or sensitive reaction steps out of the 42 reactions presented in Table 3.2. Salciccioli et al. [43] have reported that even a minor change in an activation energy can make a notable change in thermodynamic consistency of microkinetic models, which can result into considerable error in predicting the temperature profile of a chemical reactor. Thus, in this work only pre-exponential factors of the most influential reaction pairs were optimized to avoid thermodynamic inconsistency. Even though after eliminating the requirement of optimizing activation energy values, 42 parameters were left to be selected for the optimization. A blind approach to optimize all 42 parameters at once would be unproductive, because even a most powerful optimization solver will not be able to optimize these many parameters and optimizing 42 parameters at once would be computationally expensive and statistically insignificant. So, to identify the most influential reaction steps, a partial equilibrium analysis (PEA) and a local sensitivity analysis (LSA) were carried out.

5.3.3.1. Partial equilibrium analysis (PEA)

PEA identifies whether forward and reverse (backward) reactions are in equilibrium or far from equilibrium [43]. The PEA can also be applied to reduce the number of reaction steps from a multi-step microkinetic model [44]. A straightforward way of identifying whether the forward and backward reaction rates are in equilibrium or not is by calculating a partial equilibrium (PE) ratio ($\emptyset$) defined as:

$$\emptyset = \frac{\mathrm{r}_f}{\mathrm{r}_f + \mathrm{r}_b} \tag{5.10}$$

where, r_f is the forward rate of reaction and r_b is the backward rate of reaction. A value of $\emptyset$ = 0.5 indicates that reaction is in complete equilibrium. A value of $\emptyset$ close to 1 or 0 indicates that the forward or backward reaction dominates. A value of $\emptyset$ close to 0.45 or 0.55 indicates that the reaction is in partial equilibrium [45].

Fig. 5.4(A) and (B) depicts the calculated $\emptyset$ (Eq. (10)) for SC ratios of 1.25 and 1.50 respectively, for the three studied temperatures (973.15 K, 1073.15 K, and 1123.15 K). To determine $\emptyset$, kinetic parameters reported by Maier et al. [31] were applied to steady-state isothermal plug-flow model solved by using COMSOL^{TM} for inlet GHSV of 38,852.8 h^{-1} (STP). Results show that all adsorption (r_1 to r_6) and desorption (r_7 to r_{12}) reactions were found to be in complete equilibrium at all three temperatures for both SC ratios. Fig. 5.4(A) and (B) indicates that surface reactions r_{13} to r_{18} and r_{21} to r_{24} were also in complete equilibrium. Reaction pairs (r_{19}, r_{20}) and (r_{25}, r_{26}) were found to be far away from equilibrium followed by CH_4 dissociation

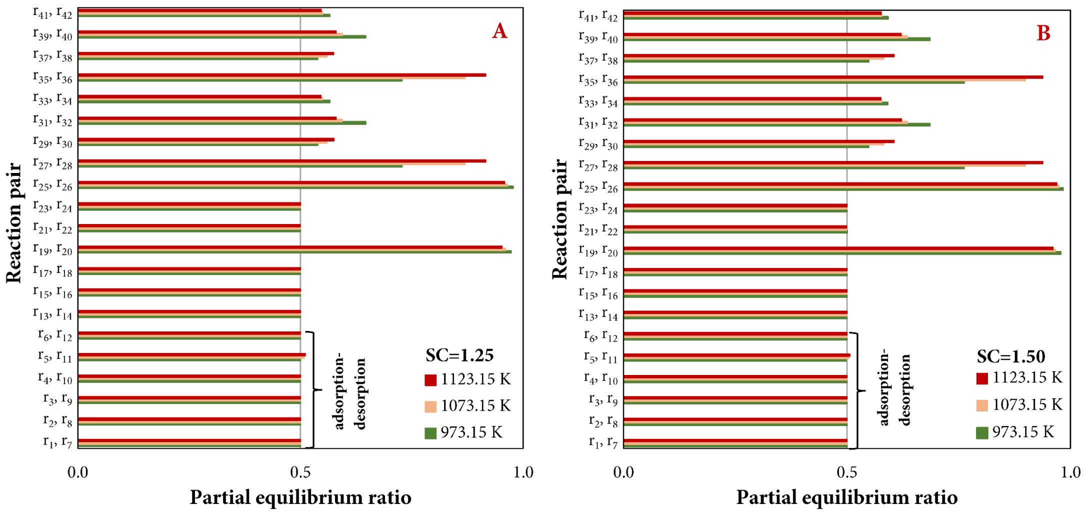

Fig. 5.4. *Partial equilibrium ratios determined for SC ratios of (A) 1.25 and (B) 1.50 at 973.15 K, 1073.15 K, and 1123.15 K.*

via (r_{27} to r_{34}) and (r_{35} to r_{42}). Experimental studies [8,31,46] on methane activation in MSR on nickel surface have reported that dissociation of methane mainly takes place by the dehydrogenation route (r_{27} to r_{34}).

The surface carbon C(s) formed via methane dehydrogenation (r_{27} to r_{34}) was then further oxidized to CO(s) by O(s) via reaction r_{19}, which either desorbed via reaction r_{12} or further oxidized to form CO_2(s) via reaction r_{21}, which eventually desorbed as CO_2 via reaction r_{11}. The PEA in Fig. 5.4 suggests that among dehydrogenation reaction steps, (r_{27}, r_{28}) and (r_{31}, r_{32}) were far from equilibrium with $\emptyset$ value more than 0.70 at all three temperatures, whereas $\emptyset$ values for reaction pairs (r_{29}, r_{30}) and (r_{33}, r_{34}) were less than 0.60 and thus considered in partial equilibrium. Using density functional theory (DFT) calculation, Blaylock et al. [47] found that surface CH(s) forming in reaction r_{31} is the most important carbon-containing reaction intermediate. Their finding also confirmed Rostrup-Nielsen's finding of CH(s) as the most important intermediate in MSR over nickel-based catalyst [48]. Furthermore, the PEA also identified (see Fig. 5.4) that among methane dissociation steps (r_{35} to r_{42}) by O(s), (r_{35}, r_{36}) and (r_{39}, r_{40}) reaction pairs were far from equilibrium than the remaining steps and thus kinetic parameters of these two reaction pairs considered influential. From the PEA, it was established that among 42 reaction steps, six reaction pairs (r_{19}, r_{20}), (r_{25}, r_{26}), (r_{27}, r_{28}), (r_{31}, r_{32}), (r_{35}, r_{36}) and (r_{39}, r_{40}) were in nonequilibrium and thus, can be consider for the parameter optimization process. However, it was found that among these possible influential reaction pairs, a few reaction pairs were eliminated based on the sensitivity analysis discussed in the next section. The PEA also indicated that adsorption–desorption reactions (r_1 to r_{12}) and ten surface reactions (r_{13} to r_{18} and r_{21} to r_{24}) were in complete equilibrium ($\emptyset = 0.5$) as illustrated in Fig. 5.4(A) and (B). Hence, to identify the most influential equilibrium reactions and to check the most sensitive nonequilibrium reaction steps identified in PEA, a local sensitivity analysis was performed on outlet mole fractions of CH_4, H_2, CO and CO_2.

5.3.3.2. Local sensitivity analysis (LSA)

LSA was performed on outlet mole fractions of CH_4, H_2, CO and CO_2 by perturbing a pre-exponential factor of an elementary reaction step by 5% one at a time while holding the others fixed. The LSA was carried out by solving steady-state isothermal plug-flow model using COMSOL^{TM} for inlet GHSV of 38,852.8 h^{-1} (STP) for SC ratio of 1.50 at 973.15 K and 1073.15 K. Fig. 5.5(A), (B), (C), and (D) compares the normalized sensitivity coefficients for the outlet mole fractions of CH_4, H_2, CO and CO_2 respectively between the two temperatures 973.15 K and 1073.15 K for SC ratio of 1.50. Same influential reactions and similar values of normalized sensitivity coefficients were also observed for the SC ratio of 1.25. It can be seen from Fig. 5.5 that all chemical species (CH_4, H_2, CO, CO_2) were sensitive to the same reaction steps. It should be noted that in Table 3.2, reactions r_1 to r_6 represent the adsorption reactions and r_7 to r_{12} represent the desorption reactions, whereas r_{13} to r_{42} represent the surface reactions. Normalized sensitivity coefficients of CH_4 mole fraction in Fig. 5.5(A) indicated that CH_4 adsorption-desorption reaction pair (r_3, r_9) was highly sensitive among all adsorption-desorption reactions followed by H_2 adsorption-desorption (r_1, r_7), CO adsorption-desorption (r_6, r_{12}), H_2O adsorption-desorption (r_4, r_{10}) and CO_2 adsorption-desorption (r_5, r_{11}). For H_2 mole fraction also the most sensitive reaction pair was (r_3, r_9) followed by H_2 adsorption-desorption (r_1, r_7), H_2O adsorption-desorption (r_4, r_{10}), CO_2 adsorption-desorption (r_5, r_{11}) and CO adsorption-desorption (r_6, r_{12}). For CO, sensitive adsorption-desorption reaction pairs in descending order were: (r_3, r_9), (r_6, r_{12}), (r_5, r_{11}), (r_4, r_{10}) and (r_1, r_7) and for CO_2, sensitive adsorption-desorption reaction pairs in descending order were: (r_6, r_{12}), (r_5, r_{11}), (r_4, r_{10}), (r_1, r_7) and (r_3, r_9). Interestingly, for CH_4, H_2 and

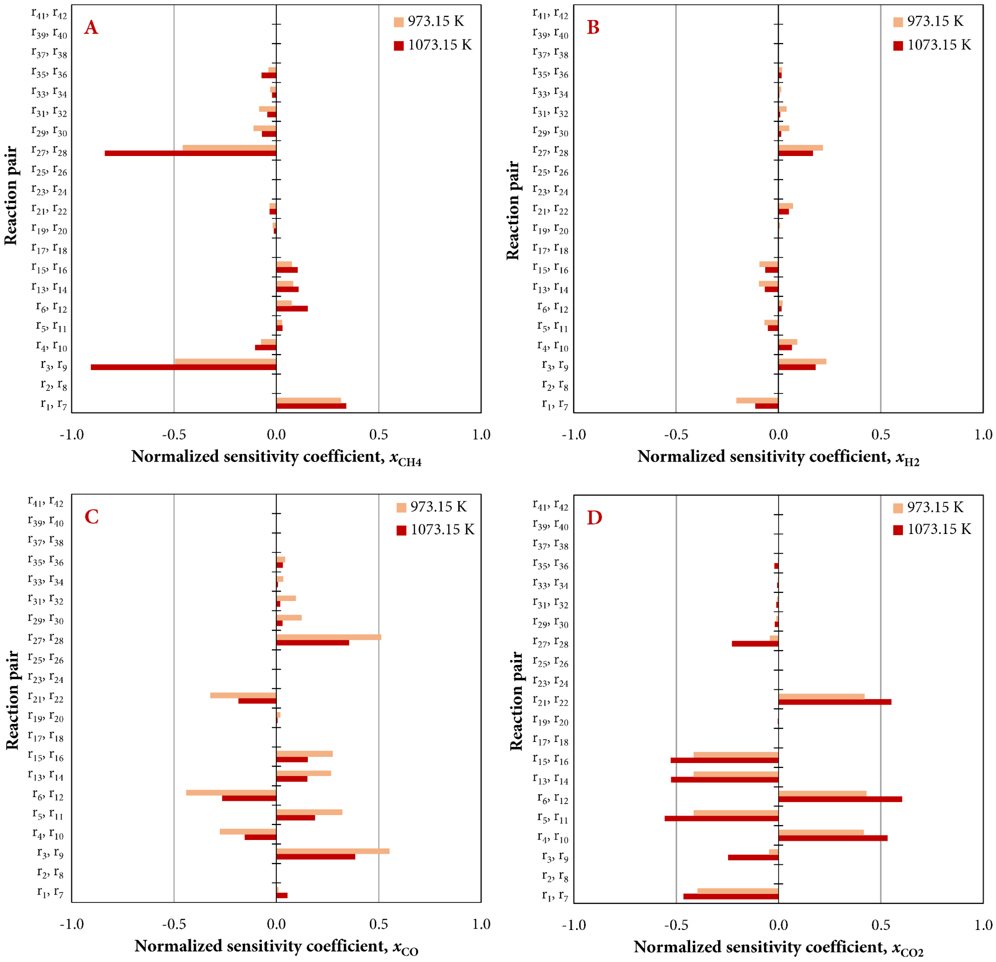

Fig. 5.5. *Comparison of the normalized sensitivity coefficients for the outlet mole fractions of (A) CH_4, (B) H_2, (C) CO and (D) CO_2 between temperatures 973.15 K and 1073.15 K for SC ratio of 1.50.*

CO the most sensitive adsorption-desorption reaction pair was (r_3, r_9), whereas for CO_2, it was CO adsorption-desorption (r_6, r_{12}). It indicated that outlet mole fractions of CO_2 influenced by the rate of production or consumption of CO. In the case of surface reactions (r_{13} to r_{42}), the sensitive surface reaction pairs for all chemical species (CH_4, H_2, CO, CO_2) were (r_{13}, r_{14}), (r_{15}, r_{16}), (r_{21}, r_{22}), (r_{27}, r_{28}), (r_{29}, r_{30}), (r_{31}, r_{32}), (r_{33}, r_{34}), and (r_{35}, r_{36}). Among these reaction pairs, (r_{27}, r_{28}), (r_{29}, r_{30}), (r_{31}, r_{32}), (r_{33}, r_{34}), and (r_{35}, r_{36}) are associated with CH_4 dissociation into carbon species (CH_3(s), CH_2(s), CH(s), C(s)) (see Table 3.2). Based on the PEA in the previous section and experimental studies in the literature [8,31,46] suggested that dissociation of CH_4(s) via (r_{27}, r_{28}) and formation of CH(s) or dissociation of CH_2(s) via (r_{31}, r_{32}) are the most important steps in MSR. It can also be seen from Fig. 5.5(A) and (B) that CH_4 dissociation via step r_{27} was highly influential compared to the dissociation by O(s) in step r_{35}. Interestingly, among nonequilibrium reaction pairs found in the PEA, three reaction pairs (r_{19}, r_{20}), (r_{25}, r_{26}) and (r_{39}, r_{40}) were found to be least sensitive to any outlet compositions in the LSA. Hence, among six nonequilibrium reaction pairs found in PEA, only (r_{27}, r_{28}) and (r_{31}, r_{32}) were found to be the most sensitive reaction pairs. Among the remaining equilibrium but sensitive surface reactions, (r_{13}, r_{14}) and (r_{15}, r_{16}) were associated with the formation of O(s) and H(s) from H_2O(s), whereas r_{21} and r_{22} were associated with the formation of CO_2(s) and CO(s). From Table 3.2, it was observed that the rate of consumption or production of CO_2(s), CO(s) and H_2O(s) also depended on adsorption-desorption reactions (r_1 to r_{12}), which were equally sensitive like the surface reactions (r_{13}, r_{14}), (r_{15}, r_{16}) and (r_{21}, r_{22}). Salciccioli et al. [43] and Blaylock et al. [47] have suggested that the accuracy associated with the kinetic parameters of the surface reactions is most likely higher than that of adsorption-desorption kinetic parameters. Hence, instead of selecting the more accurate kinetic parameters of the surface reactions, the most sensitive adsorption-desorption reaction steps for H_2O, CO_2 and CO were considered for the optimization. Earlier it is mentioned that outlet mole fractions of CO_2 were more sensitive to CO adsorption-desorption reaction (r_6, r_{12}) than CO_2 adsorption-desorption reaction (r_5, r_{11}) as illustrated in Fig. 5.5(C) and (D). Thus, CO_2 adsorption- desorption reaction pair (r_5, r_{11}) was not considered in optimization.

Based on the PEA and LSA, four adsorption-desorption and two surface reaction pairs were found to be the influential: (r_1, r_7), (r_3, r_9), (r_4, r_{10}), (r_6, r_{12}), (r_{27}, r_{28}), and (r_{31}, r_{32}). In total 12 parameters (four sticking coefficients and eight pre-exponential factors) were optimized to fit the experimental data of MSR over Ni-spinel catalyst.

5.3.3.3. Optimization procedure

Kinetic parameters of the influential reaction steps were optimized using the optimization subroutine fminsearch in the MATLAB-R2014b environment. To optimize the reaction rate constants of the microkinetic model that also include time variation of surface coverage of chemical species, it was important to solve 1D steady state plug-flow model. However, the major obstacle associated with this approach was to obtain reasonable initial values for all surface species at each iteration of a differential solver without any initialization error or convergence issue. This can be achieved if the steady state solution can be obtained via transient approach instead of direct steady state approach. Adopting transient approach for solving 1D plug-flow model can introduce partial differential equations (PDEs). Solving stiff microkinetic model consisting of PDEs was very time-consuming approach and associated with many initialization errors in trial runs. Thus, to reduce computational time and to simplify the programming work, an alternative approach of transient series-CSTR (continuous stirred tank reactor) model consisting of ordinary differential equations (ODEs) was adopted instead of 1D transient plug-flow model. Series-CSTR model is equivalent to the plug-flow model [49] with the governing equations in the form of ODEs. It was determined that solution obtained via fourteen CSTRs of equal volume connected in series was close to the solution obtained using 1D steady state plug flow model. Adopting this approach provided an interruption free optimization subroutine operation.

Any parameter optimization process requires an appropriate objective function which get minimize at the end of each iteration. The definition of the objective function is the key to successful parameter optimization. Choosing objective function which is not sensitive to the parameters to be estimated can lead to ill-posed optimization/estimation problem [50]. So, to define the sensitive objective function, the normalized sensitivity coefficients for the outlet mole fractions of CH_4, H_2, CO and CO_2 were compared in Fig. 5.6(A) and (B) at 973.15 K and 1073.15 K respectively, for SC ratio of 1.5. Fig. 5.6 shows that normalized sensitivity coefficient values greater than 0.15 (absolute) in nine reaction pairs in the case of CO_2 and in eight reaction pairs for CO were determined compared to only three reaction pairs for CH_4 and H_2. This observation indicated that CO and CO_2 may govern the sensitivity of the entire microkinetic model for the studied operating conditions. It was also noticeable that the carbon atoms in the CO and CO_2 molecules were originally dissociated from the CH_4 reactant and the O atoms from the H_2O

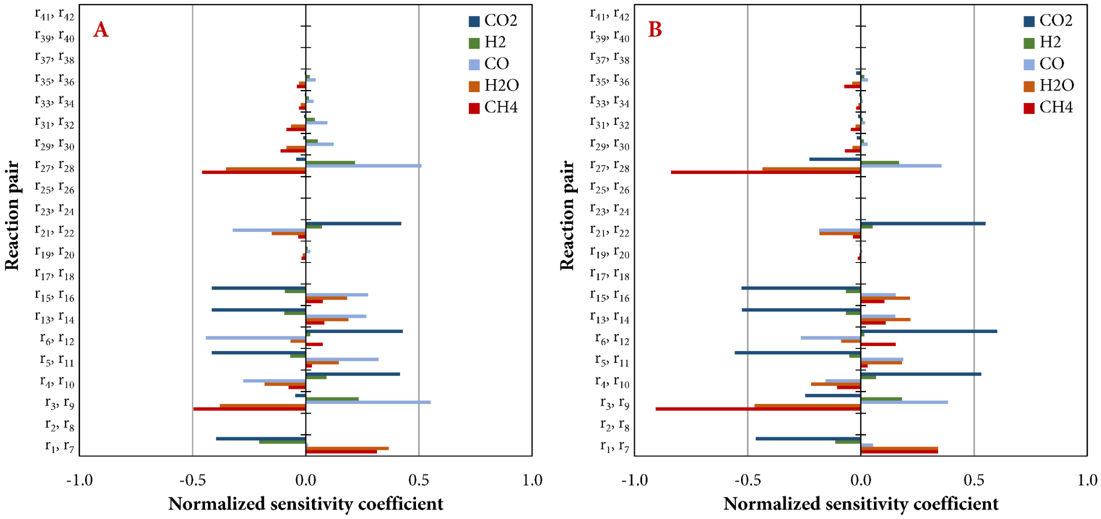

Fig. 5.6. *Comparison of the normalized sensitivity coefficients of the outlet mole fractions of CH_4, H_2, CO and CO_2 for SC ratio of 1.50 at (A) 973.15 K and (B) 1073.15 K.*

reactant and hence, the formation and the consumption of the CO and CO_2 molecules may govern the consumption rates of both the reactants (CH_4, H_2O) and the production rates of H_2. Overall the mole fractions of CO and CO_2 were found to be sensitive to the more number of elementary reaction steps than CH_4 and H_2. Therefore, in this work, the norms of the relative error between predicted and measured outlet molar flow rates of CO and CO_2 were selected as an objective function to be minimized for optimizing the selected 12 parameters:

$$F = \sqrt{\sum_{i=1}^{n}\left(\frac{\mathrm{N}_{CO,exp.} - \mathrm{N}_{CO,sim.}}{\mathrm{N}_{CO,exp.}}\right)^2 + \sum_{i=1}^{n}\left(\frac{\mathrm{N}_{CO2,exp.} - \mathrm{N}_{CO2,sim.}}{\mathrm{N}_{CO2,exp.}}\right)^2} \tag{5.11}$$

where, F represents the objective function, whereas $\mathrm{N}_{j,\ \mathrm{exp.}}$ and $\mathrm{N}_{j,\ \mathrm{sim.}}$ represent experimental and predicted or simulated molar flow rates of species *j* (CO, CO_2) at the reactor outlet. It is important to normalize the values used in the computation of the objective function. In this work, to achieve same influence by each data point to the objective function, an experimental data point was placed in the denominator of the norm of the relative error [50].

As mentioned earlier, to optimize the parameters of most influential reactions (total 12 parameters), a MATLAB code for transient series CSTR-model was developed. The governing equations with variable density for the series-CSTR and plug-flow models can be obtained from any chemical reaction engineering book [51]. To solve the series CSTR-model equations, a stiff implicit solver ODE15s was applied, which called the function for each data point where ODEs were implemented. In the next step, MATLAB code estimated the objective function (Eq. (11)) which was minimized by calling unconstrained optimization subroutine *fminsearch*. MATLAB's *fminsearch* method uses explorative Nelder-Mead simplex algorithm, which is the direct search method for multidimensional unconstrained minimization problems [52]. The decision to select unconstrained Nelder-Mead simplex method for the optimization was taken after unsuccessful trials of other constrained optimization subroutine methods such as *fmincon* and l*sqnonlin*. Before proceeding to the optimization step of the microkinetic parameters, a specific surface area of Ni was optimized by minimizing the objective function defined in Eq. (11). Achouri et al. [32] found that an equilibrium established between the Ni-spinel and alumina phases restricts the measurement of surface area of metallic nickel by CO chemisorption. Hence, the specific surface area was optimized to 3.25× 10^5 m^2/m^3 for the Ni-spinel catalyst and was implemented in the optimization of the microkinetic parameters. To keep the values of the optimized parameters to the vicinity of the original parameters reported by Maier et al. [31], original parameters values were considered as initial guesses for the optimization subroutine. The optimization stopping criteria was established by setting termination tolerance of 1×10^{-6} on the function value. After obtaining parameters by explorative and unconstrained fminsearch method, local optimization subroutine of fmincon with Sequential Quadratic Programming (SQP) was applied using parameter values obtained in fminsearch as initial guesses to further optimize the kinetic parameters. However, no change in parameters or in function value was obtained with this step. By comparing original values and optimized values of the 12 parameters in Table 5.1, one can see that the most significant improvement in MSR prediction over Ni-spinel catalyst came by the overall reaction rate of dehydrogenation of surface CH_4(s) via reaction steps (r_{27}, r_{28}) followed by the formation of surface CH(s) or dehydrogenation of CH_2(s) via reaction pair (r_{31}, r_{32}). Other important reaction steps for which parameter values changed by more than 15% from their original initial values, were adsorption of H_2O (r_4) and desorption of H_2 (r_7). The sticking coefficient value for the H_2O adsorption step was increased by 16%, whereas pre-exponential factor for the desorption of H_2 was decreased by 15.79% from the values reported by Maier et al. [31]. Less than 5% change was found in parameters for the desorption of CH_4 (r_9), H_2O (r_{10}), CO (r_{12}), and adsorption of H_2 (r_1). The % changes reported in Table 5.1 were calculated by taking the ratio of the difference between optimized value and original value to the original value of the respective parameters.

Table 5.1. *Comparison of the original and optimized microkinetic parameters.*

No.	Elementary Reactions	A [cm, mol, s]	A [cm, mol, s]	
		Original	Optimized	% Change
r_1	$H_2 + NI(s) + NI(s) \rightarrow H(s) + H(s)$	$0.010 \times 10^{-00\dagger}$	$0.0103 \times 10^{-00\dagger}$	3
r_3	$CH_4 + NI(s) \rightarrow CH_4(s)$	$8.000 \times 10^{-03\dagger}$	$7.311 \times 10^{-03\dagger}$	- 8.61
r_4	$H_2O + NI(s) \rightarrow H_2O(s)$	$0.100 \times 10^{-00\dagger}$	$0.116 \times 10^{-00\dagger}$	16
r_6	$CO + NI(s) \rightarrow CO(s)$	$5.000 \times 10^{-01\dagger}$	$4.626 \times 10^{-01\dagger}$	- 7.49
r_7	$H(s) + H(s) \rightarrow NI(s) + NI(s) + H_2$	$2.545 \times 10^{+19}$	$2.143 \times 10^{+19}$	- 15.79
r_9	$CH_4(s) \rightarrow CH_4 + NI(s)$	$8.705 \times 10^{+15}$	$8.950 \times 10^{+15}$	2.82
r_{10}	$H_2O(s) \rightarrow H_2O + NI(s)$	$3.732 \times 10^{+12}$	$3.909 \times 10^{+12}$	4.74
r_{12}	$CO(s) \rightarrow CO + NI(s)$	$3.563 \times 10^{+11}$	$3.628 \times 10^{+11}$	1.84
r_{27}	$CH_4(s) + NI(s) \rightarrow CH_3(s) + H(s)$	$3.700 \times 10^{+21}$	$4.574 \times 10^{+21}$	23.61
r_{28}	$CH_3(s) + H(s) \rightarrow CH_4(s) + NI(s)$	$6.034 \times 10^{+21}$	$1.327 \times 10^{+22}$	119.95
r_{31}	$CH_2(s) + NI(s) \rightarrow CH(s) + H(s)$	$3.700 \times 10^{+24}$	$2.370 \times 10^{+24}$	- 35.93
r_{32}	$CH(s) + H(s) \rightarrow CH_2(s) + NI(s)$	$4.089 \times 10^{+24}$	$5.722 \times 10^{+23}$	- 86.01
				†sticking coefficient

The influence of the optimized values of microkinetic parameters can also be illustrated by observing surface coverages of the most abundant reaction intermediates (MARI). Surface hydrogen H(s) and surface carbon-monoxide CO(s) were found to be the MARI for the operating conditions considered in this study. Fig. 5.7 illustrates the comparison of surface coverages of MARI and the surface coverage of H_2O(s) as well as unoccupied nickel sites between the original microkinetic model and optimized microkinetic model as a function of reactor length for the intermediate operating condition (T= 1073.15 K, GHSV = 38,852.44 h^{-1}, SC= 1.5). It can be seen from Fig. 5.7(A) that surface coverage of H(s) was increased on average by 19% in the optimized microkinetic model from its coverage in the original microkinetic model due to the influence of

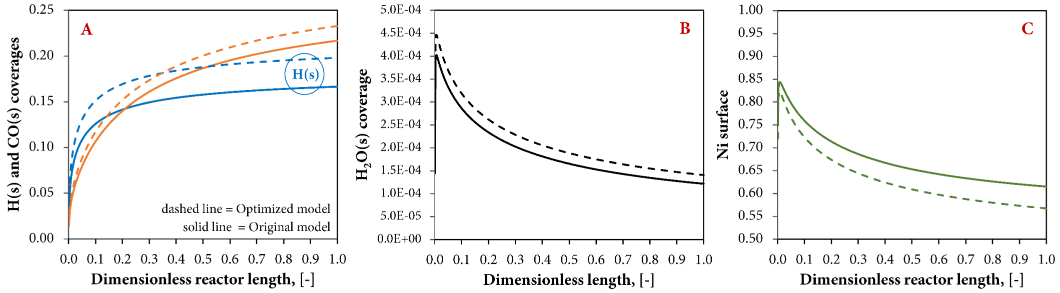

Fig. 5.7. *Comparison of surface coverages of (A) H(s) and CO(s), (B) H_2O(s), and (C) nickel, between the original microkinetic model and optimized model as a function of the reactor length for the intermediate operating condition (T =1073.15 K, GHSV = 38,852 h^{-1}, SC = 1.5).*

change in parameter value of the CH_4 dissociation into H(s) and CH(s) and due to H_2O adsorption and H_2 desorption steps. Fig. 5.7(B) also shows the evidence of influence of H_2O adsorption step in terms of increased surface coverage of H_2O(s) compared to the original microkinetic model. This finding could be linked with the earlier noted characteristic of yttria stabilized zirconia support. Increased H_2O(s) coverage in the case of optimized model of the Ni-spinel catalyst supports the experimental finding reported in the literature [22,32] that the introduction of yttria to ZrO_2 support increases the activity of the oxygen (O^{2-} or O^{-}) pumping component, which in the case of MSR is H_2O. Because of increased H(s) coverage, CO(s) coverage was also increased (Fig. 5.7(A)), as more H(s) dissociated from H_2O(s) along with OH(s) and hence more O(s) via reaction steps r_{13} to r_{18} resulted into increased coverage of CO(s) via reaction steps r_{19} to r_{26}. Due to increased surface coverages of the MARI, empty nickel sites were decreased (Fig. 5.7(C)) in the case of optimized model compared to the original microkinetic model for the same inlet condition, which indicated the improved utilization of the Ni-spinel catalyst.

5.3.4. Validation of the optimized microkinetic model against the experimental data of MSR over Ni-spinel catalyst

Fig. 5.8 presents the distribution of measured and predicted flow rates of reactants (CH_4, H_2O) and products (H_2, CO, CO_2) as well as X_{CH4} in parity plots along with 95% confidence and prediction intervals. It should be noted that flow rates of H_2O at the reactor outlet were determined from atomic balance of CO, CO_2 and H_2 compositions. The experimental data of MSR over Ni-spinel catalyst were obtained at three different temperatures (973.15 K, 1073.15 K and 1123.15 K) and at two SC ratios of 1.25 and 1.50 for five different space times between 55 ms and 277 ms. The predicted data were obtained by applying the optimized microkinetic parameters in a steady state plug-flow reactor model at the same experimental conditions. It can be seen from Fig. 5.8 that experimentally measured data at various operating conditions presented in Figs. 2 and 3 were predicted reasonably well by the optimized microkinetic model with the adjustment of only 12 parameters (Table 5.1) out of 78 parameters (Table 3.2). Fig. 5.8(A) shows a parity plot of experimentally measured and predicted X_{CH4} distribution with R-squared value of 0.8796 and with slope not too far from one. Fig. 5.8(B) to (F) shows the parity plots of CH_4, H_2O, H_2, CO and CO_2 flow rates at the reactor outlet respectively. The R-squared values found for all these chemical species are 0.9549, 0.9716, 0.8843, 0.8879 and 0.9506 respectively with slope not too far from one. Fig. 5.8 also shows that the experimentally measured and predicted data are distributed evenly on both sides of the regression line and are within 95% prediction interval range. This indicated that the systematic and stepwise

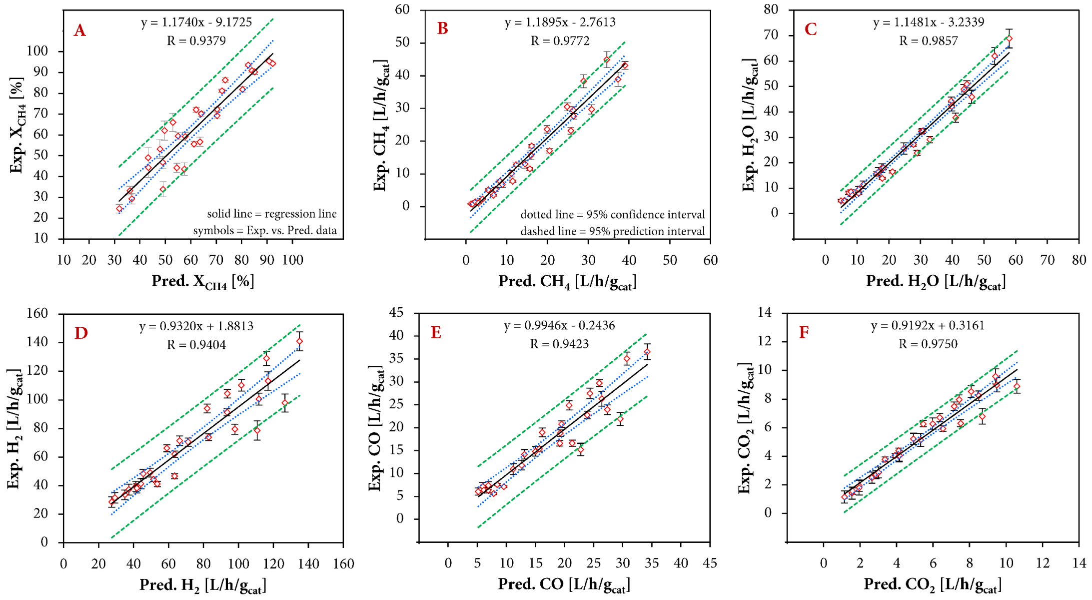

Fig. 5.8. *Validation of the optimized microkinetic model for (A) X_{CH4}, (B) molar flow (L/h/g_{cat}) of CH_4, (C) H_2O, (D) H_2, (E) CO, and (F) CO_2, against experimental data of MSR over Ni-spinel catalyst along with 95% confidence and prediction intervals.*

elimination of number of parameters via PEA and LSA was the right approach undertaken in this study. It could be possible to obtain better prediction of experimental data than presented in Fig. 5.8 if activation energy parameters being considered in the optimization. However, as noted earlier even a minor change in the values of activation energy can make the microkinetic model thermodynamically inconsistent. To conduct detail analysis and estimation of all 78 parameters with limited experimental data points for such multi-step microkinetic model was not possible and hence beyond the scope of this present study.

5.3.5. Prediction behavior of the optimized microkinetic model at the equilibrium condition

After the optimization exercise of reaction kinetic parameters, it was important to identify whether the optimized reaction kinetic model remained thermodynamically consistent or not in a sense that thermodynamic equilibrium of the gas-phase chemical species matches for a range of temperature. To investigate how the optimized microkinetic model predicts the equilibrium X_{CH4}, equilibrium S_{CO} and equilibrium H_2/CO ratio, isothermal studies were carried out utilizing the 1D steady state plug-flow model at three different steam to carbon ratios of 1.25, 1.50 and 3.0 for the temperature range of 500 °C to 1100 °C with 50 °C interval. Same runs were also carried out by applying original microkinetic parameters. In the earlier sections, experimental data of the Ni-spinel catalyst showed that all data were below equilibrium, hence to conduct an equilibrium study numerically, slow inlet feed-rate was considered to increase the residence time of the reactants. The numerical studies were conducted at GHSV of 1665 h^{-1} for SC = 1.25, 1850 h^{-1} for SC= 1.50 and 2960 h^{-1} for SC= 3.0 for the temperature range of 500 °C to 1100 °C. The GHSVs chosen at three different SC ratios were far below from the lowest studied GHSV (13,267 h^{-1} for SC = 1.25) reported in Sections 3.1 and 3.2 of the experimental work.

Fig. 5.9 shows how X_{CH4}, S_{CO} and H_2/CO ratio approach to equilibrium when optimized parameters were used compared to the original parameters. Fig. 5.9(A), (B) and (C) illustrates

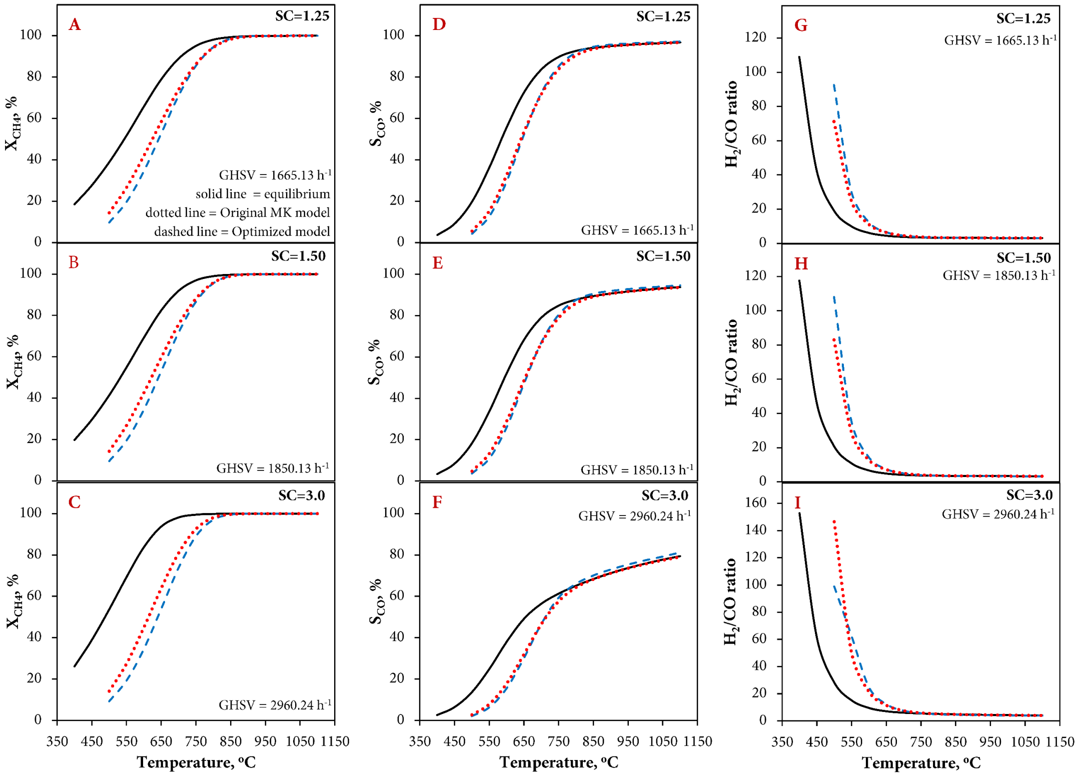

Fig. 5.9. *Equilibrium comparison of X_{CH4}, S_{CO} and H_2/CO ratio between the optimized and original microkinetic model at different SC ratios.*

X_{CH4} for the three SC ratios. It was observed that at non-equilibrium condition or at relatively low temperatures (below 750 °C), X_{CH4} obtained in the optimized kinetic model was less compared to the original microkinetic model. However, at temperatures greater than 750 °C, where equilibrium can establish rapidly, showed no significant difference in prediction of equilibrium X_{CH4} between the two models. This indicated that there was no significant difference found in predicting equilibrium X_{CH4} and hence equilibrium methane composition in the optimized microkinetic model compared to the original model. It should be noted that no experimental data at SC = 3.0 were available to consider in parameter optimization. Despite this fact, the optimized model predicted the equilibrium X_{CH4} for SC = 3 accurately, which indicated that the optimized model can also be implemented for the wide range of operating conditions. Fig. 5.9(D), (E) and (F) shows the S_{CO} at three different SC ratios. Unlike X_{CH4}, difference between the S_{CO} predicted by optimized and original microkinetic models was miniscule for the entire temperature range. For SC = 3.0, the optimized model had slightly over-predicted the S_{CO} at elevated temperatures compared to the original model. This could be attributed to the fact that optimized kinetic parameters are bound to carry uncertainties or errors associated with the experimental measurements. Similarly, Fig. 5.9(G), (H) and (I) presents the H_2/CO ratio for the three SC ratios respectively. Again, no difference was found between the optimized and the original microkinetic models at elevated temperatures. The study of equilibrium approach proved that the optimized model showed no deviation in predicting the equilibrium behavior from the original microkinetic model and hence the model remained thermodynamically consistent despite the changes in values of four sticking coefficients and eight pre-exponential factors.

5.4. Conclusions

Reaction kinetic data of methane steam reforming (MSR) at low steam to carbon ratios of 1.25 and 1.50 were measured over alumina and yttria-stabilized-zirconia (YSZ) supported Ni-spinel catalyst in a quartz reactor for five different space times between 55 ms and 277 ms at three different temperatures of 973 K, 1073 K, and 1123 K. To simulate the experimentally measured data, a steady state plug-flow reactor model was developed successfully using the COMSOL^{TM} environment by implementing microkinetic reaction mechanism. The microkinetic model was validated by optimizing the reaction kinetic parameters of the most influential elementary reaction steps. A stepwise approach based on the partial equilibrium analysis (PEA) and the local sensitivity analysis (LSA) was implemented successfully for selecting the most influential elementary reaction steps for parameter optimization. A MATLAB programming code for the transient series-CSTR model was developed successfully for solving an interruption free the system of differential equations and optimization subroutine to minimize the objective function.

The PEA and LSA showed the important equilibrium, non-equilibrium and partial equilibrium reactions, and the key sensitive reaction steps for the operating space considered. Regardless of the studied SC ratios and studied temperatures, same pairs of reaction steps found to be in equilibrium and in non-equilibrium. Reaction steps of dehydrogenation of surface CH_4(s), formation and consumption of surface CH(s) or CH_2(s), H(s), H_2O(s) and CO(s) were found to be the most influential. Increased H_2O(s) coverage in the case of optimized model of Ni-spinel catalyst supports the experimental finding reported in the literature that the introduction of yttria into ZrO_2 increases the activity of the oxygen (O^{2-} or O^{-}) pumping component. Surface H(s) and CO (s) were found to be the most abundant reaction intermediates (MARI) for the operating conditions considered. Decreased percentage of the empty nickel sites due to increase in surface coverages of the MARI in the case of optimized microkinetic model indicated the improved utilization of the Ni-spinel catalyst. In total six reaction pairs found to be the influential steps and with the adjustment of only 12 parameters out of 78, the optimized microkinetic model predicted the chemical species composition in MSR over Ni-spinel catalyst accurately for the entire operating space and at equilibrium condition.

5.5. References

[1] Joseck F, Nguyen T, Klahr B, Talapatra A. Current U.S. hydrogen production. DOE Hydrogen and Fuel Cells Program Record. 2016 May 24.

[2] Navigant Research. Demand for hydrogen for fuel cells and other emerging markets will climb sharply through 2030 [Press release]. (2014 February 13). Retrieved from http://www.navigantresearch.com/newsroom/demand-for-hydrogen-for-fuel-cells-and-other-emerging-markets-will-climb-sharply-through-2030.

[3] Bromaghim G, Gibeault K, Serfass J, Serfass P, Wagner E. Hydrogen and fuel cells: the US market report. In National Hydrogen Association 2010 Mar (Vol. 22).

[4] Gür TM. Comprehensive review of methane conversion in solid oxide fuel cells: Prospects for efficient electricity generation from natural gas. Progress in Energy and Combustion Science. 2016 May 31;54:1-64.

[5] Xu J, Froment GF. Methane steam reforming, methanation and water-gas shift: I. Intrinsic kinetics. AIChE Journal. 1989 Jan 1;35(1):88-96.

[6] Trimm DL. Catalysts for the control of coking during steam reforming. Catalysis Today. 1999 Feb 24;49(1):3-10.

[7] Hou K, Hughes R. The kinetics of methane steam reforming over a Ni/α-Al_2O_3 catalyst. Chemical Engineering Journal. 2001 Mar 15;82(1):311-28.

[8] Wei J, Iglesia E. Isotopic and kinetic assessment of the mechanism of reactions of CH_4 with CO_2 or H_2O to form synthesis gas and carbon on nickel catalysts. Journal of Catalysis. 2004 Jun 10;224(2):370-83.

[9] Rostrup-Nielsen J. 40 years in catalysis. Catalysis Today. 2006 Jan 15;111(1-2):4-11.

[10] Sprung C, Arstad B, Olsbye U. Methane Steam Reforming Over Ni/$NiAl_2O_4$ Catalyst: The Effect of Steam-to-Methane Ratio. Topics in Catalysis. 2011 Nov 1;54(16-18):1063-9.

[11] Guo J, Lou H, Zhao H, Chai D, Zheng X. Dry reforming of methane over nickel catalysts supported on magnesium aluminate spinels. Applied Catalysis A: General. 2004 Oct 8;273(1):75-82.

[12] van Beurden P. On the catalytic aspects of steam-methane reforming. Energy Research Centre of the Netherlands (ECN), Technical Report I-04-003. 2004 Dec.

[13] Hegarty ME, O'connor AM, Ross JR. Syngas production from natural gas using ZrO_2-supported metals. Catalysis Today. 1998 Jul 9;42(3):225-32.

[14] Dong WS, Roh HS, Jun KW, Park SE, Oh YS. Methane reforming over Ni/Ce-ZrO_2 catalysts: effect of nickel content. Applied Catalysis A: General. 2002 Mar 28;226(1):63-72.

[15] Choudhary VR, Banerjee S, Rajput AM. Hydrogen from step-wise steam reforming of methane over Ni/ZrO_2: factors affecting catalytic methane decomposition and gasification by steam of carbon formed on the catalyst. Applied Catalysis A: General. 2002 Aug 8;234(1):259-70.

[16] Takeguchi T, Furukawa SN, Inoue M, Eguchi K. Autothermal reforming of methane over Ni catalysts supported over CaO–CeO_2–ZrO_2 solid solution. Applied Catalysis A: General. 2003 Feb 10;240(1):223-33.

[17] Takahashi R, Sato S, Sodesawa T, Yoshida M, Tomiyama S. Addition of zirconia in Ni/SiO_2 catalyst for improvement of steam resistance. Applied Catalysis A: General. 2004 Oct 8;273(1):211-5.

[18] Pines H, Haag WO. Alumina: catalyst and support. I. alumina, its intrinsic acidity and catalytic activity. Journal of the American Chemical Society. 1960 May;82(10):2471-83.

[19] Lahousse C, Aboulayt A, Maugé F, Bachelier J, Lavalley JC. Acidic and basic properties of zirconia—alumina and zirconia—titania mixed oxides. Journal of molecular catalysis. 1993 Oct 25;84(3):283-97.

[20] Maia TA, Assaf JM, Assaf EM. Performance of cobalt catalysts supported on $Ce_xZr_{1-x}O_2$ ($0<x<1$) solid solutions in oxidative ethanol reforming. Reaction Kinetics, Mechanisms and Catalysis. 2013 Jun 1;109(1):181-97.

[21] Teterycz H, Klimkiewicz R, Łaniecki M. The role of Lewis acidic centers in stabilized zirconium dioxide. Applied Catalysis A: General. 2003 Aug 28;249(2):313-26.

[22] Bellido JD, Assaf EM. Nickel catalysts supported on ZrO_2, Y_2O_3-stabilized ZrO_2 and CaO-stabilized ZrO_2 for the steam reforming of ethanol: effect of the support and nickel load. Journal of Power Sources. 2008 Feb 15;177(1):24-32.

[23] Bellido JD, Assaf EM. Effect of the Y_2O_3–ZrO_2 support composition on nickel catalyst evaluated in dry reforming of methane. Applied Catalysis A: General. 2009 Jan 15;352(1):179-87.

[24] Fauteux-Lefebvre C, Abatzoglou N, Blanchard J, Gitzhofer F. Steam reforming of liquid hydrocarbons over a nickel–alumina spinel catalyst. Journal of Power Sources. 2010 May 15;195(10):3275-83.

[25] Fauteux-Lefebvre C, Abatzoglou N, Braidy N, Achouri IE. Diesel steam reforming with a nickel–alumina spinel catalyst for solid oxide fuel cell application. Journal of Power Sources. 2011 Sep 15;196(18):7673-80.

[26] Blanchard J, Nsungui AJ, Abatzoglou N, Gitzhofer F. Dry Reforming of Methane with a Ni/Al_2O_3-YSZ Catalyst: The Role of the Catalyst Preparation Protocol. The Canadian Journal of Chemical Engineering. 2007 Dec 1;85(6):889-99.

[27] Bangala DN, Abatzoglou N, Chornet E. Steam reforming of naphthalene on Ni–Cr/Al_2O_3 catalysts doped with MgO, TiO_2, and La_2O_3. AIChE Journal. 1998 Apr 1;44(4):927-36.

[28] Dumesic JA. The microkinetics of heterogeneous catalysis. An American Chemical Society Publication; 1993.

[29] L. Kunz, L. Maier, S. Tischer, O. Deutschmann, Modeling the Rate of Heterogeneous Reactions, in: Modeling and Simulation of Heterogeneous Catalytic Reactions, Wiley-VCH Verlag GmbH & Co. KGaA, 2012:113-148.

[30] Dixit M, Baruah R, Parikh D, Sharma S, Bhargav A. Autothermal reforming of methane on rhodium catalysts: Microkinetic analysis for model reduction. Computers & Chemical Engineering. 2016 Jun 9;89:149-57.

[31] Maier L, Schädel B, Delgado KH, Tischer S, Deutschmann O. Steam reforming of methane over nickel: development of a multi-step surface reaction mechanism. Topics in Catalysis. 2011 Sep 1;54(13-15):845-58.

[32] Achouri IE, Abatzoglou N, Braidy N, Bastien S. New insights on the role of YSZ in a $NiAl_2O_4$/Al_2O_3–YSZ catalyst. Applied Catalysis A: General. 2015 May 31;497:42-50.

[33] Afandizadeh S, Foumeny EA. Design of packed bed reactors: guides to catalyst shape, size, and loading selection. Applied thermal engineering. 2001 Apr 30;21(6):669-82.

[34] Froment GF, Bischoff KB. Chemical reactor analysis and design. New York: Wiley; 1979.

[35] Rase HF, Holmes JR. Chemical reactor design for process plants. New York: Wiley; 1977 Jan.

[36] Parmar RD. A combined gas-phase and surface reaction mechanistic model of diesel surrogate reforming for SOFC application. Ph.D. thesis, Queen’s University, Kingston, Canada; 2013.

[37] Ergun S. Fluid flow through packed columns. Chemical Engineering Progress. 1952;48:89-94.

[38] Rostrup-Nielsen JR. Steam reforming. Chapter 1. In: Anderson JR, Boudart M, editors. Catalysis, science and technology, vol. 5. Berlin: Springer-Verlag; 1984. p. 1-117.

[39] Shekhawat D, Spivey JJ, Berry DA, editors. Fuel cells: technologies for fuel processing. Elsevier, Oxford, UK; 2011 Mar 18.

[40] Taylor J. Introduction to error analysis, the study of uncertainties in physical measurements. University Science Books, Sausalito, California; 1997.

[41] Karadeniz H. Numerical Modeling of Stagnation Flows over Porous Catalytic Surfaces. KIT Scientific Publishing; 2016 Apr 8.

[42] Deutschmann O, Schmidt LD. Modeling the partial oxidation of methane in a short-contact-time reactor. AIChE Journal. 1998 Nov 1;44(11):2465-77.

[43] Salciccioli M, Stamatakis M, Caratzoulas S, Vlachos DG. A review of multiscale modeling of metal-catalyzed reactions: Mechanism development for complexity and emergent behavior. Chemical Engineering Science. 2011 Oct 1;66(19):4319-55.

[44] Dumesic JA. Analyses of reaction schemes using De Donder relations. Journal of Catalysis. 1999 Jul 25;185(2):496-505.

[45] Tao FF, Schneider WF, Kamat PV. Heterogeneous catalysis at nanoscale for energy applications. John Wiley & Sons; 2015 Feb 9.

[46] Aparicio LM. Transient isotopic studies and microkinetic modeling of methane reforming over nickel catalysts. Journal of Catalysis. 1997 Jan 15;165(2):262-74.

[47] Blaylock DW, Ogura T, Green WH, Beran GJ. Computational investigation of thermochemistry and kinetics of steam methane reforming on Ni (111) under realistic conditions. The Journal of Physical Chemistry C. 2009 Feb 27;113(12):4898-908.

[48] Rostrup-Nielsen JR. Conversion of hydrocarbons and alcohols for fuel cells. Physical Chemistry Chemical Physics. 2001;3(3):283-8.

[49] Coker AK. Modeling of chemical kinetics and reactor design. Gulf Professional Publishing, Houston, Texas; 2001.

[50] Ramanathan K, Sharma CS. Kinetic parameters estimation for three-way catalyst modeling. Industrial & Engineering Chemistry Research. 2011 Jul 21;50(17):9960-79.

[51] Fogler H S. Elements of chemical reaction engineering. Prentice Hall PTR, Upper Saddle River, N.J.; 1999.

[52] Lagarias JC, Reeds JA, Wright MH, Wright PE. Convergence properties of the Nelder--Mead simplex method in low dimensions. SIAM Journal on optimization. 1998;9(1):112-47.

Chapter 6

Improved performance of a catalytic plate reactor designed with distributed coatings of reforming and combustion catalysts to produce hydrogen by combustion assisted methane steam reforming at low steam to carbon ratio

Abstract

Study presents a numerical analysis of a catalytic plate reactor (CPR) coated with distributed reforming and combustion catalysts to produce hydrogen via methane steam reforming (MSR). Experimentally validated microkinetic model of a nickel-spinel catalyst is employed for MSR. Required energy to MSR sites is supplied by catalytic and gas-phase methane combustion. Results obtained with distributed coatings are evaluated against continuous coatings by comparing temperature distribution, conversion, yield, selectivity, H_2/CO ratio, efficiency, effectiveness-factors and plate-thickness. The study identifies the internal-diffusion limitation beyond 50μm reforming-catalyst thickness and 5μm combustion-catalyst thickness. Distributed coatings of combustion-catalyst not only improve the utilization of catalysts and hydrogen production by 5% but also reduce the maximum plate temperature by 20 °C with 74% less combustion-catalyst. Distributed coatings of reforming and combustion catalysts predicts same methane conversion as in continuous coatings but with 28% less reforming-catalyst and 74% less combustion-catalyst. The study also shows that the influence of distributed coatings on CPR performance is more pronounced with relatively thick plate.

6.1. Introduction

With high thermodynamic efficiency of 40 to 60%, fuel cells are expected to play a key role in combating against global pollution while transition from the carbon economy to low-carbon economy takes place during the next three to four decades [1]. Thus, the demand of fuel cells will continue to increase along with other clean energy sources. Consequently, the demand for hydrogen (H_2), the most important fuel for fuel cells will also continue to rise [2]. In 2015, global H_2 production was amounted between 61 and 65 million metric tons and is expected to grow further [3]. Prediction suggested that H_2 usage for sectors other than petroleum and chemicals will grow to nearly 3.5 billion kg by 2030 [4]. Though H_2 is considered as the most abundant fuel in the universe, pure H_2 exists in a very limited amount on our planet. Therefore, various methods are developed to produce H_2 from its primary sources. Two methods are commonly in use: (1) reforming and (2) electrolysis. Reforming involves H_2 separation from water and carbon compounds such as methane or higher hydrocarbons, whereas electrolysis involves H_2 separation from oxygen in water. The production of H_2 via electrolysis is not a viable choice for the power backup option and at off-grid locations because it requires electricity to produce H_2. Hence, to increase the wide spread use of fuel cells, onsite production of H_2 via reforming of hydrocarbons is the most cost-effective solution. To produce H_2 for fuel cells via reforming, methane (CH_4) is the desired fuel of choice due to its lowest carbon content and recent discoveries of vast reserves of shale gas [5] have further strengthen the choice.

The production of H_2 from CH_4 is carried out by three major processes: (1) steam reforming (SR), (2) autothermal reforming (ATR) and (3) partial oxidation (POX). SR is highly endothermic process, whereas POX is the exothermic. ATR is a combination of SR and POX and can offer the advantage of thermoneutral operation. Among these three major processes, SR provides maximum H_2 concentration and yield [6]. However, due to its highly endothermic nature, SR requires an effective way of supplying heat to its endothermic reaction sites. This can be achieved more effectively and efficiently by the spatial segregation between the methane steam reforming (MSR) and a heat-exchanging medium (e.g. methane combustion (MC) in a catalytic plate reactor (CPR). In a CPR design, thin metal plates coated with appropriate catalysts are closely arranged in a parallel fashion, where the endothermic MSR and the exothermic MC are carried out in alternating channels. Due to channel's dimensions in the micrometer to millimeter range, a CPR design can intensify both MSR and MC by increasing the rates of heat, mass and momentum transfer and by improving the surface area to volume ratio [7]. Consequently, reactant conversion, product yield and catalyst utilization can be improved, which reduces capital and operating cost of a chemical reactor [8]. Thus, adopting a CPR design and supplying the heat by the exothermic MC can greatly enhances the efficiency, effectiveness and productivity of a chemical reactor. However, the use of highly exothermic MC creates steep thermal gradients and hot-spots due to the imbalance of the heat liberating at faster rate in MC and absorbing at relatively slower rate in MSR [9]. Such imbalance of heat causes problems of catalysts delamination and material failure due to uneven thermal stresses along the reactor. Heat imbalance between the reforming and combustion sides also causes problems of cold and hot spots and steep thermal gradients in the direction of flow, which reduce the catalytic active surface area, and as a result decreases conversion rates of the reactants [10].

Many studies have attempted to address the issues of steep thermal gradients, hot and cold spots by changing the design of a CPR at various levels. Recently, Pattison et al. [11,12] proposed a complex design for a microchannel CPR designed with 60 cm plate-length, where a layer of phase change material (PCM) placed between the two plates of the reforming and combustion sides. The PCM layer acted as an energy storage buffer, which absorbs an excess thermal energy that transfers from the combustion-side plate to the reforming-side plate. Along with the concept of PCM layer, they also proposed a temperature control strategy to address the issue of persistent disturbances. Pattison et al. [13] also proposed a distributed coating design for a combustion-catalyst. They investigated numerically, a method for emulating distributed feed configuration in a CPR via two to four distributed coating layers of a combustion-catalyst, consisting of alternating active and catalytically inactive sections. Their study showed that increasing the number of distributed sections allowed for more precise tuning of a plate temperature. However, in their study, they considered only two to four relatively longer (centimeter range) distributed sections of a combustion-catalyst.

Similarly, Jeon et al. [14] conducted an optimization study to determine an optimum length of the distributed sections of a combustion-catalyst, an optimum number of combustion-catalyst sections, and an optimum length for an inter-catalyst space to reduce the thermal hot-spots in a microchannel CPR consisting of relatively shorter plate-length of 5 cm. They considered the distributed combustion-catalyst only for the initial fifty percent of the plate-length and did not address the issue of the longitudinal thermal gradients for the remaining plate-length. They reported that optimization of inter-catalyst space length is more effective in minimizing the thermal hot-spots. However, they restricted their study to 1 mm length for the inter-catalyst space on the combustion-side of a microchannel CPR.

Ramaswamy et al. [15, 16] analyzed dynamic and steady-state behavior of a heat exchanger reactor with counter-flow and co-flow modes for the coupling of exothermic MC and endothermic MSR reactions using the pseudo-homogeneous plug-flow model. They reported thermal hot-spots in both reactor designs and higher temperature peak in the case of counter-flow mode. They suggested that catalyst activity profiling can reduce steep thermal gradients and hot-spots with co-flow arrangement. Similar study was carried out by Zanfir et al. [17] to investigate the influence of flow arrangement between the MC and MSR and catalyst distribution. They showed reduction in severe hot-spots condition by selecting appropriate overlapping locations for the reforming-catalyst and combustion-catalyst and suggested that more number of distributed sections of the combustion-catalyst can improve the longitudinal temperature distribution.

Kolios et al. [18] proposed a distributed feed design for the counter current flow operation between the reforming and combustion sides. For their proposed design, reactants on the combustion-side are entered at multiple points located along the reactor to ease steep temperature gradients in the flow direction. Kolios et al. [19] also investigated the influence of periodic switching of the exothermic and endothermic reactions to eliminate the cold and hot-spots in a CPR. The concept of distributed feed requires access of all flow channels at multiple points along the length, which makes the design of a chemical reactor more complex and difficult to build. Complex CPR design also makes the loading and unloading operation of the plates difficult.

Recently, Settar et al. [20] carried out a comparative numerical study between the distributed and conventional continuous coatings of a reforming-catalyst for the endothermic MSR by steady state two-dimensional model of a single reforming-channel by considering channel wall as a heat providing source and showed performance enhancement factor up to two for CH_4 conversion with the distributed reforming-catalyst. They kept the amount of a reforming-catalyst in the distributed coating same as continuous coating by considering the same total length of active reforming-catalyst. To achieve this, they distributed coating sections of a reforming-catalyst over an extended plate-length compared to the continuous coating counterpart.

Most recently [21], we presented a comparative study on the influence of distributed and continuous coatings of the combustion-catalyst for the H_2 production via combustion assisted MSR by considering co-flow and counter-flow arrangement, inlet mass flow rates ratio ($m_{MC/MSR}$) of the combustion-side to the reforming-side and reforming-catalyst thickness. The study showed that co-flow arrangement between the reforming and combustion sides with the distributed combustion-catalyst over the entire plate-length not only increased the production of H_2 in MSR but also decreased the required fuel (CH_4) on the combustion-side by 7 to 8% to produce the same amount of H_2 to feed a 1 kW fuel cell compared to the continuous coating. The study also showed that with the distributed coating of the combustion-catalyst, maximum reactor plate temperature, hot-spots and longitudinal thermal gradients are reduced significantly along with saving of a combustion-catalyst by 70%.

In a separate study [22], we proposed a distributed coating for both reforming and combustion catalysts over the entire plate length in a CPR. Apart from reducing the thermal gradients and hot-spots, the study illustrated decrease in back diffusion of H_2 in the reforming-channel with the distributed coating of reforming and combustion catalysts. Low back-diffusion of H_2 allows more reactants to get adsorbed on the catalytic surface relatively easy, especially near the reactor inlet and hence increases the utilization of the reforming-catalyst than the situation where more H_2 is diffusing in the reverse direction and competing with the reactants in the adsorption step.

Traditionally, the production of H_2 via MSR is carried out over nickel (Ni) based catalysts with steam to carbon (SC) ratio of three or above to avoid carbon formation [23-28]. The SC ratio of three or above is very high compared to the reforming reaction stoichiometric ratio of one. High SC ratio dilutes the syngas content and is energetically unfavorable due to the requirements of more energy to produce excess steam in a boiler at the reactor upstream and to condense unreacted steam in a condenser at the reactor downstream. Noble metals such as rhodium (Rh) and ruthenium (Ru) based catalysts are more resistant to carbon formation than the traditional Ni based catalysts. However, due to excessive cost and limited availability of the noble metals, it is more profitable to develop Ni based catalysts which can be more resistant to carbon accumulation and can exhibit long term stability at low SC ratios [29]. With this aim, the study employs an alumina and YSZ supported nickel-spinel catalyst (Ni-spinel) to carry out MSR at SC ratio of 1.5. The Ni-spinel catalyst is composed of 3.6% Ni, 33.9% YSZ (7% Y_2O_3) and 62.5% alumina. The Ni-spinel catalyst has shown promising potential for the diesel steam reforming [30], methane dry reforming [31] and naphthalene reforming [32]. The use of such catalyst in a reformer can provide flexibility in selecting wide range of fuels that are available at various locations to generate H_2 and hence can further increase the usage of fuel cells.

In our previous studies [21,22], we considered a fixed length ($l_{c,\ blank}$, $l_{r,\ blank}$) for an inter-catalyst space and a fixed length ($l_{c,\ active}$, $l_{r,\ active}$) for each distributed active section of coated combustion and reforming catalysts. Whereas, the present study investigates the performance of five different distributed coating patterns of the DCCR (distributed combustion-catalyst and continuous reforming-catalyst) configuration, coated with different inter-catalyst space length ($l_{c,\ blank}$) and five different distributed coating patterns of the DCDR (distributed combustion-catalyst and distributed reforming-catalyst) configuration, where each distributed section of the reforming-catalyst is coated with different lengths ($l_{r,\ active}$). Before investigating the performance of the different distributed coating patterns of the reforming and combustion catalysts, the present study probes the internal diffusion limitations in the catalytic MC and MSR by considering different thickness of the coated catalysts at isothermal condition. Further, the study investigates the performance of the DCCR and DCDR configurations under the influence of different plate-thickness (δ_{plate}). Results obtained in different patterns of the DCCR and DCDR configurations are compared with the conventional CCCR (continuous combustion-catalyst and continuous reforming-catalyst) configuration in terms of temperature distribution, overall efficiency, methane conversions, hydrogen production rate, hydrogen yield and carbon-monoxide selectivity.

6.2. Computational framework

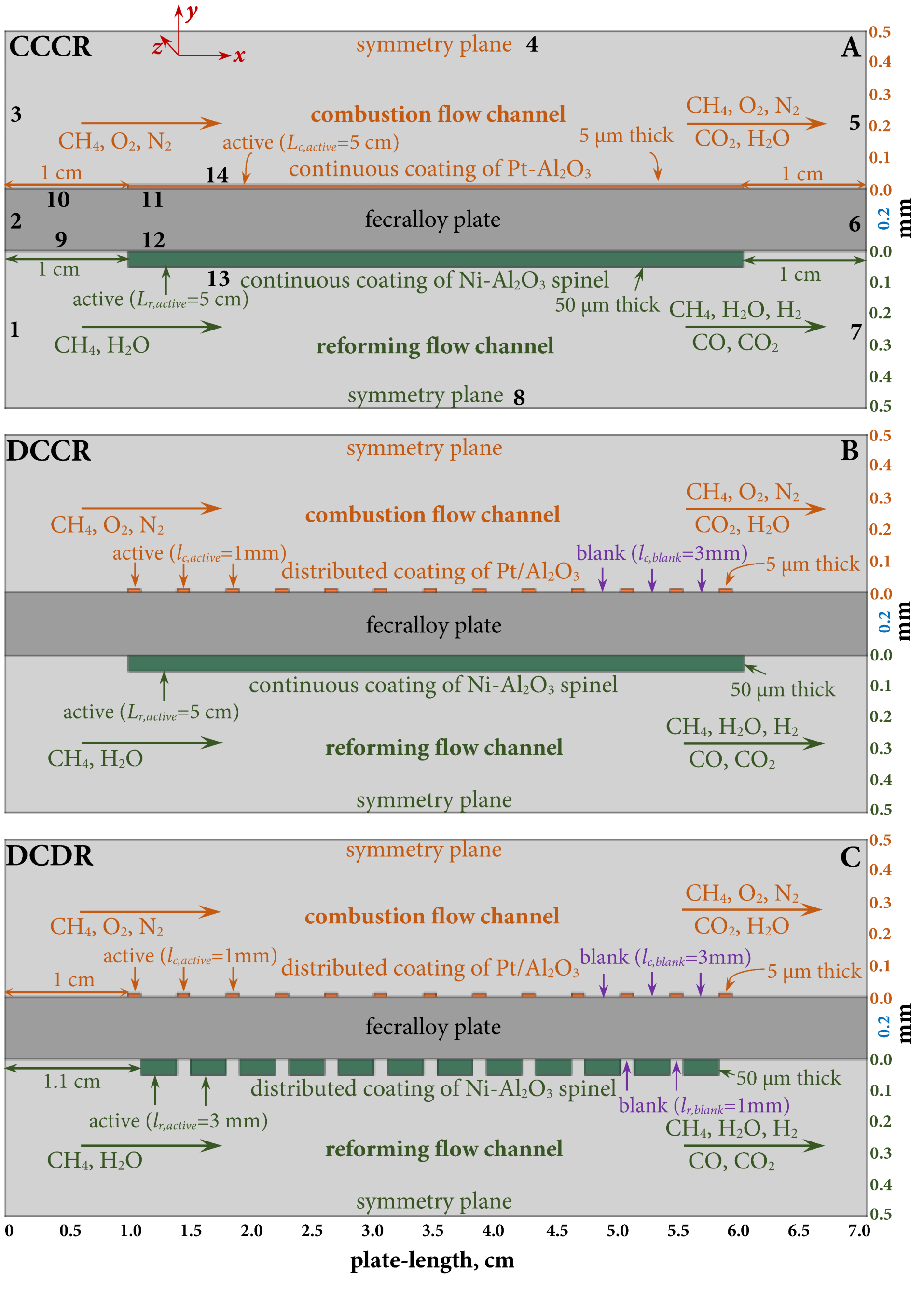

Fig. 6.1 *2D views of simulated domains of a CPR designed with three different catalyst configurations, (A) CCCR, (B) DCCR, and (C) DCDR.*

Fig. 6.1A, B and C illustrate schematic two-dimensional views of a fecralloy plate coated with the reforming and combustion catalysts for the CCCR, DCCR and DCDR configurations respectively. The study simulates a CPR consisting of 60 stacked plates each having 7 cm length and 5 cm width coated with the reforming-catalyst (Ni-spinel) on one side and the combustion-catalyst (platinum-alumina) on the other. The stacked arrangement of the 60 plates configures

30 channels for the MSR and 30 channels for the MC. The distance between the two-consecutive parallel stacked plates is considered to be 1 mm. The stacked design with alternate flow-channels for the MSR and MC allows to implement symmetry boundary conditions at the center plane in both flow channels. Hence, simulation of only one plate consisting of a reforming-channel and a combustion-channel with half-height (0.5 mm) is sufficient to carry out performance analysis of a CPR designed with N number of plates with N/2 number of reforming-channels and N/2 number of combustion-channels. As shown in Fig. 6.1A, symmetry boundary conditions are applied in the combustion flow-channel (boundary 4) and in the reforming flow-channel (boundary 8) at 0.5 mm.

Five domains are identified to simulate a CPR designed with different coating configurations: (1) combustion flow-channel, (2) combustion-catalyst, (3) fecralloy plate, (4) reforming-catalyst, and (5) reforming flow-channel. For the DCCR, continuous coating of the combustion-catalyst in the CCCR is replaced with the distributed coating sections of the combustion-catalyst (Fig. 6.1B), whereas for the DCDR, continuous coatings of the combustion as well as reforming catalysts in the CCCR are replaced with the distributed coating sections of the respective catalyst (Fig. 6.1C). Numbers in Fig. 6.1A represent boundaries of the five domains that are identified earlier. Numbers 1, 3 and 7, 5 represent inlet and outlet boundaries for the reforming and combustion flow-channels, 4 and 8 illustrate the symmetry boundaries, 13 presents the interface between the reforming-catalyst and reforming-channel and 14 presents the interface between the combustion-catalyst and combustion-channel, 9 and 10 show the interfaces between the plate and flow-channels, 2 and 6 represent insulated boundaries between the plate and surrounding, 11 illustrates the interface between the combustion-catalyst and plate and 12 represents the interface between the reforming-catalyst and plate. Similar boundaries can be identified for the same interfaces depicted in the case of DCCR and DCDR. Also, in Fig. 6.1, $L_{c,\ active}$ and $L_{r,\ active}$ represent the total active length for the coated combustion and reforming catalysts respectively, $l_{c,\ active}$ and $l_{r,\ active}$ represent the length of each distributed coating section of the active combustion and reforming catalysts respectively, and $l_{c,\ blank}$ and $l_{r,\ blank}$ represent the length of each section of the inter-catalyst space among distributed active sections of the combustion and reforming catalysts respectively. It should be noted that $l_{c,\ blank}$ or $l_{r,\ blank}$ in the distributed coating configurations (DCCR, DCDR) are in fact representing catalytically inactive porous sections with thickness same as catalytically active sections. To clearly distinguish distributed active coating sections of the catalysts, catalytically inactive porous sections with the same thickness are illustrated as blank spaces ($l_{c,\ blank}$ on the combustion side or $l_{r,\ blank}$ on the reforming-side). Consideration of such design for the distributed coatings (DCCR, DCDR) keeps the contact surface area between the plate and the active catalysts same as the CCCR coating and thus, eliminates the issue of catalyst delamination in the case of distributed coatings. However, in numerical study, whether the catalytically inactive sections are considered as inactive porous structures with thickness same as active catalyst or are considered as blank spaces or bare plate area, do not make a significant difference on the performance analysis of the distributed configurations due to very thin layer of the coatings. Table 6.1 presents the geometric parameters of the 2D domains shown in Fig. 6.1. To accommodate H_2 back diffusion and to account for the influence of inlets and outlets, bare plate areas of 1 cm (*x*-direction) × 5 cm (*z*-direction) are considered at both inlet and outlet ends on both sides of the plate. For the CCCR, the reforming-catalyst is coated continuously with 5 cm (length) × 5 cm (width) × 50 µm (thickness) and the combustion-catalyst is coated continuously with 5 cm × 5 cm × 5 µm. It should be noted that a detail study is conducted and presented under the results and discussion section to investigate the internal diffusion limitations in the

Table 6.1. *Geometric parameters of a CPR designed with different coating configurations between the combustion and reforming catalysts.*

Plate	**CCCR**	**DCCR**	**DCDR**
Length (L_{plate}), mm	70	70	70
width, mm	50	50	50
thickness (δ_{plate}), mm	0.2, 0.5, 1	0.2, 0.5, 1	0.2, 0.5, 1
Reforming & Combustion Channels	**CCCR**	**DCCR**	**DCDR**
Length ($L_{channel}$), mm	70	70	70
width, mm	50	50	50
height ($H_{channel}$), mm	1	1	1
half-height, mm	0.5	0.5	0.5
Reforming-Catalyst	**CCCR**	**DCCR**	**DCDR**
length of one active catalyst section ($l_{r,\ active}$), mm	50	50	1,2,3,4,5
length of one inactive washcoat section ($l_{r,\ blank}$), mm	0	0	1
width of active catalyst section, mm	50	50	50
thickness of active catalyst section (δ_r), µm	50	50	50
number of active catalyst sections ($N_{r,\ active}$)	1	1	25;16;12;10;8
total length of active catalyst ($L_{r,\ active}$), mm	50	50	25;32;36;40;40
catalyst bulk density (ρ_{cat}), kg/m^3	2368	2368	2368
total volume of the coated catalyst on one plate, mm^3	125	125	62.5;80;90;100;100
catalyst amount coated on one plate, g	0.296	0.296	0.148;0.189;0.213; 0.237;0.237
Combustion-Catalyst	**CCCR**	**DCCR**	**DCDR**
length of one active catalyst section ($l_{c,\ active}$), mm	50	1	1
length of one inactive washcoat section ($l_{c,\ blank}$), mm	0	1;2;3;4;5	3
width of active catalyst section, mm	50	50	50
thickness of active catalyst section (δ_c), µm	5	5	5
number of active catalyst sections ($N_{c,\ active}$)	1	25;17;13;10;9	13
total length of active catalyst ($L_{c,\ active}$), mm	50	25;17;13;10;9	13
catalyst bulk density (ρ_{cat}), kg/m^3	2368	2370	2368
total volume of the coated catalyst on one plate, mm^3	12.5	6.25; 4.25;3.25;2.5;2.25	3.25
catalyst amount coated on one plate, g	0.0296	0.0148;0.01;0.0077; 0.0059;0.00533	0.0077

reforming and combustion catalysts by altering the coating thickness at isothermal condition. Fig. 6.1B represents one of the patterns of the DCCR where each distributed section of the combustion-catalyst is coated with 1 mm (length) × 5 cm (width) × 5 µm (thickness) and a continuous section of the reforming-catalyst is coated with 5 cm × 5 cm × 50 µm. Fig. 6.1B illustrates 13 such active sections ($l_{c,\ active}$ = 1 mm) of the combustion-catalyst coated with $l_{c,\ blank}$ = 3 mm. It should be noted that a detail study is conducted and presented under the results and discussion section to investigate the influence of the inter-catalyst space length ($l_{c,\ blank}$) among the distributed coating sections of the active combustion-catalyst on the performance of MSR to produce H_2. Fig. 6.1C presents one of the patterns of the DCDR where each distributed active section of the reforming-catalyst is coated with 3 mm (length) × 5 cm (width) × 50 µm (thickness) and with $l_{r,\ blank}$ = 1 mm and each distributed active section of the combustion-catalyst is coated with 1 mm × 5 cm × 5 µm and with $l_{c,\ blank}$ = 3 mm. Fig. 6.1C illustrates 12 and 13 distributed coating sections of the active reforming and combustion catalysts respectively. It should be noted that a detail study is conducted and presented under the results and discussion section to investigate the influence of the active length ($l_{r,\ active}$) of the distributed coating sections of the active reforming-catalyst. It should also be noted that for the all coating configurations, both reforming and combustion catalysts are coated between x = 1 cm and x = 6 cm.

To simulate the fluid-flow, compressible Navier-Stokes equations are considered in both reforming and combustion flow channels; whereas to simulate the flow in catalytic and non-catalytic porous structures, the Darcy-Brinkman model is employed. To solve the mass-fraction gradients of chemical species, convection-diffusion equation is implemented in flow-channel and in porous media on both sides of the plate. To avoid the violation of species conservation, excess component's (steam (H_2O) in MSR and nitrogen (N_2) in MC) mass-fraction gradients are solved by applying the mass constraint approach, which states that the sum of mass fractions of chemical species must be equal to 1. Most of the published literature solved the diffusive-fluxes by applying simplified diffusion approaches. These simplified approaches are strictly valid for the diffusion of diluted species in a multicomponent mixture and for the binary mixtures [33]. In this study, diffusive fluxes are computed by employing the multi-component Maxwell-Stefan diffusion model. Also, to account for the collision of molecules with the surfaces of porous media, Knudsen diffusion is implemented by calculating the effective diffusion coefficients for each chemical species. Temperature profiles in both flow-channels are obtained by solving convection-conduction equation. Temperature distribution in both catalysts are obtained by solving the convection-conduction equation for the porous media, which assumes thermal equilibrium between the porous structures and fluids. Temperature distribution in the solid fecralloy plate is obtained by employing the steady state conduction heat-transfer equation.

Fecralloy plate is considered an excellent substrate for the surface coating of catalyst because it has high structural stability and a melting point of approximately 1773 K [34]. Catacel^{TM}, an industrial heat exchanger manufacturer uses fecralloy plates/foils to design CPRs. CPR patent of the Catacel^{TM} [35] states that the use of metal plate/foil for a heat exchanger with a thickness of 0.001 – 0.1 inches reduces expense using less material overall. The δ_{plate} of 0.2, 0.5 and 1 mm considered in this study are within this range. Thermal conductivity data presented in Table 6.2 for the fecralloy variant (Fe 72.2/Cr 22/Al 5.8) are obtained from the material property database [36] and applied as a linear function of temperature using Eq. (6.1) with R-squared value of 0.985.

$$k_{plate} = 0.0144T\ (\mathrm{K}) + 6.7974;\ (\mathrm{W/m\cdot K}) \tag{6.1}$$

Table 6.2. *Thermal conductivity values of fecralloy plate at different temperatures [36].*

Temperature, *T* (K)	**323.15**	**873.15**	**1073.15**	**1273.15**	**1473.15**
k_{plate} (W/m/K)	11	20	22	26	27

Thermal conductivities, heat capacities and viscosities of pure chemical species are calculated as a function of temperature. Pure component temperature dependent parameters for the heat capacities, viscosities, and thermal conductivities are obtained from Todd and Young [37] and presented in Table 6.3. It should be noted that Todd and Young [37] reported incorrect sign for b_2 parameter employed in calculating the pure viscosity of carbon-monoxide (CO). The parameter b_2 for the CO viscosity should have been reported with negative sign instead of positive. A corrected sign for the b_2 parameter (Table 6.3) is used to estimate the temperature dependent pure viscosity of CO in this study.

The gas-mixture heat capacity is evaluated using the weighted average heat capacity of the chemical species. The gas-mixture viscosity is calculated using the most accurate method of Reichenberg [38]. Required parameters for the Reichenberg method for each chemical species are given in Table 6.3. The thermal conductivity of low pressure gas-mixture is calculated using the method of Mason and Saxena [38]. The effective thermal conductivities (k_{eff}) of the coated catalysts are calculated using a volume weighted average as:

Table 6.3. *Pure component parameters for estimating temperature dependent heat capacities, viscosities and thermal conductivities. Molecule diffusion volumes are presented to estimate binary diffusion coefficients by Fuller equation. Critical temperature, critical pressure and dipole moments are also listed to estimate mixture viscosity by Reichenberg method.*

heat capacity (C_p), J/mol/K	**CH_4**	**H_2O**	**CO**	**H_2**	**CO_2**	**O_2**	**N_2**
a_0	47.964	37.373	30.429	21.157	4.3669	34.85	29.027
a_1	-178.59	-41.205	-8.1781	56.036	204.6	-57.975	4.8987
a_2	712.55	146.01	5.2062	-150.55	-471.33	203.68	-38.04
a_3	-1068.7	-217.08	41.974	199.29	657.88	-300.37	105.17
a_4	856.93	181.54	-66.346	-136.15	-519.9	231.72	-113.56
a_5	-358.75	-79.409	37.756	46.903	214.58	-91.821	55.554
a_6	61.321	14.015	-7.6538	-6.4725	-35.992	14.776	-10.35
viscosity (η), μP	**CH_4**	**H_2O**	**CO**	**H_2**	**CO_2**	**O_2**	**N_2**
b_0	-9.9989	-6.7541	-4.9137	15.553	-20.434	-1.6918	1.2719
b_1	529.37	244.93	793.65	299.78	680.07	889.75	771.45
b_2	-543.82	419.5	-875.90*	-244.34	-432.49	-892.79	-809.2
b_3	548.11	-522.38	883.75	249.41	244.22	905.98	832.47
b_4	-367.06	348.12	-572.14	-167.51	-85.929	-598.36	-553.93
b_5	140.48	-126.96	208.42	62.966	14.45	221.64	206.15
b_6	-22.92	19.591	-32.298	-9.9892	-0.4564	-34.754	-32.43
thermal conductivity (k), W/m/K	**CH_4**	**H_2O**	**CO**	**H_2**	**CO_2**	**O_2**	**N_2**
c_0	0.4796	2.0103	-0.2815	1.504	2.8888	-0.1857	-0.3216
c_1	1.8732	-7.9139	13.999	62.892	-27.018	11.118	14.81
c_2	37.413	35.922	-23.186	-47.19	129.65	-7.3734	-25.473
c_3	-47.44	-41.39	36.018	47.763	-233.29	6.713	38.837
c_4	38.251	35.993	-30.818	-31.939	216.83	-4.1797	-32.133
c_5	-17.283	-18.974	13.379	11.972	-101.12	1.491	13.493
c_6	3.2774	4.1531	-2.3224	-1.8954	18.698	-0.2278	-2.2741
	CH_4	**H_2O**	**CO**	**H_2**	**CO_2**	**O_2**	**N_2**
diffusion volume	24.42	12.7	18.9	7.07	26.9	16.6	17.9
critical temperature (T_c), K	190.56	647.14	132.85	32.98	304.12	154.58	126.2
critical pressure (P_c), bar	45.99	220.64	34.94	12.93	73.74	50.43	33.98
dipole moment (μ), debye	0	1.8	0.1	0	0	0	0

$C_p(\mathrm{J/(mol \cdot K)}) = \sum_{i=0}^{6} a_i \tau^i$, where $\tau = T(\mathrm{K})/1000$, [37]

$\eta(\mu\mathrm{P}) = \sum_{i=0}^{6} b_i \tau^i$, where $\tau = T(\mathrm{K})/1000$, [37]

*b_2 parameter for CO reported + sign by Todd and Young [37], which is incorrect; it should be negative

$k(\mathrm{W/(m \cdot K)}) = 0.01 \sum_{i=0}^{6} c_i \tau^i$, where $\tau = T(\mathrm{K})/1000$, [37]

T_c, P_c, dipole moment [38], diffusion volume [43],

$$k_{eff} = \varepsilon k_{mix} + (1 - \varepsilon) k_{cat}; \ (\mathrm{W/m \cdot K}) \tag{6.2}$$

where, k_{mix} is the gas mixture thermal conductivity, k_{cat} is the solid phase catalyst thermal conductivity. The thermal conductivity for the combustion-catalyst ($k_{cat,comb}$) is approximated based on an alumina and for the reforming-catalyst ($k_{cat,ref}$), it is approximated based on 60% alumina and 40% YSZ. Zhao et al. [39] reported the thermal conductivity of 1.55 $\mathrm{W \cdot m^{-1} \cdot K^{-1}}$ for 7% YSZ coating, which is the same amount of yttria (7%) added to the reforming-catalyst considered in this study. Hence, the thermal conductivity of the reforming-catalyst ($k_{cat,ref}$) is calculated based on the weighted average thermal conductivity of alumina and YSZ. Thermal conductivity of alumina is calculated as a function of temperature using Eq. (6.3) [40], where temperature T is in degree Celsius.

$$k_{cat,comb} = k_{Al_2O_3} = 5.85 + 15360\frac{exp(-0.002T)}{516 + T}; (\mathrm{W/m \cdot K}) \tag{6.3}$$

$$k_{cat,ref} = 0.6k_{Al_2O_3} + 0.4 \times 1.55; (\mathrm{W/m \cdot K}) \tag{6.4}$$

Both multi-component Maxwell-Stefan diffusion [41] and Knudsen diffusion [42] models are employed with the convection-diffusion equation to evaluate species diffusion fluxes inside porous catalysts, whereas only the multicomponent Maxwell-Stefan diffusion model is considered for the free flow regions in both flow channels. The Fuller equation [43] is used to obtain the binary diffusion coefficients (D_{ij}) for each chemical species involved. Required diffusion volumes (v_i) in the Fuller equation for each chemical species are given in Table 6.3. An average Bosanquet diffusion expression [44] is employed to evaluate the effective diffusion coefficients (Eq. (6.5)) involving the Knudsen diffusion (Eq. (6.6)) and the binary diffusion coefficients (Eq. (6.7)).

$$D_{ij,eff} = D_{ji,eff} = \frac{\varepsilon}{\tau}\frac{1}{2}\left(\frac{1}{1/D_i^K + 1/D_{ij}} + \frac{1}{1/D_j^K + 1/D_{ji}}\right) \tag{6.5}$$

$$\text{Knudsen diffusion: } D_i^K = \frac{d_{pore}}{3}\sqrt{\frac{8\mathrm{k}_B\mathrm{N}_A T}{\pi M_i}} \tag{6.6}$$

$$\text{Fuller equation: } D_{ij} = D_{ji} = \frac{0.00143T^{1.75}}{PM_{ij}^{0.5}\left[v_i^{\frac{1}{3}} + v_j^{\frac{1}{3}}\right]^2} \tag{6.7}$$

where, D_i^K and D_j^K are the Knudsen diffusion coefficients of chemical species *i* and *j*; D_{ij} is the diffusivity of chemical species *i* in *j*. Porosity (ε) value of 0.4 is assumed in both reforming and combustion-catalyst. The value of tortuosity (τ) in Eq. (6.5) is calculated using the Bruggeman correlation [45]. Mean pore diameter (d_{pore}) in Eq. (6.6) is assumed to be 20 nm [46] for both combustion and reforming catalysts. k_B and N_A represent the Boltzmann constant (1.38064852 × 10^{-23} J/K) and Avogadro number (6.0221409 × 10^{23} atoms/mol) respectively. M_i is the molecular weight of chemical species i, and M_{ij} is calculated as $M_{ij} = 2[(1/M_i) + (1/M_j)]^{-1}$ [38]. The permeability (κ) values for the porous structures are estimated using Kozeny-Carman relationship [44] (Eq. 3.13). Specific surface area ($A_{s,\,MSR}$) of 2.24 × 10^6 m^2/m^3 for the reforming-catalyst is determined based on 3.6 wt.% Ni with 4% dispersion and Ni site density of 2.6 × 10^{-5} mol/m^2 [47]. Ni loading of 4.2 g/m^2 is estimated based on the total coated mass of the Ni-spinel catalyst on a plate and 3.6% of metallic nickel. For the combustion-catalyst, a specific surface area ($A_{s,\,MC}$) of 1.4 × 10^6 m^2/m^3 is calculated based on 2.2 wt.% platinum with 13% dispersion [48] and platinum site density of 2.49 × 10^{-5} mol/m^2 [49]. To calculate the specific surface area (m^2/m^3), Eq. (6.8) reported by Herrera [50] is applied.

$$A_s = \mathrm{D} \cdot \frac{m_{active\ metal}}{M_{active\ metal}} \cdot \frac{1}{\Gamma} \cdot \frac{1}{V_{catalyst}} \tag{6.8}$$

where, D represents the dispersion of an active metal, *m* and *M* represent mass and molecular weight of an active metal (Ni or Pt) respectively, *Γ* represent the site density of an active metal component and $V_{catalyst}$ represents the total volume of the coated reforming or combustion catalyst.

To solve the coupled set of partial differential equations, commercially available simulation software package COMSOL™ 4.4 is used. COMSOL™ simulates the coupled set of heat, mass and flow equations using finite-element method (FEM). The CPR models are based on a distributed mapped mesh. More mesh elements are employed at the catalyst inlets where larger variations in reaction rates and thermal-gradients are occurred. All solutions are resolved using a finer mesh and mesh-independent solutions are obtained for all runs with convergence criteria of 1×10^{-5} absolute error. In all simulation runs, it is ensured that the conservation of mass in both combustion and reforming channels are satisfied. All governing partial differential equations and boundary conditions are presented in Appendix-A.

To develop the 2D steady-state numerical models of a CPR designed with different coating configurations between the combustion and reforming catalysts, following few assumptions are made. (1) Compressible ideal-gas, (2) fully-developed laminar flow in both channels, (3) both combustion and reforming catalysts coatings are isotropic and MSR takes place at porous surfaces of the reforming-catalyst, (4) total inlet flow to a CPR is distributed evenly to all flow channels, (5) catalyst particles are spherical in shape, (6) external forces including gravitational force are neglected, and (7) no radiation heat-transfer.

6.3. Validation of the microkinetic models

To simulate the MSR, widely acknowledged and accurate surface microkinetic model developed by Maier et al. [47] is implemented. Since this work is based on a nickel-spinel catalyst, our previous study [51] validated the microkinetic model of Maier et al. [47] using the experimentally measured kinetic data of MSR over Ni-spinel catalyst for the wide range of operating conditions and is presented in Table 6.4. More detail explanation about the model validation is presented elsewhere [51].

To simulate the catalytic MC, a reduced surface microkinetic model developed by Deshmukh and Vlachos [49] is implemented. Deshmukh and Vlachos [49] validated their surface rate model extensively against the experimental data of MC over different platinum based catalysts for the wide range of operating conditions. They reported the surface rate expression for MC over platinum as:

$$R_{CH_4}^{surface} = \frac{k_{CH_4}^{ads} C_{CH_4}}{\left(1 + \sqrt{\frac{k_{O_2}^{ads} C_{O_2}}{k_{O_2}^{des}}}\right)^2}, \tag{6.9}$$

where, k^{ads} and k^{des} are the reaction rate constants for the adsorption and desorption steps respectively. They are computed using the modified Arrhenius equation form for adsorption and desorption as:

$$k^{ads} = \frac{S_i^0}{\Gamma_{Pt}^{\tau}} \sqrt{\frac{\mathrm{R}_g T}{2\pi M_i}} T^{\beta^{ads}} exp\left(-\frac{E_a}{\mathrm{R}_g T}\right) \tag{6.10}$$

$$k^{des} = AT^{\beta^{des}} exp\left(-\frac{E_a}{R_g T}\right) \tag{6.11}$$

Table 6.4. *Microkinetic model for MSR over Ni-alumina spinel catalyst [51]. Original model is developed by Maier et al. [47].*

No.	Elementary Reactions	A [cm, mol, s]	β	E_a
r_1	H_2 + NI(s) + NI(s) → H(s) + H(s)	$0.0103 \times 10^{-00\dagger}$	0	0.0
r_2	O_2 + NI(s) + NI(s) → O(s) + O(s)	$0.010 \times 10^{-00\dagger}$	0	0.0
r_3	CH_4 + NI(s) → CH_4(s)	$7.311 \times 10^{-03\dagger}$	0	0.0
r_4	H_2O + NI(s) → H_2O(s)	$0.116 \times 10^{-00\dagger}$	0	0.0
r_5	CO_2 + NI(s) → CO_2(s)	$1.000 \times 10^{-05\dagger}$	0	0.0
r_6	CO + NI(s) → CO(s)	$4.626 \times 10^{-01\dagger}$	0	0.0
r_7	H(s) + H(s) → NI(s) + NI(s) + H_2	$2.143 \times 10^{+19}$	0	81.21
r_8	O(s) + O(s) → NI(s) + NI(s) + O_2	$4.283 \times 10^{+23}$	0	474.95
r_9	CH_4(s) → CH_4 + NI(s)	$8.950 \times 10^{+15}$	0	37.55
r_{10}	H_2O(s) → H_2O + NI(s)	$3.909 \times 10^{+12}$	0	60.79
r_{11}	CO_2(s) → CO_2 + NI(s)	$6.447 \times 10^{+07}$	0	25.98
r_{12}	CO(s) → CO + NI(s)	$3.628 \times 10^{+11}$	0	$111.27\text{-}50\vartheta_{CO(s)}$
r_{13}	H(s) + O(s) → OH(s) + NI(s)	$5.000 \times 10^{+22}$	0	97.9
r_{14}	OH(s) + NI(s) → H(s) + O(s)	$1.781 \times 10^{+21}$	0	36.09
r_{15}	H(s) + OH(s) → H_2O(s) + NI(s)	$3.000 \times 10^{+20}$	0	42.7
r_{16}	H_2O(s) + NI(s) → H(s) + OH(s)	$2.271 \times 10^{+21}$	0	91.76
r_{17}	OH(s) + OH(s) → H_2O(s) + O(s)	$3.000 \times 10^{+21}$	0	100.0
r_{18}	H_2O(s) + O(s) → OH(s) + OH(s)	$6.373 \times 10^{+23}$	0	210.86
r_{19}	C(s) + O(s) → CO(s) + NI(s)	$5.200 \times 10^{+23}$	0	148.1
r_{20}	CO(s) + NI(s) → C(s) + O(s)	$1.354 \times 10^{+22}$	-3	$116.12\text{-}50\vartheta_{CO(s)}$
r_{21}	CO(s) + O(s) → CO_2(s) + NI(s)	$2.000 \times 10^{+19}$	0	$123.6\text{-}50\vartheta_{CO(s)}$
r_{22}	CO_2(s) + NI(s) → CO(s) + O(s)	$4.653 \times 10^{+23}$	-1	89.32
r_{23}	HCO(s) + NI(s) → CO(s) + H(s)	$3.700 \times 10^{+21}$	0	$50\vartheta_{CO(s)}$
r_{24}	CO(s) + H(s) → HCO(s) + NI(s)	$4.019 \times 10^{+20}$	-1	132.23
r_{25}	HCO(s) + NI(s) → CH(s) + O(s)	$3.700 \times 10^{+24}$	0	95.8
r_{26}	CH(s) + O(s) → HCO(s) + NI(s)	$4.604 \times 10^{+20}$	0	109.97
r_{27}	CH_4(s) + NI(s) → CH_3(s) + H(s)	$4.574 \times 10^{+21}$	0	57.7
r_{28}	CH_3(s) + H(s) → CH_4(s) + NI(s)	$1.327 \times 10^{+22}$	0	61.58
r_{29}	CH_3(s) + NI(s) → CH_2(s) + H(s)	$3.700 \times 10^{+24}$	0	100.0
r_{30}	CH_2(s) + H(s) → CH_3(s) + NI(s)	$1.293 \times 10^{+23}$	0	55.33
r_{31}	CH_2(s) + NI(s) → CH(s) + H(s)	$2.370 \times 10^{+24}$	0	97.1
r_{32}	CH(s) + H(s) → CH_2(s) + NI(s)	$5.722 \times 10^{+23}$	0	79.18
r_{33}	CH (s) + NI(s) → C(s) + H(s)	$3.700 \times 10^{+21}$	0	18.8
r_{34}	C(s) + H(s) → CH(s) + NI(s)	$4.562 \times 10^{+22}$	0	161.11
r_{35}	CH_4(s) + O(s) → CH_3(s) + OH(s)	$1.700 \times 10^{+24}$	0	88.3
r_{36}	CH_3(s) + OH(s) → CH_4(s) + O(s)	$9.876 \times 10^{+22}$	0	30.37
r_{37}	CH_3(s) + O(s) → CH_2(s) + OH(s)	$3.700 \times 10^{+24}$	0	130.1
r_{38}	CH_2(s) + OH(s) → CH_3(s) + O(s)	$4.607 \times 10^{+21}$	0	23.62
r_{39}	CH_2(s) + O(s) → CH(s) + OH(s)	$3.700 \times 10^{+24}$	0	126.8
r_{40}	CH(s) + OH(s) → CH_2(s) + O(s)	$1.457 \times 10^{+23}$	0	47.07
r_{41}	CH(s) + O(s) → C(s) + OH(s)	$3.700 \times 10^{+21}$	0	48.10
r_{42}	C(s) + OH(s) → CH(s) + O(s)	$1.625 \times 10^{+21}$	0	128.61
				†sticking coefficient

where, τ is the number of occupied adsorption sites of species i, S_i^0 is the initial (uncovered surface) sticking coefficient, Γ_{Pt} is the site density, which is equal to 2.49×10^{-5} mol/m^2 [49]. In this study, kinetic parameters reported by Deshmukh and Vlachos [49] for the CHEMKIN are implemented and are presented in Table 6.5. To compute the rate of catalytic MC using Eq.

(6.9), one needs to know the coverage of oxygen because the activation energy for oxygen desorption is dependent on the surface coverage of oxygen (θ_O). The θ_O is computed using the following nonlinear relationship reported by Deshmukh and Vlachos [49]:

Table 6.5. *Kinetic parameters for catalytic methane combustion on platinum catalyst [49].*

S^0_{fuel}	$S^0_{O_2}$	β^{ads}_{fuel}	$\beta^{ads}_{O_2}$	$\beta^{des}_{O_2}$	$A^{des}_{O_2}$ **[1/s]**	$E^{ads}_{a\,fuel}$ **[kcal/mol]**	$E^{des}_{a\,O_2}$ **[kcal/mol]**
709.55	6.86×10^{-4}	-1.529	0.766	1.039	9.04×10^{18}	9.6	$49.5\text{-}32.0\cdot\theta_O$

$$\theta_O = \frac{\sqrt{k^{ads}_{O_2} C_{O_2} / k^{des}_{O_2}}}{1 + \sqrt{k^{ads}_{O_2} C_{O_2} / k^{des}_{O_2}}} \tag{6.12}$$

Homogeneous or gas-phase MC plays a vital role at elevated temperatures and should not be neglected completely, especially in the inter-catalyst spaces of the distributed combustion-catalyst. To account for the species consumption and production rates due to gas-phase MC, a power-law type rate-expression is adopted from Pattison et al. [13]. They reported a simplified rate law of order of -0.3 and 1.3 with respect to the CH_4 concentration (C_{CH_4}) and the oxygen concentration (C_{O_2}), an activation energy of 125.49×10^3 J·mol^{-1}, and a pre-exponential factor of 8.3×10^5 s^{-1}. The gas-phase rate expression (Eq. (6.13)) is implemented in free-flow combustion-channel as well as porous regions of the combustion-catalyst coating.

$$R^{gas-phase}_{CH4} = 8.3 \times 10^5 exp\left(\frac{-125.49 \times 10^3}{\mathrm{R}_g T}\right) C^{-0.3}_{CH_4} C^{1.3}_{O_2} \tag{6.13}$$

6.4. Results and discussion

The 2D steady-state numerical models developed for the CPR are utilized to investigate the performance of different distributed coating patterns of the DCCR and DCDR configurations. Results obtained with the different distributed coating patterns are compared with the conventional CCCR configuration in terms of temperature distribution, overall efficiency ($E_{overall}$), CH_4 conversions (X_{CH4}), H_2 production rate (N_{H2}), H_2 yield (Y_{H2}), CO selectivity (S_{CO}) and H_2/CO ratio. Before moving to the study of the coating patterns of the catalysts, it is important to investigate the internal diffusion limitations of the coated reforming and combustion catalysts. With this aim, the first part of the results and discussion section presents the isothermal study to investigate the internal diffusion limitations by determining local (η^{local}_i) and overall ($\eta^{overall}_i$) effectiveness factors for the different thickness of the coated reforming and combustion catalysts. In the second part, the study investigates the performance of the five different patterns of the DCCR, where each distributed section of the combustion-catalyst is coated with fixed $l_{c,\,active}$ but with different $l_{c,\,blank}$ in combination with the reforming-catalyst coated continuously on the opposite side of the plate with fixed $L_{r,\,active}$. In the third part, the study investigates the performance of the five different patterns of the DCDR, where each distributed section of the reforming-catalyst is coated with different $l_{r,\,active}$ but with fixed $l_{r,\,blank}$ in combination with the distributed combustion-catalyst coated on the opposite side of the plate with fixed $l_{c,\,active}$ and fixed $l_{c,\,blank}$. In the concluding part of the results and discussion section, the study investigates the influence of the δ_{plate} on the performance of CCCR, DCCR and DCDR by considering three different δ_{plate}. For all coating configurations, inlet CH_4 flow-rate of 9.94 mol/h

Table 6.6. *Inlet conditions for the different coating configurations.*

	CCCR/DCCR/DCDR	
Inlet conditions	**Reforming-channel (MSR)**	**Combustion-channel (MC)**
total CH_4 molar flow for 30 channels, mol/h	9.936	4.413 at $m_{MC/MSR}$ =3 5.886 at $m_{MC/MSR}$ =4
CH_4 molar flow in one channel, N_{CH4}, mol/h	0.3312	0.1471 at $m_{MC/MSR}$ =3 0.1962 at $m_{MC/MSR}$ =4
mass flow rates ratio ($m_{MC/MSR}$=m_{comb}/m_{ref})	n/a	3, 4
steam to carbon ratio (SC)	1.5	n/a
oxygen to carbon ratio (O_2/C)	n/a	2
H_2O molar flow in a single channel, N_{H2O}, mol/h	SC × $N_{CH4,\ MSR}$	n/a
O_2 molar flow in a single channel, N_{O2}, mol/h	n/a	(O_2/C) × $N_{CH4,\ MC}$
N_2 molar flow in a single channel, N_{N2}, mol/h	n/a	(79/21) × N_{O2}
inlet temperature, K	800	800
pressure, Pa.	101325	101325

on the reforming-side is calculated based on the requirement of H_2 feed rate of 29.80 mol/h in a 1kW fuel cell consisting of 158 individual cells with 0.7 cell voltage and 90% H_2 utilization on the anode-side and based on the 3:1 stoichiometric ratio between H_2 and CH_4 in MSR reaction. The inlet flow rate for the combustion-side is determined based on the $m_{MC/MSR}$. In this study two different $m_{MC/MSR}$ ratios of 3 and 4 are considered. Inlet conditions considered for this study are presented in Table 6.6.

Performance of the CPR designed with different coating configurations is evaluated by reactant conversion, product yield, product selectivity, and overall efficiency. X_{CH4} in both combustion and reforming channels is defined as the ratio between converted CH_4 at a position along the channel and the inlet molar rate of CH_4:

$$\mathrm{X_{CH4}} = 100 \times \left[\frac{N_{\mathrm{CH_{4,in}}} - N_{\mathrm{CH_4}}}{N_{\mathrm{CH_{4,in}}}}\right] \tag{6.14}$$

where, $N_{\mathrm{CH_{4,in}}}$ is the inlet molar flow-rate of methane and $N_{\mathrm{CH_4}}$ is the molar flow-rate of methane at a position along the flow channels. Y_{H2} characterizes the performance of the reactor with respect to H_2 production. It is defined as the ratio of the produced H_2 to the theoretical maximum amount of H_2 that can be produced in MSR and water-gas-shift (WGS) reactions:

$$\mathrm{Y_{H2}} = 100 \times \left[\frac{1}{4}\frac{N_{\mathrm{H_2}}}{N_{\mathrm{CH_{4,in}}}}\right] \tag{6.15}$$

where, $N_{\mathrm{H_2}}$ is the molar flow-rate of H_2. S_{CO} is defined as the ratio of the produced molar rate of CO to the produced molar rate of CO and carbon-dioxide (CO_2):

$$\mathrm{S_{CO}} = 100 \times \left[\frac{N_{\mathrm{CO}}}{N_{\mathrm{CO}} + N_{\mathrm{CO_2}}}\right] \tag{6.16}$$

where, N_{CO} and $N_{\mathrm{CO_2}}$ are the molar flow-rates of CO and CO_2 at a position along reforming-channel length. Another important parameter to evaluate the performance of a reformer is its overall efficiency ($E_{overall}$), which is the ratio of the lower heating value (LHV) of H_2 and CO produced to the LHV of CH_4 consumed [6]. For the CPR, where MSR is coupled with MC, LHV of CH_4 consumed on the combustion-side should also be accounted for in calculating the $E_{overall}$:

$$\mathrm{E_{overall}} = 100 \times \left[\frac{\mathrm{LHV_{H_2}}N_{\mathrm{H_2}} + \mathrm{LHV_{CO}}N_{\mathrm{CO}}}{\mathrm{LHV_{CH_4}}\left(N_{\mathrm{CH_{4,in}}} - N_{\mathrm{CH_4}}\right)_{\mathrm{MSR}} + \mathrm{LHV_{CH_4}}\left(N_{\mathrm{CH_{4,in}}} - N_{\mathrm{CH_4}}\right)_{\mathrm{MC}}}\right] \qquad (6.17)$$

The LHV of any fuel $\mathrm{C_xH}_y\mathrm{O}_z$ is calculated by the following formula [6]:

$$\mathrm{LHV}_{\mathrm{C_xH}_y\mathrm{O}_z}(\mathrm{kJ \cdot mol^{-1}}) = \left(\frac{y}{2} + 2x - z\right)198.8 + 25.4 \qquad (6.18)$$

To account for the internal diffusion limitations of the coated combustion and reforming catalysts, local and overall effectiveness factors are determined as follows [46, 54]:

$$\eta_i^{local} = \frac{\frac{1}{\delta^{cat}}\int_0^{\delta^{cat}} R_i dy}{R_i|_{surface}} \qquad (6.19)$$

$$\eta_i^{overall} = \frac{1}{L_{active}}\int_0^{L_{active}} \eta_i^{local}(x)dx \qquad (6.20)$$

where, δ^{cat} is the thickness of the combustion or reforming catalyst, η_i^{local} and $\eta_i^{overall}$ are the local and overall effectiveness factors based on the net reaction rate (R_i) of reactant *i* respectively, L_{active} is the total length of an active catalyst. Also, to compare any difference in the reaction rates between different coating configurations, an average surface reaction ($R_{avg,i}^{surface}$) and an overall reaction rate ($R_i^{overall}$) for the chemical specie i are calculated as:

$$R_{avg,i}^{surface} = \frac{1}{L_{active}}\int_0^{L_{active}} R_{surface,i}dx \qquad (6.21)$$

$$R_i^{overall} = \frac{1}{L_{active}\delta^{cat}}\int_0^{L_{active}}\int_0^{\delta^{cat}} R_i\, dydx \qquad (6.22)$$

Both sides gas hourly space velocities (GHSVs) are estimated at the normalized condition of 298.15 K and 101325 Pa, defined as the ratio of volume flow of feed ($\dot{V}_{feed}$) to active catalyst volume (V_{cat}) [6]:

$$\mathrm{GHSV}\,[\mathrm{h^{-1}}] = \frac{\dot{V}_{feed}}{V_{cat}} \qquad (6.23)$$

Based on the inlet conditions presented in Table 6.6, inlet GHSVs in the reforming-channel ($\mathrm{GHSV_{MSR}}$) and in the combustion-channel ($\mathrm{GHSV_{MC}}$) for the CCCR are equal to 81,028 $\mathrm{h^{-1}}$ and 1.5153×10^6 $\mathrm{h^{-1}}$ respectively when $m_{\mathrm{MC/MSR}} = 3$. For $m_{\mathrm{MC/MSR}} = 4$, $\mathrm{GHSV_{MC}}$ is equal to 2.0203×10^6 $\mathrm{h^{-1}}$, whereas $\mathrm{GHSV_{MSR}}$ is kept constant, 81,028 $\mathrm{h^{-1}}$.

6.4.1. Internal diffusion limitation

It is well established that a CPR design is suitable to integrate the endothermic MSR with the exothermic MC for an autothermal operation. As mentioned earlier, catalytic MC is a fast reaction relative to MSR, which creates an imbalance between the production and absorption rates of heat. Such imbalance of heat could be further propagated if MSR is limited by an internal diffusion. Thus, it is important that reactants on the reforming-side spread uniformly throughout the reforming-catalyst coating and able to utilize exothermic heat effectively. Longer diffusion paths and relatively faster MSR reaction at the interfaces (boundary 13 in Fig. 6.1) of the reforming-channel and reforming-catalyst decrease the utilization of the reforming-catalyst, resulting to internal diffusion limitation. Thus, isothermal studies at constant GHSVs are carried

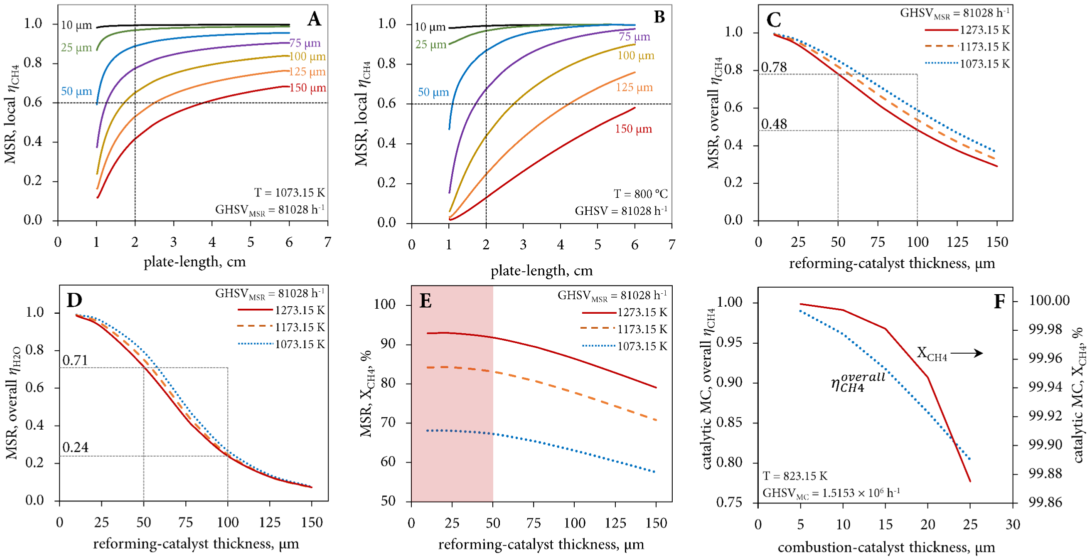

Fig. 6.2 *(A) Local effectiveness factors based on CH_4, and (B) H_2O as a function of the plate-length, (C) overall effectiveness factors based on CH_4, and (D) H_2O as a function of the reforming-catalyst thickness, (E) methane conversion obtained in MSR and (F) in catalytic MC as a function of respective catalyst thickness.*

out to investigate the influence of catalysts thickness on the diffusion limitation using single channel models developed separately for the MSR and catalytic MC. The geometric dimensions for the single channel models are same as combustion and reforming channels presented in Table 6.1 under CCCR. To determine an effective utilization of the reforming-catalyst, local and overall effectiveness factors (Eq. (6.19), Eq. (6.20)) are calculated based on the surface and overall reaction rates of CH_4 and H_2O at three different temperatures (1073.15, 1173.15, and 1273.15 K) for $GHSV_{MSR}$ of 81,028 h^{-1}. For the combustion-catalyst, an overall effectiveness factors based on the overall reaction rate of CH_4 are calculated at 823.15 K for $GHSV_{MC}$ of 1.5153 × 10^{6} h^{-1}. Reforming-catalyst thickness is varied from 10 to 150 µm, whereas for the combustion-catalyst, it is varied from 5 to 25 µm. Inlet space velocities (GHSVs) are kept constant for all thicknesses studied, thus the inlet flow rate of CH_4 is adjusted to keep the GHSV (Eq. (6.23)) constant with respect to varied thickness of the combustion and reforming catalysts. SC ratio of 1.5 and O_2/C ratio of 2 are considered for the MSR and catalytic MC respectively.

Fig. 6.2A and B present the local effectiveness factors based on the reaction rates of CH_4 and H_2O as a function of the reforming-catalyst length at 1073.15 K. Fig. 6.2A shows that the $\eta_{CH_4}^{local}$ for the respective thickness are low for the first 20% of the reforming-catalyst length and then increases slowly for the rest of the length. This is attributed to the fact that readily available reactants at the reforming-catalyst section near the reforming-channel inlet increase the reaction rates of MSR closer to its intrinsic value at the interfaces (boundary 13 in Fig. 6.1) of the reforming-catalyst and reforming-channel. High reaction rates of MSR at the interfaces of the channel and catalyst decrease the availability of reactants inside the reforming-catalyst coating, which results into lower values of $\eta_{CH_4}^{local}$ for the initial 20% of the reforming-catalyst length. For the thin (10–50 µm) coating of the reforming-catalyst, $\eta_{CH_4}^{local}$ values obtained for the entire catalyst-length are ≥ 0.6 and approach to one at the exit end of the reforming-catalyst, whereas for the relatively thicker coatings (> 50 µm), the minimum value of $\eta_{CH_4}^{local}$ obtained is less than 0.6 and unlike thinner coatings, does not reach close to one at the exit end of the reforming-catalyst. This indicates that reforming-catalyst thickness more than 50 µm plays a significant role in internal-diffusion limitation as clearly observed from the Fig. 6.2A. Similarly, Fig. 6.2B illustrates $\eta_{H_2O}^{local}$ plots for the different thickness as a function of the reforming-catalyst length. Profiles of the $\eta_{H_2O}^{local}$ for 10 to 50 µm coating thickness are like that of $\eta_{CH_4}^{local}$, low at the initial 20% of the reforming-catalyst length and then increases for the rest of the length and approach close to one at the exit end of the reforming-catalyst. Whereas for the thicker coatings (> 50 µm), the minimum value of $\eta_{H_2O}^{local}$ is less than 0.5 and unlike thinner coatings (≤ 50 µm), does not reach close to one at the exit end of the reforming-catalyst. Fig. 6.2C and D illustrate the overall effectiveness factors (Eq. (6.20)) based on the net reaction rates of CH_4 and H_2O respectively, as a function of the reforming-catalyst thickness for the three temperatures. At the highest studied temperature (1273.15 K), as expected, lowest values for the $\eta_{CH_4}^{overall}$ and $\eta_{H_2O}^{overall}$ are observed due to relatively faster reaction rate of MSR reactions at the top surface of the reforming-catalyst coating compared to the lower temperatures (1073.15 and 1173.15 K). The overall effectiveness factor values can also be linked with in determining how effectively the catalysts are being utilized by the reactants. As illustrated in Fig. 6.2C, it is observed that utilization ($\eta_{CH_4}^{overall}$) of the reforming-catalyst by the CH_4 reactant decreases with increasing thickness. Also, over 75% utilization of the reforming-catalyst is determined for the thinner coatings of 50 µm or less. For the 100 µm thick coating, the utilization is decreased to 48% and for the highest studied thickness of 150 µm, the catalyst utilization is decreased to very low 29%. It is interesting to observe in Fig. 6.2D that overall effectiveness factors based on H_2O is decreased rapidly compared to the $\eta_{CH_4}^{overall}$ with increasing thickness of the reforming-catalyst. For example, $\eta_{H_2O}^{overall}$ is 71% for 50 µm compared to 78% for $\eta_{CH_4}^{overall}$ and 24% for 100 µm compared to 48% for $\eta_{CH_4}^{overall}$. This is attributed to faster consumption of H_2O mostly at the interfaces of the reforming-catalyst and reforming-channel due to higher sticking coefficient of H_2O than CH_4 (Table 6.4). Based on this study, it is conclusive that coating thickness more than 50 µm can reduce the utilization of the reforming-catalyst significantly. This can be further confirmed in terms of X_{CH4} illustrated in Fig. 6.2E. X_{CH4} in MSR decreases with increasing reforming-catalyst thickness for all three temperatures, and it is also observed that the slope of X_{CH4} reduction is also increased for the coating thickness of greater than 50 µm.

In the case of catalytic MC, the isothermal study is conducted at 823.15 K by altering the combustion-catalyst thickness from 5 to 25 µm. As mentioned earlier, catalytic MC is the fast reaction and thus over 99% of X_{CH4} is achieved for all studied coating thicknesses as illustrated in Fig. 6.2F. However, the utilization of the combustion-catalyst by CH_4 reactant decreases sharply with increasing coating thickness of the combustion-catalyst. It can be observed based on the overall effectiveness factor values plotted in Fig. 6.2F that 100% utilization of the combustion-catalyst is achieved with 5 µm thin coating and the utilization of the combustion-catalyst decreases sharply for the coatings greater than 5 µm thickness.

Based on the isothermal studies of the coating thickness, it is concluded that reforming-catalyst thickness greater than 50 µm and combustion-catalyst thickness greater than 5 µm showed diffusion limitation for the considered operating conditions and thus, for the remainder sections, reforming-catalyst thickness of 50 µm and combustion-catalyst thickness of 5 µm is considered.

6.4.2. The study of five different patterns of the DCCR configuration

In our previous studies [21, 22], we found that hot-spots and longitudinal thermal gradients can be reduced considerably along with significant savings of combustion-catalyst in a CPR designed with the distributed coatings compared to the conventional continuous coatings. Jeon et al. [14] carried out an optimization study to determine an optimum length ($l_{c,\ active}$) of the distributed coating sections of a combustion-catalyst, an optimum inter-catalyst space length ($l_{c,\ blank}$), and an optimum number ($N_{c,\ active}$) of distributed coating sections of a combustion-catalyst to reduce the thermal hot-spots. However, they considered distributed coating of a combustion-catalyst only for the initial 50% plate-length and did not address the issue of the longitudinal thermal gradients for the remaining plate-length. They also reported that optimization of $l_{c,\ blank}$ is more effective to reduce the thermal hot-spots compared to $l_{c,\ active}$. However, they restricted their study to 1 mm size for $l_{c,\ blank}$. In this study, further analysis is carried out on the performance of a CPR configured with $l_{c,\ blank}$ beyond 1 mm by considering distributed coating of the combustion-catalyst for the entire plate-length.

For this study, $l_{c,\ active}$ of each distributed coating section of the active combustion-catalyst is considered fix at 1 mm [14]. Number of active sections ($N_{c,\ active}$) each coated with $l_{c,\ active}$ = 1 mm depends on $l_{c,\ blank}$ because of the fixed plate-length. It should be noted that the combustion and reforming catalysts are coated between x = 1 and 6 cm for all coating configurations. To investigate the influence of $l_{c,\ blank}$ in the DCCR, five different $l_{c,\ blank}$ = 1, 2, 3, 4, and 5 mm are considered. Based on the considered $l_{c,\ blank}$ of 1, 2, 3, 4, and 5 mm, $N_{c,\ active}$, each coated with $l_{c,\ active}$ = 1 mm are 25, 17, 13, 10 and 9 respectively. Thus, the total active length ($L_{c,\ active}$) corresponding to $l_{c,\ blank}$ of 1, 2, 3, 4, and 5 mm are also 25, 17, 13, 10 and 9 mm respectively. In other words, for $l_{c,\ blank}$ = 1 mm, 50% of the active combustion-catalyst is removed ($L_{c,\ active}$ = 25 mm), for $l_{c,\ blank}$ = 2 mm, 66% of the active combustion-catalyst is removed ($L_{c,\ active}$ = 17 mm), for

Table 6.7. *Parameters for the DCCR and CCCR configurations.*

<table>
<tr><th colspan="7">Combustion-side</th></tr>
<tr><th></th><th>CCCR</th><th colspan="5">DCCR</th></tr>
<tr><th></th><th>$l_{c,\ blank}$=0</th><th>$l_{c,\ blank}$=1 mm</th><th>$l_{c,\ blank}$=2 mm</th><th>$l_{c,\ blank}$=3 mm</th><th>$l_{c,\ blank}$=4 mm</th><th>$l_{c,\ blank}$=5 mm</th></tr>
<tr><td>inlet CH_4 flow (N_{CH4}), mol/h when $m_{MC/MSR}$=3</td><td>0.1471</td><td>0.1471</td><td>0.1471</td><td>0.1471</td><td>0.1471</td><td>0.1471</td></tr>
<tr><td>inlet CH_4 flow (N_{CH4}), mol/h when $m_{MC/MSR}$=4</td><td>0.1962</td><td>0.1962</td><td>0.1962</td><td>0.1962</td><td>0.1962</td><td>0.1962</td></tr>
<tr><td>oxygen to carbon ratio (O_2/C)</td><td>2</td><td>2</td><td>2</td><td>2</td><td>2</td><td>2</td></tr>
<tr><td>O_2 molar flow in a single channel, N_{O2}, mol/h</td><td>(O_2/C) × N_{CH4}</td><td>(O_2/C) × N_{CH4}</td><td>(O_2/C) × N_{CH4}</td><td>(O_2/C) × N_{CH4}</td><td>(O_2/C) × N_{CH4}</td><td>(O_2/C) × N_{CH4}</td></tr>
<tr><td>N_2 molar flow in a single channel, N_{N2}, mol/h</td><td>(79/21) × N_{O2}</td><td>(79/21) × N_{O2}</td><td>(79/21) × N_{O2}</td><td>(79/21) × N_{O2}</td><td>(79/21) × N_{O2}</td><td>(79/21) × N_{O2}</td></tr>
<tr><td>inlet temperature, K</td><td>800</td><td>800</td><td>800</td><td>800</td><td>800</td><td>800</td></tr>
<tr><td>volume of active catalyst on one plate, mm^3</td><td>12.5</td><td>6.25</td><td>4.25</td><td>3.25</td><td>2.50</td><td>2.25</td></tr>
<tr><td>active catalyst amount on one plate, mg</td><td>29.6</td><td>14.8</td><td>10.0</td><td>7.7</td><td>5.9</td><td>5.3</td></tr>
<tr><td>total length of active catalyst ($L_{c,\ active}$), mm</td><td>50</td><td>25</td><td>17</td><td>13</td><td>10</td><td>9</td></tr>
<tr><td>thickness of active catalyst section (δ_r), µm</td><td>5</td><td>5</td><td>5</td><td>5</td><td>5</td><td>5</td></tr>
<tr><td>width of active catalyst, mm</td><td>50</td><td>50</td><td>50</td><td>50</td><td>50</td><td>50</td></tr>
<tr><td>$GHSV_{MC}$, h^{-1} when $m_{MC/MSR}$=3</td><td>1.5153×10^6</td><td>3.0305×10^6</td><td>4.4566×10^6</td><td>5.8279×10^6</td><td>7.5763×10^6</td><td>8.4181×10^6</td></tr>
<tr><td>$GHSV_{MC}$, h^{-1} when $m_{MC/MSR}$=4</td><td>2.0203×10^6</td><td>4.0407×10^6</td><td>5.9422×10^6</td><td>7.7705×10^7</td><td>1.0102×10^7</td><td>1.1224×10^7</td></tr>
<tr><th colspan="7">Reforming-side</th></tr>
<tr><th></th><th>CCCR</th><th colspan="5">DCCR (for all $l_{c,\ blank}$ configurations listed above)</th></tr>
<tr><th></th><th>$l_{r,\ blank}$=0</th><th colspan="5">$l_{r,\ blank}$=0</th></tr>
<tr><td>inlet CH_4 flow (N_{CH4}), mol/h</td><td>0.3312</td><td colspan="5">0.3312</td></tr>
<tr><td>steam to carbon ratio (SC)</td><td>1.5</td><td colspan="5">1.5</td></tr>
<tr><td>H_2O molar flow in a single channel, N_{O2}, mol/h</td><td>SC × N_{CH4}</td><td colspan="5">SC × N_{CH4}</td></tr>
<tr><td>inlet temperature, K</td><td>800</td><td colspan="5">800</td></tr>
<tr><td>volume of active catalyst on one plate, mm^3</td><td>125</td><td colspan="5">125</td></tr>
<tr><td>active catalyst amount on one plate, mg</td><td>296.25</td><td colspan="5">296</td></tr>
<tr><td>thickness of active catalyst section (δ_r), µm</td><td>50</td><td colspan="5">50</td></tr>
<tr><td>width of active catalyst, mm</td><td>50</td><td colspan="5">50</td></tr>
<tr><td>total length of active catalyst ($L_{r,\ active}$), mm</td><td>50</td><td colspan="5">50</td></tr>
<tr><td>$GHSV_{MSR}$, h^{-1}</td><td>81028</td><td colspan="5">81028</td></tr>
</table>

$l_{c,\ blank}$ = 3 mm, 74% of the active combustion-catalyst is removed ($L_{c,\ active}$ = 13 mm), for $l_{c,\ blank}$ = 4 mm, 80% of the active combustion-catalyst is removed ($L_{c,\ active}$ = 10 mm), and for $l_{c,\ blank}$ = 5 mm, 82% of the active combustion-catalyst is removed ($L_{c,\ active}$ = 9 mm) compared to the conventional CCCR. For this study, $GHSV_{MSR}$ of 81028 h^{-1} is considered fix based on the required feed rate of H_2 in a 1 kW fuel cell, and $GHSV_{comb}$ corresponding to different $l_{c,\ blank}$ for $m_{MC/MSR}$ = 3 and 4 are presented in Table 6.7.

6.4.2.1. Temperature distributions in five different patterns of the DCCR coating configuration and comparison with the conventional CCCR coating configuration

Fig. 6.3A to F illustrate the temperature distribution in the CCCR and in DCCR configured with $l_{c,\ blank}$ = 1, 2, 3, 4, and 5 mm for the $m_{MC/MSR}$ = 3. Fig. 6.3A shows that in the CCCR, maximum plate temperature (T_{max}) of 1216 K (at x = 1.4 cm) and exit plate temperature (T_{exit}) of 1096 K (at x = 7 cm) are obtained, which makes the difference of 120 K between T_{max} and T_{exit}. Difference of 120 K within very short distance indicates significant thermal gradients in the direction of flow. Such large thermal gradients not only accelerate the thermal degradation rate of the plate material due to thermal stresses but also decrease the active surface area of the catalysts [10] and delaminate the coated catalysts from the plate surface. Large thermal gradients also create thermal hot-spots that increase the risk of complete failure of a thin metal plate. In Fig. 6.3A, bright regions (hot-spots) between x = 1 and 2 cm are clearly visible in the case of CCCR. Under such conditions, as noted earlier, distributed coatings of the combustion-catalyst can be effective in minimizing the thermal gradients and thus keeping the thermal degradation rate of the plate material and catalysts delamination issues in control. Fig. 6.3B to F illustrate the temperature distribution for the five different patterns of the DCCR with $l_{c,\ blank}$ = 1, 2, 3, 4, and 5 mm respectively. From the study of these different DCCR patterns, it is predicted for the δ_{plate} = 0.2 mm that T_{max} decreases and T_{exit} increases with increasing $l_{c,\ blank}$ compared to the conventional CCCR. It is shown in Fig. 6.3B to F that DCCR configured with $l_{c,\ blank}$ = 1, 2, 3, 4, 5 mm reduces T_{max} by 8, 13, 16, 18, 19 K respectively and increases T_{exit} by 23, 46, 65, 79, 93 K respectively, compared to the conventional CCCR. Such reverse trend in the predicted T_{max} and T_{exit} between the CCCR and different patterns of the DCCR indicates reduction in thermal gradients and hence, uniform temperature distribution is achieved in the direction of flow, as can be seen from the decreasing difference of 89, 61, 39, 23 and 8 K between T_{max} and T_{exit} in the DCCR configured with $l_{c,\ blank}$ = 1, 2, 3, 4, and 5 mm, respectively. This is due to the transfer of heat from the combustion-side to the reforming-side through the inter-catalyst space ($l_{c,\ blank}$) slightly lowers the combustion-side reactants temperature, boosting exothermic combustion reaction in the forward direction when reactants encounter the next active section of the combustion-catalyst [22]. Also, longer $l_{c,\ blank}$ sections (> 3 mm) decrease the combustion-side reactants temperature relatively more compared to the shorter $l_{c,\ blank}$, providing extra boost to the exothermic combustion reaction to move in the forward direction, resulting in high T_{exit} with increasing $l_{c,\ blank}$. It is important to note that bright spot region between x = 1 and 2 cm in the case of CCCR (Fig. 6.3A) decreases significantly when DCCR is configured with $l_{c,\ blank}$ of 3, 4 and 5 mm (Fig. 6.3D, E and F). It should also be noted that despite consideration of the gas-phase MC on the combustion-side, significant variation in the plate temperature is obtained by varying the length of inter-catalyst space among the distributed coating sections of the active combustion catalyst. This indicates that the contribution of the gas-phase MC is not significant compared to the catalytic MC.

To investigate how distributed coating patterns of the DCCR configuration perform at the elevated temperatures, N_{CH4} on the combustion-side is increased from $m_{MC/MSR}$ = 3 to $m_{MC/MSR}$ =

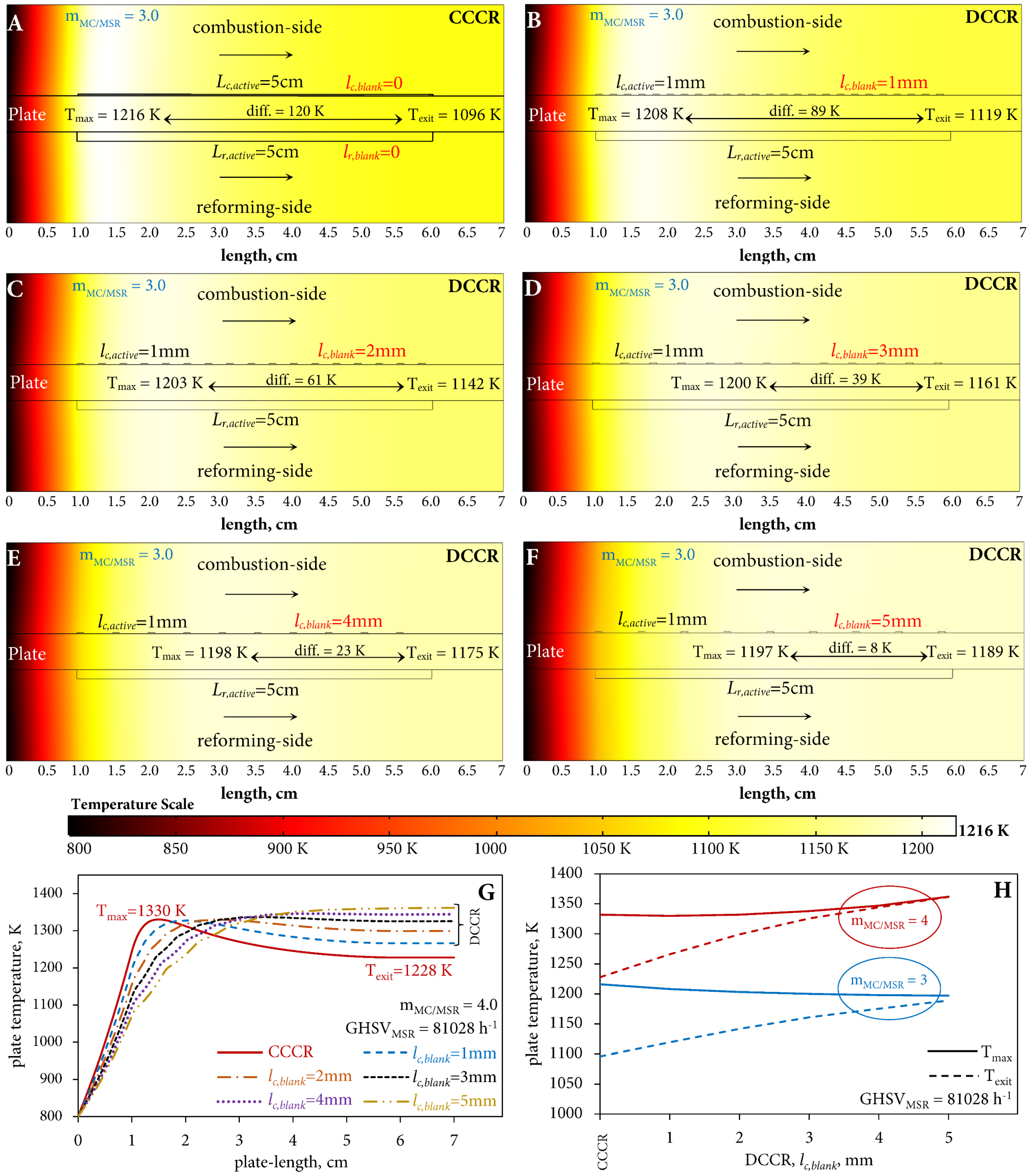

Fig. 6.3 *(A) Temperature distribution for $m_{MC/MSR}$ = 3 in CCCR, (B) in DCCR configured with $l_{c, blank}$ = 1 mm, (C) $l_{c, blank}$ = 2 mm, (D) $l_{c, blank}$ = 3 mm, (E) $l_{c, blank}$ = 4 mm, (F) $l_{c, blank}$ = 5 mm, (G) longitudinal temperature profiles at the plate center for $m_{MC/MSR}$ = 4 obtained in CCCR and in different DCCR configurations, (H) maximum and exit plate temperature as a function of different DCCR configurations ($l_{c, blank}$ = 1 to 5 mm) for $m_{MC/MSR}$ = 3 and 4.*

4 by keeping the N_{CH4} constant on the reforming-side. Fig. 6.3G illustrates the temperature profiles at the plate center for the CCCR and for the DCCR configured with $l_{c, blank}$ = 1, 2, 3, 4, 5 mm as a function of the plate-length for the $m_{MC/MSR}$ = 4. Fig. 6.3G shows that T_{max} of 1330 K (at x = 1.5 cm) and T_{exit} (at x = 7 cm) of 1228 K obtained with the CCCR configuration are increased significantly from T_{max} and T_{exit} obtained for the $m_{MC/MSR}$ = 3 in Fig. 6.3A. This is attributed to the production of more exothermic energy due to increased inlet flow rate of CH_4 in the combustion-

channel. The difference of 102 K between T_{max} (1330 K) and T_{exit} (1228 K) is again high indicating significant thermal gradients in the direction of flow. In the case of DCCR with $l_{c,\ blank}$ = 1 mm, like $m_{MC/MSR}$ = 3, T_{max} decreases slightly to 1328 K and T_{exit} increases to 1266 K compared to the CCCR. However, further increasing of $l_{c,\ blank}$ greater than 1 mm, unlike to the $m_{MC/MSR}$ = 3, T_{max} increases by 32 K (1362 K) compared to the CCCR due to inter-catalyst space length ($l_{c,\ blank}$) boosts the CH_4 combustion rate in the forward direction as mentioned earlier. It is also observed from the Fig. 6.3G that longitudinal distance of T_{max} position is increases from the reactor inlets with increasing $l_{c,\ blank}$ and hence T_{exit} is also increases with increasing $l_{c,\ blank}$. Due to increase in T_{exit}, and thus decrease in difference between T_{max} and T_{exit}, longitudinal thermal gradients are decreased significantly with the DCCR for the $m_{MC/MSR}$ = 4 as well. Fig. 6.3H clearly shows the difference between T_{max} and T_{exit} decreases with increasing $l_{c,\ blank}$ for the $m_{MC/MSR}$ = 3 and 4. It should be noted that $l_{c,\ blank}$ = 0 on abscissa in Fig. 6.3H is represented by the CCCR to show the clear comparison of the temperature difference with the different patterns of the DCCR configuration.

6.4.2.2. Conversion, yield, selectivity, overall efficiency and effectiveness factors study in five different patterns of the DCCR configuration and comparison with the CCCR configuration

Fig. 6.4A illustrates the X_{CH4} at the reforming-channel outlet in the case of CCCR ($l_{c,\ blank}$ = 0) and DCCR ($l_{c,\ blank}$ = 1, 2, 3, 4, and 5 mm). As can be seen from the Fig. 6.4A for the $m_{MC/MSR}$ = 3 that X_{CH4} in MSR increases from 78.3% in the CCCR to 83.3% (an increase of 5%) with $l_{c,\ blank}$ = 3 mm and for $m_{MC/MSR}$ = 4, X_{CH4} increases from 91.1% in the CCCR to 93.85% (an increase of 2.75%) with $l_{c,\ blank}$ = 3 mm in the DCCR. Further increase in $l_{c,\ blank}$ beyond 3 mm on the combustion-side, slightly decreases X_{CH4} on the reforming-side. This is due to decrease in surface reaction rate of CH_4 on the reforming-side. Fig, 4B illustrates that the average surface reaction rate (Eq. (6.21))

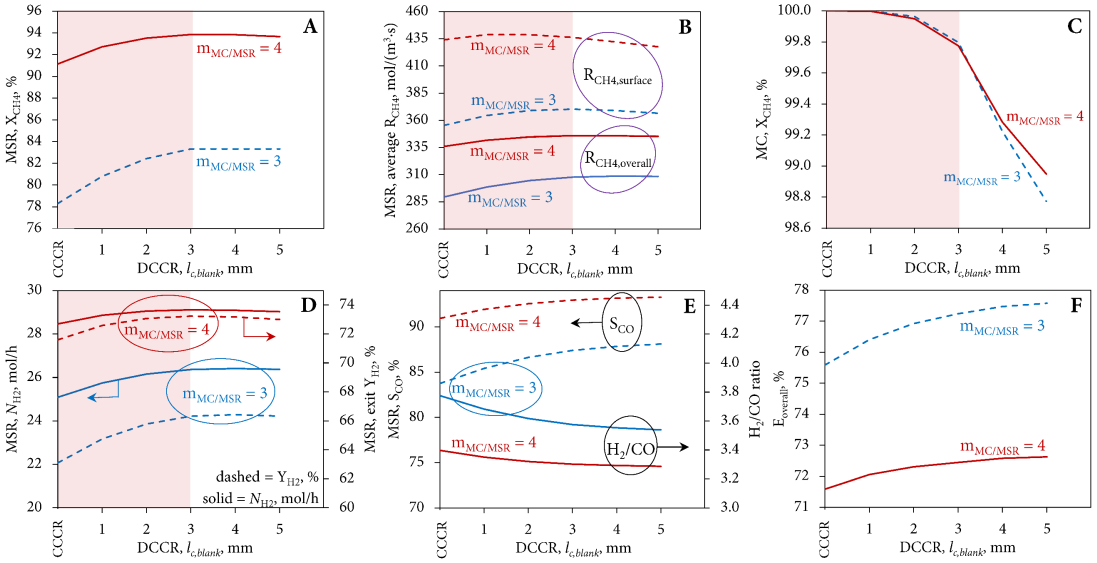

Fig. 6.4 *(A) Methane conversion in MSR ($X_{CH4,\ MSR}$), (B) average surface and overall reaction rates in MSR, (C) methane conversion in MC ($X_{CH4,\ MC}$), (D) hydrogen production (N_{H2}, mol/h) and hydrogen yield (Y_{H2}, %) in MSR, (E) CO selectivity (S_{CO}, %) and H_2/CO ratio in MSR, and (F) overall efficiency ($E_{overall}$) of CPR, as a function of different DCCR configurations ($l_{c,\ blank}$ = 1 to 5 mm) for $m_{MC/MSR}$ = 3 and 4.*

of CH_4 at the reforming-channel and reforming-catalyst interfaces (boundary 13 in Fig. 6.1) decreases when $l_{c,\ blank}$ > 3 mm, however, overall reaction rate of CH_4 (Eq. (6.22)) remains same as $l_{c,\ blank}$ = 3 mm. This is because at the higher overall temperatures (for $l_{c,\ blank}$ > 3 mm), desorption rates of the adsorbed reactants are high and residence time of the reactants is less due to increase in volumetric flow rate than in $l_{c,\ blank}$ = 3 mm. Hence, reactants adsorbed at the top surface (boundary 13 in Fig. 6.1) of the reforming-catalyst desorb easily and consequently slightly lower surface reaction rate of CH_4 is obtained with $l_{c,\ blank}$ > 3 mm than with $l_{c,\ blank}$ = 3 mm. From the study of X_{CH4} in MSR, it is observed that a CPR designed with the DCCR configured with $l_{c,\ blank}$ = 3 mm is beneficial if operated around 75 to 80% X_{CH4} in MSR. Fig. 6.4C shows that 100% X_{CH4} obtained on the combustion-side in the case of CCCR decreases with increasing $l_{c,\ blank}$ in DCCR. It is also clearly observed that beyond $l_{c,\ blank}$ = 3 mm, decrease of X_{CH4} in MC is steeper than $l_{c,\ blank} \leq 3$ mm and reaches to less than 99% with $l_{c,\ blank}$ = 5 mm despite operating at elevated temperature. This is because of two main reasons: (1) decrease of residence time due to increase in volumetric flow rate at elevated temperatures, and (2) decrease of contact time of reactants with the surface of the combustion-catalyst due to decreased overall active length and hence decreased overall active surface area of the combustion-catalyst.

Fig. 6.4D illustrates Y_{H2} (%) and N_{H2} (mol/h) at the reforming-channel outlet for the CCCR and the DCCR as a function of the inter-catalyst space $l_{c,\ blank}$. Fig. 6.4D clearly shows that Y_{H2} and N_{H2} are predicted higher in all patterns of the DCCR than in the CCCR for the both $m_{MC/MSR}$ = 3 and 4. For the $m_{MC/MSR}$ = 3, N_{H2} in the case of CCCR is predicted around 25.1 mol/h and it increases to 26.4 mol/h (an increase of 1.3 mol/h) in the DCCR configured with the $l_{c,\ blank}$ = 3 mm. In the case of $l_{c,\ blank}$ > 3 mm, the production of H_2 slightly decreases due to the reasons mentioned previously in the case of X_{CH4} in MSR. For the $m_{MC/MSR}$ = 4, N_{H2} in the case of CCCR is predicted around 28.5 mol/h and it increases to 29.1 mol/h (an increase of 0.6 mol/h) in the DCCR configured with the $l_{c,\ blank}$ = 3 mm. Similarly, Y_{H2} in the case of CCCR is predicted around 63.1% and it increases to 66.4% (an increase of 3.3%) in the DCCR configured with the $l_{c,\ blank}$ = 3 mm. For the $m_{MC/MSR}$ = 4, Y_{H2} in the case of CCCR is predicted around 71.6% and it increases to 73.2% (an increase of 1.6%) in the DCCR configured with the $l_{c,\ blank}$ = 3 mm.

Fig. 6.4E illustrates the S_{CO} and H_2/CO ratio at the reforming-channel outlet for the CCCR and DCCR. Fig.4E shows that S_{CO} increases from 83.7% in the CCCR to 88.1% (an increase of 4.4%) in the DCCR configured with the $l_{c,\ blank}$ = 5 mm for the $m_{MC/MSR}$ = 3, and from 90.9% in the CCCR to 93.3% (an increase of 2.4%) in the DCCR ($l_{c,\ blank}$ = 5 mm) for the $m_{MC/MSR}$ = 4. Hence, the trends of H_2/CO plots with respect to $l_{c,\ blank}$ are in opposite direction than S_{CO}. Lower X_{CH4} predicted in the case of CCCR (Fig. 6.4A) makes the H_2/CO ratio higher compared to the different patterns of the DCCR. This can be attributed to the lower consumption of H_2O at low X_{CH4} and thus the presence of excess H_2O favors the WGS reaction. Thus, as X_{CH4} increases in the DCCR patterns, both excess H_2O and H_2/CO ratio decrease and S_{CO} increases. In the case of $l_{c,\ blank}$ > 3 mm, where slightly low X_{CH4} in MSR but high S_{CO} is predicted compared to the $l_{c,\ blank}$ = 3 mm, is due to high overall temperatures at the reactor downstream (Fig. 6.3E, F). At elevated temperatures, reverse WGS favors CO production due to the Le Chatelier's principle.

Fig. 6.4F shows the $E_{overall}$ (Eq. (6.17)) for the CCCR and DCCR. Distributed patterns of the DCCR clearly display the improvement in the $E_{overall}$ compared to the CCCR. $E_{overall}$ increases from 75.6% in the CCCR to 77.6% (an increase of 2%) in the DCCR configured with the $l_{c,\ blank}$ = 5 mm for the $m_{MC/MSR}$ = 3, and from 71.6% in the CCCR to 72.6% in the DCCR ($l_{c,\ blank}$ = 5 mm) for the $m_{MC/MSR}$ = 4. It should be noted that $E_{overall}$ in the case of $m_{MC/MSR}$ = 4 are less than $m_{MC/MSR}$ = 3 is because equilibrium limitation reduces the rate of forward reaction. Also, $E_{overall}$ is higher in the case of $l_{c,\ blank}$ > 3 mm despite slightly lower X_{CH4} compared to $l_{c,\ blank}$ = 3, is due to the higher temperatures favor more CO production due to the Le Chatelier's principle and due to decrease in CH_4 conversion on the combustion-side increase the $E_{overall}$ (Eq. (6.17)) in the case of $l_{c,\ blank}$ > 3 mm compared to $l_{c,\ blank}$ = 3 mm.

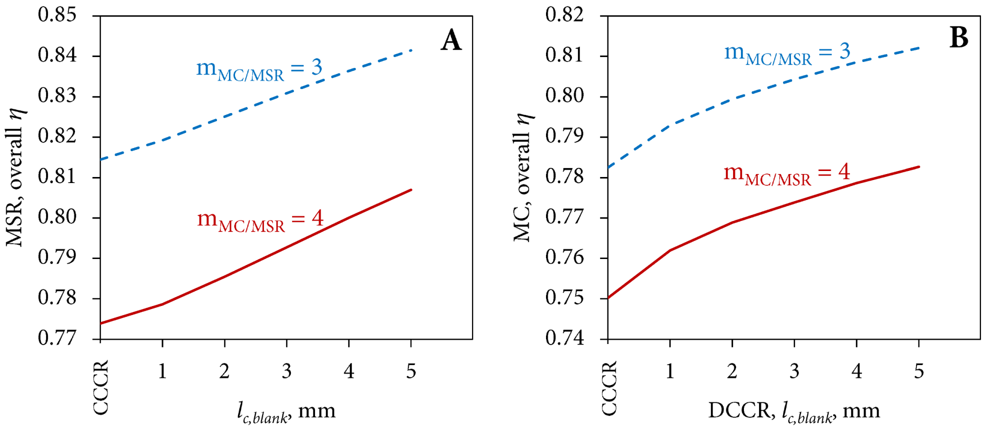

Fig. 6.5 *(A) overall effectiveness factors based on CH_4 in MSR and (B) in MC as a function of different DCCR configurations ($l_{c,\ blank}$ = 1 to 5 mm) for $m_{MC/MSR}$ = 3 and 4.*

Fig. 6.5A and B presents the overall effectiveness factors (Eq. (6.20)) for the reforming and combustion catalysts respectively, for the CCCR and DCCR as a function of the $l_{c,\ blank}$. As can be seen, $\eta_{CH_4}^{overall}$ for both combustion and reforming catalysts are increased with increasing $l_{c,\ blank}$. $\eta_{CH_4}^{overall}$ for the reforming-catalyst is increased from 0.81 in the CCCR to 0.84 in DCCR with the $l_{c,\ blank}$ = 5 mm for the $m_{MC/MSR}$ = 3, whereas it is increased from 0.77 in the CCCR to 0.81 in DCCR configured with the $l_{c,\ blank}$ = 5 mm for the $m_{MC/MSR}$ = 4. $\eta_{CH_4}^{overall}$ for the combustion-catalyst is increased from 0.78 in the CCCR to 0.81 in the DCCR configured with $l_{c,\ blank}$ = 5 mm for the $m_{MC/MSR}$ = 3, whereas it is increased from 0.75 in the CCCR to 0.78 in the DCCR configured with $l_{c,\ blank}$ = 5 mm for the $m_{MC/MSR}$ = 4. The comparative study of the $\eta_{CH_4}^{overall}$ indicates that DCCR is beneficial not only in reducing thermal gradients and increasing reactant conversions or product yield but also in improving the utilization of the both reforming and combustion catalysts.

Based on the comparative study of conversions and products output between the CCCR and different patterns of the DCCR, it is concluded that highest X_{CH4}, Y_{H2}, and N_{H2} on the reforming-side are achieved when $l_{c,\ blank}$ is near to 3 mm. Therefore, for the remaining DCDR and δ_{plate} studies, distributed sections of the combustion-catalyst are coated with the $l_{c,\ active}$ = 1 mm and $l_{c,\ blank}$ = 3 mm.

6.4.3. The study of five different patterns of the DCDR configuration

In our previous study [22], we showed that distributed reforming-catalyst coupled with the distributed combustion-catalyst could be beneficial in avoiding cold zones to maintain a balanced thermal distribution on the endothermic reforming-side. Settar et al. [20] carried out a comparative numerical study between the distributed and continuous coatings of a reforming-catalyst by developing a steady state two-dimensional model of a single reforming-channel and showed performance enhancement factor up to two in terms of X_{CH4} with the distributed coating. They kept the quantity of a reforming-catalyst in the distributed coating same as the conventional continuous coating. To achieve this, they considered distributed coating sections over the extended plate-length. However, they did not investigate the influence of different $l_{r,}$

$_{active}$ and $l_{r,\ blank}$. In this work, we found that $l_{r,\ blank}$, unlike $l_{c,\ blank}$ in the case of DCCR, is not significant compared to $l_{r,\ active}$ to improve the performance of the CPR. Thus, this study investigates the performance of five different distributed coating patterns of the reforming-catalyst by altering the length ($l_{r,\ active}$) of the active section of the reforming-catalyst. The key purpose of studying different patterns of the DCDR is to investigate whether X_{CH4} and N_{H2} obtained in MSR with the distributed reforming-catalyst is same as the CCCR or different, for the same inlet flow rate of CH_4 but with lower quantity of the reforming-catalyst.

For the study of different patterns of the DCDR, $l_{r,\ blank}$ among distributed coating sections of the active reforming-catalyst is 1 mm [20]. Number of active sections ($N_{r,\ active}$) with the $l_{r,\ blank}$ = 1 mm depends on the choice of $l_{r,\ active}$ because of the fixed plate-length of 7 cm. In the earlier section of the DCCR, it is found that the CPR designed with the distributed coating section of the combustion-catalyst with the $l_{c,\ active}$ = 1 mm and $l_{c,\ blank}$ = 3 mm shows highest X_{CH4} and N_{H2} among five different coating patterns. Hence, for the study of different patterns of the DCDR, each distributed section of the combustion-catalyst is considered to be coated with the $l_{c,\ active}$ = 1 mm and $l_{c,\ blank}$ = 3 mm. To investigate the influence of $l_{r,\ active}$ in the DCDR, five different $l_{r,\ active}$ = 1, 2, 3, 4, and 5 mm are considered. It should be noted again that catalysts are coated between x = 1 and 6 cm on 7-cm long plates. Based on the considered $l_{r,\ active}$ of 1, 2, 3, 4, and 5 mm, the $N_{r,\ active}$ are 25, 16, 12, 10 and 8 respectively. Thus, the total active length ($L_{r,\ active}$) of the reforming-catalyst corresponding to the $l_{r,\ active}$ of 1, 2, 3, 4, and 5 mm are 25, 32, 36, 40 and 40 mm respectively. In other words, for the $l_{r,\ active}$ = 1 mm, 50% of the active reforming-catalyst is removed ($L_{r,\ active}$ = 25 mm), for the $l_{r,\ active}$ = 2 mm, 36% of the active reforming-catalyst is removed ($L_{r,\ active}$ = 32 mm), for the $l_{r,\ active}$ = 3 mm, 28% of the active reforming-catalyst is removed ($L_{r,\ active}$ = 36 mm), for the $l_{r,\ active}$ = 4 and 5 mm, 20% of the active reforming-catalyst is removed ($L_{r,\ active}$ = 40 mm) compared to the CCCR coating configuration. It should be noted that $L_{r,\ active}$ is the total active length of the reforming-catalyst. Inlet flow rate of methane in the combustion-channel is determined based on the $m_{MC/MSR}$. Parameters considered for the study of five different coating patterns of the DCDR are presented in Table 6.8.

6.4.3.1. Temperature distribution in five different patterns of the DCDR coating configuration and comparison with the conventional CCCR coating configuration

Fig. 6.6A to F illustrate temperature distribution in the CCCR and in DCDR configured with $l_{r,\ active}$ = 5, 4, 3, 2, and 1 mm for the $m_{MC/MSR}$ = 3. It should be noted that Fig. 6.6A and Fig. 6.3A are identical except difference in temperature scales. From the temperature distribution study in the DCDR, it is predicted that both T_{max} and T_{exit} increase with decreasing $l_{r,\ active}$. Fig. 6.6B shows that T_{max} predicted in the DCDR configured with $l_{r,\ active}$ = 5 mm is 6 K less and T_{exit} is 74 K more than the CCCR. This is due to the distributed combustion-catalyst keeps T_{max} low and T_{exit} relatively high by distributing the exothermic heat uniformly along the plate. However, if the Fig. 6.6B is compared with the Fig. 6.3D of the DCCR ($l_{c,\ blank}$ = 3 mm), as expected both T_{max} and T_{exit} are in fact increased by 10 K and 9 K respectively. This is attributed to the fact that DCDR configured with $l_{r,\ active}$ = 5 mm contains 20% less reforming-catalyst. Thus, decreased number of endothermic reforming sites reduce the overall rate of absorption of heat in MSR compared to the DCCR configured with the $l_{c,\ blank}$ = 3 mm. Likewise, Fig. 6.6C illustrates temperature distribution in the DCDR configured with the $l_{r,\ active}$ = 4 mm, where same 20% reforming-catalyst is being reduced compared to the CCCR and DCCR. Despite having the same amount of the reforming-catalyst, the main difference between the DCDR configured with $l_{r,\ active}$ = 4 and 5 mm is the number of active and inactive sections on the reforming-side. It is observed from Fig. 6.6B and C that number of active sections of the reforming-catalyst are 8 and 10 corresponding to $l_{r,}$

Table 6.8. *Parameters for the DCDR and CCCR configurations.*

	reforming-side					
	CCCR	**DCDR ($l_{r,\ blank}$=1 mm)**				
	$L_{r,\ active}$=50 mm	**$l_{r,\ active}$=5 mm**	**$l_{r,\ active}$=4 mm**	**$l_{r,\ active}$=3 mm**	**$l_{r,\ active}$=2 mm**	**$l_{r,\ active}$=1 mm**
inlet CH_4 flow (N_{CH4}), mol/h	0.3312	0.3312	0.3312	0.3312	0.3312	0.3312
steam to carbon ratio (SC)	1.5	1.5	1.5	1.5	1.5	1.5
H_2O molar flow in a single channel, N_{O2}, mol/h	SC × N_{CH4}	SC × N_{CH4}	SC × N_{CH4}	SC × N_{CH4}	SC × N_{CH4}	SC × N_{CH4}
inlet temperature, K	800	800	800	800	800	800
volume of active catalyst on one plate, mm^3	125	100	100	90	80	62.5
active catalyst amount on one plate, mg	296	237	237	213	190	148
thickness of active catalyst section (δ_r), µm	50	50	50	50	50	50
width of active catalyst, mm	50	50	50	50	50	50
total length of active catalyst ($L_{r,\ active}$), mm	50	40	40	36	32	25
$GHSV_{MSR}$, h^{-1}	81028	1.0129×10^5	1.0129×10^5	1.1254×10^5	1.2661×10^5	1.6206×10^5
	combustion-side					
	CCCR	**DCDR (for all $l_{r,\ active}$ patterns listed above)**				
	$L_{c,\ active}$=50 mm	**$l_{c,\ active}$=1 mm, $l_{c,\ blank}$=3 mm**				
inlet CH_4 flow (N_{CH4}), mol/h when $m_{MC/MSR}$=3	0.1471	0.1471				
inlet CH_4 flow (N_{CH4}), mol/h when $m_{MC/MSR}$=4	0.1962	0.1962				
oxygen to carbon ratio (O_2/C)	2	2				
O_2 molar flow in a single channel, N_{O2}, mol/h	(O_2/C) × N_{CH4}	(O_2/C) × N_{CH4}				
N_2 molar flow in a single channel, N_{N2}, mol/h	(79/21) × N_{O2}	(79/21) × N_{O2}				
inlet temperature, K	800	800				
volume of active catalyst on one plate, mm^3	12.5	3.25				
active catalyst amount on one plate, mg	29.6	7.7				
total length of active catalyst ($L_{c,\ active}$), mm	50	13				
thickness of active catalyst section (δ_r), µm	5	5				
width of active catalyst, mm	50	50				
$GHSV_{MC}$, h^{-1} when $m_{MC/MSR}$=3	1.5153×10^6	5.8279×10^6				
$GHSV_{MC}$, h^{-1} when $m_{MC/MSR}$=4	2.0203×10^6	7.7705×10^7				

$_{active}$ = 5 and 4 mm, whereas number of inactive sections are 7 and 9 respectively. The increase in T_{max} by 3 K in the case of $l_{r,\ active}$ = 4 mm compared to 5 mm is due to the more number of inactive sections ($N_{r,\ blank}$ = 9) on the reforming-side reduce the overall rate of heat of absorption near the inlet section of the reforming-catalyst. Increase in T_{max} near the inlets increases the rate of CH_4 consumption on the combustion-side which eventually decreases at the downstream end and increase of 3 K in T_{max} is compensated by decrease of 2 K in T_{exit}. It is expected that ideally same quantity of the reforming-catalyst absorbs same heat regardless of the coating patterns of it. The comparative study of the temperature distribution between the two DCDR patterns with the $l_{r,\ active}$ = 4 and 5 mm shows that number of inactive sections ($l_{r,\ blank}$) and their position on the reforming-side can play a minor role in controlling T_{max} and T_{exit} if the amount of reforming-catalyst is kept constant. As shown in Fig. 6.6D, E and F, further decrease of the reforming-catalyst by 28%, 36% and 50% in the DCDR configured with $l_{r,\ active}$ = 3, 2, and 1 mm increases T_{max} by 1, 9, and 28 K and T_{exit} by 79, 86 and 97 K compared to the CCCR respectively. Relatively minor increase in T_{max} and substantial increase in T_{exit} makes the difference between T_{max} and T_{exit} 42, 43 and 51 K in the DCDR configured with $l_{r,\ active}$ = 3, 2, and 1 mm respectively. Relatively small difference between the two temperatures compared to the difference of 120 K between T_{max} and T_{exit} in the CCCR indicates that longitudinal thermal gradients are reduced significantly with the DCDR as well.

To investigate the performance of different patterns of the DCDR at elevated temperatures, N_{CH4} on the combustion-side is increased from $m_{MC/MSR}$ = 3 to $m_{MC/MSR}$ = 4 by keeping the N_{CH4} on the reforming-side constant. Fig. 6.6G illustrates longitudinal temperature profiles at the plate center for the CCCR and DCDR ($l_{r,\ active}$ = 1, 2, 3, 4, 5 mm) for the $m_{MC/MSR}$ = 4. As mentioned earlier, the difference of 102 K between T_{max} and T_{exit} in the CCCR is large indicating significant thermal gradients in the direction of flow. In the case of DCDR configured with $l_{r,\ active}$ = 5, 4, 3, 2, and 1

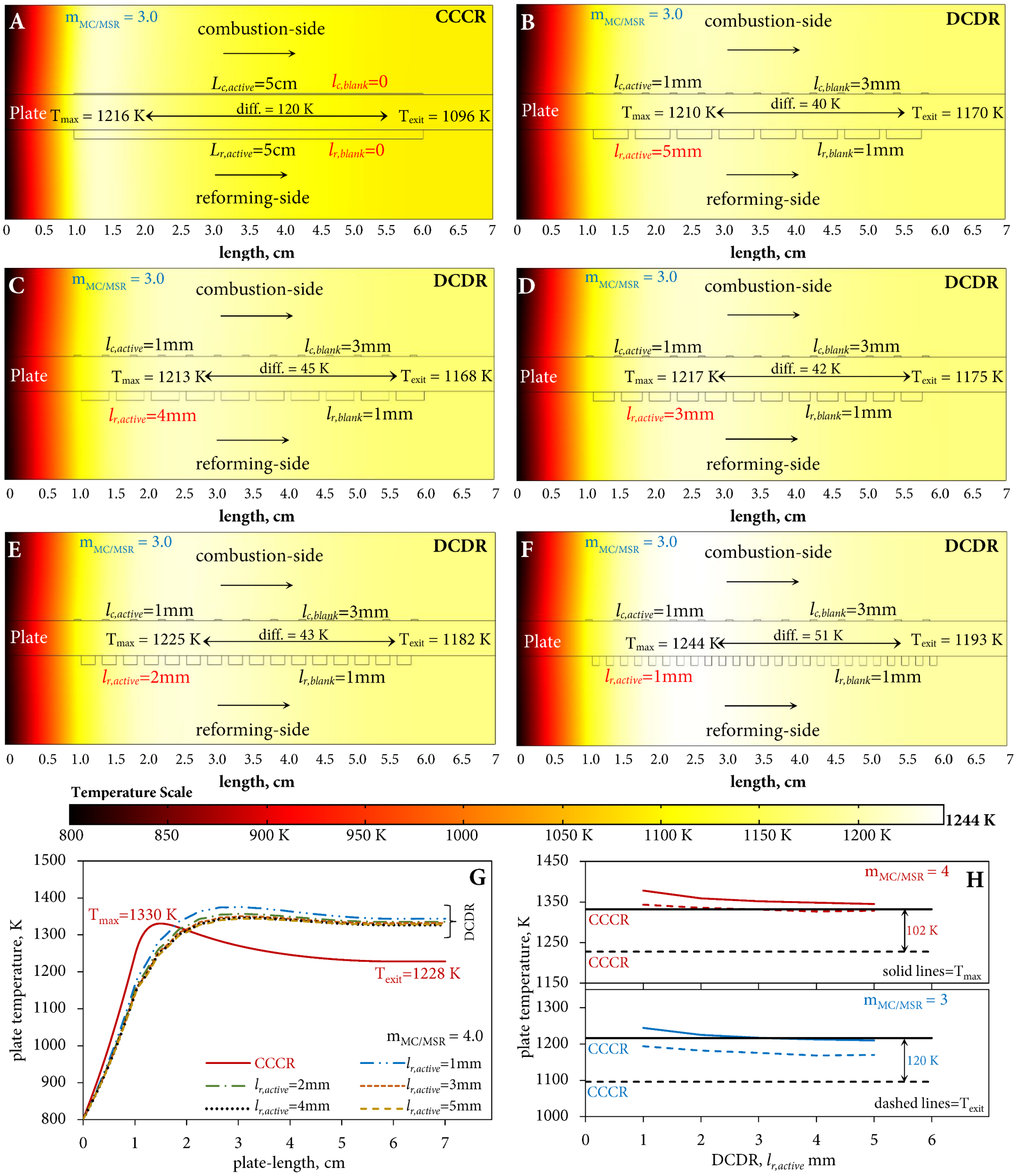

Fig. 6.6 *(A) Temperature distribution for $m_{MC/MSR}$ = 3 in CCCR, (B) in DCDR configured with $l_{r,\ active}$ = 5 mm, (C) $l_{r,\ active}$ = 4 mm, (D) $l_{r,\ active}$ = 3 mm, (E) $l_{r,\ active}$ = 2 mm, (F) $l_{r,\ active}$ = 1 mm, (G) longitudinal temperature profiles at the plate center for $m_{MC/MSR}$ = 4 obtained in CCCR and in different DCDR configurations, (H) maximum and exit plate temperature as a function of different DCDR configurations ($l_{r,\ active}$ = 1 to 5 mm) for $m_{MC/MSR}$ = 3 and 4.*

mm, T_{max} is increased by 15, 18, 22, 29, and 48 K and T_{exit} is increased by 100, 99, 104, 108, and 116 K respectively compared to the T_{max} and T_{exit} obtained in the CCCR. Relatively moderate increase in T_{max} and substantial increase in T_{exit} makes the difference between T_{max} and T_{exit} 17, 22, 20, 24, and 35 K for the $l_{r,\ active}$ = 5, 4, 3, 2, and 1 mm respectively compared to the difference of 102 K in CCCR. Fig. 6.6H clearly shows for the both $m_{MC/MSR}$ = 3 and 4 that the difference between T_{max} and T_{exit} is significantly decreased in the case of different patterns of the DCDR compared to the CCCR.

6.4.3.2. Conversion, yield, selectivity and overall efficiency study in five different patterns of the DCDR configuration and comparison with the CCCR configuration

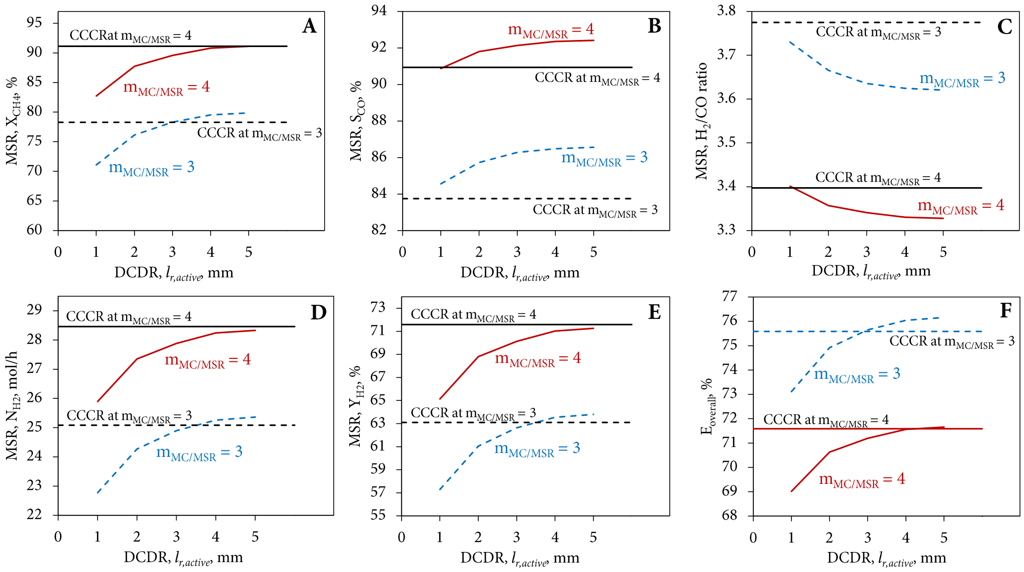

Fig. 6.7 *(A) Methane conversion ($X_{CH4,\ MSR}$), (B) CO selectivity (S_{CO}, %), (C) H_2/CO ratio, (D) hydrogen production (N_{H2}, mol/h), (E) hydrogen yield (Y_{H2}, %), and (F) overall efficiency ($E_{overall}$) of CPR, as a function of different DCDR configurations ($l_{r,\ active}$ = 1 to 5 mm) for $m_{MC/MSR}$ = 3, 4.*

Fig. 6.7A illustrates X_{CH4} at the reforming-channel outlet for the CCCR and DCDR configured with $l_{r,\ active}$ = 1, 2, 3, 4, and 5 mm for the $m_{MC/MSR}$ = 3. In Fig. 6.7A, X_{CH4} in MSR increases from 71% for $l_{r,\ active}$ = 1 mm to 79.9% for $l_{r,\ active}$ = 5 mm. Likewise, for the $m_{MC/MSR}$ = 4, X_{CH4} in MSR increases from 82.7% to 91%. X_{CH4} predicted for the conventional CCCR are displayed as straight lines at 78.3% for the $m_{MC/MSR}$ = 3 and 91% for the $m_{MC/MSR}$ = 4. Fig. 6.7A also shows that X_{CH4} of 78.3% obtained in the CCCR for the $m_{MC/MSR}$ = 3 can also be achieved in the DCDR configured with $l_{r,\ active}$ = 3 mm and 91% obtained in the CCCR for the $m_{MC/MSR}$ = 4 can also be achieved in the DCDR, when configured with $l_{r,\ active}$ = 4 and 5 mm. In other words, same X_{CH4} predicted in the CCCR for the $m_{MC/MSR}$ = 3 and 4 are obtained in the DCDR as well, but with 28% and 20% less reforming-catalyst and with reduced longitudinal thermal gradients.

Fig. 6.7B, C, D, and E illustrate S_{CO}, H_2/CO ratio, N_{H2} and Y_{H2} respectively at the reforming-channel outlet for the CCCR and different patterns of the DCDR. Fig. 6.7B shows that S_{CO} for the $m_{MC/MSR}$ = 3 increases from 84.6% to 86.6% with increasing $l_{r,\ active}$. Likewise, for the $m_{MC/MSR}$ = 4, S_{CO} increases from 90.9% to 92.4%. Hence, the profiles of H_2/CO plots in Fig. 6.7C with respect to $l_{r,\ active}$ are reverse. It is observed that S_{CO} in all studied DCDR patterns is higher than in the CCCR for the both $m_{MC/MSR}$ ratios. This is attributed to the overall higher temperature predicted in the DCDR patterns (Fig. 6.6B to F) than in the CCCR. At elevated temperatures, reverse WGS favors CO production due to the Le Chatelier's principle. Due to higher CO production, N_{H2} and Y_{H2} in Fig. 6.7D and E are predicted relatively low in the DCDR patterns compared to the CCCR. However, it is predicted in the case of $m_{MC/MSR}$ = 3 that N_{H2} and Y_{H2} meet the straight lines of CCCR when $l_{r,\ active}$ is between 3 and 4 mm. This can be understood by observing Fig. 6.7A of X_{CH4} for the $m_{MC/MSR}$ = 3.

Table 6.9. *Parameters for the CCCR, DCCR and DCDR.*

reforming-side			
	CCCR	**DCCR**	**DCDR**
	$L_{r,\ active}$=50 mm	**$L_{r,\ active}$=50 mm**	**$l_{r,\ active}$=3 mm, $l_{r,\ blank}$=1 mm**
inlet CH_4 flow (N_{CH4}), mol/h	0.3312	0.3312	0.3312
steam to carbon ratio (SC)	1.5	1.5	1.5
H_2O molar flow in a single channel, N_{O2}, mol/h	SC × N_{CH4}	SC × N_{CH4}	SC × N_{CH4}
inlet temperature, K	800	800	800
total volume of active catalyst on one plate, mm^3	125	125	90
active catalyst amount on one plate, mg	296	296	213
thickness of active catalyst section (δ_r), µm	50	50	50
width of active catalyst, mm	50	50	50
total length of active catalyst ($L_{r,\ active}$), mm	50	50	36
$GHSV_{MSR}$, h^{-1}	81028	81028	1.1254×10^5
combustion-side			
	CCCR	**DCCR**	**DCDR**
	$L_{c,\ active}$=50 mm	**$l_{c,\ blank}$=3 mm**	**$l_{c,\ active}$=1 mm, $l_{c,\ blank}$=3 mm**
inlet CH_4 flow (N_{CH4}), mol/h when $m_{MC/MSR}$=3	0.1471	0.1471	0.1471
oxygen to carbon ratio (O_2/C)	2	2	2
O_2 molar flow in a single channel, N_{O2}, mol/h	(O_2/C) × N_{CH4}	(O_2/C) × N_{CH4}	(O_2/C) × N_{CH4}
N_2 molar flow in a single channel, N_{N2}, mol/h	(79/21) × N_{O2}	(79/21) × N_{O2}	(79/21) × N_{O2}
inlet temperature, K	800	800	800
total volume of active catalyst on one plate, mm^3	12.5	3.25	3.25
active catalyst amount on one plate, mg	29.6	7.7	7.7
total length of active catalyst ($L_{c,\ active}$), mm	50	13	13
thickness of active catalyst section (δ_r), µm	5	5	5
width of active catalyst, mm	50	50	50
$GHSV_{MC}$, h^{-1} when $m_{MC/MSR}$=3	1.5153×10^6	5.8279×10^6	5.8279×10^6

Fig. 6.7F shows $E_{overall}$ at the reforming-channel outlet for the CCCR and DCDR patterns for the $m_{MC/MSR}$ = 3 and 4. As expected, based on the X_{CH4} plots in Fig. 6.7A, $E_{overall}$ of 76% in the CCCR for the $m_{MC/MSR}$ = 3 can also be achieved in the DCDR configured with $l_{r,\ active}$ = 3 mm and 72% in the CCCR for the $m_{MC/MSR}$ = 4 can also be achieved in the DCDR configured with $l_{r,\ active}$ = 4 and 5 mm. In other words, same $E_{overall}$ predicted in the CCCR for the $m_{MC/MSR}$ = 3 and 4 are obtained in the DCDR but with 28% and 20% less reforming-catalyst respectively.

From the comparative study between the DCDR and CCCR, it can be concluded that it is possible to obtain similar N_{H2}, X_{CH4} and $E_{overall}$ in the DCDR configured with $l_{r,\ active} \geq 3$ mm but with less amount of reforming-catalyst than the conventional CCCR. From this study, it is also concluded that if the DCDR operated within 75 to 80% conversion regime, around 28% of the reforming-catalyst can be saved compared to the conventional CCCR without compromising in N_{H2} and X_{CH4}. Based on the study of different patterns of the DCDR, the next section of different δ_{plate} study, considers the DCDR with the reforming-catalyst sections coated with $l_{r,\ active}$ = 3 mm and $l_{r,\ blank}$ = 1 mm and combustion-catalyst sections coated with $l_{c,\ active}$ = 1 mm and $l_{c,\ blank}$ = 3 mm.

6.4.4. Influence of the plate-thickness, δ_{plate}

As discussed earlier, $l_{r,\ blank}$ = 1 mm, $l_{r,\ active}$ = 3 mm on the reforming-side and $l_{c,\ blank}$ = 3 mm, $l_{c,\ active}$ = 1 mm on the combustion-side for the DCDR and $l_{c,\ blank}$ = 3 mm, $l_{c,\ active}$ = 1 mm on the combustion-side and $L_{r,\ active}$ = 5 cm on the reforming-side for the DCCR are considered. Inlet conditions considered to investigate the influence of δ_{plate} are presented in Table 6.9.

6.4.4.1. Temperature distribution study in the CCCR, DCCR and DCDR configurations designed with the different δ_{plate}

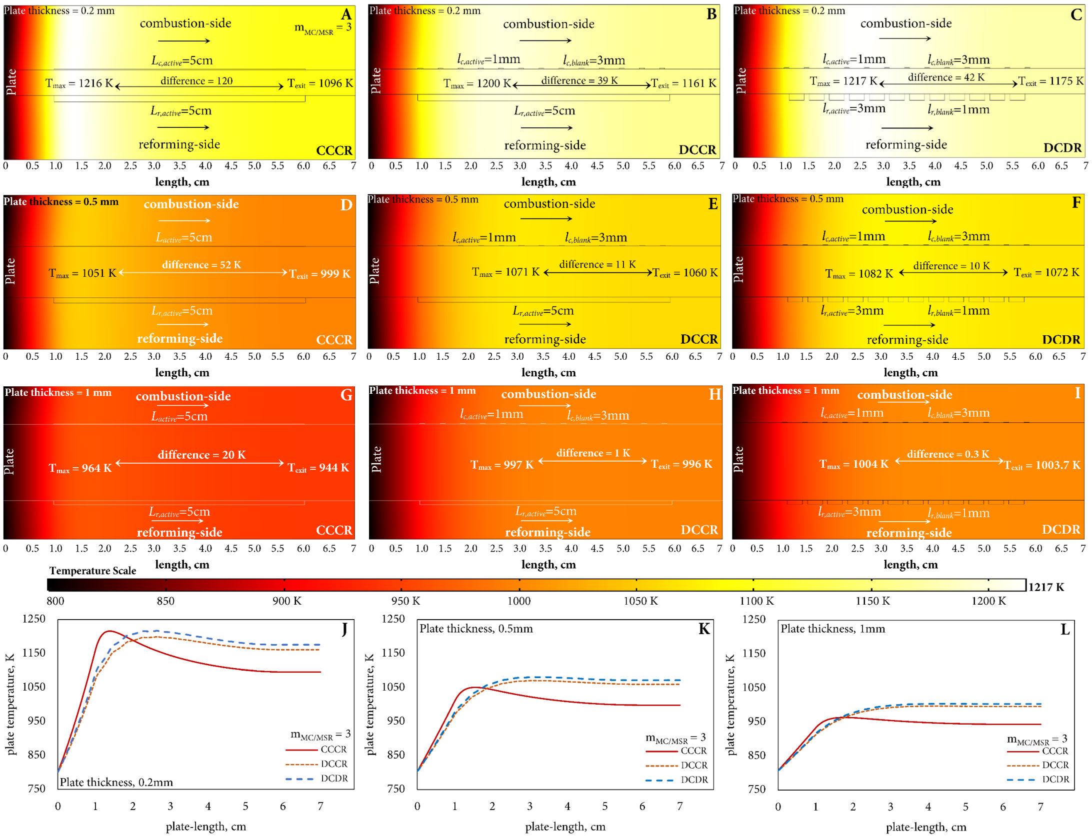

Fig. 6.8 *(A) Temperature distribution for $m_{MC/MSR}$ = 3 in CCCR, (B) in DCCR configured with $l_{c, blank}$ = 1 mm, (C) in DCDR configured with $l_{r, active}$ = 3 mm for 0.2 mm plate-thickness, (D) temperature distribution for $m_{MC/MSR}$ = 3 in CCCR, (E) in DCCR configured with $l_{c, blank}$ = 1 mm, (F) in DCDR configured with $l_{r, active}$ = 3 mm for 0.5 mm plate-thickness, (G) temperature distribution for $m_{MC/MSR}$ = 3 in CCCR, (H) in DCCR configured with $l_{c, blank}$ = 1 mm, (I) in DCDR configured with $l_{r, active}$ = 3 mm for 1 mm plate-thickness, (J) longitudinal temperature profiles at the plate center for $m_{MC/MSR}$ = 3 in CCCR, DCCR and DCDR for 0.2 mm plate-thickness, (K) for 0.5 mm plate thickness and (L) for 1 mm plate-thickness.*

Fig. 6.8A to I, show the temperature distribution in the CCCR, DCCR and DCDR designed with the δ_{plate} = 0.2, 0.5 and 1 mm for the $m_{MC/MSR}$ = 3. For the δ_{plate} = 0.2 mm, Fig. 6.8B and C illustrate that the temperature difference between T_{max} and T_{exit} in the DCCR and DCDR are reduced by 39 and 42 K respectively compared to the CCCR in Fig. 6.8A. In other words, temperature difference is reduced by 67.5% and 65% in the DCCR and DCDR respectively compared to the CCCR. It should be noted that the predicted T_{max} in the DCCR and DCDR for the δ_{plate} = 0.2 mm is ≤ T_{max} obtained in the CCCR. Likewise, Fig. 6.8D, E and F illustrate the temperature distribution in the CCCR, DCCR and DCDR for the δ_{plate} = 0.5 mm. Unlike with the δ_{plate} = 0.2 mm, T_{max} is increased by 20 and 30 K in the DCCR and DCDR respectively from T_{max} = 1051 K in the CCCR. Also, T_{exit} is increased by 61 K and 73 K in the DCCR and DCDR respectively from T_{exit} = 999 K in the CCCR. Due to increase in T_{max} and T_{exit} in the DCCR and DCDR, temperature difference is reduced by 78.8% and 80.8% respectively compared to the CCCR. Fig. 6.8G, H and I show the temperature distribution in the CCCR, DCCR and DCDR for the δ_{plate} = 1 mm. T_{max} in the DCCR and DCDR is increased by 33 K and 40 K from 964 K obtained in the CCCR, thus temperature difference is reduced by 95% and 98.5% compared to the CCCR. It is interesting to note that percent reduction in temperature difference obtained in the DCCR and DCDR are larger for the thicker plate compared to the thinner plate. By increasing thickness of the plate, significant drop in T_{max} is observed in the case of CCCR from 1216 K for the δ_{plate} = 0.2 mm to 1051 K for the δ_{plate} = 0.5 mm to 964 K for the δ_{plate} = 1 mm. This also indicates that thermal hot-spots and steep thermal gradients can be reduce by increasing δ_{plate}. However, by increasing δ_{plate}, heat-transfer rate from the combustion-side to the reforming-side is reduced significantly, which results into reduction in overall efficiency of a CPR. For clearer picture, Fig. 6.8J, K and L presents the longitudinal temperature profiles at the plate center obtained in the CCCR, DCCR and DCDR for the δ_{plate} = 0.2, 0.5 and 1 mm respectively. It can be seen clearly that for thinner plate (δ_{plate} = 0.2 mm), where relatively higher T_{max} obtained with the CCCR can get reduce when distributed coating of the combustion and reforming catalysts are applied. Whereas in the case of thicker plate (δ_{plate} = 0.5 and 1 mm), where relatively lower T_{max} obtained in the CCCR can be intensified when distributed catalysts patterns are applied. From the study of temperature distribution for the different δ_{plate}, it is concluded that the distributed patterns (DCCR, DCDR) can minimize the longitudinal thermal gradients regardless the thickness of plate.

6.4.4.2. *Conversion, yield, selectivity and overall efficiency study in the DCCR, DCCR and DCDR configurations designed with the different δ_{plate}*

Fig. 6.9A illustrates X_{CH4} at the reforming-channel outlet as a function of coating configurations designed with the δ_{plate} = 0.2, 0.5, and 1 mm for the inlet conditions presented in Table 6.9. It is clear from the figure that highest X_{CH4} in MSR is achieved for all δ_{plate} with the DCCR followed by the DCDR and the CCCR. It should be noted that the quantity of the reforming-catalyst in the DCDR is 28% less than the CCCR and DCCR and quantity of the combustion-catalyst

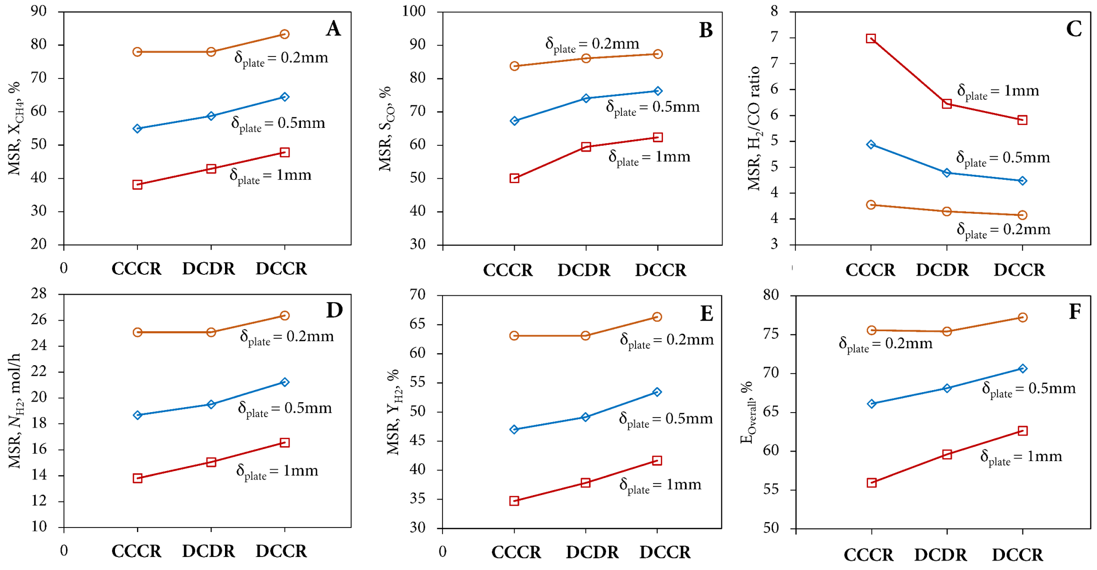

Fig. 6.9 *(A) Methane conversion ($X_{CH4,\ MSR}$), (B) CO selectivity (S_{CO}, %), (C) H_2/CO ratio, (D) hydrogen production (N_{H2}, mol/h), (E) hydrogen yield (Y_{H2}, %), and (F) overall efficiency ($E_{overall}$) of CPR, as a function of different coating configurations for $m_{MC/MSR}$ = 3.*

in the DCDR and DCCR is 74% less than the CCCR. Despite 28% less reforming-catalyst, DCDR predicted the higher X_{CH4} in MSR than the CCCR for the δ_{plate} of 1 and 0.5 mm. Whereas, for the δ_{plate} = 0.2 mm, X_{CH4} obtained in both CCCR and DCDR is same. This is attributed to the fact that further increase of conversion under high conversion regime at elevated temperature is limited by the thermodynamic equilibrium regardless of reactor designs. It can also be observed from the Fig. 6.9A that X_{CH4} on the reforming-side in the DCCR is increased by 10%, 9% and 5% from 38%, 55% and 78% obtained in the CCCR with respect to the δ_{plate} of 1, 0.5 and 0.2 mm. In the case of DCDR, X_{CH4} is increased by 5% and 4% from 28% and 55% obtained in the CCCR with respect to δ_{plate} of 1 and 0.5 mm.

Fig. 6.9B, C, D and E illustrate S_{CO}, H_2/CO ratio, N_{H2} and Y_{H2} respectively, at the reforming-channel outlet for the δ_{plate} = 0.2 0.5, and 1 mm as a function of the coating configurations. Fig. 6.9B shows that highest S_{CO} is predicted in the DCCR for all δ_{plate} followed by the DCDR and CCCR, thus as expected H_2/CO ratio is predicted in reverse order with respect to the three coating configurations (Fig. 6.9C). However, due to increase of X_{CH4} in the DCDR and DCCR compared to the CCCR, it is expected that N_{H2} and Y_{H2} will increase in the distributed patterns (Fig. 6.9D, E). It can be concluded from Fig. 6.9D, that N_{H2} in the DCCR is increased by 20%, 14% and 5% from 14 mol/h, 19 mol/h and 25 mol/h obtained in the CCCR for the δ_{plate} = 1, 0.5, and 0.2 mm respectively. N_{H2} in the DCDR is increased by 9% and 4% from 14 mol/h and 19 mol/h obtained in the CCCR for the δ_{plate} = 1 and 0.5 mm respectively. Improved N_{H2} production is resulted into improved hydrogen yield with respect to the distributed patterns as illustrated in Fig. 6.9E. As a result, $E_{overall}$ as illustrated in Fig. 6.9F, is also increased by 7%, 5% and 2% in the DCCR than in the CCCR for the δ_{plate} = 1, 0.5, and 0.2 mm respectively and by 4% and 2% in the DCDR than in the CCCR for the δ_{plate} = 1 and 0.5 mm respectively.

6.5. Conclusions

Numerical analysis of methane steam reforming (MSR) and methane combustion (MC) is performed over different distributed (DCCR, DCDR) and conventional (CCCR) coatings of reforming and combustion catalysts to produce hydrogen by developing 2D steady-state computational models of a catalytic plate reactor (CPR). The study successfully integrates continuum scale momentum, heat and mass transport phenomena. The study successfully employs the multi-step surface microkinetic model for MSR over Ni-spinel catalyst on the reforming-side coupled with the reduced surface microkinetic model for the catalytic MC over platinum-alumina catalyst and the power-law rate model for the gas-phase MC on the combustion-side. Five different patterns of distributed coatings of combustion-catalyst are investigated in combination with continuous coating of reforming-catalyst (DCCR). Also, five different patterns of distributed coatings of reforming-catalyst are investigated in combination with distributed coating of combustion-catalyst (DCDR). The study also investigates the internal-diffusion limitation by considering different thickness for reforming and combustion catalysts under constant GHSVs and temperature. Further, the study examines the influence of plate-thickness on the performance of distributed and conventional coatings. Results of MSR and MC obtained with different distributed patterns of DCCR and DCDR are compared with the conventional continuous coating (CCCR).

Isothermal studies of MSR and catalytic MC at constant GHSVs show that thickness of reforming-catalyst greater than 50 μm and thickness of combustion-catalyst more than 5 μm reduce the utilization of catalysts and methane conversions due to the internal-diffusion limitation. Among different patterns of the DCCR studied for the plate-thickness of 0.2 mm, highest hydrogen production and methane conversion in MSR are obtained when 1 mm ($l_{c, active}$)

of each active combustion-catalyst segment is coated with the inter-catalyst space length ($l_{c, blank}$) of 3 mm. DCCR ($l_{c, blank}$ = 3 mm) coatings increase the hydrogen production by 5% for $m_{MC/MSR}$ = 3 and by 3% for $m_{MC/MSR}$ = 4 for the $GHSV_{MSR}$ of 81,028 h^{-1} ($\tau_{s, MSR}$ = 44.4 ms) compared to conventional CCCR. Further, DCCR ($l_{c, blank}$ = 3 mm) coatings not only contribute in improving methane conversion and hydrogen production but also in the savings of combustion-catalyst by 74% and minimizing the maximum plate temperature by 16 K compared to CCCR. In addition to reducing the maximum plate temperature, DCCR decreases longitudinal thermal gradients and thus, hot-spots regions on the metal plate are curtailed significantly. The study found that DCCR coatings increase the utilization of both reforming and combustion catalysts by 3 to 5% compared to CCCR. The study also found that above 99% methane conversion in the combustion-channel is achieved with space-time of 0.46 ms in a CPR designed with DCCR as opposed to 1.78 ms with CCCR. In the case of DCDR coatings, same methane conversion and hydrogen production as in CCCR are obtained when each active reforming-catalyst segment is coated with $l_{r, active}$ = 3, 4 and 5 mm and $l_{r, blank}$ = 1 mm in combination with distributed combustion-catalyst coated with $l_{c, blank}$ = 3 mm and $l_{c, active}$ = 1 mm. Different patterns of DCDR configured with $l_{r, blank}$ = 1 mm and $l_{r, active}$ = 3, 4 and 5 mm and $l_{c, blank}$ = 3 mm and $l_{c, active}$ = 1 mm show that it is possible to obtain similar methane conversion and hydrogen production as in CCCR but with 20 to 28% less reforming-catalyst and 74% less combustion-catalyst along with lower longitudinal thermal gradients. The study of the plate-thickness shows that distributed catalysts configurations are equally beneficial when CPR is designed with different plate-thicknesses. In fact, the impact of improvement in the methane conversion, hydrogen production and longitudinal thermal gradients is more pronounced when the plate is relatively thicker.

6.6. References

[1] Niakolas DK, Daletou M, Neophytides SG, Vayenas CG. Fuel cells are a commercially viable alternative for the production of “clean” energy. Ambio. 2016 Jan 1;45(1):32-7.

[2] Bromaghim G, Gibeault K, Serfass J, Serfass P, Wagner E. Hydrogen and fuel cells: The US Market Report, vol. 22, National Hydrogen Association. 2010.

[3] Joseck F, Nguyen T, Klahr B, Talapatra A. Current U.S. hydrogen production. DOE Hydrogen and Fuel Cells Program Record. 2016 May 24.

[4] Navigant Research. Demand for hydrogen for fuel cells and other emerging markets will climb sharply through 2030 [Press release]. (2014 February 13). Retrieved from

http://www.navigantresearch.com/newsroom/demand-for-hydrogen-for-fuel-cellsand-other-emerging-markets-will-climb-sharply-through-2030.

[5] Gür TM. Comprehensive review of methane conversion in solid oxide fuel cells: prospects for efficient electricity generation from natural gas. Progress in Energy and Combustion Science. 2016 May 31;54:1-64.

[6] Kolb G. Fuel processing: for fuel cells, Wiley-VCH Verlag GmbH & Co. KGaA, 2008.

[7] Lerou JJ, Tonkovich AL, Silva L, Perry S, McDaniel J. Microchannel reactor architecture enables greener processes. Chemical Engineering Science. 2010 Jan 1;65(1):380-5.

[8] Murphy DM, Manerbino A, Parker M, Blasi J, Kee RJ, Sullivan NP. Methane steam reforming in a novel ceramic microchannel reactor. International Journal of Hydrogen Energy. 2013 Jul 17;38(21):8741-50.

[9] Pattison RC, Baldea M. Robust autothermal microchannel reactors. Computers & Chemical Engineering. 2015 Oct 4;81:171-9.

[10] Bartholomew CH. Mechanisms of catalyst deactivation. Applied Catalysis A: General. 2001 Apr 30;212(1):17-60.

[11] Pattison RC, Baldea M. A thermal-flywheel approach to distributed temperature control in microchannel reactors. AIChE journal. 2013 Jun 1;59(6):2051-61.

[12] Baldea M, Pattison RC, inventors; Board of regents, system, assignee. Catalytic plate reactors. United States patent application US 20,150,217,259. 2015 Aug 6.

[13] Pattison RC, Estep FE, Baldea M. Pseudodistributed feed configurations for catalytic plate microchannel reactors. Industrial & Engineering Chemistry Research. 2013 Aug 9;53(13):5028-37.

[14] Jeon SW, Yoon WJ, Baek C, Kim Y. Minimization of hot spot in a microchannel reactor for steam reforming of methane with the stripe combustion catalyst layer. international journal of hydrogen energy. 2013 Oct 25;38(32):13982-90.

[15] Ramaswamy RC, Ramachandran PA, Duduković MP. Recuperative coupling of exothermic and endothermic reactions. Chemical engineering science. 2006 Jan 31;61(2):459-72.

[16] Ramaswamy RC, Ramachandran PA, Duduković MP. Coupling exothermic and endothermic reactions in adiabatic reactors. Chemical engineering science. 2008 Mar 31;63(6):1654-67.

[17] Zanfir M, Baldea M, Daoutidis P. Optimizing the catalyst distribution for countercurrent methane steam reforming in plate reactors. AIChE Journal. 2011 Sep 1;57(9):2518-28.

[18] Kolios G, Frauhammer J, Eigenberger G. Efficient reactor concepts for coupling of endothermic and exothermic reactions. Chemical Engineering Science. 2002 May 31;57(9):1505-10.

[19] Kolios G, Glöckler B, Gritsch A, Morillo A, Eigenberger G. Heat-Integrated Reactor Concepts for Hydrogen Production by Methane Steam Reforming. Fuel Cells. 2005 Feb 1;5(1):52-65.

[20] Settar A, Nebbali R, Madani B, Abboudi S. Numerical study on the effects of the macropatterned active surfaces on the wall-coated steam methane reformer performances. International Journal of Hydrogen Energy. 2017 Jan 12;42(2):1490-8.

[21] Mundhwa M, Parmar RD, Thurgood CP. A comparative parametric study of a catalytic plate methane reformer coated with segmented and continuous layers of combustion catalyst for hydrogen production. Journal of Power Sources. 2017 Mar 15;344:85-102.

[22] Mundhwa M, Thurgood CP. Numerical study of methane steam reforming and methane combustion over the segmented and continuously coated layers of catalysts in a plate reactor. Fuel Processing Technology. 2017 Apr 30;158:57-72.

[23] Xu J, Froment GF. Methane steam reforming, methanation and water-gas shift: I. Intrinsic kinetics. AIChE Journal. 1989 Jan 1;35(1):88-96.

[24] Trimm DL. Catalysts for the control of coking during steam reforming. Catalysis Today. 1999 Feb 24;49(1):3-10.

[25] Hou K, Hughes R. The kinetics of methane steam reforming over a Ni/α-Al_2O_3 catalyst. Chemical Engineering Journal. 2001 Mar 15;82(1):311-28.

[26] Wei J, Iglesia E. Isotopic and kinetic assessment of the mechanism of reactions of CH_4 with CO_2 or H_2O to form synthesis gas and carbon on nickel catalysts. Journal of Catalysis. 2004 Jun 10;224(2):370-83.

[27] Rostrup-Nielsen J. 40 years in catalysis. Catalysis Today. 2006 Jan 15;111(1-2):4-11.

[28] Sprung C, Arstad B, Olsbye U. Methane Steam Reforming Over Ni/$NiAl_2O_4$ Catalyst: The Effect of Steam-to-Methane Ratio. Topics in Catalysis. 2011 Nov 1;54(16-18):1063-9.

[29] Guo J, Lou H, Zhao H, Chai D, Zheng X. Dry reforming of methane over nickel catalysts supported on magnesium aluminate spinels. Applied Catalysis A: General. 2004 Oct 8;273(1):75-82.

[30] Fauteux-Lefebvre C, Abatzoglou N, Braidy N, Achouri IE. Diesel steam reforming with a nickel–alumina spinel catalyst for solid oxide fuel cell application. Journal of Power Sources. 2011 Sep 15;196(18):7673-80.

[31] Blanchard J, Nsungui AJ, Abatzoglou N, Gitzhofer F. Dry Reforming of Methane with a Ni/Al2O3-YSZ Catalyst: The Role of the Catalyst Preparation Protocol. The Canadian Journal of Chemical Engineering. 2007 Dec 1;85(6):889-99.

[32] Bangala DN, Abatzoglou N, Chornet E. Steam reforming of naphthalene on Ni–Cr/Al2O3 catalysts doped with MgO, TiO2, and La2O3. AIChE Journal. 1998 Apr 1;44(4):927-36.

[33] Krishna R, Wesselingh JA. The Maxwell-Stefan approach to mass transfer. Chemical Engineering Science. 1997 Mar 31;52(6):861-911.

[34] Venkataraman K, Wanat EC, Schmidt LD. Steam reforming of methane and water-gas shift in catalytic wall reactors. AIChE Journal. 2003 May 1;49(5):1277-84.

[35] Whittenberger WA, inventor; Catacel Corp., assignee. Heat exchanger. United States patent US D560,276. 2008 Jan 22.

[36] Thermalloys AB, chemical composition and properties of FeCrAl alloys. Available at: http://www.thermalloys.com/index.php/en/alloys/fecralalloys.html.

[37] Todd B, Young JB. Thermodynamic and transport properties of gases for use in solid oxide fuel cell modelling. Journal of power Sources. 2002 Jul 20;110(1):186-200.

[38] Poling BE, Prausnitz JM, John Paul OC, Reid RC. The properties of gases and liquids. New York: McGraw-Hill; 2001.

[39] Zhao H, Yu F, Bennett TD, Wadley HN. Morphology and thermal conductivity of yttria-stabilized zirconia coatings. Acta Materialia. 2006 Nov 30;54(19):5195-207.

[40] Munro M. Evaluated material properties for a sintered alpha-alumina. Journal of the American ceramic society. 1997 Aug 1;80(8):1919-28.

[41] Bird RB, Stewart WE, Lightfoot EN. Transport phenomena. New York, USA: John Wiley & Sons, revised second ed. 2007.

[42] Welty JR, Wicks CE, Rorrer G, Wilson RE. Fundamentals of momentum, heat, and mass transfer. John Wiley & Sons; 2009 Oct 1.

[43] Fuller EN, Schettler PD, Giddings JC. New method for prediction of binary gas-phase diffusion coefficients. Industrial & Engineering Chemistry. 1966 May 1;58(5):18-27.

[44] Bessler WG, Gewies S, Vogler M. A new framework for physically based modeling of solid oxide fuel cells. Electrochimica Acta. 2007 Dec 31;53(4):1782-800.

[45] Tjaden B, Cooper SJ, Brett DJ, Kramer D, Shearing PR. On the origin and application of the Bruggeman correlation for analysing transport phenomena in electrochemical systems. Current Opinion in Chemical Engineering. 2016 May 31;12:44-51.

[46] Zanfir M, Gavriilidis A. Catalytic combustion assisted methane steam reforming in a catalytic plate reactor. Chemical Engineering Science. 2003 Sep 30;58(17):3947-60.

[47] Maier L, Schädel B, Delgado KH, Tischer S, Deutschmann O. Steam reforming of methane over nickel: development of a multi-step surface reaction mechanism. Topics in Catalysis. 2011 Sep 1;54(13-15):845-58.

[48] Ronane MJ. An investigation of gauze supported platinum alumina and cobalt supported oxide oxidation catalysts (Master dissertation, Dublin City University).

[49] Deshmukh SR, Vlachos DG. A reduced mechanism for methane and one-step rate expressions for fuel-lean catalytic combustion of small alkanes on noble metals. Combustion and Flame. 2007 Jun 30;149(4):366-83.

[50] Herrera Delgado K. Surface Reaction Kinetics for Oxidation and Reforming of H_2, CO, and CH_4 over Nickel-based Catalysts (Doctoral dissertation, Karlsruhe, Karlsruher Institut für Technologie (KIT), Diss., 2014).

[51] Mundhwa M, Christopher CP. Methane steam reforming at low steam to carbon ratios over alumina and yttria-stabilized-zirconia supported nickel-spinel catalyst: Experimental study and optimization of microkinetic model. Fuel Processing Technology. 2017;168:27-39.

Chapter 7

Contributions and recommendations

In this thesis, novel design of distributed coating configuration of reforming and combustion catalysts was proposed in a CPR to produce H_2 by MC assisted MSR. The proposed distributed coating design not only showed decrease of thermal stresses along the plate-length but also showed significant savings in reforming and combustion catalysts compared to the conventional continuous coating design with no loss in hydrogen generating capacity. This Chapter briefly recaps the key contributions of this thesis. The Chapter concludes by presenting recommendations for the future work.

7.1 Summary and key contributions

The CPR design provides an excellent heat and mass transfer features to drive endothermic process (*e.g.* methane steam reforming) in forward direction with the help of exothermic process (*e.g.* methane combustion) compared to the conventional packed bed reactor design. Better heat transfer rate in a CPR lead to a compact design and hence higher thermal efficiency. Due to its compact design with higher thermal efficiency, CPR doesn't have the thermal mass of a packed bed reactor and thus it responds to any load changes of fuel cell quickly. Also, due to enhanced mass transfer rates due to thin coatings of catalysts, the CPR requires smaller amount of reforming and combustion catalysts compared to the conventional packed bed reactor design. At first glance, the CPR design looks very simple but physical and chemical phenomena happening on both side of a thin metal plate are very complex and not easy to capture experimentally. Hence, it is best to investigate the CPR, even only possible, with advanced, credible simulation tools. To capture all physical and chemical phenomena in a CPR, a numerical model is required that can co-ordinate all the heat and mass transfer phenomena coupled with detailed multi-step reaction scheme. The numerical model allows to vary all the different parts (design and operating parameters) of a CPR (individually or simultaneously), which otherwise time consuming and expensive if carried out experimentally. Hence, the development of a numerical model is extremely important for the development of the efficient and effective CPR technology for the H_2 production.

The thesis introduced with the requirement of fuel cell technology and outlined the issues/problems in plate reformers to produce H_2 for fuel cells. As mentioned earlier, significant difference in heat liberation rate on combustion-side and heat absorption rate on reforming-side generates thermal stresses in a metal plate, which increases thermal degradation rate of the plate material and hence decreases lifespan of a CPR. Thermal stresses in a metal plate also delaminates the surface coatings of the reforming and combustion catalysts due to different thermal expansion coefficients between the plate and catalysts materials. Thermal stresses also reduce the active catalytic surface area resulting in low conversion of reactants and hence, rapidly degrade the performance of a CPR. This work was motivated to solve the problem of thermal stresses in a CPR design by proposing novel distributed coating configuration of combustion and reforming catalysts over the entire plate-length.

The primary purpose of the Chapter 3 in this thesis was to investigate how different coating configurations (segmented and continuous) of MSR and MC catalysts influence the temperature and product distributions in a CPR at constant GHSV (gas hourly space velocity). For this preliminary study, I developed four different 2D steady-state CFD models of a CPR designed with the four different configurations between segmented and continuous coatings of combustion and reforming catalysts to produce H_2 for a 1 kW fuel cell. The inlet flow of methane for all four numerical models was selected based on the required hydrogen flow in a 1 kW fuel-cell. Such choice of flow can facilitate the future engineering and scaling calculations to integrate a CPR with a fuel-cell stack of different scale. The four configurations were: (1) continuous combustion-catalyst and continuous reforming-catalyst (conventional CPR design), (2) continuous combustion-catalyst and segmented reforming-catalyst, (3) segmented combustion-catalyst and continuous reforming-catalyst, and (4) segmented combustion-catalyst and segmented reforming-catalyst. All four numerical models were developed and simulated using the COMSOL^{TM} simulation software and their results were compared with each other. I simulated MSR on one side of a plate by implementing multi-step surface microkinetic model for Ni/alumina catalyst. Required thermal energy to the endothermic MSR is provided by simulating catalytic MC on the opposite-side of the plate by implementing reduced surface microkinetic model for Pt/alumina catalyst. Before simulating the different coating configurations between the reforming and combustion catalysts, I developed a separate CFD model to validate the multi-step surface microkinetic model against the experimental data of MSR in a CPR available in the literature. In all these four models, I successfully integrated continuum scale transport, heat and mass transfer with the reduced microkinetic model of catalytic MC and with the experimentally validated multi-step surface microkinetic model of MSR. Results obtained from four different coating configurations showed that significant reduction in hotspots and uniform temperature distribution were achieved with the segmented (or distributed) coatings of combustion and reforming catalysts compared to the conventional continuous coating design. Further, the distributed coating design saved considerable proportion (about 66%) of the precious combustion-catalyst without losing hydrogen generation capacity in MSR process compared to the conventional CPR design. The study also showed that maximum temperature obtained with the conventional CPR design was reduced by about 30 °C in the case of distributed coating design with no loss in methane conversions. From this study, it was established that with the help of distributed coating design of the combustion-catalyst, uniform temperature distribution along the plate-length can be achieved and also hydrogen production can be enhanced if the inter catalyst space between the segmented layers of the combustion-catalyst is optimized.

It was clearly established in Chapter 3 that by adopting distributed coating design of the combustion-catalyst in a CPR is beneficial in controlling the issues due to thermal stresses. Hence, in Chapter 4, I carried out a parametric comparison study between the conventional and distributed coatings of the combustion-catalyst to study the influence of design and operating parameters (flow-direction, reforming-catalyst thickness and gas-hourly space velocity) on the performance of a CPR for the production of H_2 by MSR. For this study, I considered inter-catalyst space of 2.5 mm for the distributed coating layers of the combustion-catalyst, as opposed to 2 mm considered in the preliminary study of Chapter 3. It was determined that with increased inter-catalyst space, CPR designed with the segmented (or distributed) coating of the combustion-catalyst showed improvement. Further it showed that 7 to 8% less combustion-side fuel is required to produce same H_2 flow compared to the conventional continuous coating. Flow direction study between the reforming and combustion sides showed higher conversion with respect to the co-current flow compared to the counter-current flow in both continuous and distributed configurations. Also, reforming-catalyst thickness study indicated diffusion limitation with increasing thickness for both configurations. Nevertheless, CPR designed with the distributed coating showed improved performance for all studied parameters compared to the CPR designed with the continuous coating of the combustion-catalyst. This parametric explorative study determined that distributed coating configuration is beneficial over a wide range of operating and design parameters and is not limited for any specific operating condition.

Traditionally, the production of H_2 by MSR is carried out over nickel (Ni) based catalysts with steam to carbon (SC) ratio of three or above to avoid carbon formation. Hence, for preliminary and explorative studies in chapters 3 and 4, I chose traditional route by considering SC ratio of three. However, the SC ratio of three or above is very high compared to the reforming reaction stoichiometric ratio of one. High SC ratio dilutes the syngas content and is energetically unfavorable due to the requirements of more energy to produce excess steam in a boiler at the reactor upstream and to condense unreacted steam in a condenser at the reactor downstream. Thus, with the aim of making MSR process more energy efficient, I conducted an experimental work of MSR on promising Ni-spinel catalyst at low steam to carbon ratios and is presented in Chapter 5. The Ni-spinel catalyst has shown promising potential for the reforming of different fuels. The use of such catalyst in a reformer can provide flexibility in selecting wide range of fuels that are available at various locations to produce H_2 and hence can further increase the usage of fuel cells. To evaluate the performance of any catalytic reactor design, it is important to develop reaction rate expression based on the underlying chemical phenomena. To simplify the kinetic model or rate expression development stage, I adopted a surface microkinetic model of MSR over Ni/alumina catalyst from the literature and validated it against the experimental data of MSR over Ni-spinel catalyst by optimizing the kinetic parameters of the most influential elementary reaction steps. I scrutinized the most influential reaction steps based on the partial equilibrium analysis (PEA) and local sensitivity analysis (LSA).

For the development of a CPR design based on a coating of the Ni-spinel catalyst and for low SC ratio in MSR, I implemented optimized surface microkinetic model of chapter 5 into the CFD models of a CPR in Chapter 6. The CFD models presented in Chapter 6 were developed to optimize the quantity of distributed coatings of both reforming and combustion catalysts. Unlike in Chapters 3 and 4, in Chapter 6, I studied internal diffusion limitation with respect to the coating thickness of the Ni-spinel (reforming-catalyst) and Pt-alumina (combustion-catalyst) by developing single-channel 2D steady-state isothermal models separately for the catalytic MC and MSR. I also determined effective utilization of both catalysts for different coating thickness by estimating overall effectiveness factors. From the study of internal diffusion limitation, it was concluded that reforming-catalyst thickness greater than 50 µm and combustion-catalyst thickness greater than 5 µm showed diffusion limitation for the considered operating conditions. Further, to improve the prediction accuracy of the CFD models, unlike in Chapters 3 and 4, I implemented gas-phase MC kinetics on the combustion-side of the plate. To determine the optimum amount of both reforming and combustion catalysts, I studied different patterns of distributed coating configurations of both reforming and combustion catalysts. I found that it is possible to improve both methane conversion and hydrogen production with 74% less combustion catalyst compared to the conventional continuous coating design when inter-catalyst space length of 3 mm for the distributed combustion-catalyst was considered. I also found that distributed coating design saved 20 to 28% reforming-catalyst for the same H_2 production as in conventional CPR designed with the continuous coatings. In chapter 6, I also carried out an investigation of the influence of plate-thickness on the performance of distributed coatings and found that performance of the distributed coating patterns is more pronounced in a CPR designed with relatively thicker plate, which again confirmed that distributed coating configuration is beneficial over a wide range of operating and design parameters and is not limited for any specific operating condition.

7.2 Recommendations for future work

In this study, it was established by numerical analysis that distributed or segmented coating configuration of both reforming and combustion catalysts is beneficial in controlling the temperature distribution and hence unwanted thermal stresses. The study was based on available literature data of operating and design parameters of a CPR, therefore results obtained using CFD models of a CPR designed with the distributed coatings need to be validated against experimental CPR reactor built with the distributed coatings. The models developed in this study were two-dimensional, hence, it would be intriguing to consider spatial segmentation patterns on a 3D plate, which might further enhance the performance of a CPR. All simulation runs in this study were carried out at steady-state condition. A transient model is required to evaluate the dynamic performance of a CPR to study the influence of distributed coatings at the start-up compared to the conventional continuous design. The developed code for the CPR can be further modified to establish the design criteria for the development of commercial CPR design.

Kinetic parameters estimated in this study was based on limited experimental data, hence it was not possible to develop a comprehensive and accurate reaction kinetics model for the MSR over Ni-spinel catalyst. To predict the performance of any reformer design, an accurate reaction kinetics model plays a crucial role and hence I recommend developing such model for the Ni-spinel catalyst for better predictability of a reformer performance based on experimental data obtained over wide range of operating conditions.

It is possible to further enhance the heat transfer rate by developing new concept designs, such as micro-fins and micro-baffles in combination with catalytic plate reactor.

Appendix A

Governing equations

Note: Reference number cited in Appendix A are listed at the end of chapter 6.

A. Reforming and combustion flow-channels (free-flow)

i. Momentum transport and mass conservation

x-component of momentum

$$\rho_{mix}\left(u_x\frac{\partial u_x}{\partial x}+u_y\frac{\partial u_x}{\partial y}\right)=-\frac{\partial P}{\partial x}+\frac{\partial}{\partial x}\left(2\mu_{mix}\frac{\partial u_x}{\partial x}-\frac{2}{3}\mu_{mix}\left(\frac{\partial u_x}{\partial x}+\frac{\partial u_y}{\partial y}\right)\right)+\frac{\partial}{\partial y}\left(\mu_{mix}\left(\frac{\partial u_x}{\partial y}+\frac{\partial u_y}{\partial x}\right)\right) \quad \text{(A1)}$$

y-component of momentum

$$\rho_{mix}\left(u_x\frac{\partial u_y}{\partial x}+u_y\frac{\partial u_y}{\partial y}\right)=-\frac{\partial P}{\partial y}+\frac{\partial}{\partial y}\left(2\mu_{mix}\frac{\partial u_y}{\partial y}-\frac{2}{3}\mu_{mix}\left(\frac{\partial u_x}{\partial x}+\frac{\partial u_y}{\partial y}\right)\right)+\frac{\partial}{\partial x}\left(\mu_{mix}\left(\frac{\partial u_x}{\partial y}+\frac{\partial u_y}{\partial x}\right)\right) \quad \text{(A2)}$$

continuity equation

$$\rho_{mix}\left(\frac{\partial u_x}{\partial x}+\frac{\partial u_y}{\partial y}\right)+\left(u_x\frac{\partial \rho_{mix}}{\partial x}+u_y\frac{\partial \rho_{mix}}{\partial y}\right)=0 \quad \text{(A3)}$$

where, ρ_{mix} is the density of a gas mixture, estimated using the ideal-gas state equation and μ_{mix} is the gas mixture viscosity, estimated using the Reichenberg method [38] in chapter 6. Gas mixture viscosity in chapters 3 and 4 are estimated using the method developed by Wilke [38].

ii. Heat transport and energy conservation

$$\rho_{mix}C_{p,mix}\left(u_x\frac{\partial T}{\partial x}+u_y\frac{\partial T}{\partial y}\right)=k_{mix}\left(\frac{\partial^2 T}{\partial x^2}+\frac{\partial^2 T}{\partial y^2}\right) \quad \text{(A4)}$$

where, $C_{p,mix}$ is the heat capacity of a gas mixture, evaluated using the weighted average heat capacity of chemical species and k_{mix} is the gas mixture thermal conductivity, estimated by applying the Mason and Saxena method [38]. It should be noted that the numerical models developed in chapters 6 consider gas-phase MC on the combustion-side and thus, for the combustion-channel, a heat source term $R^{gas-phase}\Delta H_r$ is added on the right-hand side of Eq. A4 to account for the heat liberated due to the gas-phase MC in the combustion-channel. It should also be noted that the gas-phase MC is neglected in numerical models developed in chapters 3 and 4.

iii. Mass transport

$$\begin{aligned}\rho_{mix}\left(\left(u_x\frac{\partial\omega_i}{\partial x}+u_y\frac{\partial\omega_i}{\partial y}\right)+\omega_i\left(\frac{\partial u_x}{\partial x}+\frac{\partial u_y}{\partial y}\right)\right)\\ =\frac{\partial}{\partial x}\left(\rho_{mix}\omega_k\sum_{j=1,j\neq i}^{N_g}D_{ij}^{F}\left(\frac{\partial \mathrm{x}_j}{\partial x}+\frac{\partial \mathrm{x}_j}{\partial y}+\left(\frac{\mathrm{x}_j-\omega_j}{P}\right)\left(\frac{\partial P}{\partial x}+\frac{\partial P}{\partial y}\right)\right)\right)\\ +\frac{\partial}{\partial y}\left(\rho_{mix}\omega_k\sum_{j=1,j\neq i}^{N_g}D_{ij}^{F}\left(\frac{\partial \mathrm{x}_j}{\partial x}+\frac{\partial \mathrm{x}_j}{\partial y}+\left(\frac{\mathrm{x}_j-\omega_i}{P}\right)\left(\frac{\partial P}{\partial x}+\frac{\partial P}{\partial y}\right)\right)\right)\end{aligned}\tag{A5}$$

where, ω and x represent mass-fraction and mole-fraction of chemical species, D_{ij}^{F} are the multicomponent Fick diffusivities, and are related with the Maxwell-Stefan diffusivities as [41]:

$$D_{ij}^{MS}=\frac{\mathrm{x}_i\mathrm{x}_j}{\omega_i\omega_j}\frac{\sum_{k\neq i}D_{ij}^{F}(adj\ B_i)_{kj}}{\sum_{k\neq i}(adj\ B_i)_{kj}};where(B_i)_{jk}=-D_{jk}^{F}+D_{ik}^{F}\tag{A6}$$

For multicomponent diffusion in gases at low density, the Maxwell-Stefan diffusivities (D_{ij}^{MS}) can be replaced by binary diffusivities (D_{ij}) [41], which are estimated using Fuller equation [38]. It should be noted that to account for the gas-phase MC, a rate expression term ≈ $R_i^{gas-phase}M_i$ for chemical species i is added on the right-hand side of Eq. A5 for the numerical models developed in chapter 6 only.

iv. Boundary conditions

Inlet conditions (boundaries 1 and 3 in Fig. 3.2(A))

- Velocity profile (fully developed laminar inflow): $u_x=1.5u_{x,in}\left(1-\left(\frac{y}{h_{ch}}\right)^2\right)$
- Temperature: $T=T_{in}$
- Mass fraction: $\omega_i=\omega_{i,in}$

Outlet conditions (boundaries 5 and 7 in Fig. 3.2(A))

- Pressure: $P=P_{out}$
- Zero flux: $\frac{\partial\omega_i}{\partial x}=0;\frac{\partial T}{\partial x}=0$

Symmetry conditions at channels center planes (boundaries 4 and 8 in Fig. 3.2(A))

- $\frac{\partial u_x}{\partial y}=0;\ \frac{\partial\omega_i}{\partial y}=0;\ \frac{\partial T}{\partial y}=0$

Interfaces between plate surface and flow channels (boundaries 9 and 10 in Fig. 3.2(A))

- No slip: $u_x=0$
- Heat flux continuity: $\vec{n}\cdot\left(N_{plate}-N_{ch}\right)=0$

- Zero flux: $\frac{\partial \omega_i}{\partial y} = 0$

B. Reforming and combustion catalyst (porous media)

i. Momentum transport and mass conservation

x-component of momentum

$$\frac{\mu_{mix}}{\kappa} u_x = -\frac{\partial P}{\partial x} + \frac{\partial}{\partial x}\left(2\frac{\mu_{mix}}{\varepsilon}\frac{\partial u_x}{\partial x} - \frac{2}{3}\mu_{mix}\left(\frac{\partial u_x}{\partial x} + \frac{\partial u_y}{\partial y}\right)\right) + \frac{\partial}{\partial y}\left(\frac{\mu_{mix}}{\varepsilon}\left(\frac{\partial u_x}{\partial y} + \frac{\partial u_y}{\partial x}\right)\right) \quad \text{(A7)}$$

y-component of momentum

$$\frac{\mu_{mix}}{\kappa} u_y = -\frac{\partial P}{\partial y} + \frac{\partial}{\partial y}\left(2\frac{\mu_{mix}}{\varepsilon}\frac{\partial u_y}{\partial y} - \frac{2}{3}\mu_{mix}\left(\frac{\partial u_x}{\partial x} + \frac{\partial u_y}{\partial y}\right)\right) + \frac{\partial}{\partial x}\left(\frac{\mu_{mix}}{\varepsilon}\left(\frac{\partial u_x}{\partial y} + \frac{\partial u_y}{\partial x}\right)\right) \quad \text{(A8)}$$

continuity equation

$$\rho_{mix}\left(\frac{\partial u_x}{\partial x} + \frac{\partial u_y}{\partial y}\right) + \left(u_x\frac{\partial \rho_{mix}}{\partial x} + u_y\frac{\partial \rho_{mix}}{\partial y}\right) = 0 \quad \text{(A9)}$$

where, κ is the permeability of porous media, estimated using Kozeny-Carman relationship [44] and is defined as:

$$\kappa = \frac{\varepsilon^3 d_p^2}{72\tau(1-\varepsilon)^2} \quad \text{(A10)}$$

ii. Heat transport and energy conservation

$$\rho_{mix}C_{pmix}\left(u_x\frac{\partial T}{\partial x} + u_y\frac{\partial T}{\partial y}\right) = k_{eff}\left(\frac{\partial^2 T}{\partial x^2} + \frac{\partial^2 T}{\partial y^2}\right) + A_s(1-\varepsilon)\sum_r R_i^{surface}\Delta H_r \quad \text{(A11)}$$

where, H_r is the enthalpy of reaction r, k_{eff} is the effective thermal conductivity of porous catalyst domains and is calculated using volume weighted average using Eq. 6.2. Combustion-catalyst thermal conductivity ($k_{cat,comb}$) is approximated based on alumina and is calculated using Eq. 6.3, whereas reforming-catalyst thermal conductivity ($k_{cat,ref}$) is approximated based on alumina and YSZ and is calculated using Eq. 6.4. It should be noted that for the combustion-channel, a heat source term $\varepsilon R^{gas-phase}\Delta H_r$ is added on the right-hand side of Eq. A11 to account for the heat liberated due to the gas-phase MC in porous regions of the combustion-catalyst.

iii. Mass transport

$$\rho_{mix}\left(\left(u_x\frac{\partial \omega_i}{\partial x} + u_y\frac{\partial \omega_i}{\partial y}\right) + \omega_i\left(\frac{\partial u_x}{\partial x} + \frac{\partial u_y}{\partial y}\right)\right)$$
$$= \frac{\partial}{\partial x}\left(\rho_{mix}\omega_k\sum_{j=1,j\neq i}^{N_g} D_{ij,eff}^F\left(\frac{\partial \mathrm{x}_j}{\partial x} + \frac{\partial \mathrm{x}_j}{\partial y} + \left(\frac{\mathrm{x}_j - \omega_j}{P}\right)\left(\frac{\partial P}{\partial x} + \frac{\partial P}{\partial y}\right)\right)\right)$$
$$+ \frac{\partial}{\partial y}\left(\rho_{mix}\omega_k\sum_{j=1,j\neq i}^{N_g} D_{ij,eff}^F\left(\frac{\partial \mathrm{x}_j}{\partial x} + \frac{\partial \mathrm{x}_j}{\partial y} + \left(\frac{\mathrm{x}_j - \omega_i}{P}\right)\left(\frac{\partial P}{\partial x} + \frac{\partial P}{\partial y}\right)\right)\right) + A_s(1-\varepsilon)R_i^{surface}M_i \quad \text{(A12)}$$

To incorporate Knudsen diffusion in the multicomponent mass transport of porous media, as mentioned earlier, an average Bosanquet diffusion coefficients are determined using Eq. 6.5. It should be noted that to account for the gas-phase MC in the porous regions of the combustion-catalyst, the last term in Eq. A12 for the combustion-catalyst is modified by:

$$A_s(1-\varepsilon)R_i^{surface}M_i + \varepsilon R_i^{gas-phase}M_i \qquad (A13)$$

iv. *Boundary conditions:*

Boundaries between catalyst and free-flow channels (boundaries 12 and 13 in Fig. 3.2(A))

- Continuity: momentum, mass and heat flux components normal to the boundary are continuous across the boundary; $\vec{n}\cdot(N_{ch}-N_{cat})=0$

Boundaries between plate surface and catalyst layers (boundaries 11 and 14 in Fig. 3.2(A))

- No slip: $u_x = 0$
- Heat flux continuity: $\vec{n}\cdot\left(N_{plate}-N_{cat}\right)=0$
- Zero flux: $\frac{\partial \omega_i}{\partial y} = 0$

C. Fecralloy plate

i. Heat transport

$$\frac{\partial}{\partial x}\left(k_{plate}\frac{\partial T}{\partial x}\right)+\frac{\partial}{\partial y}\left(k_{plate}\frac{\partial T}{\partial y}\right)=0 \qquad (A14)$$

where, k_{plate} is the thermal conductivity of metal plate and is calculated using Eq. 6.1. It should be noted that constant value of 16 W/m/K value for the k_{plate} is considered for the numerical models developed in chapters 3 and 4.

ii. Boundary conditions:

Thermal insulation (boundaries 2 and 6 in Fig. 3.2(A))

- Zero flux: $\frac{\partial T}{\partial x} = 0$

Appendix B

Catalytic plate reactor model parameters and grids

B1. Parameters used for the development of the models in Chapter 6

Name	Expression
N_channel	30
FCH4in_r	0.00276[mol/s]/N_channel
SC	1.5
FH2Oin_r	SC*FCH4in_r
FCH4in_c	factor*FCH4in_r
factor	4*0.14808
m_ratio	(F_c*MW_c)/(F_r*MW_r)
O2C	2
FO2in_c	O2C*FCH4in_c
FN2in_c	(0.79/0.21)*FO2in_c
F_r	FCH4in_r + FH2Oin_r
F_c	FCH4in_c + FO2in_c + FN2in_c
V_r	F_r/cfeed_r
V_c	F_c/cfeed_c
height	1[mm]
width	5[cm]
height_c	1[mm]
Across	height*width
Across_c	height_c*width
uin_r	V_r/Across
uin_c	V_c/Across_c
Tc	800[K]
Tr	800[K]
T_initial	800[K]
P	1[atm]
cfeed_c	P/R_const/Tc
cfeed_r	P/R_const/Tr
xCH4in_c	FCH4in_c/(FCH4in_c + FO2in_c + FN2in_c)
xO2in_c	FO2in_c/(FCH4in_c + FO2in_c + FN2in_c)
xN2in_c	FN2in_c/(FCH4in_c + FO2in_c + FN2in_c)
xCO2in_c	0
xH2Oin_c	0
xCH4in	FCH4in_r/(FCH4in_r + FH2Oin_r)
xH2Oin	FH2Oin_r/(FCH4in_r + FH2Oin_r)
xCOin	0
xH2in	0
xCO2in	0
xO2in	1 - (xCH4in + xH2Oin + xCOin + xH2in + xCO2in)
MW_r	xCH4in*MCH4 + xH2Oin*MH2O + xCOin*MCO + xH2in*MH2 + xCO2in*MCO2 + xO2in*MO2

Name	Expression
MW_c	xCH4in_c*MCH4 + xH2Oin_c*MH2O + xCO2in_c*MCO2 + xO2in_c*MO2 + xN2in_c*MN2
w_CH4in	xCH4in*MCH4/MW_r
w_H2Oin	xH2Oin*MH2O/MW_r
w_COin	xCOin*MCO/MW_r
w_H2in	xH2in*MH2/MW_r
w_CO2in	xCO2in*MCO2/MW_r
w_O2in	xO2in*MO2/MW_r
w_fraction_r	w_CH4in + w_H2Oin + w_COin + w_H2in + w_CO2in + w_O2in
w_CH4in_c	xCH4in_c*MCH4/MW_c
w_H2Oin_c	xH2Oin_c*MH2O/MW_c
w_CO2in_c	xCO2in_c*MCO2/MW_c
w_O2in_c	xO2in_c*MO2/MW_c
w_N2in_c	xN2in_c*MN2/MW_c
w_fraction_c	w_CH4in_c + w_H2Oin_c + w_CO2in_c + w_O2in_c + w_N2in_c
CH4in_c	xCH4in_c*cfeed_c
O2in_c	xO2in_c*cfeed_c
H2Oin_c	xH2Oin_c*cfeed_c
CO2in_c	xCO2in_c*cfeed_c
N2in_c	xN2in_c*cfeed_c
CH4in	xCH4in*cfeed_r
H2Oin	xH2Oin*cfeed_r
COin	xCOin*cfeed_r
H2in	xH2in*cfeed_r
CO2in	xCO2in*cfeed_r
O2in	xO2in*cfeed_r
vCH4in_c	uin_c*Across*CH4in_c
vO2in_c	uin_c*Across*O2in_c
vCH4in	uin_r*Across*CH4in
vH2Oin	uin_r*Across*H2Oin
vH2in	uin_r*Across*H2in
vCOin	uin_r*Across*COin
vCO2in	uin_r*Across*CO2in
MCH4	0.01604[kg/mol]
MH2O	0.01802[kg/mol]
MCO	0.02801[kg/mol]
MH2	0.00202[kg/mol]
MCO2	0.04404[kg/mol]
MN2	0.02802[kg/mol]
MO2	0.032[kg/mol]
MAl2O3	101.96[g/mol]
MFe	55.847[g/mol]
MCr	51.996[g/mol]
MAl	26.98[g/mol]
MNi	58.71[g/mol]
MPt	195.08[g/mol]
vCH4	24.42
vH2O	12.7
vCO	18.9
vH2	7.07
vCO2	26.9
vN2	17.9
vO2	16.6
a0_CH4	47.964
a1_CH4	-178.59
a2_CH4	712.55

Name	**Expression**
a3_CH4	-1068.7
a4_CH4	856.93
a5_CH4	-358.75
a6_CH4	61.321
a0_H2O	37.373
a1_H2O	-41.205
a2_H2O	146.01
a3_H2O	-217.08
a4_H2O	181.54
a5_H2O	-79.409
a6_H2O	14.015
a0_CO2	4.3669
a1_CO2	204.6
a2_CO2	-471.33
a3_CO2	657.88
a4_CO2	-519.9
a5_CO2	214.58
a6_CO2	-35.992
a0_CO	30.429
a1_CO	-8.1781
a2_CO	5.2062
a3_CO	41.974
a4_CO	-66.346
a5_CO	37.756
a6_CO	-7.6538
a0_H2	21.157
a1_H2	56.036
a2_H2	-150.55
a3_H2	199.29
a4_H2	-136.15
a5_H2	46.903
a6_H2	-6.4725
a0_N2	29.027
a1_N2	4.8987
a2_N2	-38.04
a3_N2	105.17
a4_N2	-113.56
a5_N2	55.554
a6_N2	-10.35
a0_O2	34.85
a1_O2	-57.975
a2_O2	203.68
a3_O2	-300.37
a4_O2	231.72
a5_O2	-91.821
a6_O2	14.776
b0_CH4	-9.9989
b1_CH4	529.37
b2_CH4	-543.82
b3_CH4	548.11
b4_CH4	-367.06
b5_CH4	140.48
b6_CH4	-22.92
b0_H2O	-6.7541
b1_H2O	244.93

Name	Expression
b2_H2O	419.5
b3_H2O	-522.38
b4_H2O	348.12
b5_H2O	-126.96
b6_H2O	19.591
b0_CO2	-20.434
b1_CO2	680.07
b2_CO2	-432.49
b3_CO2	244.22
b4_CO2	-85.929
b5_CO2	14.45
b6_CO2	-0.4564
b0_CO	-4.9137
b1_CO	793.65
b2_CO	-875.90
b3_CO	883.75
b4_CO	-572.14
b5_CO	208.42
b6_CO	-32.298
b0_H2	15.553
b1_H2	299.78
b2_H2	-244.34
b3_H2	249.41
b4_H2	-167.51
b5_H2	62.966
b6_H2	-9.9892
b0_N2	1.2719
b1_N2	771.45
b2_N2	-809.2
b3_N2	832.47
b4_N2	-553.93
b5_N2	206.15
b6_N2	-32.43
b0_O2	-1.6918
b1_O2	889.75
b2_O2	-892.79
b3_O2	905.98
b4_O2	-598.36
b5_O2	221.64
b6_O2	-34.754
c0_CH4	0.4796
c1_CH4	1.8732
c2_CH4	37.413
c3_CH4	-47.44
c4_CH4	38.251
c5_CH4	-17.283
c6_CH4	3.2774
c0_H2O	2.0103
c1_H2O	-7.9139
c2_H2O	35.922
c3_H2O	-41.39
c4_H2O	35.993
c5_H2O	-18.974
c6_H2O	4.1531
c0_CO2	2.8888

Name	Expression
c1_CO2	-27.018
c2_CO2	129.65
c3_CO2	-233.29
c4_CO2	216.83
c5_CO2	-101.12
c6_CO2	18.698
c0_CO	-0.2815
c1_CO	13.999
c2_CO	-23.186
c3_CO	36.018
c4_CO	-30.818
c5_CO	13.379
c6_CO	-2.3224
c0_H2	1.504
c1_H2	62.892
c2_H2	-47.19
c3_H2	47.763
c4_H2	-31.939
c5_H2	11.972
c6_H2	-1.8954
c0_N2	-0.3216
c1_N2	14.81
c2_N2	-25.473
c3_N2	38.837
c4_N2	-32.133
c5_N2	13.493
c6_N2	-2.2741
c0_O2	-0.1857
c1_O2	11.118
c2_O2	-7.3734
c3_O2	6.713
c4_O2	-4.1797
c5_O2	1.491
c6_O2	-0.2278
Tc_CH4	190.56[K]
Tc_H2O	647.14[K]
Tc_CO	132.85[K]
Tc_H2	32.98[K]
Tc_CO2	304.12[K]
Tc_O2	154.58[K]
Tc_N2	126.2[K]
Pc_CH4	45.99[bar]
Pc_H2O	220.64[bar]
Pc_CO	34.94[bar]
Pc_H2	12.93[bar]
Pc_CO2	73.74[bar]
Pc_O2	50.43[bar]
Pc_N2	33.98[bar]
mu_CH4	0[debye]
mu_H2O	1.8[debye]
mu_CO	0.1[debye]
mu_H2	0[debye]
mu_CO2	0[debye]
mu_O2	0[debye]
mu_N2	0[debye]

Name	Expression
C_Ni	2.6E-5[mol/m^2]
A1	1.029E-02
A2	0.010
A3	7.312E-03
A4	1.158E-01
A5	1e-5
A6	4.626E-01
A7	2.143E+19[cm^2/mol/s]
A8	4.283e23[cm^2/mol/s]
A9	8.950E+15[1/s]
A10	3.909E+12[1/s]
A11	6.447e7[1/s]
A12	3.628E+11[1/s]
A13	5e22[cm^2/mol/s]
A14	1.781e21[cm^2/mol/s]
A15	3e20[cm^2/mol/s]
A16	2.271e21[cm^2/mol/s]
A17	3e21[cm^2/mol/s]
A18	6.373e23[cm^2/mol/s]
A19	5.20e23[cm^2/mol/s]
A20	1.354e22[cm^2/mol/s]
A21	2e19[cm^2/mol/s]
A22	4.653e23[cm^2/mol/s]
A23	3.7e21[cm^2/mol/s]
A24	4.019e20[cm^2/mol/s]
A25	3.7e24[cm^2/mol/s]
A26	4.604e20[cm^2/mol/s]
A27	4.574E+21[cm^2/mol/s]
A28	1.327E+22[cm^2/mol/s]
A29	3.7e24[cm^2/mol/s]
A30	1.293e22[cm^2/mol/s]
A31	2.370E+24[cm^2/mol/s]
A32	5.722E+23[cm^2/mol/s]
A33	3.7e21[cm^2/mol/s]
A34	4.562e22[cm^2/mol/s]
A35	1.7e24[cm^2/mol/s]
A36	9.876e22[cm^2/mol/s]
A37	3.7e24[cm^2/mol/s]
A38	4.607e21[cm^2/mol/s]
A39	3.7e24[cm^2/mol/s]
A40	1.457e23[cm^2/mol/s]
A41	3.7e21[cm^2/mol/s]
A42	1.625e21[cm^2/mol/s]
B20	-3
B22	-1
B24	-1
B25	-3
E7	81.21[kJ/mol]
E8	474.95[kJ/mol]
E9	37.55[kJ/mol]
E10	60.79[kJ/mol]
E11	25.98[kJ/mol]
E12	111.27[kJ/mol]
e12	-50[kJ/mol]
E13	97.9[kJ/mol]

Name	Expression
E14	36.09[kJ/mol]
E15	42.7[kJ/mol]
E16	91.76[kJ/mol]
E17	100[kJ/mol]
E18	210.86[kJ/mol]
E19	148.1[kJ/mol]
E20	116.12[kJ/mol]
e20	-50[kJ/mol]
E21	123.6[kJ/mol]
e21	-50[kJ/mol]
E22	89.32[kJ/mol]
E23	0[kJ/mol]
e23	50[kJ/mol]
E24	132.23[kJ/mol]
E25	95.8[kJ/mol]
E26	109.97[kJ/mol]
E27	57.7[kJ/mol]
E28	61.58[kJ/mol]
E29	100[kJ/mol]
E30	55.33[kJ/mol]
E31	97.1[kJ/mol]
E32	79.18[kJ/mol]
E33	18.8[kJ/mol]
E34	161.11[kJ/mol]
E35	88.3[kJ/mol]
E36	30.37[kJ/mol]
E37	130.1[kJ/mol]
E38	23.62[kJ/mol]
E39	126.8[kJ/mol]
E40	47.07[kJ/mol]
E41	48.1[kJ/mol]
E42	128.61[kJ/mol]
H1	-81[kJ/mol]
H_2	-474.95[kJ/mol]
H3	-37.55[kJ/mol]
H4	-60.79[kJ/mol]
H5	-25.98[kJ/mol]
H6	-111.27[kJ/mol]
H7	81[kJ/mol]
H8	474.95[kJ/mol]
H9	37.55[kJ/mol]
H10	60.79[kJ/mol]
H11	25.98[kJ/mol]
H12	111.27[kJ/mol]
H13	61.81[kJ/mol]
H14	-61.81[kJ/mol]
H15	-49.06[kJ/mol]
H16	49.06[kJ/mol]
H17	-110.86[kJ/mol]
H18	110.86[kJ/mol]
H19	31.98[kJ/mol]
H20	-31.98[kJ/mol]
H21	34.28[kJ/mol]
H22	-34.28[kJ/mol]
H23	-132.23[kJ/mol]

Name	Expression
H24	132.23[kJ/mol]
H25	-14.17[kJ/mol]
H26	14.17[kJ/mol]
H27	-3.88[kJ/mol]
H28	3.88[kJ/mol]
H29	44.67[kJ/mol]
H30	-44.67[kJ/mol]
H31	17.92[kJ/mol]
H32	-17.92[kJ/mol]
H33	-142.31[kJ/mol]
H34	142.31[kJ/mol]
H35	57.93[kJ/mol]
H36	-57.93[kJ/mol]
H37	106.48[kJ/mol]
H38	-106.48[kJ/mol]
H39	79.73[kJ/mol]
H40	-79.73[kJ/mol]
H41	-80.51[kJ/mol]
H42	80.51[kJ/mol]
chan_length	7[cm]
H_plate	0.2[mm]
cat_length_c	5[cm]
cat_thick_c	5[um]
cat_width_c	5[cm]
vol_bed_c	cat_thick_c*cat_width_c*cat_length_c
taw_c	1/sqrt(porosity)
porosity_c	0.4
rho_Al2O3	3.95[g/cm^3]
rho_cat_c	(1 - porosity_c)*rho_Al2O3
cat_amt_c	rho_cat_c*vol_bed_c
dpore_c	20[nm]
Rp_c	dpore_c/2
kappa_c	dpore_c^2*porosity_c/(32*taw_c)
s_fuel	709.55
B_fuel_ad	-1.529
A_O2_des	9.04E18[1/s]
B_O2_des	1.039
s_O2	6.86E-4
B_O2_ad	0.766
E_fuel_ad	9.6[kcal/mol]
E_O2	49.5[kcal/mol]
eO2	32[kcal/mol]
M_Pt	195.078[g/mol]
C_Pt	2.49E-5[mol/m^2]
Pt_percent	2.2
Disp_c	13
Pt_amt	cat_amt_c*(Pt_percent/100)
Asr_c	(Disp_c/100)*(Pt_amt/M_Pt)*(1/C_Pt)*(1/vol_bed_c)
cat_length	5[cm]
cat_thick	50[um]
cat_width	5[cm]
vol_bed	cat_length*cat_width*cat_thick
porosity	0.4
taw	1/sqrt(porosity)
rho_cat	(1 - porosity)*rho_Al2O3

Name	Expression
cat_amt	rho_cat*vol_bed
dpore	20[nm]
Rp	dpore/2
kappa	dpore^2*porosity/(32*taw)
Ni_loading	Ni_amt/(vol_bed)/Asr
Ni_percent	3.57
Disp	4
Ni_amt	cat_amt*Ni_percent/100
Asr	2.24E6[1/m]
kc0_g	8.3E5[1/s]
Ec_g	125.49[kJ/mol]
n_CH4	-0.3
n_O2	1.3

B2. Distributed grids applied to solve numerical models

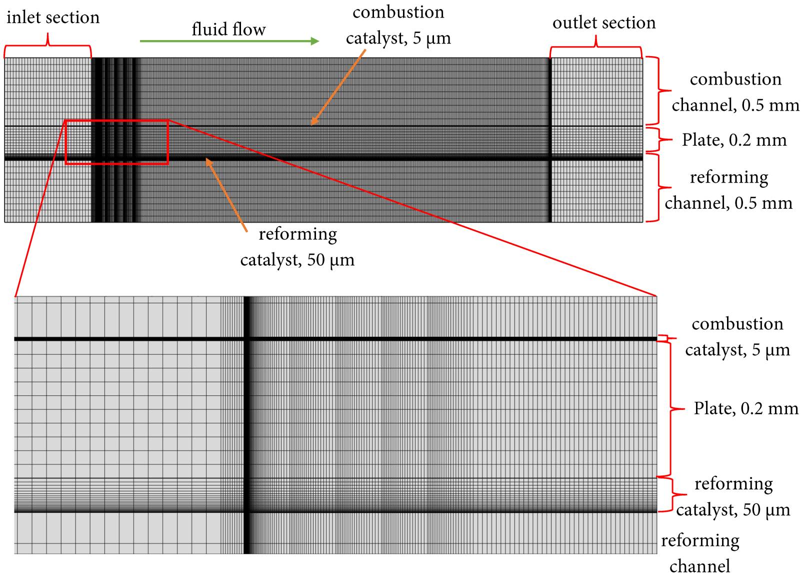

Appendix C

Experimental data of MSR over Ni-spinel catalyst

T	P	SC	W/FCH4in	CH4_in	CH4_in	H2O_in	N2_in	N2_out	CH4_out	H2O_out	CO_out	H2_out	CO2_out	X_CH4
[oC]	[psia]	[-]	[g*h/mol]	[ml/min]	[mol/min]	[mol/min]	[mol/min]	[mol/min]	[mol/min]	[mol/min]	[mol/min]	[mol/min]	[mol/min]	[%]
849.3	16	1.5	1.45	19.34	8.63E-04	1.30E-03	6.08E-03	6.08E-03	4.83E-05	4.60E-04	6.60E-04	2.31E-03	8.76E-05	94.4
851.4	17	1.5	0.80	35.27	1.57E-03	2.36E-03	1.18E-02	1.18E-02	2.85E-04	8.84E-04	1.05E-03	3.94E-03	2.12E-04	81.9
850.5	18	1.5	0.54	52.24	2.33E-03	3.50E-03	1.79E-02	1.79E-02	7.16E-04	1.52E-03	1.27E-03	5.11E-03	3.51E-04	69.3
853.1	19	1.5	0.41	68.51	3.06E-03	4.59E-03	2.37E-02	2.37E-02	1.32E-03	2.36E-03	1.34E-03	5.62E-03	4.46E-04	56.8
850.8	20	1.5	0.33	85.17	3.80E-03	5.70E-03	2.96E-02	2.96E-02	2.14E-03	3.47E-03	1.23E-03	5.47E-03	5.03E-04	43.6
803.6	16	1.5	1.45	19.33	8.63E-04	1.29E-03	6.08E-03	6.08E-03	8.30E-05	4.79E-04	6.13E-04	2.21E-03	1.01E-04	90.4
798.7	17	1.5	0.80	35.26	1.57E-03	2.36E-03	1.18E-02	1.18E-02	4.36E-04	1.01E-03	8.62E-04	3.47E-03	2.46E-04	72.3
801.4	18	1.5	0.54	52.23	2.33E-03	3.50E-03	1.78E-02	1.78E-02	1.03E-03	1.82E-03	9.29E-04	4.13E-03	3.76E-04	55.6
801.2	19	1.5	0.41	68.53	3.06E-03	4.59E-03	2.37E-02	2.37E-02	1.71E-03	2.74E-03	9.30E-04	4.45E-03	4.61E-04	44.2
799.9	20	1.5	0.33	85.16	3.80E-03	5.70E-03	2.96E-02	2.96E-02	2.51E-03	3.85E-03	8.53E-04	4.40E-03	4.98E-04	33.9
699.2	16	1.5	1.45	19.34	8.63E-04	1.30E-03	6.09E-03	6.09E-03	2.93E-04	6.36E-04	3.38E-04	1.60E-03	1.60E-04	66.1
701.6	16	1.5	1.04	26.94	1.20E-03	1.80E-03	8.89E-03	8.89E-03	5.62E-04	9.98E-04	3.56E-04	1.88E-03	2.25E-04	53.3
702.0	17	1.5	0.80	35.28	1.58E-03	2.36E-03	1.18E-02	1.18E-02	8.77E-04	1.43E-03	3.53E-04	2.13E-03	2.88E-04	44.3
702.0	17	1.5	0.54	52.26	2.33E-03	3.50E-03	1.79E-02	1.79E-02	1.65E-03	2.48E-03	3.15E-04	2.30E-03	3.53E-04	29.4
700.9	18	1.5	0.41	68.50	3.06E-03	4.59E-03	2.37E-02	2.37E-02	2.42E-03	3.56E-03	2.77E-04	2.32E-03	3.77E-04	20.8
850.6	16	1.25	1.26	22.25	9.93E-04	1.24E-03	5.77E-03	5.77E-03	4.41E-05	2.82E-04	8.31E-04	2.75E-03	6.46E-05	95.6
851.9	16	1.25	0.88	32.01	1.43E-03	1.79E-03	8.67E-03	8.67E-03	1.28E-04	4.05E-04	1.16E-03	4.00E-03	1.09E-04	91.0
850.0	18	1.25	0.54	51.88	2.32E-03	2.90E-03	1.44E-02	1.44E-02	4.34E-04	7.75E-04	1.67E-03	5.84E-03	2.27E-04	81.3
851.4	19	1.25	0.39	71.76	3.20E-03	4.00E-03	2.02E-02	2.02E-02	9.54E-04	1.34E-03	1.97E-03	7.22E-03	3.52E-04	70.2
851.9	20	1.25	0.31	91.67	4.09E-03	5.12E-03	2.60E-02	2.60E-02	1.66E-03	2.11E-03	2.05E-03	7.89E-03	4.78E-04	59.4
802.9	16	1.25	1.26	22.23	9.93E-04	1.24E-03	5.77E-03	5.77E-03	6.31E-05	2.86E-04	7.94E-04	2.70E-03	8.01E-05	93.6
798.8	16	1.25	0.88	32.02	1.43E-03	1.79E-03	8.67E-03	8.67E-03	1.93E-04	4.45E-04	1.06E-03	3.71E-03	1.40E-04	86.5
799.0	18	1.25	0.54	51.88	2.32E-03	2.89E-03	1.44E-02	1.44E-02	6.45E-04	9.18E-04	1.39E-03	5.26E-03	2.92E-04	72.2

802.3	19	1.25	0.39	71.77	3.20E-03	4.01E-03	2.02E-02	2.02E-02	1.30E-03	1.63E-03	1.54E-03	6.17E-03	4.20E-04	59.5
800.4	19	1.25	0.31	91.68	4.09E-03	5.12E-03	2.60E-02	2.60E-02	2.18E-03	2.57E-03	1.47E-03	6.33E-03	5.37E-04	46.8
698.9	16	1.25	1.26	22.24	9.93E-04	1.24E-03	5.77E-03	5.77E-03	3.76E-04	5.36E-04	4.01E-04	1.76E-03	1.52E-04	62.1
698.1	16	1.25	0.88	32.03	1.43E-03	1.79E-03	8.67E-03	8.67E-03	7.27E-04	9.20E-04	4.15E-04	2.08E-03	2.26E-04	49.2
699.5	17	1.25	0.54	51.90	2.32E-03	2.90E-03	1.44E-02	1.44E-02	1.55E-03	1.81E-03	4.24E-04	2.49E-03	3.32E-04	33.3
701.3	18	1.25	0.39	71.76	3.20E-03	4.00E-03	2.02E-02	2.02E-02	2.42E-03	2.85E-03	3.98E-04	2.61E-03	3.81E-04	24.6
699.9	19	1.25	0.31	91.69	4.09E-03	5.12E-03	2.60E-02	2.60E-02	3.39E-03	3.96E-03	3.39E-04	2.57E-03	4.07E-04	17.1

Appendix D

Matlab code for optimization of kinetic parameters

```
close all;
clear all;
clc;
tic;
global history
cc0 = [1 1 1 1 1 1 1 1 1 1 1 1];
history = [];
options = optimset('OutputFcn', @outfun,'Display','iter','MaxIter',5000,'TolFun',1e-6);
[x, fval] = fminsearch(@cstr_mk_series_run, cc0, options);
toc

function objective_value = cstr_mk_series_run(cc)
global R_gas T MCH4 MH2O MCO MH2 MCO2 MN2 MO2 u_feed rho_feed a_cross As C_Ni vflow_in v1
v2 v3 v4 v5 v6 v7 v8 v9 v10 v11 v12 v13 v14 c0 ctotal_14 F_flow_14
global km S11 S22 DET
          Input = [849.3   17.5    19.3    1.5     7.04
                   851.4   17.5    35.3    1.5     7.51
                   850.5   17.5    52.2    1.5     7.65
                   853.1   17.5    68.5    1.5     7.74
                   850.8   17.5    85.2    1.5     7.79
                   803.6   17.5    19.3    1.5     7.04
                   798.7   17.5    35.3    1.5     7.52
                   801.4   17.5    52.2    1.5     7.65
                   801.2   17.5    68.5    1.5     7.74
                   799.9   17.5    85.2    1.5     7.79
                   699.2   17.5    19.3    1.5     7.06
                   701.6   17.5    26.9    1.5     7.39
                   702.0   17.5    35.3    1.5     7.51
                   702.0   17.5    52.3    1.5     7.65
                   700.9   17.5    68.5    1.5     7.74
                   850.6   17.5    22.3    1.25    5.81
                   851.9   17.5    32.0    1.25    6.07
                   850.0   17.5    51.9    1.25    6.24
                   851.4   17.5    71.8    1.25    6.31
                   851.9   17.5    91.7    1.25    6.35
                   802.9   17.5    22.2    1.25    5.81
                   798.8   17.5    32.0    1.25    6.06
                   799.0   17.5    51.9    1.25    6.24
                   802.3   17.5    71.8    1.25    6.31
                   800.4   17.5    91.7    1.25    6.35
                   698.9   17.5    22.2    1.25    5.81
                   698.1   17.5    32.0    1.25    6.06
                   699.5   17.5    51.9    1.25    6.23
                   701.3   17.5    71.8    1.25    6.31
```

```
                    699.9    17.5      91.7       1.25       6.35];

FCH4_store = zeros(30,1); FH2O_store = zeros(30,1); FCO_store = zeros(30,1);
FH2_store = zeros(30,1); FCO2_store = zeros(30,1); FN2_store = zeros(30,1);

X_CH4_store = zeros(30,1);
CO2_CO_store = zeros(30,1);

 A1  =  1.0000E-02  ;
 A3  =  8.0000E-03  ;
 A4  =  1.0000E-01  ;
 A6  =  5.0000E-01  ;
 A7  = 2.5450E+19 ;
 A9  = 8.7050E+15 ;
 A10 =3.7320E+12 ;
 A12 = 3.5630E+11 ;
 A27 = 3.7000E+21 ;
 A28 = 6.0340E+21 ;
 A31 = 3.7000E+24 ;
 A32 = 4.0890E+24  ;

Km =     [A1*cc(1)                    0        0;                 % 1
          1.0000E-02                  0        0;                 % 2
           A3*cc(2)                   0        0;                 % 3
           A4*cc(3)                   0        0;                 % 4
           1.0000E-05                 0        0;                 % 5
          A6*cc(4)                    0        0;                 % 6
           A7*cc(5)                   0        81210;              % 7
          4.2830E+23                  0        474950;            % 8
           A9*cc(6)                   0        37550;             % 9
          A10*cc(7)                   0        60790;             % 10
          6.4470E+07                  0        25980;             % 11
          A12*cc(8)                   0        111270;            % 12
           5.0000E+22                 0        97900;              % 13
          1.7810E+21                  0        36090;             % 14
           3.0000E+20                 0        42700;             % 15
          2.2710E+21                  0        91760;             % 16
           3.0000E+21                 0        100000;            % 17
           6.3730E+23                 0        210860;            % 18
           5.2000E+23                 0        148100;            % 19
          1.3540E+22                  -3       116120;            % 20
           2.0000E+19                 0        123600;            % 21
          4.6530E+23                  -1       89320;             % 22
           3.7000E+21                 0        0;                 % 23
           4.0190E+20                 -1       132230;            % 24
          3.7000E+24                  -3       95800;             % 25
          4.6040E+20                  0        109970;            % 26
          A27*cc(9)                   0        57700;             % 27
           A28*cc(10)                 0        61580;             % 28
          3.7000E+24                  0        100000;            % 29
          1.2930E+23                  0        55330;             % 30
          A31*cc(11)           0        97100;            % 31
           A32*cc(12)          0        79180;            % 32
```

```
             3.7000E+21           0        18800;          % 33
            4.5620E+22           0        161110;         % 34
            1.7000E+24           0        88300;          % 35
            9.8760E+22           0        30370;          % 36
            3.7000E+24           0        130100;         % 37
            4.6070E+21           0        23620;          % 38
            3.7000E+24           0        126800;         % 39
            1.4570E+23           0        47070;          % 40
            3.7000E+21           0        48100;          % 41
            1.6250E+21           0        128610];        % 42

for inputindex=1:length(Input);
   T_reactor=Input(inputindex,1);
   P_reactor=Input(inputindex,2);
   CH4in_std=Input(inputindex,3);
   SC=Input(inputindex,4);
   N2_CH4=Input(inputindex,5);

H2Oin_std=SC*CH4in_std;                 % Inlet H2O at standard condition in [ml/min]
N2in_std=N2_CH4*CH4in_std;              % Inlet N2 at standard condition in [ml/min]
COin_std=0;                             % Inlet CO at standard condition in [ml/min]
H2in_std=0;                             % Inlet H2 at standard condition in [ml/min]
CO2in_std=0;                            % Inlet CO2 at standard condition in [ml/min]
O2in_std=0;                             % Inlet CO2 at standard condition in [ml/min]

volume=8.1126E-07;              % [m^3]
a_cross=9.36559E-05;            % [m^2]

v1=volume/14;
v2=volume/14;
v3=volume/14;
v4=volume/14;
v5=volume/14;
v6=volume/14;
v7=volume/14;
v8=volume/14;
v9=volume/14;
v10=volume/14;
v11=volume/14;
v12=volume/14;
v13=volume/14;
v14=volume/14;

As=3.25E+5;                     % Specific surface area [m^2/m^3],
C_Ni=2.6e-5;                    % Surface site density for Ni [mol/m^2]

T_std=273.15;                   % Standard temperature in Kelvine
P_std=101325;                   % Standard pressure in Pascal
T=T_reactor+273.15;             % Temperature of the reactor in Kelvine
P=P_reactor*6894.75729;         % Pressure of the reactor in Pascal
R_gas=8.3144621;                % Gas constant J/mol/K

% Volumetric flow rate at reactor temperature
```

```
CH4in_act=1e-6*(T/T_std)*(P_std/P)*CH4in_std/60;          % in [m^3/s]
H2Oin_act=1e-6*(T/T_std)*(P_std/P)*H2Oin_std/60;          % in [m^3/s]
N2in_act=1e-6*(T/T_std)*(P_std/P)*N2in_std/60;            % in [m^3/s]
COin_act=1e-6*(T/T_std)*(P_std/P)*COin_std/60;            % in [m^3/s]
H2in_act=1e-6*(T/T_std)*(P_std/P)*H2in_std/60;                      % in [m^3/s]
CO2in_act=1e-6*(T/T_std)*(P_std/P)*CO2in_std/60;          % in [m^3/s]
O2in_act=1e-6*(T/T_std)*(P_std/P)*O2in_std/60;            % in [m^3/s]

vflow_in=CH4in_act+H2Oin_act+N2in_act+COin_act+H2in_act+CO2in_act;
u_feed=vflow_in/a_cross;

% Molecular weight of chemical species
MCH4=0.01604;                   % Molecular weight of CH4  [kg/mol]
MH2O=0.01802;                   % Molecular weight of H2O  [kg/mol]
MCO=0.02801;                    % Molecular weight of CO   [kg/mol]
MH2=0.00202;                    % Molecular weight of H2   [kg/mol]
MCO2=0.04404;                   % Molecular weight of CO2  [kg/mol]
MO2 =0.032;                     % Molecular weight of O2   [kg/mol]
MN2=0.02802;                    % Molecular weight of N2   [kg/mol]

cfeed=P/R_gas/T;                % Feed concentration [mol/m^3]

% Molar flow rates
FCH4_0=CH4in_act*cfeed;                 % [mol/s]
FH2O_0=H2Oin_act*cfeed;                 % [mol/s]
FCO_0=COin_act*cfeed;                   % [mol/s]
FH2_0=H2in_act*cfeed;                   % [mol/s]
FCO2_0=CO2in_act*cfeed;                 % [mol/s]
FO2_0=O2in_act*cfeed;                   % [mol/s]
FN2_0=N2in_act*cfeed;                   % [mol/s]

F_total_in=FCH4_0+FH2O_0+FCO_0+FH2_0+FCO2_0+FN2_0;

% Inlet mole fractions
xCH4in=CH4in_act/vflow_in;              % Inlet mole fraction of CH4
xH2Oin=H2Oin_act/vflow_in;              % Inlet mole fraction of H2O
xCOin=COin_act/vflow_in;                % Inlet mole fraction of CO
xH2in=H2in_act/vflow_in;                % Inlet mole fraction of H2
xCO2in=CO2in_act/vflow_in;              % Inlet mole fraction of CO2
xO2in=O2in_act/vflow_in;                % Inlet mole fraction of O2
xN2in=N2in_act/vflow_in;                % Inlet mole fraction of N2
xtotal=xCH4in+xH2Oin+xCOin+xH2in+xCO2in+xO2in+xN2in;
Mavg=xCH4in*MCH4+xH2Oin*MH2O+xCOin*MCO+xH2in*MH2+xCO2in*MCO2+xO2in*MO2+xN2in*M
N2; % Average molecular weight of feed [kg/mol]

rho_feed=cfeed*Mavg;                    % feed density [kg/m^3]

cCH4in=xCH4in*cfeed;
cH2Oin=xH2Oin*cfeed;
cCOin=xCOin*cfeed;
cH2in=xH2in*cfeed;
cCO2in=xCO2in*cfeed;
cO2in=xO2in*cfeed;
```

```
cN2in=xN2in*cfeed;

tHin = 0;
tOin = 0;
tCH4in = 0;
tH2Oin = 0;
tCO2in = 0;
tCOin = 0;
tOHin = 0;
tCin = 0;
tCHin = 0;
tCH2in = 0;
tCH3in = 0;
tHCOin = 0;

c0=[cCH4in cH2Oin cCOin cH2in cCO2in cO2in cN2in tHin tOin tCH4in tH2Oin tCO2in tCOin tOHin tCin tCHin tCH2in tCH3in
tHCOin...
   cCH4in cH2Oin cCOin cH2in cCO2in cO2in cN2in tHin tOin tCH4in tH2Oin tCO2in tCOin tOHin tCin tCHin tCH2in tCH3in tHCOin...
   cCH4in cH2Oin cCOin cH2in cCO2in cO2in cN2in tHin tOin tCH4in tH2Oin tCO2in tCOin tOHin tCin tCHin tCH2in tCH3in tHCOin...
   cCH4in cH2Oin cCOin cH2in cCO2in cO2in cN2in tHin tOin tCH4in tH2Oin tCO2in tCOin tOHin tCin tCHin tCH2in tCH3in tHCOin...
   cCH4in cH2Oin cCOin cH2in cCO2in cO2in cN2in tHin tOin tCH4in tH2Oin tCO2in tCOin tOHin tCin tCHin tCH2in tCH3in tHCOin...
   cCH4in cH2Oin cCOin cH2in cCO2in cO2in cN2in tHin tOin tCH4in tH2Oin tCO2in tCOin tOHin tCin tCHin tCH2in tCH3in tHCOin...
   cCH4in cH2Oin cCOin cH2in cCO2in cO2in cN2in tHin tOin tCH4in tH2Oin tCO2in tCOin tOHin tCin tCHin tCH2in tCH3in tHCOin...
   cCH4in cH2Oin cCOin cH2in cCO2in cO2in cN2in tHin tOin tCH4in tH2Oin tCO2in tCOin tOHin tCin tCHin tCH2in tCH3in tHCOin...
   cCH4in cH2Oin cCOin cH2in cCO2in cO2in cN2in tHin tOin tCH4in tH2Oin tCO2in tCOin tOHin tCin tCHin tCH2in tCH3in tHCOin...
   cCH4in cH2Oin cCOin cH2in cCO2in cO2in cN2in tHin tOin tCH4in tH2Oin tCO2in tCOin tOHin tCin tCHin tCH2in tCH3in tHCOin...
   cCH4in cH2Oin cCOin cH2in cCO2in cO2in cN2in tHin tOin tCH4in tH2Oin tCO2in tCOin tOHin tCin tCHin tCH2in tCH3in tHCOin...
   cCH4in cH2Oin cCOin cH2in cCO2in cO2in cN2in tHin tOin tCH4in tH2Oin tCO2in tCOin tOHin tCin tCHin tCH2in tCH3in tHCOin...
   cCH4in cH2Oin cCOin cH2in cCO2in cO2in cN2in tHin tOin tCH4in tH2Oin tCO2in tCOin tOHin tCin tCHin tCH2in tCH3in tHCOin...
   cCH4in cH2Oin cCOin cH2in cCO2in cO2in cN2in tHin tOin tCH4in tH2Oin tCO2in tCOin tOHin tCin tCHin tCH2in tCH3in tHCOin];

%tspan = 0:1e-2:1;
tspan = [0 10];
abstolc = (1e-5*ones(266,1));
opts = odeset('Events',@event,'reltol',1e-5,'abstol',abstolc,...
   'Stats','off','Vectorized',{'on','off'}, 'NonNegative',ones(size(c0)));
[t,c]=ode15s(@cstr_mk_series,tspan,c0,opts);

n_CH4_14=length(c(:,248)); n_H2O_14=length(c(:,249)); n_CO_14=length(c(:,250));
n_H2_14=length(c(:,251));
n_CO2_14=length(c(:,252)); n_O2_14=length(c(:,253));  n_N2_14=length(c(:,254));

xCH4_14=c(n_CH4_14,248)/ctotal_14; xH2O_14=c(n_H2O_14,249)/ctotal_14;
xCO_14=c(n_CO_14,250)/ctotal_14; xH2_14=c(n_H2_14,251)/ctotal_14;
xCO2_14=c(n_CO2_14,252)/ctotal_14; xO2_14=c(n_O2_14,253)/ctotal_14;
xN2_14=c(n_N2_14,254)/ctotal_14;

F_CH4_14=xCH4_14*F_flow_14*60; F_H2O_14=xH2O_14*F_flow_14*60;
F_CO_14=xCO_14*F_flow_14*60; F_H2_14=xH2_14*F_flow_14*60;
F_CO2_14=xCO2_14*F_flow_14*60; F_O2_14=xO2_14*F_flow_14*60;
F_N2_14=xN2_14*F_flow_14*60;

FCH4_store(inputindex,1)=F_CH4_14;
FH2O_store(inputindex,1)=F_H2O_14;
FCO_store(inputindex,1)=F_CO_14;
FH2_store(inputindex,1)=F_H2_14;
```

```
FCO2_store(inputindex,1)=F_CO2_14;
FN2_store(inputindex,1)=F_N2_14;

X_CH4 = 100*(60*FCH4_0-F_CH4_14)/(60*FCH4_0);
CO2_CO=F_CO2_14/F_CO_14;

X_CH4_store(inputindex,1)=X_CH4;
CO2_CO_store(inputindex,1)=CO2_CO;

end

load expt;

objective_value=sqrt(sum(((expt(:,1)-FCO_store)./expt(:,1)).^2)+ sum(((expt(:,2)-
FCO2_store)./expt(:,2)).^2));
```